# The Oceanographic and Geochemical Effects of Mixed Layer Depth Variability and Increasing Anthropogenic $CO_2$ on the Inorganic Carbon System of the Coral Sea

Thesis submitted by

Jasmine Bernadette Denise Jaffrés BSc(Hons) QLD

In September 2011

for the degree of Doctor of Philosophy

in the School of School of Earth and Environmental Sciences

James Cook University

# STATEMENT OF ACCESS

I, the undersigned, the author of this thesis, understand that James Cook University of North Queensland will make it available for use within the University Library and, by microfilm or other means, allow access to users in other approved libraries. All users consulting this thesis will have to sign the following statement:

> In consulting this thesis I agree not to copy or closely paraphrase it in whole or in part without the written consent of the author; and to make proper public written acknowledgement for any assistance which I have obtained from it.

Substantial portions of this thesis may be used for international publication only if I am first author.

Beyond this, I do not wish to place any restrictions on access to this thesis.

…….. ……..

(Signature) (Date)

# STATEMENT OF SOURCES

# DECLARATION

I declare that this thesis is my own work and has not been submitted in any form for another degree or diploma at any university or other institution of tertiary education. Information derived from the published or unpublished work of others has been acknowledged in the text and a list of references is given.

# STATEMENT ON THE CONTRIBUTION OF OTHERS


| | | |
|---|---|---|
| Intellectual support | Proposal writing | Graham Shields, Dr (University College London, UK) |
| | Editorial assistance | Nick Oliver, Prof. (James Cook University, Australia)<br>Gregg Brunskill, Dr (James Cook University, Australia) |
| | technical support with ROMS | John Luick, Dr (SARDI, Australia)<br>Patrick Marchesiello, Dr (IRD, New Caledonia)<br>Jérôme Lefèvre, Dr (IRD, New Caledonia) |
| Financial support | Research grants | AIMS@JCU<br>Australian Research Council Research Network for Earth System Science (ARC NESS) |
| | Stipend | School of School of Earth and Environmental Sciences, James Cook University |


…….. ……..

(Signature) (Date)

# ACKNOWLEDGEMENTS

I wish to thank my supervisors Dr Gregg Brunskill, Dr Nick Oliver and Dr Michael Ridd, as well as Dr Graham Shields, for their patience and continuous support throughout my PhD. Particular thanks also to my research student monitor, Dr Peter Ridd, for the guidance during my PhD. I also would like to express my gratitude towards all those people who helped me in my modelling endeavour, including Dr John Luick, Dr Patrick Marchesiello, Dr Jérôme Lefèvre, Dr Christophe Menkes, Dr Cameron Huddlestone-Holmes, Dr Wayne Mallett, and Dr Yvette Everingham. Thanks also to the Laboratory of Physical Oceanography of the Institute of Research for Development (IRD) in Nouméa, New Caledonia, for their modelling and administrative support during my two visits. Finally, I would like to thank John Dawson, not only for his great computer skills (especially for his help with the multiple laptop and external hard drive failures and associated data retrievals), but also for the emotional support over the last five years. This work was financially supported by James Cook University (JCU), AIMS@JCU and the Australian Research Council Research Network for Earth System Science (ARC NESS).

# ABSTRACT

Global warming is predicted to result in a significant shallowing of the mixed layer depth (MLD) in many ocean regions and, thus, warmer surface waters (within the MLD), which could have dire consequences for coral reef ecosystems and the ocean's capability for $CO_2$ uptake. The seasonal to long-term variability of the MLD within the Coral Sea was examined using conductivity-temperature-depth (CTD) profiles from the World Ocean Database (WOD), and of Argo floats deposited within the Coral Sea or its vicinity since July 2001. A distinct seasonality in the MLD is evident throughout the Coral Sea, but was generally more pronounced in higher latitudes as a result of greater seasonality in sea surface temperature and wind stress. While summer mixed layers are relatively homogeneously shallow throughout the Coral Sea, winter mixed layers in higher latitudes tend to be significantly deeper compared to tropical regions. No long-term trends in mean monthly MLD are evident, possibly due to the relative data scarcity prior to the onset of the Argo project. The Argo program represents a significant advancement for marine studies. In the future, it will enable more detailed studies on long-term variability and trends of the MLD and its associated impact on the photic zone and the Great Barrier Reef.

Due to the absence of a similar program for ocean biogeochemistry, seasonal and long-term changes in fugacity of $CO_2$ ($fCO_2$) and $p$H within the Coral Sea were investigated not only using observational data (from WOD and other sources), but also with the sophisticated coupled regional model ROMS-PISCES. Both observational $fCO_2$ and $p$H exhibit some seasonality in the Coral Sea. Seawater $fCO_2$ ($fCO_2$sea) values tend to increase towards summer, which is linked to the positive relationship between fugacity and sea surface temperature. As a result, the capacity of the Coral Sea to act as a sink of atmospheric $CO_2$ is reduced during summer, and is more likely to act as a source of $CO_2$ to the atmosphere. No long-term changes were discernible in the very sporadically observed $p$H values, whereas $fCO_2$sea appears to have increased at a rate of 1.41 ± 0.04 μatm/year from 1983 to 2001.

As a result of increased atmospheric $CO_2$ levels, oceanic geochemistry has already significantly changed since 1880. The effects of higher atmospheric $fCO_2$ will likely be further aggravated by shallower MLDs as a result of reduced upper ocean mixing due to warmer sea surface temperatures. Various IPCC scenarios for predicted atmospheric $CO_2$

levels were used to determine likely changes in the geochemistry of the Coral Sea during the 21st century. Projected increases of atmospheric $CO_2$ to 650-1000 ppmv results in a decrease of sea surface *p*H by 0.14-0.38 units in the numerical model, with the Coral Sea simultaneously changing from a seasonal source of atmospheric $CO_2$ to a predominant sink. Concurrent with increased ocean acidification and $fCO_2$, the saturation state of aragonite and calcite will decline significantly, which would have wide-reaching effects on the coral calcification rates and the general health, and structural strength, of calcifying organisms. These biogeochemical effects will be exacerbated by an expected decrease in the MLD throughout the Coral Sea, and concomitant higher temperatures within the mixed layer. To this date, there has been surprisingly little effort to monitor the changes in biogeochemistry within the Coral Sea and, specifically, within the GBR as a result of increased atmospheric $fCO_2$. Further large-scale studies are required throughout the entire Coral Sea in order to accurately determine the long-term trends in the oceanic carbon cycle.

# TABLE OF CONTENTS

# LIST OF FIGURES AND TABLES

# 1 Introduction and Study Objectives

## 1.1 Background

The atmospheric $CO_2$ concentration has increased by more than 100 parts per million per volume (ppmv) from pre-industrial levels as a consequence of anthropogenic activities (e.g. fossil fuel burning, change in land use practices). The atmospheric $pCO_2$ concentration is now exceeding 380 µatm (Hoegh-Guldberg *et al.*, 2007), and it is forecast that $pCO_2$atm will increase to 650-1000 µatm by the end of the 21st century (Houghton *et al.*, 2001). Increasing atmospheric $pCO_2$ is having multi-faceted impacts, including on global warming and ocean circulation. If and to what extent higher greenhouse gas levels are influencing issues associated with climate change, such as ice melting, sea level rise and extreme weather events, are currently part of active debates (e.g. Hennessy *et al.*, 2007; Bamber *et al.*, 2009; Ivins, 2009).

There are numerous methods to measure past, present and future environmental changes to due natural and anthropogenic climate variability. Paleoclimate studies commonly involve isotope studies (e.g. boron, oxygen, carbon) of polar ice cores, marine carbonates (e.g. coral cores, brachiopods) and speleothems (e.g. Broecker and Peng, 1989; Ku and Li, 1998; Petit *et al.*, 1999; Joachimski *et al.*, 2005; Wilson *et al.*, 2006; Jaffrés *et al.*, 2007). Studies of current climate patterns include ship cruise measurements of physical and biogeochemical ocean properties, in-situ data collection by buoys and drifters, satellite based observations, and numerical modelling, of which the latter is regularly used for climate predictions.

As a result of increased atmospheric $pCO_2$ due to anthropogenic activities (e.g. fossil fuel burning, change in land use practices), oceanic biogeochemistry has already significantly changed since 1880, with *p*H levels in the surface ocean having decreased by 0.1 units as a result of higher oceanic $pCO_2$ (Wolf-Gladrow *et al.*, 1999). Concurrent with increased ocean acidification and $pCO_2$, the saturation state of seawater with respect to aragonite and calcite will decline significantly, which would have wide-reaching effects on the coral calcification rates and the general health, and structural strength, of calcifying organisms. Already now, several studies have found discernible effects such as greater frequency and severity in coral bleaching events, lower calcification rates and growth instability due to changing carbon chemistry (cf. section 4.4).

Global warming is also predicted to result in a significant shallowing of the mixed layer depth (MLD) due to increased upper ocean stratification and reduced mixing in many ocean regions, which could also have dire consequences for coral reef ecosystems and the ocean's capability for $CO_2$ uptake. A thinning MLD induces both a reduced nutrient supply from the deep ocean due to reduced mixing (resulting in lower primary productivity) and a greater susceptibility to warmer sea surface temperatures (SSTs).

To this date, there has been surprisingly little effort to monitor the changes in biogeochemistry within the Coral Sea and, specifically, within the Great Barrier Reef (GBR) as a result of increased atmospheric $pCO_2$. This is astonishing considering the high socio-economic value of the GBR to Australia (Fenton *et al.*, 2007), and the world as one of the great natural wonders.

## 1.2 Thesis Structure

### 1.2.1 Context

The impact and interaction of anthropogenic $CO_2$ is a very broad topic with rapid historical evolution of ideas and methods. It is also a very complex problem, with numerous interdisciplinary components and systems interacting with the carbon system (i.e. Earth System Science). As a result of the highly multifaceted nature of this matter, and the public and political interest in climate-related research, data collection and analysis is also very intricate.

Complex systems typically lend themselves to numerical modelling as the interactions are too convoluted to be solved empirically or analytically. Numerous modelling and observational studies have investigated patterns and trends of $pCO_2$ from reefal to global scale. However, no $CO_2$ study has specifically focused on the Coral Sea, and it is currently still unknown whether the Coral Sea is a net source or sink for atmospheric $CO_2$. Furthermore, no in-depth Coral Sea survey has been conducted about the variability of the marine homogenised near-surface zone or 'mixed layer', the thickness of which greatly impacts on the sea-air $CO_2$ flux.

### 1.2.2 Specific Aims

In order to address the research gaps outlined above, the specific aims of this study are to:

1. Determine and present all major parameters and systems affecting carbon chemistry of the Coral Sea in order to assess which factors to focus the thesis on.
2. Obtain the most accurate mixed layer depth.
3. Evaluate whether the mixed layer depth and heat content within the Coral Sea display any seasonal or long-term changes, which would affect carbon chemistry.
4. Determine the overall patterns and seasonality of carbon chemistry within the Coral Sea.
5. Forecast potential changes in mixed layer depth and carbon chemistry based on various atmospheric $CO_2$ level scenarios.
6. Evaluate the skill of the model to represent the Coral Sea physics and geochemistry accurately by comparing modelling and observational results.

### 1.2.3 Thesis Methods

In order to address the research aims outlined above, the specific aims of this study are to:

1. Provide an in-depth review of all aspects affecting mixed layers and carbon chemistry of the Coral Sea.
2. Assess the importance of method used to derive the mixed layer depth.
3. Evaluate the seasonal and long-term variability of the mixed layer depth and heat content within the Coral Sea based on observational data.
4. Collect all available observational Coral Sea carbon data for a preliminary estimation of overall patterns and seasonal variability of carbon chemistry.
5. Employ a coupled high-resolution regional model to investigate seasonal and centennial changes in mixed layer depth and carbon chemistry.
6. Compare modelling and observational results.

### 1.2.4 Thesis Outline

The thesis is structured into five main sections. In chapter 1 (this chapter), the context of the overall thesis is defined, the aims stated and a brief chapter outline given. In addition, an extensive literature review (chapters 2-4) is presented that covers many aspects of Earth System Science affecting carbon chemistry, including sea-air $CO_2$ flux, the mixed layer, and possible impacts of rising $CO_2$. The study site is introduced in chapter 5. Chapter 6 then considers seasonal to multi-decadal mixed layer variability in the Coral Sea. Variability of carbon chemistry (e.g. $fCO_2$) in the Coral Sea is presented in chapter 7. These empirical records are followed by chapter 8, which contains numerical methods, as well as comparison of results from previous chapters and numerical modelling. In chapter 9, final discussions and conclusions are presented.

In appendix A1, a glossary lists and defines terms and symbols. MATLAB scripts used for the Giovanni-satellite data are provided in appendix A2. Model descriptions are given in appendices A3 (CO2SYS) and A4 (ROMS-PISCES).

# 2 Sea-Air $CO_2$ Flux

## 2.1 Atmospheric $CO_2$

For decades, the rapidly rising atmospheric $CO_2$ due to anthropogenic fossil fuel burning (6.5 Pg C/yr; Steffen, 2006) has lead to widespread concern about the impact and pathways of $CO_2$. Rising atmospheric $CO_2$ levels over the industrial period have led to increased $CO_2$ uptake by the oceans (Feely *et al.*, 2004). Over this period, anthropogenic emissions into the atmosphere accumulated to about 290 Pg C (cf. Marland *et al.*, 2005). At present, the atmospheric $CO_2$ concentration is around 380 ppmv (Figure 2.1.1; Feely *et al.*, 2004; Sabine *et al.*, 2004; Blackford and Gilbert, 2007), while in the Last Glacial Maximum, the concentration was around 195 ppmv (Barnola *et al.*, 1987; Broecker and Peng, 1989; Petit *et al.*, 1999; Smith *et al.*, 1999). It is expected that atmospheric $CO_2$ will reach more than twice pre-industrial levels (~280 ppmv in 1750; Siegenthaler and Oeschger, 1987; Etheridge *et al.*, 1996; Sarmiento *et al.*, 2000; Houghton *et al.*, 2001; Caldeira and Wickett, 2003) by the end of the 21st century (Houghton *et al.*, 2001). The upper limit of atmospheric $CO_2$ is assumed to be around 2000 ppmv (cf. Caldeira and Wickett, 2003: their Fig. 1). Currently, the atmospheric $CO_2$ concentration is increasing at a rate of about 0.4%/yr (Houghton *et al.*, 2001), or at about 1.4 ppmv/yr (Conway *et al.*, 1994).

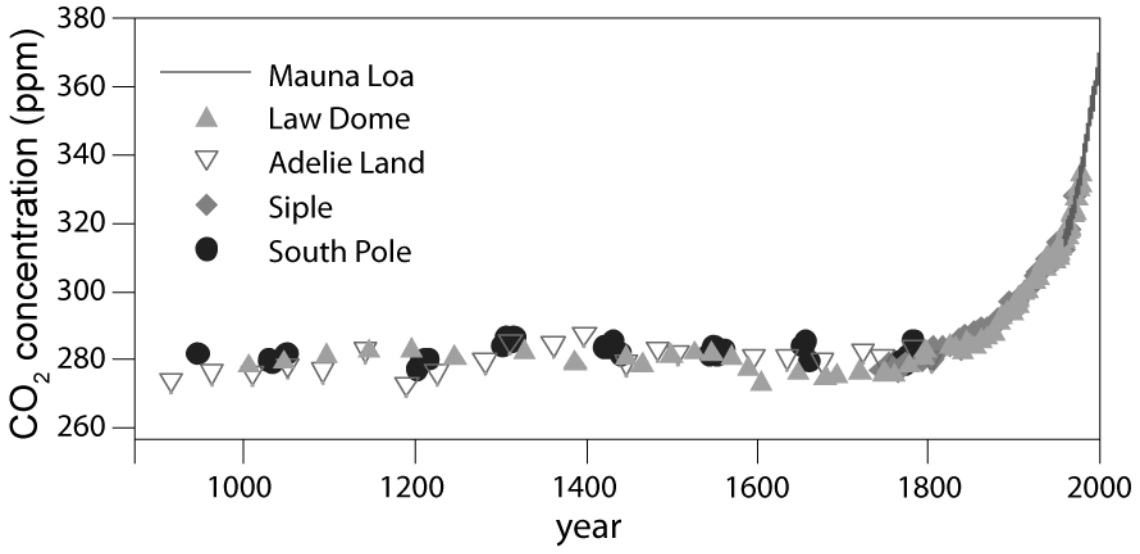


**Figure 2.1.1. Evolution of atmospheric $CO_2$ levels since 900 B.C. The data shown is based on ice core data with the exception of the Mauna Loa data, which is derived from direct measurements (figure adapted from Houghton *et al.*, 2001).**

## 2.2 Oceanic $CO_2$ Uptake

In the recent years, ocean acidification due to oceanic $CO_2$ uptake has received a lot of publicity. The tracing of the increasing oceanic $CO_2$ concentrations, [$CO_2$], was made possible by the capability to separate the oceanic uptake of fossil fuel $CO_2$ from the natural background of dissolved inorganic carbon (DIC) (Brewer, 1978; Gruber *et al.*, 1996). Only about 50% of released anthropogenic $CO_2$ (about 2 µatm/yr in recent times; Takahashi *et al.*, 1997; Wong and Matear, 1998) remains in the atmosphere, 20-30% being consumed by the (northern) terrestrial ecosystems (Keeling *et al.*, 1996; Prentice *et al.*, 2001; Sabine *et al.*, 2004). About 25-35% of anthropogenic $CO_2$ emissions are absorbed by the ocean, which helps to moderate the effect of anthropogenic $CO_2$ emissions (e.g. Callendar, 1938; Broecker *et al.*, 1979; Keeling *et al.*, 1996; Takahashi *et al.*, 1997; Matear, 2001; Prentice *et al.*, 2001; Sabine *et al.*, 2004).

It is estimated that the net anthropogenic $CO_2$ flux into the ocean over the 1980s and 1990s ranged from 1.5-2.4 Pg C/yr (1 Gt C = 1 Pg C = $1 \cdot 10^{15}$ g C = $83.26 \cdot 10^{12}$ mol C) (Tans *et al.*, 1990; Sarmiento and Sundquist, 1992; Keeling *et al.*, 1996; Battle *et al.*, 2000; Sarmiento *et al.*, 2000; Gruber and Keeling, 2001; Matear, 2001; Orr *et al.*, 2001; Prentice *et al.*, 2001; Bopp *et al.*, 2002; Dufresne *et al.*, 2002; Keeling and Garcia, 2002; Plattner *et al.*, 2002; Gloor *et al.*, 2003; McNeil *et al.*, 2003; Quay *et al.*, 2003; Matsumoto *et al.*, 2004; Mikaloff Fletcher *et al.*, 2006; Naegler *et al.*, 2006; Jacobson *et al.*, 2007a; Sweeney *et al.*, 2007), whereas atmospheric $CO_2$ has increased by 1.49 ppmv/yr from 1976 to 1995 (cf. Takahashi *et al.*, 2003). Generally, higher atmospheric [$CO_2$] are found in the northern hemisphere than in the southern hemisphere (Fan *et al.*, 1999). Currently, the rate of oceanic $CO_2$ uptake is 2-2.5 Pg C/yr (Nakayama *et al.*, 2005), while the land carbon sink in the northern hemisphere is approximated to be about 1.7 Pg C/yr (Fan *et al.*, 1998; Gloor *et al.*, 2003). Since 1800, an estimated 118 ± 19 Pg C has been taken up by the ocean until 1994 (Sabine *et al.*, 2004). Without this oceanic $CO_2$ uptake, current atmospheric $CO_2$ levels would be around 55 ppmv higher (Sabine *et al.*, 2004). The Southern Ocean (SO) plays an important part in the oceanic $CO_2$ uptake, with estimates ranging from 30-50% of the global uptake (south of 30°S; cf. Orr *et al.*, 2001; Thomas *et al.*, 2001). The total sea surface [$CO_2$] varies between around 2150 µmol/kg in polar waters and 1850 µmol/kg in the tropics (Takahashi *et al.*, 2002).

### 2.2.1 Sea-Air Flux Calculation

The magnitude of the $CO_2$ flux is determined by the product of the sea-air $pCO_2$ (partial pressure of $CO_2$) difference and the gas exchange coefficient K (Etcheto and Merlivat, 1988; Frankignoulle *et al.*, 1996a; Dore *et al.*, 2003), the latter of which is commonly parameterised as a function of wind speed (Wanninkhof, 1992; Wanninkhof and McGillis, 1999; Krakauer *et al.*, 2006; Fangohr *et al.*, 2008). The sea-air $pCO_2$ difference controls the direction and magnitude of the sea-air flux of $CO_2$, whereas K determines the rate of $CO_2$ exchange (Smith, 1985; Wanninkhof, 1992; Bates and Merlivat, 2001; Bates, 2002a). The net sea-air $pCO_2$ flux (F) can be expressed as

$$F = K*(\Delta pCO_2)_{sea\text{-}air} = k*s*(\Delta pCO_2)_{sea\text{-}air}$$ (Henry's Law), where

k is the $pCO_2$ gas transfer velocity, s is the solubility of $CO_2$ in seawater (see also Figure 2.2.1), and $(\Delta pCO_2)_{sea\text{-}air}$ is the $pCO_2$ difference between the ocean and atmosphere (Frankignoulle *et al.*, 1996a; 1996b; Feely *et al.*, 1997; Takahashi *et al.*, 2002). Both k and s are temperature-dependent, but vary in the opposite direction (Etcheto and Merlivat, 1988).

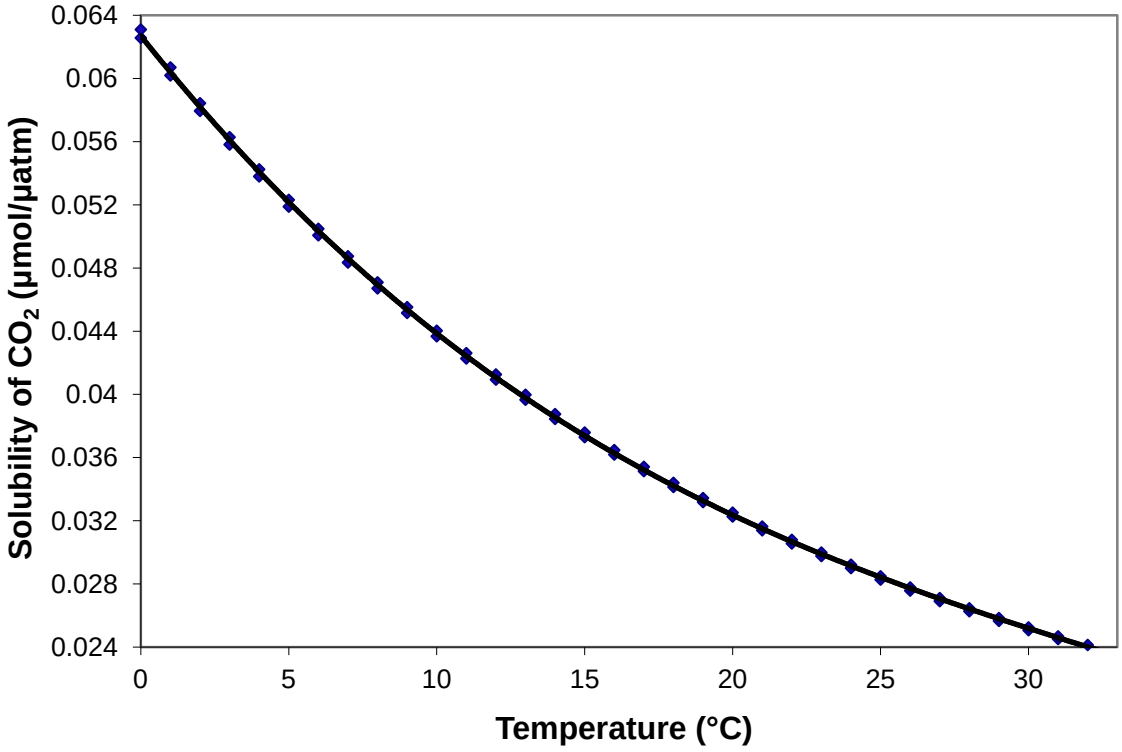


**Figure 2.2.1. Solubility of $CO_2$ as a function of temperature. Salinity values of 34.4 and 35.8 were utilised at each temperature point. The relationship between $CO_2$ solubility and temperature was derived with the constants of Weiss (1974) for the solubility of $CO_2$. The $CO_2$ solubility decreases exponentially with an increase in temperature, whereas salinity has a relatively minor influence on $CO_2$ solubility.**

### 2.2.2 Physical Parameters

Globally, the seasonal and geographical variability of sea surface $pCO_2$ is much greater than in the atmosphere (Weiss *et al.*, 1982; Takahashi *et al.*, 2002; Borges and Frankignoulle, 2003: Fig. 7a; González-Dávila *et al.*, 2003: Fig. 3f) such that the direction and magnitude of the $CO_2$ flux between the ocean and atmosphere are predominantly controlled by marine $pCO_2$. In the open ocean, sea surface $pCO_2$ varies geographically and seasonally over a wide range from about 150 to 550 µatm (Takahashi *et al.*, 2002). Significantly large interannual variability of $pCO_2$ (>100 µatm) can be caused by shifts in the location of upwelled waters and warm pool waters (Boutin *et al.*, 1999). Large differences in $pCO_2$ (~100-700 ppmv) are also observed in coastal regions (cf. Frankignoulle *et al.*, 1996a; Borges, 2005), potentially resulting in large $pCO_2$ fluxes

across the sea-air interface (Frankignoulle *et al.*, 1996a; Borges, 2005; Borges *et al.*, 2005). Oceanic $CO_2$ also varies diurnally, with $pCO_2$ increasing in the night due to plant respiration, and decreasing during daytime as a result of photosynthesis (Frankignoulle and Borges, 2001; Shirayama and Thornton, 2005).

The gas transfer velocity is dependent on various physical parameters including turbulence, the degree of mixing of the water layer, bubbles, and wind speed (Table 2.2.1) (Smith, 1985; Liss and Merlivat, 1986; Nightingale *et al.*, 2000; Bates and Merlivat, 2001; Takahashi *et al.*, 2002; Borges *et al.*, 2004). The total anthropogenic $CO_2$ uptake is dominated by both zonal wind stress and MLD (Friedrich *et al.*, 2006; Mignone *et al.*, 2006). Wind patterns in the southern hemisphere strongly influence the regional distribution of anthropogenic $CO_2$ uptake and the gas transfer rate by altering the magnitude of the northward Ekman volume transport out of the Southern Ocean, and, thus, the residence time of $CO_2$ at the Southern Ocean surface (Takahashi *et al.*, 2003; Mignone *et al.*, 2006). Some studies (e.g. Wanninkhof *et al.*, 2001) have shown that the usage of daily to monthly wind speed data and/or the use of monthly air pressure data might result in substantial bias in the $CO_2$ flux estimate due to the non-linear wind-$CO_2$ flux relationship (e.g. Bates and Merlivat, 2001) and the negative correlation of wind speed and air pressure (cf. Kettle and Merchant, 2005). The net sea-air flux is also governed by sea surface temperature (SST), salinity and changes in total carbon dioxide ($tCO_2$) or alkalinity (Bates *et al.*, 1998; Takahashi *et al.*, 2003; Lee *et al.*, 2006; McKinley *et al.*, 2006). Increasing water temperature raises $pCO_2$ (Ishii, 2001; Dore *et al.*, 2003), resulting in a doubling of $pCO_2$ in the sea surface for every 16°C increase (Takahashi *et al.*, 2002). Whereas water temperature is mainly regulated by physical processes (i.e. solar energy input, sea-air heat exchange, and the mixed layer depth, see also chapter 3) (Takahashi *et al.*, 2002), $tCO_2$ and alkalinity are predominantly regulated by biological processes (i.e. photosynthesis, respiration, calcification and dissolution) and by upwelling of $CO_2$- and nutrient-rich subsurface water (Gruber *et al.*, 1996; Lee *et al.*, 2006).

**Table 2.2.1. Processes affecting oceanic $CO_2$ uptake that are reported in the literature cited.**

| physical processes | biological and chemical processes |
|---|---|
| temperature ($CO_2$ solubility) | biological pump |
| continental shelf pump | calcification/dissolution |
| stratification/mixed layer thickness | respiration |
| solubility pump | plant decay |
| wind speed | photosynthesis |
| turbulence | *p*H |
| air bubbles | sea-air $\Delta pCO_2$ |
| skin layer thickness | remineralisation |
| upwelling/downwelling | |

## 2.3 $CO_2$ Flux into the Deep Ocean - Vertical, Diapycnal and Isopycnal Diffusion

The air-sea $CO_2$ exchange is also strongly influenced by the rate at which $CO_2$ is transported into the deep ocean by ocean circulation and mixing (Broecker and Peng, 1982; Morse and Mackenzie, 1990; Joos *et al*., 1991; Wong and Matear, 1998; Matear, 2001), whereby freshwater forcing (i.e. precipitation, river discharge, ice) in the Southern Ocean plays a significant role on global deep water properties (Schmittner *et al*., 2005). The ocean mixes on time-scales of ten to hundreds of years (Gloor *et al.*, 2003), whereas the upper equatorial ocean currents tend to adjust to wind changes on a 1-2 year timescale (Philander, 1979; Dawe and Thompson, 2006). Similarly, atmospheric $CO_2$ is equilibrated with the mixed layer region within one year (Broecker and Peng, 1982; Wong and Matear, 1998; Wolf-Gladrow *et al.*, 1999; Sarmiento *et al.*, 2000).

The factors affecting the distribution of $CO_2$ in the ocean interior are freshwater in the sea surface, vertical diffusivity ($K_v$), isopycnal advection, convection, as well as downwelling and upwelling (Wong and Matear, 1998). Usually, a $CO_2$ flux into the ocean occurs in downwelling zones and flux into the atmosphere in upwelling regions (Broecker and Peng, 1982). Thus, downwelling at temperate latitudes is linked to the deepest $CO_2$ transport into the ocean whereas upwelling regions such as the eastern equatorial Pacific are characterised by low vertical $CO_2$ penetration (Sabine *et al.*, 2004).

Freshwater forcing in the Southern Ocean and diapycnal mixing in the low-latitude pycnocline play an important role in determining the properties (e.g. heat, salinity and $CO_2$ concentration) and circulation of the global deep water masses (Schmittner *et al*.,

2005). High mixing rates (diapycnal diffusivity > $10^{-4}$ $m^2/s$) in the deep Southern Ocean (Heywood *et al.*, 2002; Naveira Garabato *et al.*, 2004) have a much more limited impact (cf. Schmittner *et al*., 2005).

Minimal movement of $CO_2$-rich waters into the ocean interior generally also occurs at equatorial locations due to the isopycnal layers in the tropical thermocline being shallow and thin, thus inhibiting vertical mixing (Sabine *et al.*, 2004). The marine thermocline properties depend on mixing along and across surfaces of equal density (isopycnal and diapycnal surfaces, respectively) (Ledwell *et al.*, 1993). Thermohaline circulation is significantly regulated by the strength of diapycnal mixing, especially in the Southern Ocean and the North Pacific (Saenko and Merryfield, 2005). The strength of diapycnal mixing, in turn, is dependent on the amount of turbulent kinetic energy provided by winds and tides (Cameron *et al*., 2005). The $CO_2$ transport occurs mainly along isopycnal surfaces (Sabine *et al*., 2004). Vertical mixing, in turn, is important in the transfer of dissolved $CO_2$ in the interior of the oceans (Wong and Matear, 1996). The effectiveness of turbulent vertical mixing in the ocean is linked to the eddy or diapycnal diffusivity ($K_v$) (Wong and Matear, 1996; St. Laurent *et al.*, 2002). Diapycnal mixing is very slow over most of the ocean ($K_v$ ~0.1-0.3 × $10^{-4}$ $m^2/s$) (Ledwell *et al.*, 1993; 1998; Schmittner *et al.*, 2005). Little mixing (~$10^{-5}$ $m^2/s$) occurs in the ocean interior, whereas mixing is enhanced ($\geq$ $10^{-4}$ $m^2/s$) over rough topography (Polzin *et al.*, 1997; Ganachaud and Wunsch, 2000; Ledwell *et al.*, 2000; Naveira Garabato *et al.*, 2004; Saenko and Merryfield, 2005). High values of $K_v$ are also linked to more intense equatorial upwelling (Gnanadesikan, 1999; Schmittner *et al*., 2005).

The deep ocean contains much higher $pCO_2$ and DIC levels than the mixed layer, with [$CO_2$] of both the intermediate and deep ocean waters exceeding the current atmospheric $CO_2$ concentration (Takahashi, 1989: Fig. 1; Wong and Matear, 1998). The deep Pacific (>3000 m) already contains 500-600 μatm, whereas the intermediate ocean (1000-1500 m) is supersaturated with $CO_2$ ranging from 1000 to 1200 μatm (Wong and Matear, 1998) due to the decomposition of particulate organic matter raining down from the surface (e.g. Cameron *et al*., 2005). About 30% of the anthropogenic $CO_2$ (as opposed to total $CO_2$) is located at depths shallower than 200 m and nearly 50% at depths above

400 m (Sabine *et al.*, 2004). Currently, only 7% of the total oceanic anthropogenic $CO_2$ inventory is located deeper than 1500 m (Sabine *et al.*, 2004).

## 2.4 Dissolved Inorganic Carbon Pumps

The air-sea $CO_2$ exchange and the $CO_2$ flux into the deep ocean is also significantly affected by DIC pumps, which remove DIC from the surface and result in higher $CO_2$ levels in the deep ocean (c.f. Volk and Hoffert, 1985; Sarmiento *et al.*, 1988; Takahashi, 1989; Archer *et al.*, 1996; Wolf-Gladrow *et al.*, 1999). $CO_2$ is transported to the deep ocean through both the solubility pump and the biological pump (e.g. Volk and Hoffert, 1985; Broecker and Henderson, 1998; Palmer and Totterdell, 2001). The absolute and relative strengths and net impact on atmospheric $CO_2$ of the pumps depend on the ocean circulation (Cameron *et al.*, 2005). The organic pump and the solubility pump are generally believed to have a greater impact on $CO_2$ than the carbonate ($CO_3^{2-}$) pump (Volk and Hoffert, 1985; Archer *et al.*, 1996; Cameron *et al*., 2005). A modelling study indicated that atmospheric $CO_2$ would be significantly higher (525 ppmv) in the absences of all pumps (Cameron *et al*., 2005).

### 2.4.1 Biological Pump

The soft-tissue (organic) pump and the hard tissue pump (also called carbonate or alkalinity pump) are usually grouped together and named the biological pump (e.g. Sarmiento *et al*., 2000; Palmer and Totterdell, 2001; Iglesias-Rodriguez *et al.*, 2002a; Cameron *et al*., 2005). The carbonate pump is also known as the counter pump since it exerts an opposite effect on atmospheric $CO_2$ to the organic pump (cf. Cameron *et al*., 2005). The soft-tissue pump and the carbonate pump result from the biological flux of dissolved and particulate organic carbon (DOC and POC, respectively) and calcium carbonate ($CaCO_3$) from the sea surface (Volk and Hoffert, 1985; Toggweiler and Carson, 1995). The carbonate pump tends to increase atmospheric $CO_2$ since it removes two moles of alkalinity from the sea surface for each mole of carbon (Smith and Kinsey, 1978), therefore shifting the carbonate system equilibrium toward higher [$CO_2$] (Zondervan *et al.*, 2001; Cameron *et al*., 2005). Reducing the $C_{CaCO3}$:$C_{org}$ export ratio by either increasing the organic pump or decreasing the carbonate pump enhances $CO_2$

storage in the deep ocean via increased $CO_2$ removal from the surface ocean (Iglesias-Rodriguez *et al.*, 2002a), and, thus, causes a decrease in atmospheric $CO_2$ (Sigman and Boyle, 2000). The global average export ratio is estimated to be around 0.06 ± 0.03 (Sarmiento *et al.*, 2002), with higher ratios occurring towards the equator (Koeve, 2002; Sarmiento *et al.*, 2002).

The biological pump stems from the removal of carbonate minerals (i.e. biogenically precipitated $CaCO_3$ and photosynthetically produced material) from the euphotic zone, and their dissolution, deposition and burial in deep-sea sediments (Broecker and Peng, 1982; Morse and Mackenzie, 1990; Archer and Maier-Reimer, 1994; Wong and Matear, 1998; Milliman *et al.*, 1999; Wolf-Gladrow *et al.*, 1999; Sigman and Boyle, 2000). Production of organic matter through photosynthesis removes DIC from the euphotic zone (Sarmiento *et al.*, 2000; Schmittner *et al.*, 2005), most of which is exported by diatoms (Cermeño *et al.*, 2008). Since much of the organic material remineralises after sinking to deeper levels (e.g. Sarmiento *et al.*, 2000), biological activity retains atmospheric $CO_2$ at a lower concentration than it would be in the absence of the biological pump (Raven, 1993; Schmittner *et al.*, 2005).

### 2.4.2 Solubility Pump

Another DIC pump is the temperature-dependent solubility (or physical) pump (e.g. Broecker and Henderson, 1998). The solubility pump stems from increased $CO_2$ solubility in downwelling cold water (cf. Weiss, 1974; Volk and Hoffert, 1985; Murnane *et al.*, 1999; Wolf-Gladrow *et al.*, 1999). The strength of the solubility pump is directly related to the meridional SST gradient and inversely related to the mean deep ocean temperature (Cameron *et al.*, 2005). Therefore, the locations with the weakest SST gradients and the warmest deep ocean temperatures have the weakest solubility pump. The $pCO_2$ sensitivity to temperature change is determined to be 4.23% $pCO_2$/ºC (or ~10 μatm/ºC) if the effects of circulation and the biological pump are excluded (Archer *et al.*, 2004). The solubility pump's downward vertical movement of water mainly occurs in the Polar Regions (Volk and Hoffert, 1985).

The temperature-dependent solubility of $CO_2$ also results in a horizontal solubility gradient, with greater solubility occurring in cold, high-latitude seawater (Archer *et al.*,

2000). Conversely, upwelling of cold, $CO_2$-rich deep waters in equatorial regions leads to a $CO_2$ flux into the atmosphere due to the warming of the upwelled water and the consequent decrease in $CO_2$ solubility (Murnane *et al.*, 1999).

### 2.4.3 Continental Shelf Pump

The uptake of $CO_2$ is also facilitated by the 'continental shelf pump', first described by Tsunogai *et al.* (1999). Water in shallow continental shelf areas is cooled more rapidly after releasing heat to the atmosphere than surface water of the open ocean since less water is available for convection of cool water (Tsunogai *et al.*, 1999). The most important impact of this decrease in SST, which simultaneously also augments the uptake of atmospheric $CO_2$ due to greater solubility, is an increase in density of near coastal waters. Due to the resulting pressure gradient, $CO_2$ is moved from the shelf to the open ocean via isopycnal mixing (including advection and diffusion) (Tsunogai *et al.*, 1999). Warm, tropical regions may have a weaker continental shelf pump (Tsunogai *et al.*, 1999) due to increased stratification inhibiting the mixing of surface and deeper water. An estimated 1 Gt C/yr may be removed from the global shelf area via this process (Tsunogai *et al.*, 1999).

## 2.5 Skin Effect

Satellite measurements of SST may lead to an underestimation of $CO_2$ uptake (Mobasheri, 1995). The upper 0.05-2 mm of the subtropical and tropical oceans represents a skin, which is normally cooler than the bulk mixed layer by about 0.2-0.3°C due to the upward heat flux (Saunders, 1967; Katsaros, 1980; Simpson and Paulson, 1980: Fig. 1; Schluessel *et al.*, 1990; Robertson and Watson, 1992; Mobasheri, 1995; Donlon *et al.*, 2002). Its thickness is a function of local heat flux and wind speed, and it perseveres at wind speeds up to at least 10 m/s (cf. Robertson and Watson, 1992). It rapidly re-forms within 10-12 s (Katsaros, 1977) once the wind speed drops to below 10 m/s. The cool skin is produced and maintained via the loss of radiant and latent heat (via evaporation; Saunders, 1967), with the outgoing thermal flux balancing incoming radiant heating (Robertson and Watson, 1992).

The skin effect (slightly higher solubility due to colder temperature; cf. Weiss, 1974) results in an additional oceanic uptake of about 0.4 Gt C/yr (Van Scoy *et al.*, 1995). However, Zhang and Cai (2007) derived a much lower effect of the cool skin layer, which, in addition, is nearly entirely counteracted by the so called salty-skin effect, so that the net impact of the two skin layer types on the oceanic $CO_2$ uptake is negligible.

## 2.6 Regional Sinks and Sources – Past and Present

The pre-industrial ocean was generally a net source of atmospheric $CO_2$ (Sabine and Mackenzie, 1991; Andersson and Mackenzie, 2004; Mackenzie *et al.*, 2004), with outgassing occurring at low latitudes and uptake at temperate and high latitudes (Gloor *et al.*, 2003). The rise in atmospheric $CO_2$ concentrations and the increase in inorganic nutrient load has led to a reversal of the direction of the $CO_2$ flux, resulting in the ocean being a net sink of anthropogenic $CO_2$ (Sabine and Mackenzie, 1991; Andersson and Mackenzie, 2004; Mackenzie *et al.*, 2004). Temperate and high-latitude northern and southern oceans contribute most significantly to the removal of atmospheric $CO_2$, whereas the equatorial oceans are the dominant $CO_2$ sources (Tans *et al.*, 1990; Quay, 1997; Takahashi *et al.*, 1997; 2002; Feely *et al.*, 1999; 2002; Gurney *et al.*, 2002; Gloor *et al.*, 2003; Patra *et al.*, 2005; Cai *et al.*, 2006; Jacobson *et al.*, 2007b).

The equatorial oceans between 15°N and 15°S constitute a net flux of 0.6-l.6 Pg C/yr (Tans *et al.*, 1990: Table 2; Feely *et al.*, 1999; Takahashi *et al.*, 2002: Fig. 2; Patra *et al.*, 2005; Jacobson *et al.*, 2007b). The equatorial Pacific is currently the largest oceanic source of $CO_2$ to the atmosphere, with up to 72% of the equatorial sea-air flux being emitted from this region (Tans *et al.*, 1990: Table 2; Feely *et al.*, 1999; 2002; McPhaden and Zhang, 2002). Most of this $CO_2$ evasion occurs in the central and eastern equatorial Pacific between 0ºS and 10ºS (Feely *et al.*, 1995; 1997; Takahashi *et al.*, 1997; Le Borgne *et al.*, 2002; Takahashi *et al.*, 2002). This efflux is linked to the upwelling of the $CO_2$- and nutrient-rich Equatorial Undercurrent (Harrison, 1996) to the sea surface, which results in high seawater $pCO_2$ and high nutrient concentrations (Chavez and Toggweiler, 1995; Toggweiler and Carson, 1995; Feely *et al.*, 1997; 1999). The trend of decreasing surface $pCO_2$ from east to west in the equatorial Pacific Ocean is consistent with biological utilisation of $CO_2$, a deepening of the thermocline and reduced upwelling

from east to west along the equator linked to easterly trade winds (Philander, 1979; Feely *et al.*, 1997; Le Borgne *et al.*, 2002; Takahashi *et al*., 2002). Upwelling at the equator has a major impact on the carbon and nutrient cycle as it supplies deep ocean $CO_2$ and nutrients (both macro and micro) to the sea surface, resulting in increased $CO_2$ release to the atmosphere (Quay, 1997) and higher primary productivity (Barth *et al.*, 2007). Oceanic $CO_2$ release also occurs in low latitude shelf areas, which is attributed to the warm SSTs and high terrestrial organic carbon input (Cai *et al.*, 2006).

Conversely, major sink areas are located at latitudes 40°N-60°N and 40°S-60°S (Sabine *et al.*, 2002a; Takahashi *et al.*, 2002; Gloor *et al.*, 2003), where poleward-flowing warm waters mix with the cold, nutrient-rich subpolar waters, resulting in a reduction of $pCO_2$ in the surface water due to the cooling effect on warm waters and to the biological drawdown of $pCO_2$ in the nutrient-rich subpolar waters (Takahashi *et al*., 2002). Furthermore, these areas are characterised by high wind speeds, which further increase the oceanic $CO_2$ uptake rate (Takahashi *et al*., 2002).

## 2.6.1 Coastal Dynamics

### *2.6.1.1 Coastal Ocean Characteristics*

The coastal ocean and continental margins, which comprise about 7% ($28.3 \times 10^6$ $km^2$) of the global sea surface area (Mackenzie *et al.*, 2002; Andersson *et al.*, 2006), are characterised by higher biological productivity than the open ocean (Doney and Glover, 2005). The coastal ocean is represented by the proximal zone, which includes bays, lagoons, estuaries, estuarine plumes, deltas, inland seas and salt marshes, and the distal zone, which comprises the open continental shelves (Rabouille *et al.*, 2001; Mackenzie *et al.*, 2002). The proximal zone is very shallow, with an average water depth of 20 m (Rabouille *et al.*, 2001) and an estimated area of $1.8 \times 10^{12}$ $m^2$ (Smith and Hollibaugh, 1993). The distal zone, with an aerial extent of approximately $27 \times 10^{12}$ $m^2$ (Smith and Hollibaugh, 1993) and an average depth of 130 m, includes the open continental shelves down to a depth of 200 m, which is the mean depth of the shelf break (Rabouille *et al.*, 2001).

Before the anthropocene, the global coastal ocean was a net autotrophic system (Rabouille *et al.*, 2001). However, whereas the distal coastal ocean was autotrophic, the

proximal coastal region was slightly heterotrophic (Rabouille *et al.*, 2001). The heterotrophy of the proximal zone is predominantly a result of the remineralisation of fluvial organic matter (cf. Smith and Hollibaugh, 1993; Rabouille *et al.*, 2001). The autotrophy of the distal zone, on the other hand, results from the large export of marine organic matter to the open ocean (Rabouille *et al.*, 2001).

#### *2.6.1.2 Coastal Ocean – Source or Sink*

In the last century, not many studies have focused on whether coastal regions are a source or a sink of $CO_2$ to the air, with these regions only in the last decade starting to get more attention. It is believed that during the anthropocene, the (proximal) coastal ocean became more heterotrophic as a result of the increased flux of terrestrial organic matter and nutrients from river runoff, which resulted in the coastal ocean becoming a net source of $CO_2$ (Mackenzie *et al.*, 2001; Rabouille *et al.*, 2001; Andersson *et al.*, 2006). The $pCO_2$ in estuarine areas (including estuarine plumes, cf. Borges and Frankignoulle, 2002a) tends to be significantly higher than in both the open ocean and the atmosphere, with values exceeding 6000 μatm having been measured (Frankignoulle *et al.*, 1998: Table 1; Borges and Frankignoulle, 2002a). Several studies (e.g. Raymond *et al.*, 2000; Brasse *et al.*, 2002) have shown a marked seasonality in the $CO_2$ content of estuaries, with the timing of $pCO_2$ maxima and minima varying in each location. In the York River estuary, the $CO_2$ maxima is occurring in summer-late autumn due to increased benthic and pelagic respiration as a result of higher water temperature, whereas the winter-spring minima is linked to colder water and phytoplankton blooms (Raymond *et al.*, 2000). Conversely, the Elbe estuary displays maxima in early spring as a result of high river discharge, whereas intensive primary production during late spring and summer generates the yearly $pCO_2$ minima (Brasse *et al.*, 2002).

Currently, estuaries (~$1\times10^6$ $km^2$) and salt marshes are contributing most to the $CO_2$ efflux in the coastal oceans (Borges, 2005; Borges *et al.*, 2005; Andersson *et al.*, 2006), whereas distal continental shelves still tend to act as a sink of atmospheric $CO_2$ (Chen and Borges, 2009). Intense biological productivity and subsequent offshore export of organic matter may enable the coastal ocean to take up significant amount of $CO_2$, resulting in the area to be a strong net $CO_2$ sink (Doney and Glover, 2005; Chen and

Borges, 2009). Specifically, numerous studies (cf. Borges and Frankignoulle, 2002b; Borges *et al.*, 2004; 2005; 2006) indicate the potential of high-latitude and temperate coastal oceans to remain a sink of $CO_2$ due to net autotrophy.

Coastal regions where downwelling of cold and $CO_2$-rich water occurs may also act as a significant sink for $CO_2$ (Doney and Glover, 2005). Furthermore, with rising atmospheric $CO_2$ levels, a possible increase in inorganic nutrient input from river runoff, increased organic production and decreased calcification rates, it is expected that the $CO_2$ flux will reverse in future, with the coastal oceans becoming increasingly autotrophic and the region acting as a net sink for $CO_2$ (Mackenzie *et al.*, 2002; Andersson and Mackenzie, 2004; Andersson *et al.*, 2006). Presently, atmospheric $CO_2$ absorption of the global continental shelves is estimated at 0.33-0.36 Pg C/yr, whereas the less constrained proximal coastal regions (estuaries, mangroves and salt marshes) are emitting up to 0.5 Pg C/yr (cf. Chen and Borges, 2009).

#### *2.6.1.3 Reefal $CO_2$ and pH*

The $CO_2$ flux is also strongly influenced by the local variability of *p*H (Pelejero *et al.*, 2005). During plankton blooms, diurnal and seasonal *p*H changes in productive coastal waters can be as large as the long-term multi-decadal decrease in *p*H due to the increase in oceanic $pCO_2$ (Wong and Matear, 1998). In addition, coral reef calcification and the residence time of reef water also significantly impact on the extent of the build-up of $pCO_2$ within a reef, and therefore on the variability of *p*H (Suzuki and Kawahata, 1999; 2003; Pelejero *et al.*, 2005). Generally, higher calcification rates and longer residence times of the reefal water result in lower *p*H and higher $pCO_2$ levels (Pelejero *et al*., 2005). It was found that reefal *p*H varies seasonally with the strength of the SEC (cf. Taft and Kessler, 1991), with lower values occurring from October to March when the SEC is relatively weak, and higher values in March/April as the SEC intensifies (Pelejero *et al*., 2005).

In addition, reefal $CO_2$ concentrations are also higher during El Niño events and during the positive phase of the Inter-decadal Pacific Oscillation (IPO). Both El Niño and positive IPO are associated with weaker trade winds. Reduced wind strength, in turn, lowers sea level in the western Pacific (by up to ~30 cm in areas of the SEC) and

weakens the SEC (Cane, 1983), both of which reduce the flushing of reefal waters (Pelejero *et al.*, 2005). Conversely, lower $pCO_2$ levels and higher *p*H occur during La Niña conditions and periods of negative IPO due to more efficient renewal of the water attributable to the stronger SEC and higher sea levels (Pelejero *et al.*, 2005).

## 2.7 Variability in $CO_2$ uptake

The variation in the oceanic $CO_2$ sink is related to seasonal rainfall and salinity patterns (cf. Wang and Chao, 2004), with lower rainfall (and/or increased evaporation) leading to an increase in the sea surface $pCO_2$, and, thus, to a decrease in the strength of the $CO_2$ sink (Takahashi *et al.*, 2002; Dore *et al.*, 2003). Additionally, $CO_2$ flux anomalies in the equatorial Pacific ocean and other regions are closely linked to inter-annual (e.g. El Niño and La Niña) and decadal (e.g. the Pacific Decadal Oscillation) climate signals (Inoue and Sugimura, 1992; Feely *et al.*, 1995; 1997; 1999; Wanninkhof *et al.*, 1996; Prentice *et al.*, 2001; Gruber *et al.*, 2002; Takahashi *et al.*, 2002; McKinley *et al.*, 2004; Patra *et al.*, 2005; Peylin *et al.*, 2005; McKinley *et al.*, 2006; Wang *et al.*, 2006) due to their impact on $pCO_2$ via changes in upwelling (upwelling of $CO_2$-rich deep water and increased $CO_2$ consumption by photosynthetic activity due to greater availability of nutrients), wind speed and SSTs (cf. McKinley *et al.*, 2004; Friedrich *et al.*, 2006; Wang *et al.*, 2006). Whereas the tropical oceanic $CO_2$ flux is strongly influenced by the El Niño-Southern Oscillation (ENSO), the high-latitude $CO_2$ flux is dominated by upwelling of deep waters during winter and plankton blooms during spring and summer (Takahashi *et al.*, 1993; Patra *et al.*, 2005; Fransson *et al.*, 2006). The $CO_2$ flux variability in the Southern Ocean also displays a significant correlation with the southern annular mode (SAM), an index of atmospheric variability in the Southern Ocean (Le Quéré *et al.*, 2007).

### 2.7.1 Impact of ENSO

Most researchers estimate that the global variability in the sea-air $CO_2$ flux is ±0.4-0.5 Pg C/yr (e.g. Le Quéré *et al.*, 2000; McKinley *et al.*, 2004), although other studies inferred a variability of around ±1.0 Pg C/yr (e.g. Bates, 2002a). The sea-air $CO_2$ flux anomalies are strongly linked to the ENSO over the entire Pacific, and the subarctic and

temperate North Atlantic Ocean (Cox *et al.*, 2000; Patra *et al.*, 2005; Park *et al.*, 2006). The $CO_2$ fluxes over the global oceans tend to diminish during El Niño events (Feely *et al.*, 1987; 1997; Patra *et al.*, 2005), the $CO_2$ flux in the equatorial Pacific decreasing by about 0.4-0.7 Pg C/yr (Wong *et al.*, 1993; Feely *et al.*, 1995; 2002; Peylin *et al.*, 2005). The equatorial Pacific is a significant source of $CO_2$ to the atmosphere during non-El Niño (neutral or La Niña) periods (0.8-1.0 Pg C/yr) but nearly zero (0.0-0.4 Pg C/yr) during strong El Niño events (Feely *et al.*, 1987; 1995: Table 1; 1997: Table 3; 1999; 2002; Inoue and Sugimura, 1992; Wong *et al.*, 1993; Le Quéré *et al.*, 2000; Loukos *et al.*, 2000; Wang *et al.*, 2006), leading to higher net oceanic $CO_2$ uptake.

El Niño is characterised by the manifestation and persistence of anomalously warm water in the coastal and equatorial ocean off Peru and Ecuador (Figure 2.7.1) over a period of 6-18 months (Barber and Chavez, 1983; Cane, 1983; Philander, 1983; Niiler *et al.*, 2004). Usually, trade winds push the warm sea surface water westward, thus producing a cold tongue in the central and eastern equatorial Pacific via horizontal advection (cf. Niiler *et al.*, 2004), and increasing the mixed layer depth towards the west (Philander, 1979). In the absence of the trade winds for an extended period such as during El Niño events, upwelling and horizontal advection will be reduced and the mixed layer will have a uniform depth (Philander, 1979). On average, El Niño events occur every 4 years, with intervals between successive events varying between 2 and 10 years (Nicholls, 1992: Fig. 7.1).

Sea surface $pCO_2$ is mainly influenced by upwelling, which is controlled by local and remote wind patterns (Toggweiler and Carson, 1995; Harrison, 1996). Warmer SSTs during El Niño events result in the suppression of equatorial upwelling of $CO_2$-rich deep waters in the central and eastern Pacific (Philander, 1979; Feely *et al.*, 1987; 2002; Inoue and Sugimura, 1992; Wanninkhof *et al.*, 1996), thus reducing the magnitude of sea-to-air $CO_2$ fluxes and increasing the net ocean $CO_2$ uptake (Francey *et al.*, 1995; McKinley *et al.*, 2004; Patra *et al.*, 2005; Peylin *et al.*, 2005). Furthermore, the equatorial thermocline is deepened and the upwelling is from shallow depths due to propagating Kelvin waves and a decrease in wind speed in the east (Busalacchi *et al.*, 1983; Feely *et al.*, 1995; 1997; 2002). These processes lead to a reduction in $pCO_2$ in the eastern and central equatorial

Pacific whereas $pCO_2$ increases slightly in the western equatorial Pacific during strong El Niño periods (Feely *et al*., 2002).

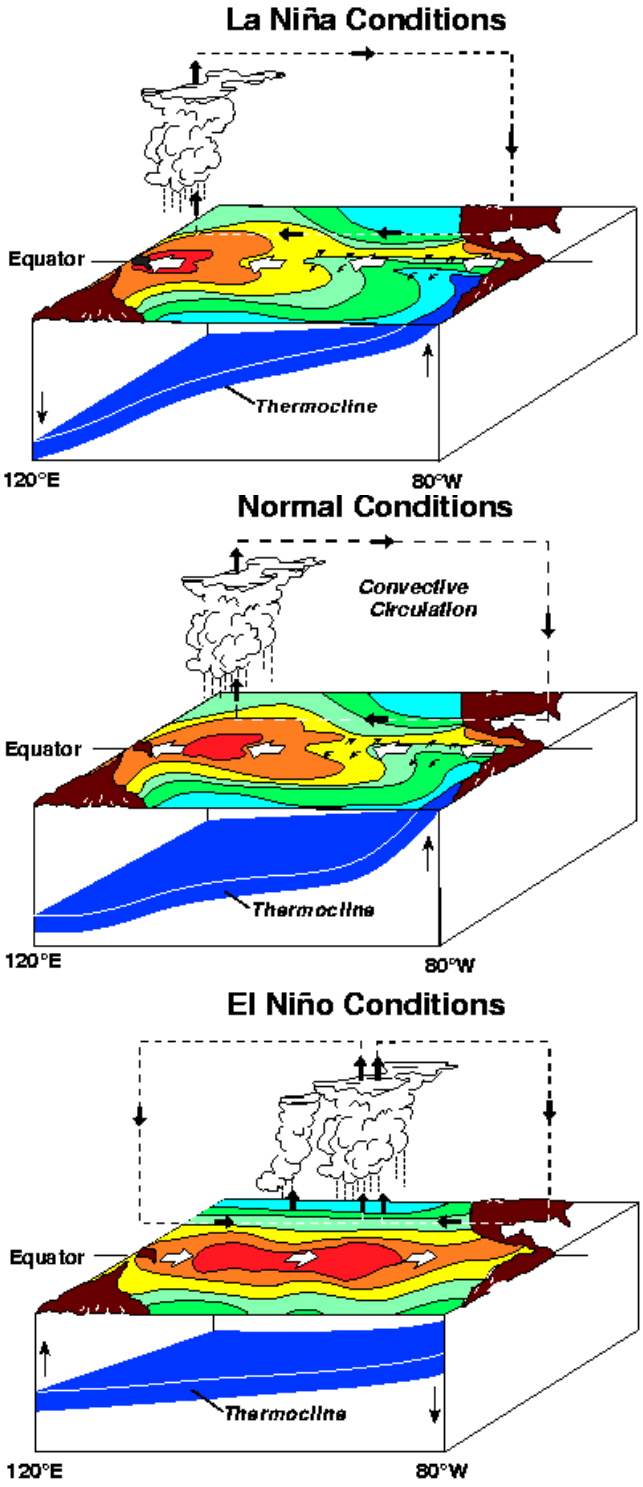


**Figure 2.7.1. Trends in atmospheric and oceanic circulation patterns, cloud cover, sea surface temperature and thermocline depth during different El Niño-Southern Oscillation phases. During La Niña events (top), easterly trade winds strengthen, resulting in a westerly shift of the warm pool compared to normal conditions (middle). In addition, the intensification of the trade winds enhances upwelling and, consequently, results in a shallowing of the thermocline (and mixed layer) in the eastern equatorial Pacific. As a result, more $CO_2$-rich deep water is circulated to the upper ocean, promoting a greater efflux of oceanic $CO_2$ into the atmosphere in the central and eastern Pacific.**

**The converse is the case during El Niño events (bottom), in which easterly trade winds weaken and predominant wind direction may reverse, inducing reduced upwelling and deeper thermocline in the eastern Pacific, as well as an easterly shift of the warm pool (figures from NOAA/PMEL/TAO).**

Counteracting the effect of reduced upwelling are reduced biological activity and warmer SST, which both directly result from reduced upwelling (Peylin *et al.*, 2005): El Niño reduces the amount of cold ($CO_2$-rich) water and nutrients transported to the surface, the latter of which, in turn, results in a significantly diminished primary production of organic matter (Barber and Chavez, 1983; Keeling and Revelle, 1985). Furthermore, the amount of light available for photosynthesis is reduced by a deepened mixed layer (Barber and Chavez, 1983). Even though both these effects tend to increase seawater $pCO_2$, their total impact on the $pCO_2$ is minor compared to the increasing effect of upwelling (Peylin *et al.*, 2005). In addition, a deeper thermocline results in upwelling of warmer and $CO_2$-depleted water, causing a further reduction of $CO_2$ flux to the atmosphere (Feely *et al*., 1997). However, atmospheric $CO_2$ increases during El Niño phases (Cox *et al.*, 2000; Sarmiento and Gruber, 2002: Fig. 3) due to the reduced $CO_2$ uptake by the terrestrial biota (e.g. Keeling and Revelle, 1985; Tian *et al.*, 1998), which is only partially counterbalanced by reduced efflux from the tropical Pacific Ocean. Conversely, global $CO_2$ uptake by the ocean is reduced due to enhanced upwelling, whereas the uptake by land is greater during La Niña periods (Bates, 2002a; Cox *et al*., 2000; Prentice *et al*., 2001). This combined effect of the ocean and land $CO_2$ fluxes results in a dampening of atmospheric $pCO_2$ variability (Doney *et al.*, 2006).

### 2.7.2 Impact of Inter-decadal $CO_2$ Variability

The Inter-decadal Pacific Oscillation (IPO; Power *et al.*, 1999; Jaffrés and Everingham, 2005; Power and Colman, 2006; Calvo *et al.*, 2007), the Pacific Decadal Oscillation (PDO; Mantua and Hare, 2002) and the North Atlantic Oscillation (NAO; Cayan, 1992; Hurrell, 1995) are also associated with decadal $CO_2$ variability (Gruber *et al.*, 2002; Takahashi *et al.*, 2003; Patra *et al.*, 2005; Schuster and Watson, 2007). The IPO is a low-frequency index based on Pacific Ocean SST (Folland *et al.*, 1999; Meinke *et al.*, 2005). Folland *et al*. (1999) obtained the IPO using the third unrotated empirical orthogonal function (EOF) of low frequency near-global SST. When the IPO index is positive, tropical Pacific water is warmer than usual whereas the water in higher latitudes is cooler than average (Power *et al*., 199; Salinger *et al*., 2001). Similarly, a positive PDO index tends to coincide with warmer SST in the Eastern Pacific and colder SST in the

North Pacific (Mantua and Hare, 2002). On average, the positive phase of the IPO is linked to enhanced and more frequent El Niño events (Salinger *et al.*, 2001), thus leading to a decrease in equatorial $CO_2$ flux (Patra *et al.*, 2005).

### 2.7.3 Impact of cyclones

Cyclones and tropical storms between 40°S and 40°N may also significantly contribute to the ocean-to-air flux of $CO_2$, with an estimated additional flux of 0.04-0.51 Pg C/yr, because they pass over warm surface waters with relatively high sea surface $pCO_2$ (Bates *et al.*, 1998). A surface cooling (~2°C) is observed in the wake of cyclones (Price, 1981; Stramma *et al.*, 1986; Bates *et al.*, 1998) due to upwelling during the deepening of the mixed layer, with greatest cooling response expected when the mixed layer was initially shallow (Price, 1981). The resulting reduction of sea surface $pCO_2$ is 4.1-4.25%/1°C (Takahashi, 1975; Takahashi *et al.*, 1993; Millero, 1995; Archer *et al.*, 2004). During La Niña events, there tend to be fewer tropical cyclones in the Pacific Ocean (cf. Camargo and Sobel, 2005 and references therein), but higher $\Delta pCO_2$ values in the low-latitudes facilitate the loss of $CO_2$ from the ocean (Bates, 2002a). Conversely, during an El Niño event, warmer SSTs in the tropical Pacific Ocean tend to result in greater cyclone frequency (Camargo and Sobel, 2005: Fig. 6), which, however, coincides with relatively low $\Delta pCO_2$ values, so that the ability of $CO_2$ removal from the ocean is reduced (Bates, 2002a). Accordingly, tropical cyclones cause the ocean to act as a stronger $CO_2$ sink during El Niño years compared to La Niña years (Bates, 2002a). In the mid- and high-latitudes, however, extra-tropical cyclones (ETC) derived storms pass over sea surface with negative $\Delta pCO_2$, so that they possibly contribute to an atmosphere to ocean $CO_2$ flux (Bates, 2002a).

# 3 Physical Oceanography

A good understanding of the physical behaviour of the ocean is required to comprehend and predict the biogeochemical patterns and trends. The predominant ocean circulation, heat content and extend of upper ocean mixing all greatly impact on the carbon cycle, the distribution and flux of nutrients and, thus, biological productivity. This chapter is introducing the physical characteristics (ocean heat content, mixed layer depth and circulation) of the global ocean, with a focus on the western Pacific.

## 3.1 Ocean Heat Budget

### 3.1.1 Heat Transport

The heat budget of the sea surface includes the net shortwave (solar) and longwave radiative fluxes, the latent heat flux (LHF; heat flux to the atmosphere due to evaporation), and sensible heat fluxes (SHF; flux owing to water-air and water-rain temperature differences, respectively) (Cronin *et al.*, 2006; Matsoukas *et al.*, 2007). Within the Coral Sea, the mean annual LHF is estimated to range between 100 W/m$^2$ and 180 W/m$^2$ (Chou *et al.*, 2005: Fig. 1b; Wu *et al.*, 2007: Fig. 1a), with LHF being greater in the southern regions and during winter months (Chou *et al.*, 2005). LHF and SHF are given by:

$$\mathrm{LHF} = \mathrm{L}\rho_a \overline{w'q'} = \mathrm{L}\rho_a \mathrm{C}_{\mathrm{lat}} \mathrm{U}(q_s - q_a)$$

$$\mathrm{SHF} = c_{\mathrm{p}}\rho_a \overline{w'\theta'} = c_{\mathrm{p}}\rho_a \mathrm{C}_{\mathrm{sen}} \mathrm{U}(\theta_s - \theta_a)$$

where L = latent heat of vaporisation (2440 J/g), $\rho_a$ = air density (1.15 kg/m$^3$), $\overline{w'q'}$ = kinematic flux of specific humidity (m/s g/g), $C_{lat}$ = exchange coefficient for latent heat (Dalton number), U = wind speed (m/s), $q_s$ = saturation specific humidity, $q_a$ = specific humidity of air (g/g), $c_\rho$ = specific heat capacity for air at constant pressure (1.0048 J g$^{-1}$ K$^{-1}$), $C_{sen}$ = exchange coefficient for sensible heat (Stanton number), $\theta_s$ = potential sea surface temperature (K), $\theta_a$ = potential air temperature (K) (cf. Cayan, 1992; Sahlée *et al.*, 2009).

Solar radiation displays a strong diurnal (~1000 W/m2; Price *et al.*, 1986; Cronin *et al.*, 2006) and seasonal (Kraus, 1972; Gent, 1991; Chou *et al.*, 2005; Gleckler *et al.*,

2006; Aumann *et al.*, 2007) cycle due to the seasonal movement of the sun and the Intertropical Convergence Zone (ITCZ), resulting in the seasonal variability of SST (Chou *et al.*, 2005). In general, highest SSTs in the region of 0°S-30°S can be expected around two months after the southern solstice (Aumann *et al.*, 2007). Whereas most regions display an annual variation in solar heat fluxes, the tropical area exhibits semi-annual cycles due to the biannual overhead crossing of the sun (Gleckler *et al.*, 2006).

Conversely, the sea surface LHF, the second largest constituent of the sea surface heat budget (Chou *et al.*, 2004; Liu and Curry, 2006), mainly exhibits significant (>100 $W/m^2$) seasonal variability (e.g. Chou *et al.*, 2005; Cronin *et al.*, 2006), consequently dominating the net surface heat flux fluctuations on timescales exceeding the diurnal (cf. Liu and Curry, 2006). In general, LHF is strongly positively correlated to surface wind stress (Chou *et al.*, 2005). Within the Coral Sea, mean annual LHF is estimated to range between around 100-180 $W/m^2$ (Chou *et al.*, 2005: Fig. 1b; Wu *et al.*, 2007: Fig. 1a), with LHF being greater in the southern regions and during winter months (Chou *et al.*, 2005).

In the western subtropical Pacific, it was estimated that a slight (~0.2 PW) northward heat flux occurs due to a large warm water flux into the Indian Ocean via the Indonesian Throughflow (ITF) (Ganachaud and Wunsch, 2000). Conversely, it was determined that the poleward ocean heat transport (OHT) in the southern Pacific via Ekman-driven subtropical gyres peaks at 0.92 PW at 10°S (Trenberth and Caron, 2001). Changes in poleward OHT are often linked to modifications in the oceanic overturning cells, which are, in turn, positively correlated to variations in the Hadley Cell (cf. Hazeleger, 2005).

Poleward OHT away from the equatorial Pacific is increased during El Niño events (Sun and Trenberth, 1998). However, the impact of ENSO events on OHT in the Pacific Ocean is relatively minor (~0.5 PW) due to compensating effects of changes in heat transport via meridional overturning (equatorward OHT) and subtropical gyres (poleward OHT) (Hazeleger *et al.*, 2004; 2005). The poleward OHT in the Pacific is further reduced due to a decrease in ITF heat transport (Hazeleger *et al.*, 2004).

## 3.1.2 Equatorial Pacific Ocean

### *3.1.2.1 Paleoclimate*

The SST of the global oceans has undergone significant variability on millennial and longer timescales (cf. Jaffrés *et al.*, 2007 and references therein). Comparatively small SST changes are ascribed to tropical oceans (de Garidel-Thoron *et al.*, 2005; Brierley *et al.*, 2009) and, specifically, to the Coral Sea (e.g. Lawrence and Herbert, 2005) over similar timescales. Throughout the Holocene, a general trend of decreasing SST (by about 0.5°C) is evident in the tropical Pacific Ocean (Stott *et al.*, 2004).

There has also been an overall trend of decreasing SST in the tropical Indo-Pacific during the last millennium, maxima and minima coinciding with the Medieval Warm Period (~1000-1400 AD) and the Little Ice Age (~1400-1850 AD), respectively (cf. Newton *et al.*, 2006). The latter is strongly linked to periods of anomalously low solar activity (e.g. Maunder Minimum: 1645-1715 AD) and increased volcanic activity (e.g. Lean *et al.*, 1995).

### *3.1.2.2 Modern Climate Regime*

In most global oceans, a warming trend in sea surface temperatures (SSTs) (Cane *et al.*, 1997; Lau and Weng, 1999; Gagan *et al.*, 2000: Fig. 2; Levitus *et al.*, 2000; Wilson *et al.*, 2006; AchutaRao *et al.*, 2007) and an increase in the total ocean heat content (e.g. Gouretski and Koltermann, 2007) has been detected over the last few decades, parallel to atmospheric warming (Folland *et al.*, 2001). The latter is mainly attributed to the increase in atmospheric $CO_2$ concentration, which results in enhanced radiative forcing (Crowley, 2000; Houghton *et al.*, 2001; Sarmiento and Gruber, 2002). It is estimated that global radiative forcing has already increased by 2.63 ± 0.26 W/m$^2$ due to anthropogenic emissions of greenhouse gases (Forster *et al.*, 2007). Both global mean SSTs (Nicholls *et al.*, 1996) and annual tropical SSTs (Wilson *et al.*, 2006) have increased by about 0.4°C in the 20$^{th}$ century. However, due to increasing air temperatures, cloud cover is increasing as well in some regions (e.g. western equatorial Pacific) resulting in a reduction of shortwave radiation and therefore also a decrease in the net surface heat flux into those locations (Curtis and Hastenrath, 1999; Liu and Huang, 2000). Changes in cloud cover are also linked to variability in large-scale atmospheric circulation. Chen *et al.* (2002)

have linked variability in cloud cover in the 1990s to the strengthening of the atmospheric Hadley-Walker circulation (cf. Bjerknes, 1966), with lower cloud cover occurring in tropical subsidence regions (western Pacific), and an increase in cloud density in convective regions.

The large-scale tropical Hadley and Walker atmospheric circulations are strongly coupled with each other (Oort and Yienger, 1996), generating the strongest convection centre around the western equatorial Pacific (Tanaka *et al.*, 2004). The Walker circulation (Bjerknes, 1969) is characterised by a large-scale zonal (east-west) overturning of air across the equatorial Pacific Ocean, with convection to the west and subsidence to the east (Bjerknes, 1969; Julian and Chervin, 1978; Philander, 1983; Oort and Yienger, 1996; Chen *et al.*, 2002), which may reverse during strong El Niño events (Oort and Yienger, 1996). It is driven by the east-west temperature contrast in the underlying SST along the equatorial Pacific (Bjerknes, 1969; Tanaka *et al*., 2004). Changes in the intensity of the Walker circulation are closely associated with those of the ENSO (Julian and Chervin, 1978) and monsoonal circulations over neighbouring continents (Philander, 1983; Webster *et al.*, 1998). The Walker circulation is three times stronger than the Hadley circulation (Tanaka *et al*., 2004). The strength of the Hadley Cell is at its minimum in summer (Bjerknes, 1966).

The Hadley circulation, in turn, is a roughly zonally symmetric meridional circulation, rising over the ITCZ and descending over the subtropical high-pressure belt (Bjerknes, 1966; Philander, 1983; Oort and Yienger, 1996; Trenberth *et al*., 2000). It is driven by meridional differential heating (Trenberth *et al.*, 2000; Tanaka *et al.*, 2004), with the equatorial warm pool supplying most of the thermal energy to drive the Hadley Cell (Bjerknes, 1966). The strength of the Hadley cells controls the intensity of the large-scale summer monsoon (Tanaka *et al*., 2004).

The rate of increase of SST varies on decadal time scales. In the equatorial Pacific, it was determined that the mean SST increase of about 0.8°C over the last four decades (cf. Zhang *et al.*, 1997) is linked to a reduction of oceanic cold advection due to a weakening of the equatorial trade winds, and the concomitant decrease in the South Equatorial Current, the off-equatorial Ekman divergence and upwelling (Liu and Huang, 2000), which can be associated with the PDO changing into its warm phase. SST variability on

inter-decadal timescales is also linked to the IPO (Power *et al.*, 1999; Jaffrés and Everingham, 2005; Power and Colman, 2006) and the PDO (Mantua and Hare, 2002). The IPO changed into its positive phase in 1978 (Salinger *et al.*, 2001), resulting in warmer SSTs in the Coral Sea (Calvo *et al.*, 2007). The wind-driven meridional overturning circulation in the upper Pacific Ocean has been slowing down since the 1970s, resulting in a decrease in upwelling of about 25% (about $35\text{-}47\times10^6$ $m^3/s$) between 9°N and 9°S (McPhaden and Zhang, 2002). Whereas the heating of the eastern and central equatorial Pacific is attributed to reduced upwelling and off-equatorial divergence of cold water, the warming in the western Pacific is linked to zonal advection of warm water (Liu and Huang, 2000). In the western Pacific, the net heat flux is determined to be less than 10 $W/m^2$, significantly less than the heat flux into the eastern equatorial Pacific (~50 $W/m^2$) (Gent, 1991; Liu and Huang, 2000). Surface heat flux and heat advection are the main controlling factors of the seasonal variability of surface heat content in the tropical western Pacific (Qu, 1996).

## 3.2 Surface Mixed Layer

Turbulent mixing leads to the formation and maintenance of a quasi-homogenous surface region of salinity, temperature and density that is generally interpreted as the ocean surface mixed layer (Kraus, 1972; Gregg *et al.*, 1985; Weller, 1987; Bauer *et al.*, 1991; Sprintall and Tomczak, 1992; Kraus and Businger, 1994; Alexander *et al.*, 2000; Kara *et al.*, 2003; Babu *et al.*, 2004; de Boyer Montégut *et al.*, 2004; Acreman, 2005; Zawada *et al.*, 2005). This turbulent layer plays an important role in air-sea interactions through the flux and storage of heat, gases (e.g. $CO_2$), and momentum (Kraus, 1972; Price *et al.*, 1986; Kraus and Businger, 1994). The ocean mixed layer controls both the depth from which nutrients are supplied to the surface (Polovina *et al.*, 1995; Schmittner *et al.*, 2005), and the depth over which the net surface heat flux is distributed (Chen *et al.*, 1994). Its depth is also found to be proportional to biological productivity (Behrenfeld and Falkowski, 1997).

Turbulent mixing is mainly caused by mixing via turbulent eddies due to wind forcing and is most prominent along isopycnal surfaces (Kara *et al.*, 2003). Buoyancy forcing (e.g. due to surface cooling), which is predominantly influenced by the net

surface heat flux, is also a significant (but secondary) cause for turbulent mixing (Kara *et al.*, 2002; Qu *et al.*, 2007). The surface heat flux, in turn, is governed by short-wave radiation and latent heat flux (Gregg *et al.*, 1985). The extent of turbulent mixing, and therefore the magnitude of the eddy viscosity for horizontal and vertical advection, depends on the vertical density stratification of the water (Pickard and Emery, 1990). In the absence of strong stratification, turbulent mixing will easily overturn the water column, whereas turbulent mixing is suppressed in a highly stratified water column (Kara *et al*., 2003).

The variability of the mixed layer is studied in terms of the mixed layer depth (MLD), a zone of very abrupt change in temperature and/or salinity, which defines the lower limit of the turbulent mixed layer (Kara *et al.*, 2003). Due to limited amount of temperature and salinity data available in some areas, the ocean MLD is not as well known and studied as the atmospheric boundary layer.

### 3.2.1 Methods of Mixed Layer Depth Determination

#### *3.2.1.1 Temperature vs Density*

The definition of MLD is unstandardised and often subjective, and can be based on various parameters (i.e. temperature, density, salinity) (Polovina *et al.*, 1995; You, 1995; de Boyer Montégut *et al.*, 2004; Zawada *et al.*, 2005; Lorbacher *et al.*, 2006; Udaya Bhaskar *et al.*, 2006). Furthermore, mixed layer depths are averaged over different time periods (e.g. day, month, year; de Boyer Montégut *et al*., 2004), further complicating the analysis and intercomparison of the results of multiple studies.

The most commonly used algorithms for MLD determination require vertical profiles of either temperature or density (cf. Brainerd and Gregg, 1995; Lukas and Lindstrom, 1991; Zawada *et al*., 2005). Normally, the mixed layer depth can be defined by a density-based criterion that takes into account the effects of both temperature and salinity (Lewis *et al.*, 1990; Lukas and Lindstrom, 1991; Sprintall and Tomczak, 1992; Kara *et al.*, 2003). However, since generally more temperature data is available compared to salinity or density data (Boyer and Levitus, 2002; Lorbacher *et al.*, 2006), the MLD is more commonly inferred from a temperature-based criterion (e.g. Rao *et al.*, 1989; Brainerd and Gregg, 1995; Obata *et al.*, 1996; de Boyer Montégut *et al.*, 2004; Zawada *et al.*,

2005), which yields the isothermal layer depth (ILD; cf. Kara *et al*., 2003). These differences in the determination of the MLD make the interpretation of the spatial and temporal variability of the ocean mixed layer complicated.

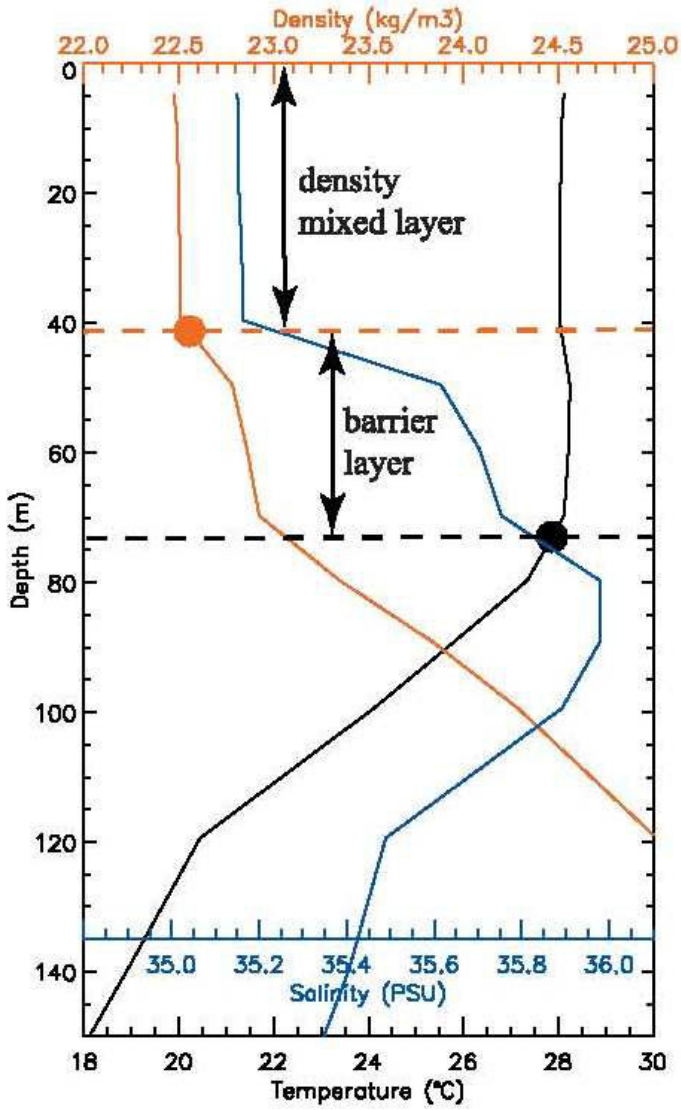


**Figure 3.2.1. CTD profiles of temperature (black), salinity (blue), and density (orange). The orange, solid dot shows the depth of the density mixed layer (MLD). The black, solid dot shows the isothermal layer depth (ILD). The area in between the MLD and ILD denotes the barrier layer (BL), created as a result of a shallow halocline. Within the BL, the temperature profile remains relatively invariable (figure adapted from de Boyer Montégut *et al*., 2007).**

Additionally, while the ILD generally corresponds to the MLD over most of the global ocean due to the presence of a strong thermocline and a weak halocline (Brainerd and Gregg, 1995; Qu and Meyers, 2005), there are regions such as the western equatorial Pacific (Vialard and Delecluse, 1998), where the ILD and MLD differ significantly, the MLD generally being more shallow (Lukas and Lindstrom, 1991; Delcroix *et al.*, 1992; Qu and Meyers, 2005). In such cases (MLD < ILD), a barrier layer is formed (Figure 3.2.1), which is defined as the region between the MLD and ILD (Delcroix *et al.*, 1992; Sprintall and Tomczak, 1992; You, 1995; Kara *et al.*, 2003). In the western equatorial Pacific, barrier layers form as a result of the freshening of sea surface water by rainfall, which influences the density structure by generating shallow and strong haloclines (Lewis *et al.*, 1990; Lukas and Lindstrom, 1991; Roemmich *et al.*, 1994; You, 1995; Vialard and Delecluse, 1998; Ando and Kuroda, 2002; Kara *et al.*, 2003). As a consequence of the barrier layer formation, cold water is prevented from entraining into the shallowing mixed layer, resulting in a warming of the surface ocean (Vialard and Delecluse, 1998; Ando and Kuroda, 2002). High-latitude regions are another example where ILD and MLD diverge since salinity dominates the density gradient (Levitus, 1982; Vialard and Delecluse, 1998; de Boyer Montégut *et al*., 2004). In the North Pacific, a seasonal barrier layer is formed due to strong sea surface cooling in winter, which results in a deepening of the thermocline so that salinity stratification generates an MLD that is shallower than the ILD (Kara *et al.*, 2000b). Therefore, density-based methods are more reliable for areas affected by intense freshwater input (e.g. Vialard and Delecluse, 1998), where salinity stratification is significant (Levitus, 1982; Brainerd and Gregg, 1995; Kara *et al.*, 2000b) or where evaporation, and correspondingly more saline and cool surface waters, can destabilise the mixed layer (Gardner *et al.*, 1999; Lee *et al.*, 2000).

#### *3.2.1.2 Threshold vs Gradient Method*

Most methods employed to determine the MLD use criteria based on either a finite difference (threshold method) from the surface value or a gradient (gradient method) exceeding a specific value to determine the MLD (cf. Lukas and Lindstrom, 1991; Brainerd and Gregg, 1995; Kara *et al*., 2000a). Other methods include the split-and-

merge method, the integral method and the regression method (cf. Thomson and Fine, 2003 and references therein).

Often, the MLD is defined using the threshold method with a fixed difference criterion (e.g. Kara *et al.*, 2000a; de Boyer Montégut *et al.*, 2004). The threshold method identifies the depth at which the potential density changes by a fixed value ($\Delta\rho$) relative to the one at a near-surface reference depth (Lukas and Lindstrom, 1991; Sprintall and Tomczak, 1992). Similarly, the ILD is defined as the depth, where the temperature has altered by a finite amount ($\Delta T$) from the temperature at a reference depth (Kara *et al.*, 2003). The reference depth is usually set at 10 m to avoid much of the strong diurnal variability in the top few meters of the ocean in equatorial regions (de Boyer Montégut *et al.*, 2004). Previous studies have determined that, on a global ocean scale, the optimal criterion value for $\Delta T$ is between 0.2°C (de Boyer Montégut *et al.*, 2004) to 0.6°C (Kara *et al.*, 2003), whereas a threshold value of 0.03 kg/m$^3$ was considered most suitable for $\Delta\rho$ (de Boyer Montégut *et al.*, 2004). However, the most accurate $\Delta\rho$ and $\Delta T$ values vary significantly both seasonally and regionally (Kara *et al.*, 2000a; 2003; Lorbacher *et al.*, 2006). For the high southern latitudes and equatorial regions, for example, the $\Delta T$ values are considerably less than 0.6°C (0.1 and 0.4°C, respectively) due to strong salinity stratification in these locations (Kara *et al.*, 2003). The MLD estimated with the finite difference (threshold) method tends to be more reliable than the MLD based on the gradient method (Schneider and Müller, 1990; Brainerd and Gregg, 1995; Gardner *et al.*, 1999) since the latter requires highly resolved profiles for an accurate gradient determination (de Boyer Montégut *et al.*, 2004). In the gradient method, the MLD is defined as the depth, where the vertical temperature or density gradient is significantly smaller than is observed deeper in the water column (Polovina *et al.*, 1995), i.e. where a certain pre-determined value of rate of change (in either temperature or density) is not exceeded (Figure 3.2.2).

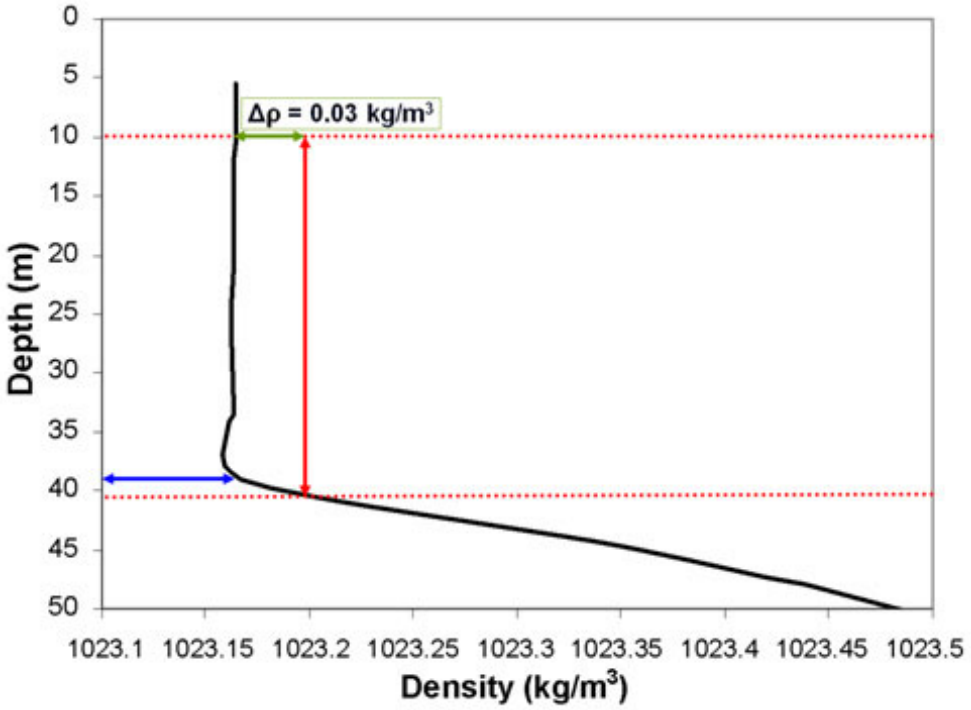


**Figure 3.2.2. Illustration of threshold method (red lines) and gradient method (blue arrow) based on a density profile derived from Argo float 5900607. The threshold method determines the mixed layer depth (MLD) at the point where density has increased by a given increment, Δρ (in this case, 0.03 kg/m$^3$, green lines) from the density value at 10 m depth. The gradient method, in turn, defines the MLD as being the depth were the gradient rapidly changes (e.g. >0.01 kg/m$^3$ per meter).**

### 3.2.2 Variability in Mixed Layer Depth

The main temporal variability of the MLD is directly connected to changes in wind and buoyancy forcing (e.g. surface forcing, lateral advection, internal waves) within the mixed layer, and ranges from diurnal (Gregg *et al.*, 1985; Schneider and Müller, 1990; Brainerd and Gregg, 1995) to interannual variability (McCreary *et al.*, 2001; Kara *et al.*, 2003). Surface heat flux (cf. Chen *et al.*, 1994; Kako and Kubota, 2007), equatorial Kelvin waves (cf. Cane, 1983), precipitation, surface wind mixing (Niiler, 1975; Delcroix *et al.*, 1992) and cooling convection (Davis *et al.*, 1981; Rao *et al.*, 1989; Chen *et al.*, 1994; Qu, 2003) all significantly influence the seasonal variation of ILD, MLD, and BLT (barrier layer thickness), but their relative importance differs from one region to another (Delcroix *et al.*, 1992; Qu and Meyers, 2005). Generally, mixed (and isothermal) layers

are shallower in summer than in winter in both hemispheres due to sea surface heating (Bathen, 1972; Kara *et al.*, 2003; Qu and Meyers, 2005; Nilsen and Falck, 2006), with greater seasonality displayed at higher latitudes (Bathen, 1972). The warming of the mixed layer during summer is fairly uniform with latitude, whereas the salinity of the mixed layer changes little with time (Rintoul *et al.*, 1997). Deep winter mixed layers are produced by winter cooling and stronger winds (Kara *et al*., 2003; Nilsen and Falck, 2006). In the North Pacific and North Atlantic, the MLD is shallowing from winter to spring, coinciding with spring blooms of phytoplankton (cf. Obata *et al.*, 1996). Strong seasonality of MLD is found in the subtropical Pacific Ocean and in middle to high latitudes (Kara *et al*., 2003). The Antarctic, however, is characterised by a continuously shallow MLD (Kara *et al*., 2003). The greatest annual change (~25 m) of both the MLD and ILD occurs at 10°S-15°S (Masumoto and Meyers, 1998: Fig. 8a; Qu and Meyers, 2005). On the equator, the ILD and MLD vary by about 15-20 m annually (Schneider and Müller, 1990; Qu and Meyers, 2005). Because of a large excess of precipitation over evaporation (large P-E), the MLD is significantly shallower than the ILD during most seasons of the year (Qu and Meyers, 2005).

### 3.2.3 Bias in MLD Measurement

There are numerous biases and inaccuracies associated with the determination of the MLD, with the precision of the MLD determination generally limited to about 20 m due to the intrinsic fluctuations of the MLD (Kara *et al.*, 2000a). The accuracy of the MLD is also dependent on the vertical resolution of the profiles, with the precision increasing for high-resolution profiles (e.g. Lorbacher *et al.*, 2006). Furthermore, the older mechanical bathythermographs (MBT) often sampled only down to 100 m, so that only relatively shallow MLD were able to be determined, therefore undersampling deeper MLD and thus leading to an underestimation of the average MLD (e.g. Polovina *et al*., 1995). Additionally, CTD measurements are rarely taken during storm events, which are correlated with deepened mixing (Polovina *et al*., 1995).

## 3.3 Oceanic Circulation

### 3.3.1 Circulation and Wind Forcing

Vertical diffusion, Southern Ocean winds and eddies seem to strongly influence global circulation and density patterns (Gnanadesikan, 1999). Downwelling in high latitudes induces a large-scale meridional circulation, in which warm surface water flows poleward, cooling down in the process (Toggweiler and Samuels, 1998). Consequently, the water density is increasing, thus allowing the polar surface water to sink and subsequently flow towards low latitudes (Toggweiler and Samuels, 1998). The meridional overturning circulation leads to upwelling of cold pycnocline water at low latitudes (McPhaden and Zhang, 2002). Most of the upwelling transport (≥90%) in the tropical Pacific occurs in the eastern and central equator region (McPhaden and Zhang, 2002) and along the Peruvian coast (Chavez and Toggweiler, 1995). Upwelling results in the replacement of all deep ocean water about every 500-1000 years (Stuiver *et al.*, 1983; Matsumoto, 2007) at an overturning rate of 20-40 Sv ($Sv \equiv 10^6$ $m^3/s$) (Stuiver *et al.*, 1983). In the tropical Pacific, the circulation is strongest in the upper ocean (Johnson *et al.*, 2001: Fig. 2). Meridional Ekman transports are limited to about the upper 50 m in the tropical oceans (McPhaden and Zhang, 2002), and are to the right of the wind stress in the northern hemisphere and to the left of the wind stress in the southern hemisphere (Ralph and Niiler, 1999: Fig. 1), whereas the pycnocline flows extend to several hundred metres depth (McPhaden and Zhang, 2002). Trade and monsoonal winds converge to areas of the highest SST in the equatorial western Pacific, where the largest cloud cover and smallest wind speed occur (Chou *et al.*, 2005).

It is the wind stress curl, as opposed to the wind stress itself, which mainly forces ocean circulation (Cai *et al*., 2005). The change of the wind stress curl is controlled by the meridional gradient of changes in zonal wind stress (Cai *et al*., 2005). The maximum change in zonal wind stress is located at about 60°S (Thompson and Solomon, 2002; Gillett and Thompson, 2003), whereas the maximum change in surface wind stress curl is situated at about 48°S (Cai *et al.*, 2005). One of the effects of the change in the wind stress curl is a southward strengthening of the East Australia Current (EAC), resulting in a warming of the Tasman Sea (Cai *et al*., 2005).

#### *3.3.1.1 Long-term Changes in Wind Forcing and Circulation*

In the tropical Indo-Pacific, changes in the trade winds govern variability in the strength of Subtropical Cells (STCs) (Hazeleger, 2005; Meehl *et al.*, 2006). A wind stress reduction also causes a slow-down of the South Equatorial Current (SEC) (Dawe and Thompson, 2006). Furthermore, trade winds and SSTs are tightly coupled with each other. Warmer eastern tropical Pacific SSTs as a result of increased greenhouse gas forcing would reduce the east-west temperature gradient and, thus, be supporting weaker trade winds (McPhaden and Zhang, 2002; Meehl *et al.*, 2006). Weaker easterly trade winds in the equatorial Pacific, in turn, would cause a reduction of the Ekman and geostrophic meridional transports, a shallowing MLD (Dawe and Thompson, 2006), a decrease in equatorial upwelling and, thus, an increase in the eastern equatorial SSTs (Meehl and Washington, 1996; McPhaden and Zhang, 2002). Additionally, lower wind speeds, and, thus, smaller wind stress, reduces the latent and sensible heat fluxes (Kara *et al.*, 2005). The reduced evaporative cooling due to weakened winds surpasses the reduced solar heating due to increased cloudiness, resulting in a maximum surface heating in the strong convective and high SST regions, which follow the seasonal movement of the sun (Chou *et al*., 2005).

Over the last century, the zonal sea level pressure (SLP) gradient and the strength of the equatorial Pacific zonal-mean easterlies have decreased, causing a weakening of surface equatorial currents, a vertical shift in sub-surface currents, a reduction in the intensity and depth of equatorial upwelling, and a substantial shoaling of the western equatorial Pacific thermocline depth (Vecchi *et al.*, 2006). A reduction of the trade winds influences both the east-west tilt of the equatorial Pacific thermocline and its mean depth (Jin, 1997), which could impact on the nature of El Niño variability (Federov and Philander, 2000). On yearly and longer timescales of equatorial thermocline adjustment to wind changes, the impact of reductions in trade winds is felt almost entirely by the western equatorial Pacific thermocline depth (Vecchi *et al.*, 2006).

In the Southern Ocean, on the other hand, the wind strength, which is tightly linked to the southern hemisphere annular mode (SAM), also called Antarctic Oscillation, has been increasing over the last decades (Thompson and Solomon, 2002). This increase has been attributed to the depletion of stratospheric ozone and to changes in the SST pattern due to

global warming (Fyfe *et al.*, 1999; Thompson and Solomon, 2002; Shindell and Schmidt, 2004; Toggweiler and Russell, 2008). The wind strength in the Southern Ocean is expected to further increase in future (Kushner *et al.*, 2001; Le Quéré *et al.*, 2007). The net impact of the intensification in wind strength on the $CO_2$ uptake by the Southern Ocean is currently disputed. Some research groups (e.g. Mignone *et al.*, 2006) predicted that both the relative importance of the Southern Ocean $CO_2$ sink and the absolute magnitude of total anthropogenic $CO_2$ uptake will augment. More recently, however, Le Quéré *et al.* (2007) projected that the fraction of anthropogenic $CO_2$ uptake of this region will decrease in future due to increased upwelling (see also Saenko *et al.*, 2005) and outgassing of $CO_2$ in some regions. Furthermore, several studies predict that the formation of Antarctic Bottom Water will decrease in future due to freshening and warming of the Southern Ocean (e.g. Marsland *et al.*, 2007), thus further reducing the storage of $CO_2$ in the deep ocean.

# 4 Impacts of Climate Change and Rising Atmospheric $CO_2$

## 4.1 Biological Impacts

It is forecast that future climate change impacts will include ocean temperature increases, lower *p*H, significant changes in oceanic circulation, variations in mixed layer thickness, and changes in cloud cover and sea ice, and, therefore, light supply to the surface ocean (e.g. Houghton *et al.*, 2001). Global warming will strengthen the stability of the ocean stratification in many regions, leading to a reduction in overturning circulation and vertical mixing (Sarmiento *et al.*, 1998; 2004b; Matear and Hirst, 1999; Bopp *et al.*, 2001; Delille *et al.*, 2005; Schmittner, 2005). Along the NE coast of Australia, for example, average SSTs have already been increasing by 0.12°C/decade since 1950 (Lough, 2008).

Furthermore, it is predicted that evaporation will increase in the tropical and subtropical regions, while increased precipitation in the high latitudes will lead to a freshening of surface waters (Houghton *et al.*, 2001; Sarmiento *et al.*, 2004). Both higher temperature and lower salinity result in reduced surface density, which will lead to increased vertical stratification and more shallow mixed layers (Smith *et al.*, 2000; Sarmiento *et al.*, 2004; Orr *et al.*, 2005a). These changes will have significant impacts on biological productivity (e.g. Denman *et al.*, 1996; Kleypas *et al.*, 1999a; Cox *et al.*, 2000; Bopp *et al.*, 2001; Sarmiento *et al.*, 2004) since an increase in ocean temperature and light supply affect photosynthesis directly, whereas reduced vertical mixing has a significant impact on primary productivity through reduced nutrient supply (e.g. Orr *et al.*, 2005a; Huisman *et al.*, 2006). Since vertical mixing in the low-latitude pycnocline determines the amount of deep water upwelling at the equator (Gnanadesikan *et al.*, 2002), the upward nutrient-flux will be suppressed, resulting in a decline in oceanic primary production (Sarmiento *et al.*, 1998; 2004b; Bobb *et al.*, 2001; Schmittner, 2005; see also Huisman *et al.*, 2006).

### 4.1.1 Terrestrial Photosynthesis

It is expected that terrestrial and oceanic photosynthesis and plant growth will be augmented with increased atmospheric $CO_2$ concentration and warming when sufficient

water and nutrients are available (Melillo *et al.*, 2002; Govindasami *et al*., 2005; Langdon and Atkinson, 2005). On land, as soil carbon is oxidised, nitrogen is released to the soil (Steffen, 2006), which can lead to increased photosynthesis and, therefore, enhanced uptake of atmospheric $CO_2$ (Melillo *et al.*, 2002). However, the enhanced physiological effects of $CO_2$ on terrestrial productivity and efficiency of water use levels off at high $CO_2$ concentrations (Cao and Woodward, 1998). Furthermore, terrestrial $CO_2$ uptake begins to decrease at higher $CO_2$ concentrations, since the direct effect of $CO_2$ on photosynthesis saturates, whereas the increasing temperature leads to a rise in evapotranspiration, which acts to increase soil aridity (Cox *et al.*, 2000; Friedlingstein *et al.*, 2001; Berthelot *et al.*, 2002; Dufresne *et al.*, 2002). In addition, heterotrophic respiration rates are also anticipated to increase due to global warming, resulting in lower or even reversed $CO_2$ flux from the atmosphere to the terrestrial biosphere (Cox *et al.*, 2000; Cramer *et al.*, 2001; Joos *et al.*, 2001).

## 4.2 Carbonate System and $[CO_3^{2-}]$ in Seawater

The oceanic carbon system is expected to be significantly affected by global warming and increased atmospheric $CO_2$. Three main DIC species exist in the ocean, which are molecular dissolved $CO_2$ (or aqueous $CO_2$, consisting of $CO_2$ and $H_2CO_3$), bicarbonate ($HCO_3^-$) and carbonate ($CO_3^{2-}$) (Wolf-Gladrow *et al.*, 1999; Leclercq *et al.*, 2000). They are interlinked according to $CO_2 + H_2O \leftrightarrow H_2CO_3 \leftrightarrow HCO^-_3 + H^+ \leftrightarrow CO_3^{2-} + 2H^+$ (Leclercq *et al.*, 2000), with the relative abundance of the three DIC species depending on *p*H (Figure 4.2.1) (Usdowski and Hoefs, 1993). Ocean *p*H values generally range from 7.7. to 8.2 (Brewer *et al.*, 1995: Fig. 1; Haugan and Drange, 1996). The highest *p*H values are observed at the sea surface in high latitudes during summer, whereas the lowest *p*H values predominate in the deep ocean (Haugan and Drange, 1996) and in sediment pore water (Zhu *et al.*, 2006). At seawater *p*H of 8.2, less than 1% of dissolved $CO_2$ remains as $CO_2$ ($CO_{2(aq)}$ + $H_2CO_3$), while most dissociates into $HCO_3^-$ (90%) and $CO_3^{2-}$ (9%) (Kleypas *et al.*, 1999a; Wolf-Gladrow *et al.*, 1999).

Oceanic uptake of atmospheric $CO_2$ leads to higher concentrations of dissolved inorganic $CO_2$, $pCO_2$ and $HCO_3^-$, and a decrease in $[CO_3^{2-}]$ and *p*H in the ocean mixed layer (Fairhall, 1973; Gattuso *et al.*, 1998; Kleypas *et al.*, 1999a; Wolf-Gladrow *et al.*,

1999; Marubini *et al.*, 2001; 2003; Iglesias-Rodriguez *et al.*, 2002a; Andersson *et al.*, 2003; Reynaud *et al.*, 2003). The lower *p*H levels result in the additional formation of $HCO_3^-$ via the combination of some $CO_3^{2-}$ with $H^+$ (Wong and Matear, 1998; Kleypas *et al.*, 1999a) since *p*H determines the ratio of $HCO_3^-$ to $CO_3^{2-}$ in solution (Zeebe, 1999). Relative to pre-industrial concentrations, oceanic uptake of anthropogenic $CO_2$ has already reduced the surface $CO_3^{2-}$ concentration by more than 10% (a drop of 29 μmol/kg in the tropics and 18 μmol/kg in the Southern Ocean; Orr *et al.*, 2005). Presently, surface $[CO_3^{2-}]$ varies meridionally from average Southern Ocean values of 105 μmol/kg to average equatorial $[CO_3^{2-}]$ of 240 μmol/kg (Orr *et al.*, 2005). Low $[CO_3^{2-}]$ in the Southern Ocean is due to low surface temperatures (facilitating $CO_2$ uptake; Archer *et al.*, 2000) and large amounts of upwelled deep water, which contain high $[CO_{2(aq)}]$ from organic matter remineralisation (Orr *et al.*, 2005), and consequently a lower *p*H.

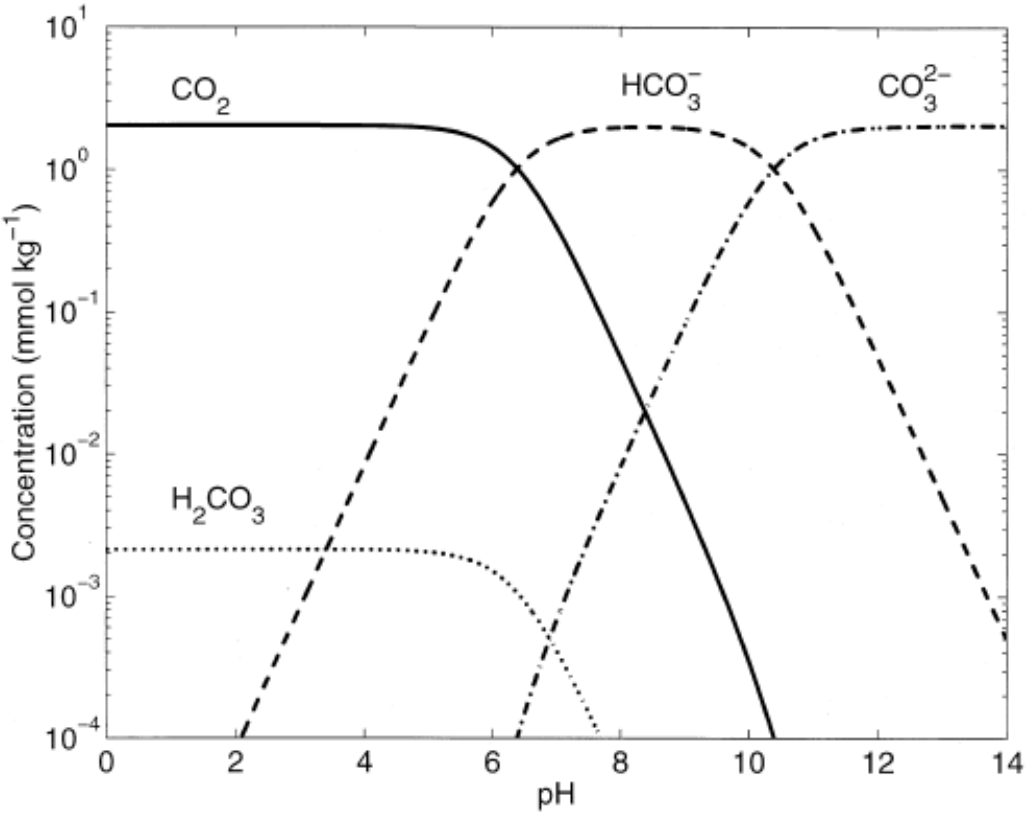


**Figure 4.2.1. Schematic relationship between *p*H and the dissolved carbonate species $CO_2$ (solid line), $H_2CO_3$ (dotted line), $HCO_3^-$ (dashed line), and $CO_3^{2-}$ (dash-dotted line). The values correspond to fresh water conditions (*T* = 19°C, $tCO_2$ ~2 mmol/kg; figure from Zeebe, 1999).**

### 4.2.1 Revelle Factor

Oceanic $CO_2$ (or carbonic acid) uptake neutralises (or titrates) $CO_3^{2-}$ in seawater and decreases the buffer capacity of the ocean, i.e. the capacity of the ocean to resist *p*H changes due to addition of $CO_2$ or other acids (Wong and Matear, 1998; Sabine *et al.*, 2002b; Andersson *et al.*, 2006). The ability of the ocean to act as a sink for anthropogenic $CO_2$ from the atmosphere is inversely proportional to the value of the buffer factor, also called Revelle factor (Siegenthaler and Oeschger, 1978; Sabine *et al*., 2004). Its value is proportional to the ratio between the relative change in seawater $pCO_2$ and the relative change in DIC in seawater (i.e. $[CO_2] + [HCO_3^-] + [CO_3^{2-}]$) (Broecker *et al.*, 1979; Holmen, 1992; Wolf-Gladrow *et al.*, 1999; Sabine *et al*., 2004). This definition of the Revelle factor assumes that the temperature, salinity, and alkalinity of seawater remain constant and that $[tCO_2]$ is much greater than $\Delta[tCO_2]$ (Broecker *et al.*, 1979). As $[CO_3^{2-}]$ decreases, the Revelle factor increases and the ocean's capability to absorb more $CO_2$ from the atmosphere is reduced (Sabine *et al*., 2004). The warm tropical and subtropical oceans are generally characterised by low Revelle factors, whereas high Revelle factors are found in polar areas (Holmen, 1992; Sabine *et al.*, 2004). Globally, the Revelle factor ranges from 8 to 15 in the sea surface (Broecker *et al.*, 1979), with a global average of around 9-10 (cf. Oeschger *et al.*, 1975; Siegenthaler and Oeschger, 1978).

## 4.3 Impact on *p*H

The present rise in atmospheric and oceanic $CO_2$ levels results in significant changes in sea surface *p*H and carbonate chemistry (Wolf-Gladrow *et al*., 1999; Caldeira and Wickett, 2003; Pelejero *et al*., 2005). Boron isotope analysis in foraminifera revealed that glacial-period oceans had higher *p*H by about 0.3 *p*H units and higher $[CO_3^{2-}]$ than today (Sanyal *et al.*, 1995; Spero *et al.*, 1997). Presently, the *p*H level in the tropical sea surface mixed layer is about 8.1 (Gattuso *et al.*, 1998; Caldeira and Wickett, 2005). Modern ocean *p*H displays a range of 0.5 units worldwide, and a seasonal amplitude of up to 0.1 *p*H units locally (Haugan and Drange, 1996). Throughout the tropical Pacific, surface-ocean *p*H variations of ~0.2 units are occurring (Pelejero *et al.*, 2005). This variability mainly occurs due to the temperature-related $CO_2$ solubility (colder water characterised by higher $CO_2$ solubility), and upwelling of cold, $CO_2$-rich water, with colder surface

water and upwelling both leading to a *p*H decrease (Pelejero *et al.*, 2005; Blackford and Gilbert, 2007; Feely *et al.*, 2008). In coastal regions, *p*H may display a variability exceeding 1.0, especially nearby major river plumes (Hinga, 2002; Blackford and Gilbert, 2007).

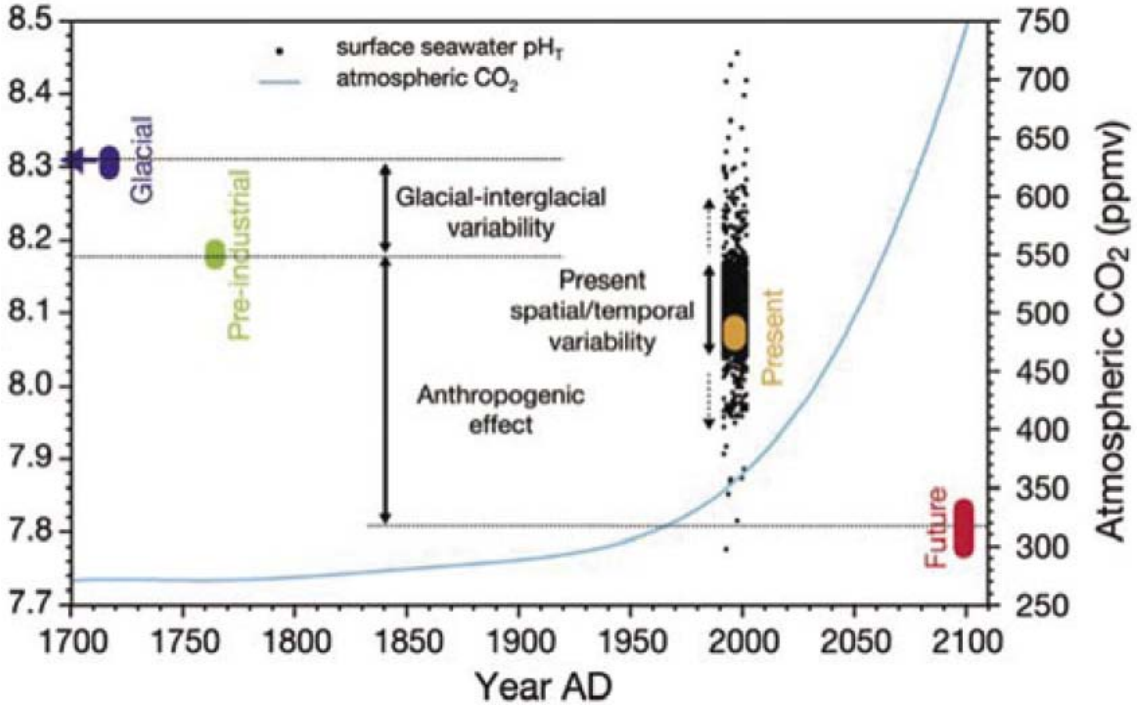


**Figure 4.3.1. Observed and estimated decrease in oceanic *p*H with increasing atmospheric $CO_2$ concentration. Future *p*H is compared to the pre-industrial and glacial-interglacial period, as well as the present sea surface *p*H range (Figure from Steffen, 2006)(Figure from Steffen, 2006)(Figure from Steffen, 2006)(Figure from Steffen, 2006)(figure from Steffen, 2006).**

$CO_2$ uptake by the world oceans lowers ocean *p*H, leading to a reduction in the oceans' capacity to continue to absorb $CO_2$ (Sabine *et al.*, 2002b; Pelejero *et al.*, 2005). It is estimated that average ocean *p*H already has decreased by 0.1 *p*H units (30% increase in $[H^+]$) in cold waters and about 0.09 *p*H units in the warmest surface waters over the anthropocene (Haugan and Drange, 1996; Brewer, 1997: their Table 2; Wolf-Gladrow *et al.*, 1999: their Fig. 1; Caldeira and Wickett, 2003; Nakayama *et al.*, 2005; Orr *et al.*, 2005a). A further reduction of 0.2 to 0.4 *p*H units is predicted for the 21$^{st}$ century (Figure 4.3.1) (Haugan and Drange, 1996; Brewer, 1997; Gattuso *et al.*, 1998; Wong and Matear,

1998; Wolf-Gladrow *et al.*, 1999; Langdon *et al.*, 2000; Caldeira and Wickett, 2005; Kleypas *et al.*, 2006; Blackford and Gilbert, 2007), and continued emission of fossil-fuel $CO_2$ could result in a *p*H reduction of 0.7 units by 2300 (Caldeira and Wickett, 2003). When [$CO_2$] varies very rapidly ($<10^4$ years), ocean *p*H is relatively sensitive to changes in [$CO_2$] (Caldeira and Wickett, 2003). When [$CO_2$] changes relatively slowly ($>10^5$ years), on the other hand, ocean chemistry is buffered by increased terrestrial weathering reactions with aluminosilicate rocks, and interactions with terrestrial and marine carbonate minerals, thereby reducing sensitivity to *p*H changes (cf. Caldeira and Wickett, 2003; Blackford and Gilbert, 2007). Relative to the direct effects of increased $CO_2$ in the atmosphere, *p*H is only modestly affected by other climate change feedbacks because the effects of warmer SSTs (reducing *p*H) and diminished solubility of $CO_2$ in the upper ocean with ocean warming (increasing *p*H) on *p*H show a tendency to counteract each other (McNeil and Matear, 2006; 2007). It is thus more likely that future *p*H and ocean acidification will mainly be influenced by the atmospheric $CO_2$ concentration (McNeil and Matear, 2007).

## 4.4 Effect on Coral Reefs

Coral reefs are confined to areas where the annual minimum seawater temperature exceeds 18°C (Vaughan, 1919). For most coral systems, the optimum temperature is about 26-27°C and growth significantly declines ±5°C from the optimum condition (Jokiel and Coles, 1977; Coles and Jokiel, 1978; Reynaud-Vaganay *et al.*, 1999: Fig. 2). Corals are less likely to recover when exposed to low temperatures (lower limit = 18°C) (Jokiel and Coles, 1977). Most reefs occur in tropical waters (cf. Gattuso and Buddemeier, 2000: Fig. 1) with average annual SSTs greater than 27°C (Kleypas *et al.*, 1999b) and at water depth of less than 30 m (Achituv and Dubinsky, 1990: Fig. 1.2; Kleypas *et al.*, 2005). Light and saturation state of aragonite are also strongly linked to reef development, with both lower light intensity and lower saturation state leading to reduced calcification rate (Table 4.4.1) (e.g. Goreau and Goreau, 1959; Chalker and Taylor, 1978; Barnes, 1982; Kleypas *et al.*, 1999b). Light intensity is strongly controlled by latitude and depth and, on a regional scale, can be significantly attenuated by particulate and dissolved organic matter in the water column (Marubini *et al.*, 2001).

**Table 4.4.1. Physical and biogeochemical processes impacting on or impacted by the coral reef system. For each process, forcing factors and variables (dependent factors) affected by a given process are listed. The 'feedback mechanism' column refers to the relationship between certain processes (1st column) and other parameters, with a positive [negative] feedback enhancing [reducing] the impact of the given process. On the next page, observed trends in the processes are tabulated, together with a summary of the main impacts on the reefs due to predicted changes in each process.**

| parameter | forcing factors | dependent factors | feedback mechanism |
|---|---|---|---|
| **biogeochemical processes** | | | |
| saturation state | $pCO_2$, $p$H, $CO_3^{2-}$, temperature | calcification rate, carbonate dissolution rate (mainly hmc and aragonite) | |
| calcification | $CO_3^{2-}$, saturation state, SST | $p$H, $CO_2$ | negative with $CO_2$ |
| dissolution | $CO_3^{2-}$, saturation state, SST | $p$H, $CO_2$ | negative with $CO_2$ |
| coral bleaching | SST | calcification | positive with structural strength |
| atmospheric $pCO_2$ | anthropogenic greenhouse emissions | air-sea $CO_2$ flux; saturation state | positive with SST |
| air-sea $CO_2$ flux | wind stress, temperature, circulation, atmospheric $pCO_2$ | $p$H, $CO_3^{2-}$ | |
| $p$H | (rate of) oceanic $CO_2$ uptake, circulation, temperature | carbon species distribution | |
| buffer factor | circulation, $CO_2$, $CO_3^{2-}$ | $pCO_2$, carbonate dissolution rate | |
| biological pump | warming, circulation, stratification, $p$H, $pCO_2$, $CaCO_3$ production | $p$H, $CO_2$, nutrient supply, respiration, microbial decomposition of organic matter | positive with nutrient supply |
| **physical processes** | | | |
| SST | radiation, greenhouse gas concentration, circulation, wind stress | stratification, ocean circulation, coral bleaching, $pCO_2$/solubility of $CO_2$; $CO_3^{2-}$ | positive with MLD/stratification |
| light intensity | suspended particulate and dissolved organic matter, latitude, depth | calcification rate, primary productivity/biological pump | |
| stratification/MLD | wind stress, temperature | SST, nutrients, biological pump, air-sea $CO_2$ flux | positive with SST |
| circulation | stratification/MLD, wind stress | biological pump, nutrients, light | |
| storm activity | wind stress, temperature | mixing, structural strength | |

**Table 4.4.1 continued.**

| parameter | main observed trend | Positive impact | negative impact | reef impact |
|---|---|---|---|---|
| **biogeochemical processes** | | | | |
| saturation state | decreasing (-0.6 since 1880) | | lower saturation states result in reduced calcification rates | important |
| calcification | mainly decreasing (-6 to -10% since 1880) | reduction reduces the amount of $CO_2$ released into the ocean | reduction may induce weaker skeletons, increased bioerosion | dominant |
| dissolution | increasing | reduction in the amount of $CO_2$ released into the ocean | | important |
| coral bleaching | increasing | | reduction in calcification rate | intermediate |
| atmospheric $pCO_2$ | increasing (+100 µatm since 1880) | | increase ultimately results in lower saturation state | important |
| air-sea $CO_2$ flux | variable, mainly increasing | | | |
| *p*H | decreasing (-0.1 since 1880) | | lower *p*H shifts carbon species equilibrium towards larger $CO_2$ and lower $CO_3^{2-}$ proportion | important |
| buffer factor | decreasing | | more rapid increase in $CO_2$ | important |
| biological pump | unknown | increase would induce greater $CO_2$ export into deep ocean | decline in pump efficiency causing lower $CO_2$ export into deep ocean | subordinate |
| **physical processes** | | | | |
| SST | increasing (+0.61 since 1861) | small SST increases may cause expansion of area suitable for coral growth; also improves photosynthesis and induces minor increase in $CO_3^{2-}$ | large SST changes increases likelihood of thermal stress (coral bleaching and mortality) | important |
| light intensity | unknown | | a reduction would cause lower calcification rates and primary productivity | subordinate |
| stratification/MLD | variable | decreased stratification increases SST and $pCO_2$ | increased stratification increases SST and $pCO_2$ | intermediate |
| circulation | unknown | | | intermediate |
| storm activity | potentially increasing | deepening of MLD, cooler SST | increases likelihood of physical storm damage (reduction in structural strength) | subordinate |

The area of the coral reef habitat could potentially expand in association with predicted warmer SSTs (McNeil *et al.*, 2004), and because a temperature increase of surface waters will induce a general increase in sea surface [$CO_3^{2-}$] (Orr *et al.*, 2005a). However, it is also believed that an upper temperature limit for coral reef calcification may exist (Jokiel and Coles, 1977; Buddemeier *et al.*, 2004), with different corals displaying different sensitivities to changes in $\Omega_{arag}$ and SST (cf. Reynaud *et al.*, 2003). Furthermore, the predicted magnitude of the [$CO_3^{2-}$] increase due to warmer SSTs is small, generally counteracting less than 10% of the decrease due to the effect of rising $CO_2$ (Orr *et al.*, 2005a). The smallest increases, and in some cases even minor decreases, in [$CO_3^{2-}$] are observed in high-latitude surface waters (Orr *et al.*, 2005a). Moreover, higher $CO_2$ levels lead to increased dissolution rates or lower rates of carbonate production by marine benthos and plankton (Iglesias-Rodriguez *et al.*, 2002; Shirayama and Thornton, 2005).

### 4.4.1 Saturation State

The negative impact of elevated $pCO_2$ on calcification in corals and coral communities is now well documented (Gattuso *et al.*, 1999; Langdon *et al.*, 2000; 2003; Leclercq *et al.*, 2000; 2002; Marubini *et al.*, 2003; Reynaud *et al.*, 2003). Increasing atmospheric [$CO_2$] also leads to a reduction in seawater [$CO_3^{2-}$], and thus the level of $CaCO_3$ saturation, making it more difficult for marine calcifying organisms to form $CaCO_3$ (Marubini and Atkinson, 1999; Wolf-Gladrow *et al.*, 1999; Orr *et al.*, 2005a). An increase of atmospheric $CO_2$ to 788 ppmv by the year 2100, as predicted under the IS92a scenario (Houghton *et al.*, 2001: p. 14, Fig. 5), would result in average tropical surface [$CO_3^{2-}$] and surface water *p*H reduction of around 45-50% and 0.35 units, respectively, relative to pre-industrial levels (Broecker *et al.*, 1979: Fig. 8; Kleypas *et al.*, 1999a; Wolf-Gladrow *et al.*, 1999; Orr *et al.*, 2005a). The atmospheric $CO_2$ concentration is forecast to reach twice the pre-industrial level by 2065, which will reduce the concentration of $CO_3^{2-}$ and $CaCO_3$ saturation state of the surface ocean by 30% relative to the pre-industrial level (Langdon *et al.*, 2000). The reduction in super-saturation of seawater with respect to calcite and aragonite may result in both the dissolution of $CaCO_3$

in sediments (Wollast, 1994) and in a drop of $CaCO_3$ production rate (Broecker and Takahashi, 1966; Wolf-Gladrow *et al.*, 1999; Marubini *et al.*, 2008).

The $CaCO_3$ saturation state ($\Omega$) is defined as

$$\Omega = \frac{[Ca^{2+}][CO_3^{2-}]}{K_{sp}}, \text{ where}$$

$K_{sp}$ is the stoichiometric solubility product for a specific mineral phase of $CaCO_3$: calcite from coccolithophorids and foraminifera, aragonite from corals, green algae and pteropods (open ocean planktonic molluscs; cf. Berner, 1977; Doney and Glover, 2005), or high-magnesian calcite (hmc) from coralline algae (Morse and Mackenzie, 1990; Kleypas *et al.*, 1999a; Feely *et al.*, 2004; McNeil *et al.*, 2004; Langdon and Atkinson, 2005). $\Omega$ is largely determined by variations in $[CO_3^{2-}]$ since $[Ca^{2+}]$ is quasi-conservative in the ocean (Smith and Pesret, 1974; Kleypas *et al.*, 1999a; Marubini *et al.*, 2001; Reynaud *et al.*, 2003; McNeil *et al.*, 2004; Andersson *et al.*, 2006). Tropical surface waters are presently supersaturated ($\Omega > 1.0$) with respect to all carbonate mineral phases, but the extent of saturation varies: $\Omega_{calcite}$ is 5-6, $\Omega_{arag}$ (saturation of aragonite) is 3-4, and $\Omega_{hmc}$ is 2-3 (Smith and Buddemeier, 1992; Kleypas *et al.*, 1999a; 1999b; McNeil *et al.*, 2005). Coral reef habitats are associated with a $\Omega_{arag}$ value of about 3.8 or higher (Kleypas *et al.*, 1999b; McNeil *et al.*, 2004). Supersaturation of sea water with respect to $CaCO_3$ declines with decreasing temperature (due to higher solubility of $CO_2$) and increasing atmospheric $CO_2$ concentration (Smith and Buddemeier, 1992; Marubini *et al.*, 2001; Lerman and Mackenzie, 2005), with supersaturation of calcite being around 2.0-2.5 in the polar surface oceans (Takahashi, 1975). Supersaturation of aragonite is also significantly correlated to SST, with $\Omega_{arag}$ values below 2 being measured in high-latitudes (Broecker *et al.*, 1979; Kleypas *et al.*, 1999a; 1999b), whereas $\Omega_{arag}$ is relatively invariable within the tropical belt (Kleypas *et al.*, 1999b). Locally, $\Omega$ can also be noticeably affected by biological, physical and chemical processes on reefs such as photosynthesis, calcification, water residence time, upwelling and freshwater inputs (Marubini *et al.*, 2001).

Continued $CO_2$ emission to the atmosphere may eventually lead to undersaturation of high-magnesian calcite and aragonite in the sea surface (Broecker *et al.*, 1971; Fairhall, 1973), which could potentially have severe biological impacts, including greater

susceptibility to dissolution (Shirayama and Thornton, 2005). It is predicted that high-saturation areas will undergo the greatest decrease in saturation state (Kleypas *et al.*, 1999a). Undersaturation would first occur in the Antarctic and subarctic surface waters during winter, where seawater $pCO_2$ values are highest because of cold temperatures (i.e. greater $CO_2$ solubility) and wind-driven mixing of subsurface waters into the mixed layer, and would then progressively expand toward the equator (Feely *et al.*, 2004). McNeil and Matear (2008) estimate that seasonal $\Omega_{arag}$ undersaturation will begin in the Southern Ocean when atmospheric $CO_2$ levels reach about 450 ppm. It is expected that the current $\Omega_{arag}$ of 4.0 ± 0.2 will drop to 3.1 ± 0.3 by the year 2065 and to 2.8 ± 0.2 by 2100 (Gattuso *et al.*, 1999; Kleypas *et al.*, 1999a; Langdon *et al.*, 2000; Andersson *et al.*, 2003: Fig. 2). Tropical $\Omega_{arag}$ already has decreased about 0.6 units (from an estimated average value of 4.6) since 1880 (Kleypas *et al.*, 1999a).

### 4.4.2 Calcification - Interacting Effects of $pCO_2$ and Temperature

Changes in the observed and predicted saturation levels of this extent have been shown to invoke a marked decline in calcification of corals, coralline macroalgae and planktonic organisms (Figure 4.4.1) (Gattuso *et al.*, 1998; Langdon *et al.*, 2000; Leclercq *et al.*, 2000; Riebesell *et al.*, 2000; Marubini *et al.*, 2003; Kleypas *et al.*, 2006) since calcification is strongly controlled by $CO_3^{2-}$, $\Omega$ and SST (Broecker and Takahashi, 1966; Smith and Buddemeier, 1992; Gattuso *et al.*, 1999; Kleypas *et al.*, 1999a; Marubini and Atkinson, 1999; Leclercq *et al.*, 2000; 2002; Riebesell *et al.*, 2000; Marubini *et al.*, 2001; Iglesias-Rodriguez *et al.*, 2002; Andersson *et al.*, 2003; Buddemeier *et al.*, 2004; Feely *et al.*, 2004; McNeil *et al.*, 2004; Langdon and Atkinson, 2005). The calcification rate of all calcifying organisms examined so far in experimental mesocosm studies was reduced in response to a decreased $CaCO_3$ saturation state, even when $\Omega$ exceeds 1 (Gattuso *et al.*, 1998; Langdon *et al.*, 2000; Leclercq *et al.*, 2000; 2002; Marubini *et al.*, 2001; 2003). The calcification rate reacts to changes in the concentrations of both $Ca^{2+}$ and $CO_3^{2-}$ as a positive linear function of the ion concentration product, $[Ca^{2+}]^{0.69}[CO_3^{2-}]$ (Burton and Walter, 1987: Fig. 1; Zhong and Mucci, 1989; Zuddas and Mucci, 1998; Marubini and Thake, 1999; Langdon *et al.*, 2000). The present-day calcification of marine calcifying

ecosystems has already declined by about 6-10% from pre-industrial levels (Gattuso *et al.*, 1999; Leclercq *et al.*, 2002).

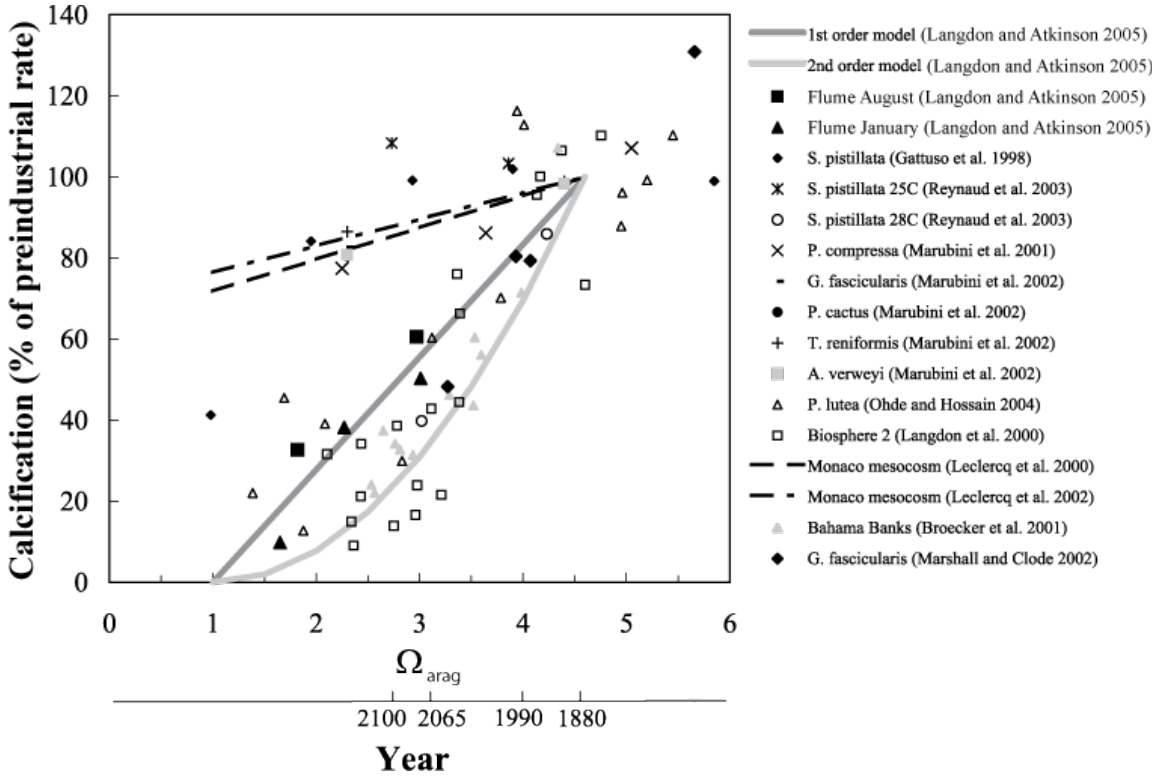


**Figure 4.4.1**. **Relationship between aragonite saturation state ($\Omega_{arag}$) and calcification rate as a percentage of the pre-industrial rate (adapted from Langdon and Atkinson, 2005). Bold shaded lines indicate estimates of relationship between saturation state and calcification based on controlled biological (mesocosm and laboratory) experiments. Predicted saturation states and calcification rates vary greatly among the experimental studies, which can be attributed to both experimental design and differences in physiological response of the calcifying organisms studied.**

Because of the complex feedback loops (cf. Table 4.4.1), there is some disagreement as to whether coral reef and planktonic calcification will increase or decrease in future. A further decrease of 9-50% in the 21$^{st}$ century is predicted by controlled biological experiments, analytical calculations and model scenarios (Gattuso *et al.*, 1999; Kleypas *et al.*, 1999a; Marubini *et al.*, 2001; Leclercq *et al.*, 2002; Reynaud *et al.*, 2003). The wide range of predicted calcification decline by the end of this century is partially caused by the relatively poorly constrained atmospheric $CO_2$ levels for 2100, with various IPCC scenarios being chosen for the forecasts. In addition, physiological and metabolic

differences in the various calcifying organisms, and the experimental design (e.g. whether temperature is included in the analysis) chosen to predict calcification, also impact on the calcification trend estimations. The effect of lower calcification rates will likely be greater for calcareous skeletons such as branching corals that have large surface areas to mass ratio, and that are remote from the buffering capacity of carbonate-rich sediments (Brunskill, pers. comm.). Large massive corals (such as *Porites* spp.) and other large benthic carbonate skeletons will likely be least affected (Anthony *et al.*, 2008).

However, some research groups (e.g. McNeil *et al*., 2004) believe that the coral reef calcification rate will increase with future ocean warming and eventually exceed pre-industrial rates by about 35% by 2100 (see also Burton and Walter, 1987). $pCO_2$ and temperature interact extensively in calcification (Reynaud *et al*., 2003). The temperature increase induces an enhancement of the calcification rate at normal $pCO_2$ in supersaturated seawater, while it leads to a decrease of calcification at elevated $pCO_2$ (Reynaud *et al*., 2003). Whereas the response of calcification to changes in $\Omega_{arag}$ seems to be generally linear with increasing $CO_2$ (e.g. Langdon *et al.*, 2000; Leclercq *et al.*, 2000), coral response to increasing temperature is not linear (cf. Kleypas *et al.*, 2005). Calcification increases up to a thermal optimum (normally at or 1-2°C below the local normal peak summer temperature) as the temperature is elevated, and then rapidly declines beyond that (Clausen and Roth, 1975: Fig. 2; Jokiel and Coles, 1977: Fig. 2; Coles and Jokiel, 1978; Reynaud-Vaganay *et al.*, 1999; Marshall and Clode, 2004). It is generally considered that an increase in both $CO_2$ and temperature (and their impact on saturation state) will lead to a net reduction in coral reef calcification (Gattuso *et al*., 1999; Kleypas *et al*., 1999a; Langdon *et al*., 2000; Reynaud *et al*., 2003). Presently, corals have responded more to ocean warming (growing faster through enhanced metabolism and/or increased photosynthetic rates of their zooxanthellae) than to decreases in $[CO_3^{2-}]$ and the consequent change in saturation state (Table 4.4.1) (Lough and Barnes, 2000; Buddemeier *et al.*, 2004; McNeil *et al.*, 2004). A study by Lough and Barnes (2000) based on cores from Porites colonies showed that the calcification rate has been increasing since 1880, which they attributed to warmer SST (cf. Levitus *et al.*, 2005). Some researchers (e.g. McNeil *et al*., 2004) predict that rising SSTs will continue to outweigh the negative effects of declining $[CO_3^{2-}]$ and result in a significant rise in the

annual calcification rate by 2100. However, in general, it is considered that calcification rates will start to decrease once a certain lower limit in the saturation state (due to $pCO_2$ increase) is reached (e.g. Andersson *et al*., 2006). Furthermore, it is predicted that coral bleaching events will increase in future due to warmer SSTs (Hoegh-Guldberg, 1999).

### 4.4.3 Coral Bleaching

Elevated SST results in coral bleaching due to the loss of zooxanthellae (algal symbionts), or in the decrease in chlorophyll (photosynthetic pigments) concentration in the algal cells (Szmant and Gassman, 1990; Glynn, 1996; Hoegh-Guldberg, 1999; Reynaud *et al.*, 2003). Coral bleaching also leads to a significant reduction in the skeletal extension rate, with complete recovery of surviving corals of severe bleaching events often exceeding one year (Suzuki *et al.*, 2003). The frequency and geographical extent of coral bleaching events have increased significantly, and coral bleaching is anticipated to occur on a yearly basis by around the mid-21$^{st}$ century (cf. Hoegh-Guldberg, 1999).

It was initially assumed that coral reef organisms could not acclimatise to rising $pCO_2$, lower $\Omega_{arag}$ and bleaching events (Hoegh-Guldberg, 1999; Langdon *et al.*, 2000; Leclercq *et al.*, 2002; Reynaud *et al.*, 2003). However, it is now evident that corals have a variety of methods by which they can adapt to environmental processes such as heat stress and bleaching events (Kinzie *et al.*, 2001; Brown *et al.*, 2002; Baker *et al.*, 2004; Little *et al.*, 2004; Rowan, 2004). Corals have at least partially adapted to warmer sea surface temperatures by hosting thermally tolerant algal symbionts such as *Symbiodinium* clade D (Glynn *et al.*, 2001; Baker *et al.*, 2004; Rowan, 2004). *Pocillopora* spp. living in frequently warm (>31.5°C) habitats contain only *Symbiodinium* D, while those living in cooler regions mainly host *Symbiodinium* strain C (Rowan, 2004). Corals hosting thermally tolerant *Symbiodinium* D are more profuse on reefs after severe bleaching events (Glynn *et al.*, 2001; Baker *et al.*, 2004; van Oppen *et al.*, 2005), such that these reefs more closely resemble those found in high-temperature environments (Baker *et al.*, 2004). There is a trade-off, however, for corals hosting the thermally resistant *Symbiodinium* D strain. Although they are less affected by coral bleaching (e.g. Glynn *et al.*, 2001), their growth rate is reduced by 2-3 times compared to corals containing clade C1 zooxanthellae (Little *et al*., 2004).

### 4.4.4 $CaCO_3$ Dissolution

It is expected that reduced calcification due to lower saturation levels will result in weaker skeletons, reduced extension rates, and increased susceptibility to bioerosion and other environmental stress factors (Langdon *et al.*, 2003; Hoegh-Guldberg *et al.*, 2007), the extent of which would be highly species specific (Marubini *et al.*, 2003). Scanning electron microscopy in controlled biological experiments indicates that the proportion of malformed coccoliths and incomplete coccospheres increases with increasing [$CO_2$] (Riebesell *et al.*, 2000).

Additionally, the geographical extent and scale of dissolution will expand as a result of increased ocean acidity and declining $CaCO_3$ saturation state (Feely *et al*., 2004; 2008). Global annual new production of $CaCO_3$ currently ranges from 0.7 to 1.4 Pg of $CaCO_3$-C/yr (Kinsey and Hopley, 1991; Milliman and Droxler, 1996; Lee, 2001; Iglesias-Rodriguez *et al.*, 2002). Approximately 20% of this net community production accumulates in the surface layer as suspended or dissolved organic matter (Hansell *et al.*, 1997), whereas about 50-80% of the $CaCO_3$ produced is exported vertically and dissolved in the upper water column and in sediments (Morse and Mackenzie 1990; Hansell *et al.*, 1997; Milliman *et al*., 1999; Iglesias-Rodriguez *et al*., 2002a: Table 1; Feely *et al*., 2004; Lerman and Mackenzie, 2005). The maximum dissolution rate occurs just below the saturation depth for aragonite (Sabine *et al.*, 2002). The total water column $CaCO_3$ dissolution rate for the global oceans is approximately 0.5 ± 0.2 Pg of $CaCO_3$-C/yr (Feely *et al*., 2004). In the Pacific, the highest dissolution rates (up to ~1.2 μmol $kg^{-1}$ $yr^{-1}$) occur between 400 and 600 m (Feely *et al*., 2004).

The dissolution of $CaCO_3$ is mainly driven by remineralisation of sinking organic matter in the ocean, dissolution within guts and faeces of grazers, or $CO_2$-producing organic matter degradation in sediments (Emerson and Bender, 1981; Morse and Mackenzie, 1990; Milliman, 1993; Archer and Maier-Reimer, 1994; Harris, 1994; Milliman *et al.*, 1999). No more than about 20-30% of the total annually produced $CaCO_3$ is buried in shallow and deep sediments (Feely *et al.*, 2004), the composition of which is greatly dependent on both temperature and $CaCO_3$ saturation state in seawater (cf. Burton and Walter, 1987). Aragonite and high magnesium calcite (>4 mol% $MgCO_3$)

are most affected by increased dissolution since they are significantly more soluble in seawater compared to low magnesium calcite (e.g. Jamieson, 1953; Chave *et al.*, 1962; Smith and Pesret, 1974; Berner, 1977; Mucci, 1983).

#### *4.4.4.1 Sediment $CaCO_3$ Accumulation*

The present-day accumulation of $CaCO_3$ in deep-sea sediments is estimated to be about 0.1-0.14 Pg C/yr in the pelagic environment (Milliman, 1993; Milliman and Droxler, 1996; Catubig *et al.*, 1998; Iglesias-Rodriguez *et al.*, 2002). Continental shelves, even though they cover a significantly smaller area, are approximated to accumulate a similar amount of $CaCO_3$ (0.11-0.13 Pg C/yr) to that of the open ocean since $CaCO_3$ production rates on shelves are high, whereas removal and dissolution rates are low (Iglesias-Rodriguez *et al.*, 2002). On coral reef systems, the removal and dissolution rates are both estimated to be about 10% of the total $CaCO_3$ produced (Milliman, 1993).

The dissolution rate of $CaCO_3$ is expected to increase in future due to rising oceanic $CO_2$ concentrations and increased deposition of riverine and *in situ* organic matter in coastal sediments, which both result in a reduction of the pore water saturation state of $CaCO_3$ (Andersson *et al.*, 2005; 2006). Concurrently, the carbonate composition in sediments is expected to change in future, with low-Mg calcite and aragonite more likely to be preserved in the sediments than the more soluble high-Mg calcites (Andersson *et al.*, 2005; 2006).

## 4.5 Change in Ocean $CO_2$ Storage Capacity

Global warming reduces the influx of $CO_2$ into the oceans (Sarmiento and Le Quéré, 1996; Sarmiento *et al.*, 1998; Joos *et al.*, 1999; Lerman and Mackenzie, 2005). The oceanic $CO_2$ uptake is projected to decrease in future due to a combination of 1) increased upper ocean stratification and the commensurate thinning of the surface mixed layer of the ocean (e.g. Sarmiento *et al.*, 1998; Mignone *et al.*, 2006), 2) a slowdown of the thermohaline circulation (Manabe and Stouffer, 1994; Sarmiento and Le Quéré, 1996; Sarmiento *et al.*, 1998; Mackenzie *et al.*, 2001), which both tend to inhibit downward transport of anthropogenic $CO_2$ (Govindasami *et al.*, 2005), and 3) decreased $CO_2$ solubility due to higher SST (cf. Milliman, 1974; Weiss, 1974; Broecker and Peng,

1982), with the greatest reduction of $CO_2$ storage occurring at high latitudes (Friedlingstein *et al.*, 2001; Winguth *et al.*, 2005). A reduction in the biological pump strength would lead to a further decline in the marine $CO_2$ storage (Matear and Hirst, 1999; Bopp *et al.*, 2005; Winguth *et al.*, 2005). Increased stratification will reduce the supply of nutrient and increase light efficiency, resulting in a net reduction in marine export production (Bopp *et al.*, 2001; Riebesell *et al.*, 2007). The reduction in sea surface nutrients is predicted to cause a decrease in the diatom abundance, in favour of smaller phytoplankton, which ultimately will result in increased recycling of nutrients and carbon, and a decrease in the export ratio, due to the reduction in sinking speed of smaller organic particles (Bopp *et al.*, 2005). However, the positive effect of the improved photosynthetic efficiency during spring and summer and, correspondingly, the longer growing season, reduces the negative effect due to decreased nutrient supply in equatorial regions and even results in increased export in high latitudes (Bopp *et al.*, 2001). Marine $CO_2$ uptake is also predicted to be significantly reduced (by 16-22%) because of an enhanced equatorial $CO_2$ exchange from the ocean to the atmosphere by increased upwelling (Winguth *et al.*, 2005). Equatorial upwelling is expected to increase due to a decrease in the pole-to-equator temperature gradient and an increase in moisture transport (Winguth *et al.*, 2005). Similarly, the terrestrial anthropogenic $CO_2$ uptake is also predicted to decrease in future due to an increase in soil aridity, especially in the subtropics (Friedlingstein *et al.*, 2001; Winguth *et al.*, 2005). This positive feedback of both marine and terrestrial carbon cycle would result in a greater rate of atmospheric $CO_2$ increase (e.g. Friedlingstein *et al.*, 2001; Winguth *et al.*, 2005).

### 4.5.1 $CaCO_3$ Impact on $CO_2$

Calcification is a well-known source of $CO_2$ to the surrounding water, and, thus, to the atmosphere, since calcification lowers alkalinity and *p*H, and results in higher $pCO_2$ (Wollast *et al.*, 1980; Kinsey and Hopley, 1991; Smith and Buddemeier, 1992; Ware *et al.*, 1992; Gattuso *et al.*, 1993; Frankignoulle *et al.*, 1994; 1996b; Kawahata *et al.*, 1997; Suzuki, 1998; Zondervan *et al.*, 2001; Bates, 2002b; Delille *et al.*, 2005), although there is some debate as to whether reefs are a net source or sink of $CO_2$ to the atmosphere (cf. Frankignoulle *et al.*, 1996b; Chisholm and Barnes, 1998). Several reefs were found to be

sources of $CO_2$ during the night, whereas they act as a sink for atmospheric $CO_2$ during the day (e.g. Ohde and van Woesik, 1999), which can be attributed to a decrease in photosynthesis during night-time. $CaCO_3$ precipitation releases $CO_2$, whereas dissolution consumes $CO_2$ and produces $HCO_3^-$ (Iglesias-Rodriguez *et al.*, 2002a; Feely *et al.*, 2004; Lerman and Mackenzie, 2005):

$$Ca^{2+} + 2HCO_3^- \underset{\text{dissolution}}{\overset{\text{precipitation}}{\rightleftharpoons}} CaCO_3 + H_2O + CO_2$$

Presently, the yearly $CO_2$ release due to calcification is estimated at 0.02-0.08 Gt C (Ware *et al.*, 1992). This increase in $CO_2$ concentration via calcification is related to the buffer capacity of the ocean, with more rapid $CO_2$ increases occurring when the buffer capacity is low (Riebesell *et al.*, 2000; Zondervan *et al.*, 2001). In addition, the buffer capacity decreases as $CO_2$ increases (Zondervan *et al.*, 2001; Sabine *et al.*, 2002; see also section 4.2.1), resulting in a positive feedback. The oceanic uptake of anthropogenic $CO_2$ is facilitated by processes that increase the total alkalinity (TA) in the upper ocean, one of which is the dissolution of marine $CaCO_3$ in the water column and in shelf sediments, which removes dissolved $CO_2$ (Smith and Pesret, 1974; Tribble and Mackenzie, 1998; Wolf-Gladrow *et al.*, 1999; Sabine *et al.*, 2002b; Feely *et al.*, 2004). Similarly, a decrease in calcification would also increase the capacity of $CO_2$ storage in the upper ocean (cf. Kinsey and Hopley, 1991; Zondervan *et al.*, 2001; Feely *et al.*, 2004).

At the present $pCO_2$ of 380 µatm and 25°C, the released $CO_2$:precipitated carbonate ratio ($\Psi$) is estimated to be 0.6 in seawater (Ware *et al.*, 1992; Frankignoulle *et al.*, 1994: Fig. 2; Koeve, 2002: Fig. 6). Thus, for each mole of $CaCO_3$ deposition, only 0.6 moles of $CO_2$ are liberated due to the ocean's buffering capacity, which is highly temperature- and $pCO_2$-dependent (Ware *et al.*, 1992). In high latitudes, $\Psi$ reaches values of up to 0.82 (Koeve, 2002), therefore increasing the $CO_2$-release accordingly. Whereas the amount of $CO_2$ released during calcification increases with rising seawater $pCO_2$ concentration, $\Psi$ decreases with increasing temperature (at $pCO_2$ = 350 µatm, $\Psi = 0.8 - 8.3 \times 10^{-3}$ t, t in °C; Frankignoulle *et al.*, 1994). Therefore, the warming of surface water due to global warming results in a smaller increase of $\Psi$ with $pCO_2$ than would occur at a constant temperature (Frankignoulle *et al.*, 1994). In the pre-industrial ocean, 0.64 mole $CO_2$ was released per mole $CaCO_3$ precipitated (with temperature = 15°C and salinity = 35: Frankignoulle *et al.*, 1994). Due to the temperature effect, doubling of the pre-industrial

$pCO_2$ and an SST increase of 3°C will augment Ψ to 0.74 (cf. Frankignoulle *et al.*, 1994), and it is expected to reach about 0.79 by 2100 (Riebesell *et al*., 2000). Whereas such an increase in Ψ would result in a positive feedback on increasing atmospheric $CO_2$ levels, a decrease in the biogenic calcification rate would counteract this effect.

Negative feedbacks may also result from the effects of enhanced phytoplankton growth rate and changing elemental composition of organic matter (Wolf-Gladrow *et al.*, 1999). Photosynthetic production of organic matter from $CO_2$ and its net storage in sediments counteracts the $CO_2$ emission by $CaCO_3$ precipitation, resulting in lower $CO_2$ release from the surface layer (Delille *et al*., 2005; Lerman and Mackenzie, 2005). Whereas primary production removes $CO_2$, respiration or remineralisation of organic matter produces $CO_2$ (Keeling *et al.*, 1993; Lerman and Mackenzie, 2005):

$$CO_2 + H_2O \underset{\text{autorespiration}}{\overset{\text{gross primary production}}{\rightleftharpoons}} CH_2O + O_2$$

Interestingly, several studies (e.g. Borowitzka and Larkum, 1976; Suzuki *et al.*, 1995) have indicated that a positive reinforcement can exist between the rates of photosynthesis and calcification in coral reef systems, which is a direct result of their respective influence on local *p*H and $CO_2$ levels.

### 4.5.2 $C_{CaCO3}$:$C_{org}$ and its Impact on the Biological Pump

The increase in $pCO_2$ seems to encourage organic carbon production in nonsaturating light and nutrient-rich conditions (Riebesell *et al*., 2000; Zondervan *et al*., 2002) but the calcification rate decreases significantly when $CO_2$ exceeds an upper limit (Nimer *et al.*, 1994). On the contrary, in nutrient-limited environments, organic carbon production remains constant (Delille *et al*., 2005) or even decreases (Sciandra *et al*., 2003) with increasing $pCO_2$. In addition, as discussed earlier, elevated $pCO_2$ results in a reduction in calcification (Riebesell *et al*., 2000; Zondervan *et al*., 2002; Sciandra *et al*., 2003; Delille *et al*., 2005) when irradiance is not significantly reduced (cf. Zondervan *et al.*, 2002), leading to a decrease of the $C_{CaCO3}$:$C_{org}$ ratio - unless the system is nutrient depleted (cf. Sciandra *et al.*, 2003). Such a reduction results in a weakening of the carbonate pump (Wolf-Gladrow *et al.*, 1999). The removal of $CaCO_3$ out of the sea surface lowers surface alkalinity (e.g. Sarmiento *et al*., 2000; cf. section 2.4.1). It also modifies DIC and total

alkalinity in the ratio 1:2 and thereby increases $CO_2$ in surface water (Wolf-Gladrow *et al.*, 1999). Therefore, the expected future decrease in the $CaCO_3$ export production (Heinze, 2004) due to lower calcification rates would increase the ocean's ability to store atmospheric $CO_2$ (Wolf-Gladrow *et al.*, 1999; Heinze, 2004).

Conversely, it was proposed that a reduction in calcification rates would induce a decline in the export of POC (ballast hypothesis) (Barker *et al.*, 2003) since currently most of the organic carbon is transported into the deep ocean by relatively dense $CaCO_3$ aggregates (Klaas and Archer, 2002); Such a decrease in the POC rain would result in higher [$CO_2$] in the upper ocean, therefore providing a positive feedback for rising atmospheric $CO_2$ levels (Heinze, 2004).

## 4.6 Mitigation Methods

### 4.6.1 $CO_2$ Disposal

To mitigate rising atmospheric $CO_2$ levels, one proposal to remove $CO_2$ from the atmosphere is by actively sequestering $CO_2$ into the deep ocean (e.g. Haugan and Drange, 1996; Teng *et al.*, 1997; Drange *et al.*, 2001; Hoffert *et al.*, 2002; Orr *et al.*, 2003; Aumont and Bopp, 2006). $CO_2$ injected into the deep ocean is retained in the poorly ventilated isopycnal layers of the deep ocean below the main thermocline but is emitted back to the atmosphere from the well-ventilated layers of the upper thermocline (Drange *et al.*, 2001; Mignone *et al.*, 2004; Caldeira and Wickett, 2005). Deep-sea storage of anthropogenic $CO_2$ is relatively economical and offers large storage capacity compared to other alternatives such as reforestation (House *et al.*, 2002), or various geological storage methods (Hansen *et al.*, 2005; Shi *et al.*, 2008). However, although the impact of anthropogenic $CO_2$ on climate and the surface ocean would be reduced due to the injection of $CO_2$ into the deep ocean, much larger chemical changes are expected in the deep ocean (Caldeira and Wickett, 2005), which could have deleterious effects particularly in the longer term. These deep sea modifications include a reduction in *p*H and $CO_3^{2-}$, a shift of the buffering factor of the affected seawater, and a change in the flux of detritus reaching the seafloor by processes of dissolution and preservation (Wong and Matear, 1998). Disposal of $CO_2$ at fixed locations in the ocean can result in strong *p*H reduction in the deep ocean where natural variability in *p*H is smaller and tolerance limits

for biota likely narrower (Haugan and Drange, 1996). It is estimated that deep ocean $CO_2$ sequestration from a stationary point (e.g. at 1000 m depth) would reduce the local *p*H by 2-3 units within a dissolution zone of a few hundred meter vertical extent and a few tens of meters horizontal extent (cf. Haugan and Drange, 1996 and references therein). Nakayama *et al.* (2005) showed experimentally that the $CO_2$ system equilibrates faster at 1000 m, with waters at 4°C, than at 1 atm, implying a significant effect of pressure on the rate constants. To reduce the environmental impact of $CO_2$ sequestration into the deep ocean, it was proposed to use a pipe towed by a moving ship rather than a stationary pipe (Haugan and Drange, 1996).

### 4.6.2 Iron Fertilisation

Deep sea $CO_2$ sequestration can be combined with simultaneous iron fertilisation of the sea surface to stimulate the biological pump, which transports $CO_2$ into the deep ocean (see section 2.4.1). Iron is an essential component for ocean biogeochemistry, influencing the ballast effect, phytoplankton growth, and nitrogen fixation by photosynthetic diazotrophs such as Trichodesmium (Jickells *et al.*, 2005). Iron fertilisation experiments have shown that even minute increases in iron levels promotes enhanced phytoplankton productivity (Martin *et al.*, 1994) and carbon export (e.g. Coale *et al.*, 1996a).

Most of the iron flux into the ocean is derived as fluvial suspended sediment (Poulton and Raiswell, 2002). However, since most of the particulate iron is retained in near-coastal ocean regions, the principal iron source to the surface of the open ocean is from aeolian dust (Jickells *et al.*, 2005). The subarctic and tropical eastern Pacific, as well as the Southern Ocean, are nutrient-rich areas where biological productivity is believed to be restricted by iron (Martin *et al.*, 1990; Watson and Lefèvre, 1999; Fung *et al.*, 2000; Schmittner *et al.*, 2005; Rothstein *et al.*, 2006: Fig. 5). In the immediate vicinity of the Coral Sea, the low-nutrient, low-chlorophyll South Pacific gyre also appears to be iron limited (Falkowski *et al.*, 1998; Behrenfeld and Kolber, 1999), with the nearest significant source for aeolian dust being arid regions of Australia (mainly the Great Artesian Basin) (Prospero *et al.*, 2002; Mackie *et al.*, 2008). Iron fertilisation might counteract the continuing increase in atmospheric $CO_2$ by enhancing the biological

uptake of carbon. The associated decrease in sea surface $pCO_2$ and, thus, increase of the uptake of atmospheric $CO_2$ was demonstrated experimentally (Martin *et al.*, 1990; Coale *et al.*, 1996b; Watson *et al.*, 2000) and numerically (e.g. Joos *et al.*, 1991; Aumont and Bopp, 2006). However, iron fertilisation may have serious side effects on oceanic chemistry and biology, including a decrease in dissolved $O_2$ and decreased nutrient concentrations nearby the fertilisation site (Wong and Matear, 1998; Gnanadesikan *et al.*, 2003; Orr *et al.*, 2005b).

## 4.7 Summary

In conclusion, the highly complex interplays described between atmospheric, biological and chemical processes have led to many controversies and ongoing uncertainties about the predictability of the effects of climate change on ocean health (Table 4.4.1). The very multi-dimensional nature of the problem poses a serious challenge, and it is with this in mind that computational modelling of broad subsets of the problems is desirable (chapter 8), because such modelling has the capacity to consider a much broader range of inter-relationships than has been achieved to date.

# 5 Study Location - Coral Sea

This chapter is introducing the study region, which includes the Coral Sea and, to a minor extent, the Great Barrier Reef. Previous findings in relation to mixed layer depth, predominant circulation patterns and biological features are presented.

## 5.1 Introduction

The Coral Sea is a marginal sea located in the southwest Pacific off of the northeast coast of Queensland (QLD), Australia (142°48’E), and bordered by the Solomon Islands and Papua New Guinea to the north (9°22’S), New Caledonia and Vanuatu to the east (170°14’E), and the Tasman Sea to the south (30°S) (Figure 5.1.1) (Rotschi and Lemasson, 1967; Longhurst, 1998). The mean depth of the Coral Sea is around 2400 m, with a maximum depth of 7660 m in the New Hebrides Trench, and the shallowest area being located on the continental coast of Queensland, Australia (Rotschi and Lemasson, 1967; Ewing *et al.*, 1970). The near-coastal Marion Plateau, separated from the bigger Coral Sea Plateau (or Queensland Plateau) to the north of the Townsville trough (Pigram *et al.*, 1992), is also characterised by relatively shallow topography. In this section, key Coral Sea features of the bathymetry, circulation patterns and biological variations are described in order to provide a basis for the following chapters concerned with large dataset analysis and computer modelling.

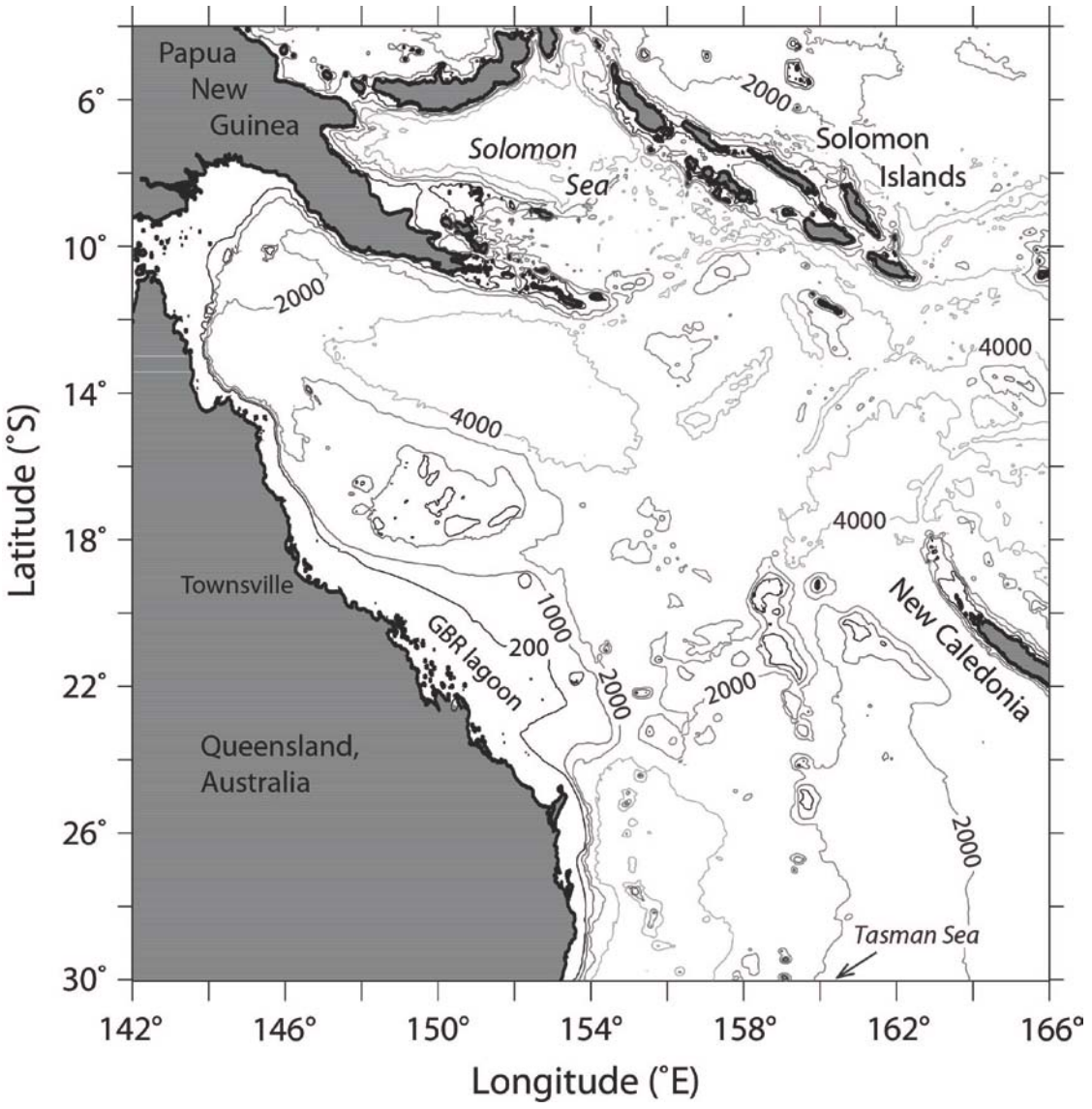


**Figure 5.1.1. Bathymetry of the Coral Sea, derived from the Digital Bathymetric Data Base (an ongoing project of the U. S. Naval Research Laboratory). Isobaths for 200 m, 1000 m, 2000 m and 4000 m are displayed.**

## 5.2 Characteristics of the Coral Sea Mixed Layer Depth

In summer, the sea surface temperature (SST) is fairly homogenous throughout the entire Coral Sea at about 27-28°C (Rotschi and Lemasson, 1967). In winter, however, a strong zonal temperature gradient is present, with the southern Coral Sea exhibiting SST down to 20°C, whereas SSTs to the north remain at around 27°C (Rotschi and Lemasson, 1967; Condie and Dunn, 2006). Salinity displays a range of 34.5-35.5 ppt, with lower

values occurring towards the equator due to the strong influence of heavy precipitation (Condie and Dunn, 2006). Coastal regions affected by river runoff also display lower salinity concentrations than the offshore ocean.

The oligotrophic Coral Sea is characterised by a highly stratified subsurface (Longhurst, 1998), leading to a shallow mixed layer (generally < 60 m; Condie and Dunn, 2006). Winter MLD are significantly deeper (~50-120 m) than in summer (10-50 m) due to enhanced vertical mixing as a result of increased wind stress and heat loss (Wolanski *et al.*, 1988; Condie and Dunn, 2006; Lorbacher *et al.*, 2006). In addition, whereas summer MLD tends to be relatively constant throughout the Coral Sea, in winter, the MLD displays a zonal gradient, increasing towards higher latitudes (Figure 8.4.3) (Condie and Dunn, 2006). In general, the interannual variability of the MLD in the Coral Sea is greater than the change due to annual seasonal patterns, which is linked to both the weak seasonality and the influence of ENSO in this region (cf. Condie and Dunn, 2006).

In the northern and north-eastern sections of the Coral Sea, formation of barrier layers (MLD < ILD) is common (cf. de Boyer Montégut *et al.*, 2007: their Fig. 3), especially during summer months characterised by heavy monsoonal rainfall (Hendon and Liebmann, 1990).

## 5.3 Coral Sea Circulation

### 5.3.1 South Equatorial Current

The southern West Pacific (0°-15°S) is mainly influenced by the westward-flowing South Equatorial Current (SEC) (Patra *et al.*, 2005), whose strength is proportional to the Pacific trade wind velocity (Julian and Chervin, 1978; Pelejero *et al.*, 2005), with the maximum intensity located at about 17°S and 200 m depth (Ridgway and Dunn, 2003). The SEC varies seasonally, with the maximum geostrophic flow occurring in February/March (Taft and Kessler, 1991: their Fig. 11).

The SEC also displays significant interannual variability, which is linked to the ENSO phenomenon. During La Niña events, increased upwelling in the eastern equatorial Pacific enhances the strength of the SEC, resulting in an import of surface waters characterised by high *p*H into the western Coral Sea (Pelejero *et al.*, 2005).

Conversely, a reduction in the easterly trade winds during an El Niño event significantly decreases the strength of the SEC (Wyrtki, 1977).

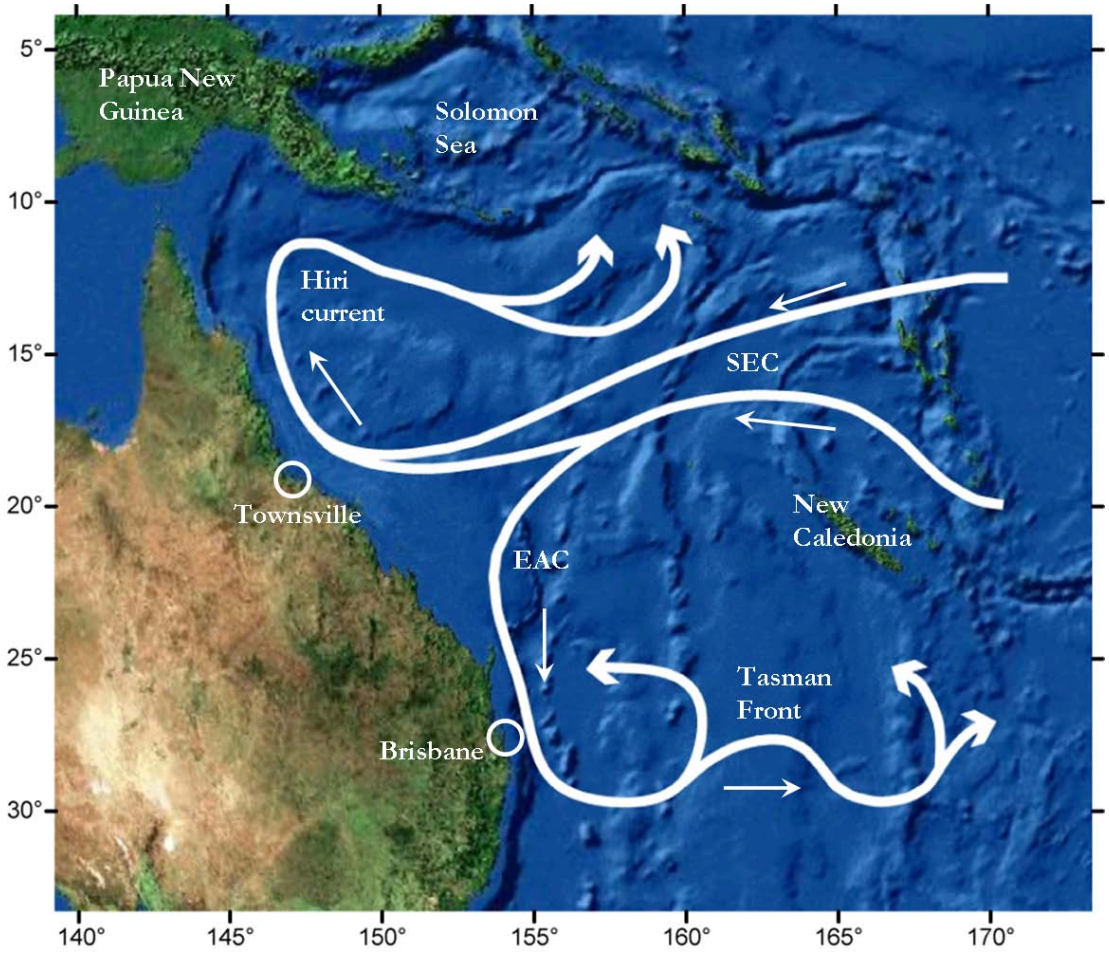


**Figure 5.3.1. Simplified surface circulation in the Coral Sea and Tasman Sea (adapted from Sokolov and Rintoul, 2000; topography derived from ESRI ARCGLOBE).**

In the eastern Pacific Ocean, the SEC mixes with the upwelling Equatorial Undercurrent (EUC) (Toggweiler and Carson, 1995; Feely *et al.*, 1997; 1999; Kessler, 2006). In the western Pacific, the SEC flows into the Coral Sea between the Solomon Islands and New Caledonia (Figure 5.3.1) where it divides into several jets due to the shallow and complex topography (Webb, 2000; Maes *et al.*, 2007; Gourdeau *et al.*, 2008). The SEC then bifurcates near the Queensland Plateau between 17°S and 20°S, forming the Eastern Australian Current (EAC) to the south, and a clockwise coastal circuit, the Hiri current, to the north around the Gulf of Papua (Thompson and Veronis, 1980; Andrews and Clegg, 1989; Burrage, 1993; Tomczak and Godfrey, 1994;

Longhurst, 1998; Ridgway and Dunn, 2003; Mata *et al.*, 2006; Kessler and Gourdeau, 2007). The zone of bifurcation changes seasonally, with the divergence occurring further north (~14°S) during the austral summer (Church, 1987; Kessler and Gourdeau, 2007).

An undercurrent, the South-Tropical Counter-Current, has been described by Donguy and Henin (1975) and Godfrey *et al.* (1980). The undercurrent flows eastwards at around 18°S with a transport of about 2 x $10^6$ $m^3/s$ (Donguy and Henin, 1975).

### 5.3.2 Eastern Australian Current

The EAC, a warm western boundary current of the South Pacific gyre moving southward along the eastern Australian coast, is characterised by a transport varying from 10 to 25 Sv (1 Sv = $l0^6$ $m^3/s$) (Rotschi and Lemasson, 1967; Tomczak and Godfrey, 1994; Mata *et al.*, 2000). The main jet of the EAC is mostly confined to the top 500 m (Mata *et al.*, 2006). The EAC displays significant variability on geological and interannual timescales as a result of changing strength in the SEC, which is also strongly influenced by ENSO (and ENSO-like) events (Bostock *et al.*, 2006). In general, the EAC is weaker during an El Niño event as a result of reduced upwelling in the eastern Pacific and, correspondingly, a weaker SEC (Bostock *et al.*, 2006), potentially resulting in anomalously cold climate conditions in nearby regions (Sprintall *et al.*, 1995).

In the deep ocean, the EAC undercurrent transports water northward along the continental slope (Church and Boland, 1983; Ridgway and Godfrey, 1994; Mata *et al.*, 2000; 2006; Schiller *et al.*, 2008), with a stronger flow occurring during winter (Church and Boland, 1983). The transition zone between the EAC and the northward flow occurs at about 2500 m (Mata *et al.*, 2006). The EAC and its main jet change their position laterally, changing from inshore to offshore phases (Mata *et al.*, 2000; 2006), the shifts occurring rapidly (within a few days; Mata *et al.*, 2006). The EAC is generally separating from the coast at around 30°S, concomitantly producing changeable and vigorous (mainly anticyclonic) eddies (~3/year) (Tomczak and Godfrey, 1994; Fig. 8.19; Mata *et al.*, 2000; 2006). Once separated, part of the EAC recirculates back northwards, whereas the remainder flows eastwards, forming the Tasman Front (Figure 5.3.1) (Boland and Church, 1981; Sokolov and Rintoul, 2000). The EAC, however, is not always present in the southern Coral Sea due to an earlier separation from the coast, resulting in the

development of a northward cyclonic and more barotropic circulation, thus reversing the dominant current direction (up to 50 Sv northward) (Mata *et al.*, 2000; 2006).

### 5.3.3 Circulation within the Great Barrier Reef Lagoon

The Great Barrier Reef (GBR) lagoon, with an estimated area of 225,000 $km^2$ (Luick *et al.*, 2007), is located on the continental shelf to the east of the Queensland coast, with a maximum depth of 200m (Burrage *et al.*, 2003), and is linked to the Coral Sea via deep channels between the reefs. The GBR stretches over a distance of about 2600 km from the Torres Strait off the coast of Papua New Guinea (9.2°S) to Fraser Island (25°S) (Figure 5.3.2) (Wolanski, 1994) and is composed of more than 2900 individual reefs (Hopley *et al.*, 1989; Suzuki and Kawahata, 2003). The width of the "GBR lagoon", a shallow body of open water on the continental shelf been the outer reefs and the coast, varies latitudinally, with the lagoon narrowing northwards. The GBR lagoon is characterised by varying topographic and biological features both along and across its area. Near the coast (<25 km), numerous fringing reefs are located adjacent to the coast and islands, and other marine habitats such as mangroves and seagrass beds are widespread in the inshore area (Hancock *et al.*, 2006). This relatively reef-free inner lagoon is separated from the outer lagoon by submerged reefs in the midshelf area, which determine the interaction of inner and outer lagoon water (Hancock *et al.*, 2006). Similarly, in the outer shelf, "barrier reefs" limit the water exchange between the GBR lagoon and the Coral Sea (Brinkman *et al.*, 2002). The EAC, which is predominantly a slope current adjacent to the GBR shelf (e.g. Church and Boland, 1983), is nonetheless linked to a southward water motion within the outer reef matrix (cf. Luick *et al.*, 2007), with more than half of the incoming EAC-derived inflow (total of 0.58 Sv) entering the GBR lagoon in locations of low reef density (Brinkman *et al.*, 2002). "Barrier reefs", contrary to the term's meaning, are not a continuous band of reefs along the shelf break. Instead, these outer reefs are characterised by variable 'linear density' of the reefs, with the southern (>16°S) GBR displaying much lower densities (~10%) than the northern GBR (up to 90%) (Pickard *et al.*, 1977; Suzuki and Kawahata, 2003).

The main circulation within the GBR lagoon is a seasonally reversible north-south current, with the current moving southward between August and December, and

northwards between January and August (Luick *et al.*, 2007). The direction of the current is determined by a combination of the prevailing wind stress and the geostrophic pressure gradients (cf. Burrage *et al.*, 1994; 1995; Luick *et al.*, 2007). The northward current season coincides with the period when the southeasterly trade winds are strongest, whereas the southward current is predominantly the result of a combination of weaker southeasterly trade winds and a stronger EAC (Luick *et al.*, 2007).

In a study by Hancock *et al*. (2006), it was determined that the inner lagoon eddy diffusivity ($K_h$) varies latitudinally, with, for example, higher rates occurring between 15.8°S and 19.0°S (265 ± 36 $m^2/s$) than between 14.3°S and 15.8°S (104 ± 6 $m^2/s$). These differences in diffusivity likely derive from differences in topography, with the northern section characterised by greater reef density than southern sections, such as the presence of the "ribbon reefs' (cf. Wolanski and Spagnol, 2000: Fig. 1), therefore inhibiting exchange of water between the inner and outer GBR lagoon and the Coral Sea (e.g. Brinkman *et al.*, 2002). Accordingly, the flushing time of the inner lagoon is greater for the northern section (45 days) than for the southern section (18 days) (Hancock *et al.*, 2006).

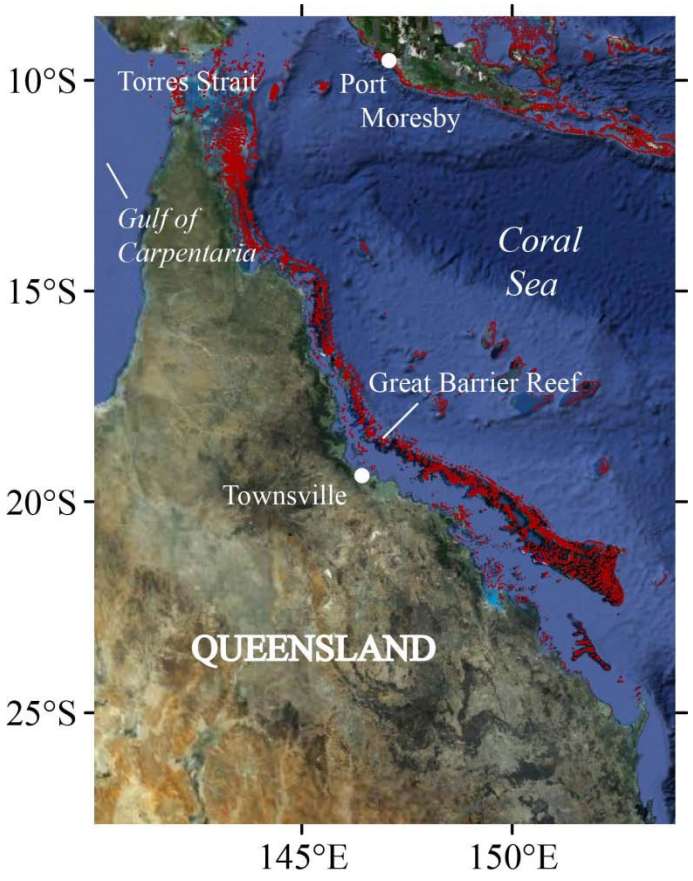


**Figure 5.3.2. Distribution of reefs (in red) on the Queensland continental shelf (adapted from Google Earth 2010).**

The eddy diffusivity in the outer lagoon tends to strengthen toward the slope, increasing to twice the inner lagoon $K_h$ values, due to more complex water motion within the reef matrix (Hancock *et al.*, 2006). Mixing in the middle and outer lagoon is also enhanced by reefal water modification, generating eddies, tidal jets and stagnation zones (e.g. King and Wolanski, 1996; Drew, 2001). Based on estimated diffusivity levels, it was estimated that the exchange between the outer GBR lagoon and the Coral Sea occurs within 47 days in the southern section, whereas the northern section replenishes already after about 30 days due to a smaller area requiring flushing (Hancock *et al.*, 2006). In a study by Wolanski and Spagnol (2000), it was shown that the flushing time in locations of high reef density also depends on the tidal regime, with the flushing time being greater during spring tides than at neap tides as a result of increased turbulence and larger energy dissipation behind reefs.

## 5.4 Biological Features of the Coral Sea

The Coral Sea is an oligotrophic (nutrient poor) region characterised by relatively low chlorophyll concentrations (<0.2 mg/m$^3$; Figure 5.4.1). In the offshore ocean, nanoplankton (2-20 µm) and picoplankton (0.2-2 µm) represent the majority (70-95%) of the chlorophyll mass (Jeffrey and Hallegraeff, 1990: Table 14.5). The yearly primary production within the Coral Sea is approximately 100 to 200 g C/m$^2$ (Furnas and Mitchell, 1996b), likely mainly based on recycled nutrients (Condie and Dunn, 2006).

### 5.4.1 Inner Shelf

In contrast to the offshore ocean, the shelf region (including the GBR) displays much greater chlorophyll concentrations (>0.3 mg/m$^3$, cf. Figure 5.4.1) (see also Andrews, 1983). The nutrients in the inner shelf (including estuaries) at least partially derive from river runoff (Condie and Dunn, 2006), with an estimated 42 km$^3$ draining into the GBR each year (Furnas *et al.*, 1997). Whereas the southern rivers (south of the Herbert River catchment area) display a strong seasonality, with most of the discharge occurring during the wet season (austral summer), the northern rivers tend to deliver nutrients and low-salinity water to the inner shelf throughout the year (Mitchell and Furnas, 1996).

The dry catchments of the Burdekin (discharging at 19°30'S) and Fitzroy Rivers (river outlet at 23°37'S) provide the greatest source of terrestrial sediment to the GBR lagoon (Moss *et al.*, 1992), with most of the organic matter-rich sediment being retained in near-coastal areas such that most fluvial nutrients do not reach the reefs (Brunskill *et al.*, 2002; Orpin *et al.*, 2004). Most of the terrestrial sediment at the east coast of QLD is transported northwards along the shore due to a strong coastal current (e.g. Burrage *et al.*, 1994; Woolfe *et al.*, 1998), and is subsequently deposited in northward facing embayments (Neil *et al.*, 2002; Orpin *et al.*, 2004). The littoral current, which may seasonally reverse its flow and can reach 0.3 m/s (Burrage *et al.*, 1994), is driven by southeasterly trade winds (Orpin *et al.*, 1999) and generally overrides southward directed (ebb) tidal currents (Woolfe *et al.*, 2000).

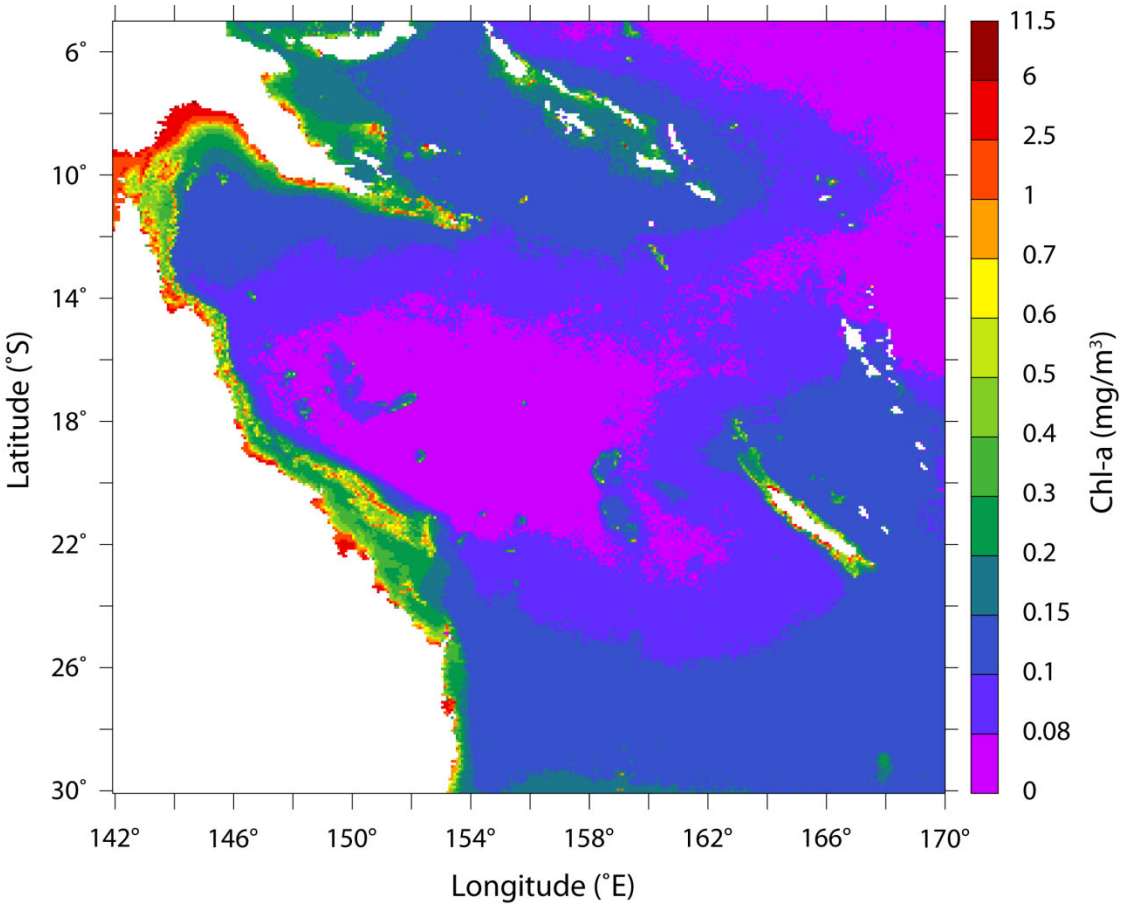


**Figure 5.4.1. Mean chlorophyll-a distribution between September 1997 and August 2008 based on SeaWifs.R2009. The figure is adapted from the display produced by Giovanni (cf. section 6.2.5 for further details).**

### 5.4.2 Outer Shelf

Conversely, the much more oligotrophic outer shelf obtains its nutrients predominantly from offshore through summer upwelling events onto the outer continental shelf (Furnas and Mitchell, 1986; 1996a), upwelling induced by an episodically stronger EAC (Andrews and Gentien, 1982) and supply by tidal currents (Thompson and Golding, 1981; Thomson and Wolanski, 1984; Wolanski *et al.*, 1988; Nof and Middleton, 1989; Drew, 2001). In a study by Monbet *et al*. (2007), it was determined that the input of dissolved phosphorus onto the continental shelf via upwelling of Coral shelf edge water may be higher by up to a factor of 40 compared to the supply through river runoff. Relatively nutrient- and chlorophyll-rich water is brought up from below the offshore thermocline by the tidal pressure gradient caused by the large tides in the GBR region (average maximum tidal range: 3 m; maximum tides of up to ~10 m occurring in the Broad Sound area at 21-23°S, cf. Figure 5.1.1) (Maxwell, 1968; Thompson and Golding, 1981; Thomson and Wolanski, 1984; Drew, 2001). These tidal currents can reach 2 m/s through the reef edge (Pickard *et al.*, 1977). While cold and nutrient-rich Coral Sea water is propagated onto the GBR lagoon during spring tide (Nof and Middleton, 1989), warm and relatively nutrient-poor water is flowing from the GBR out to the Coral Sea during ebb tide (Drew, 2001).

In a study by Suzuki *et al.* (2001), it was deduced that the concentration of $CO_2$ in the shelf region is greatly influenced by both $CaCO_3$ production and river runoff, the latter adding excess DIC to the system. Both calcification and riverine inflow result in higher $fCO_2$ levels near the coast compared to the open ocean, such that near coastal regions are potentially a source of $CO_2$ to the atmosphere (Kawahata *et al.*, 2000; Suzuki *et al.*, 2001). The residence time in the individual reefs also affects the $fCO_2$ levels, with longer residence times being linked to higher $fCO_2$ levels (Suzuki and Kawahata, 2004) as a result of longer calcification periods per water volume.

Conversely, a considerable amount of DIC (including $CO_2$) may be removed from the continental shelf due to the continental shelf pump (cf. section 2.4.3), first described by Tsunogai *et al.* (1999). Assuming that the rate of removal by the continental shelf pump is the same for the GBR region as in the East China Sea (cf. Tsunogai *et al.*, 1999), a total amount of $8 \cdot 10^{-3}$ Gt C/yr would be removed from the shelf. In addition, similar to the

East China Sea (Tsunogai *et al.*, 1999), the presence of the EAC may further aid the removal of $CO_2$. To this date, no studies have been undertaken on the GBR shelf in regard to the potential presence and effects of the continental shelf pump. Any such future investigation could greatly enhance the understanding of the DIC cycle in the GBR lagoon.

## 5.5 Summary – Coral Sea

The Coral Sea exhibits several characteristics that have a strong bearing on the results shown in subsequent chapters:

- The topography in many regions (e.g. the Queensland Plateau) is relatively shallow (<1000 m);
- Several prominent currents (SEC, EAC, Hiri Current) are present, strongly influencing the predominant physical and geochemical patterns;
- Monsoonal activity greatly impacts on the vertical stratification;
- and the near-coastal areas (e.g. GBR) have a tendency towards higher $fCO_2$ levels compared to the open ocean, increasing the likelihood of coastal and shallow regions acting as a source of $CO_2$ to the atmosphere.

# 6 Physical Oceanography - Seasonal to Interannual Variability in the Coral Sea

Global warming is predicted to result in a significant shallowing of the mixed layer depth (MLD) in many ocean regions (cf. Figures 8.6.4 and 8.6.5), which could have dire consequences for coral reef ecosystems and the ocean's capability for $CO_2$ uptake. The aim of this chapter is to use all available observational data in order to investigate mixed layer variability on seasonal and longer timescales within the Coral Sea. MLD data reviewed in this chapter is derived from various observational sources, including the Argo project and the World Ocean Database.

## 6.1 Introduction

The collection of oceanic data to investigate the variability of the sea surface temperature (SST), sea surface salinity (SSS) and mixed layer depth (MLD) in the Coral Sea, over timescales varying from diurnal to centennial, have not received much attention, and consequently not many conductivity-temperature-depth (CTD) profiles are available to investigate the short- and long-term variability of the MLD within the Coral Sea. The MLD displays significant variability on various timescales, ranging from diurnal (Gregg *et al.*, 1985; Schneider and Müller, 1990; Brainerd and Gregg, 1995) to interannual changes (McCreary *et al.*, 2001; Kara *et al.*, 2003).

The MLD is also expected to vary on geological timescales. Specifically, higher salinity (Stott *et al.*, 2004) and temperatures (Gagan *et al.*, 2000; Stott *et al.*, 2004) in the Great Barrier Reef (GBR) region during the Holocene would likely have led to a more shallow MLD compared to modern times. With climate warming currently occurring worldwide (Houghton *et al.*, 2001), it is likely that the resulting warmer SST (Cane *et al.*, 1997; Lau and Weng, 1999; Levitus *et al.*, 2000; Wilson *et al.*, 2006; AchutaRao *et al.*, 2007) will also result in a shallowing of the MLD within the Coral Sea (Yeh *et al.*, 2009), unless a significant decrease in precipitation occurs. The latter would result in an increase in salinity, which could partially counteract the decrease in sea surface density due to higher SST. For a predicted SST increase of 2°C by the end of the 21$^{st}$ century (Meehl *et al.*, 2007), a salinity increase of at least 0.7 psu would be required to offset the density

decline by warmer SSTs. However, an increase in rainfall is forecast throughout the Coral Sea, with the exception of a predicted decrease in austral winter precipitation in the southern (south of 20°S) Coral Sea (Christensen *et al.*, 2007).

No mixed layer study has previously focused on the Coral Sea alone. As a result, mixed layer characteristics and variability on seasonal and longer timescales within the Coral Sea is not well known. This chapter focuses on analysing salinity and temperature profiles from the Argo project and the World Ocean Database (WOD). MLDs derived from the CTD profiles are compared with the MLD maps from the CSIRO Atlas of Regional Seas (CARS). An attempt is made to correlate the relatively sparse ocean data to ENSO events, and to predict likely future changes in the MLD. A better knowledge of the behaviour of the MLD in the Coral Sea will also improve understanding of changes in heat content, nutrient cycling and ocean-atmosphere interaction.

## 6.2 Methods

### 6.2.1 WOD CTD Profiles

To investigate the seasonal and long-term variability of the MLD, all available high resolution CTD containing SST and SSS profiles were analysed individually. Only CTD profiles containing both SST and SSS were included in this analysis as the presence of a barrier layer (cf. section 3.2.1.1) throughout much of the year was expected in some areas, which could significantly bias the determination of the MLD if only one type of profile per location were used. Altogether, 3380 salinity-temperature CTD profiles were obtained from the WOD (http://www.nodc.noaa.gov), which is maintained by the National Oceanographic Data Center (NODC). These sea surface data were collected by various cruises and research teams in the Coral Sea between March 1982 and June 2003.

The density ($\rho$, kg/m$^3$) was calculated using the One Atmosphere International Equation of State of Seawater, 1980 (UNESCO, 1983):

$$\rho(S,T,p) = \rho_w + (8.24493 \times 10^{-1} - 4.0899 \times 10^{-3} \times T + 7.6438 \times 10^{-5} \times T^2 - 8.2467 \times 10^{-7} \times T^3 + 5.3875 \times 10^{-9} \times T^4) \times S + (-5.72466 \times 10^{-3} + 1.0227 \times 10^{-4} \times T - 1.6546 \times 10^{-6} \times T^2) \times S^{3/2} + 4.8314 \times 10^{-4} \times S^2$$

where T = temperature [°C], S = practical salinity and $\rho_w$ = density of the Standard Mean Ocean Water (SMOW) taken as pure water reference, computed using

$$\rho_w = 999.842594 + 6.793952 \times 10^{-2} \times T - 9.09529 \times 10^{-3} \times T^2 + 1.001685 \times 10^{-4} \times T^3 - 1.120083 \times 10^{-6} \times T^4 + 6.536332 \times 10^{-9} \times T^5$$

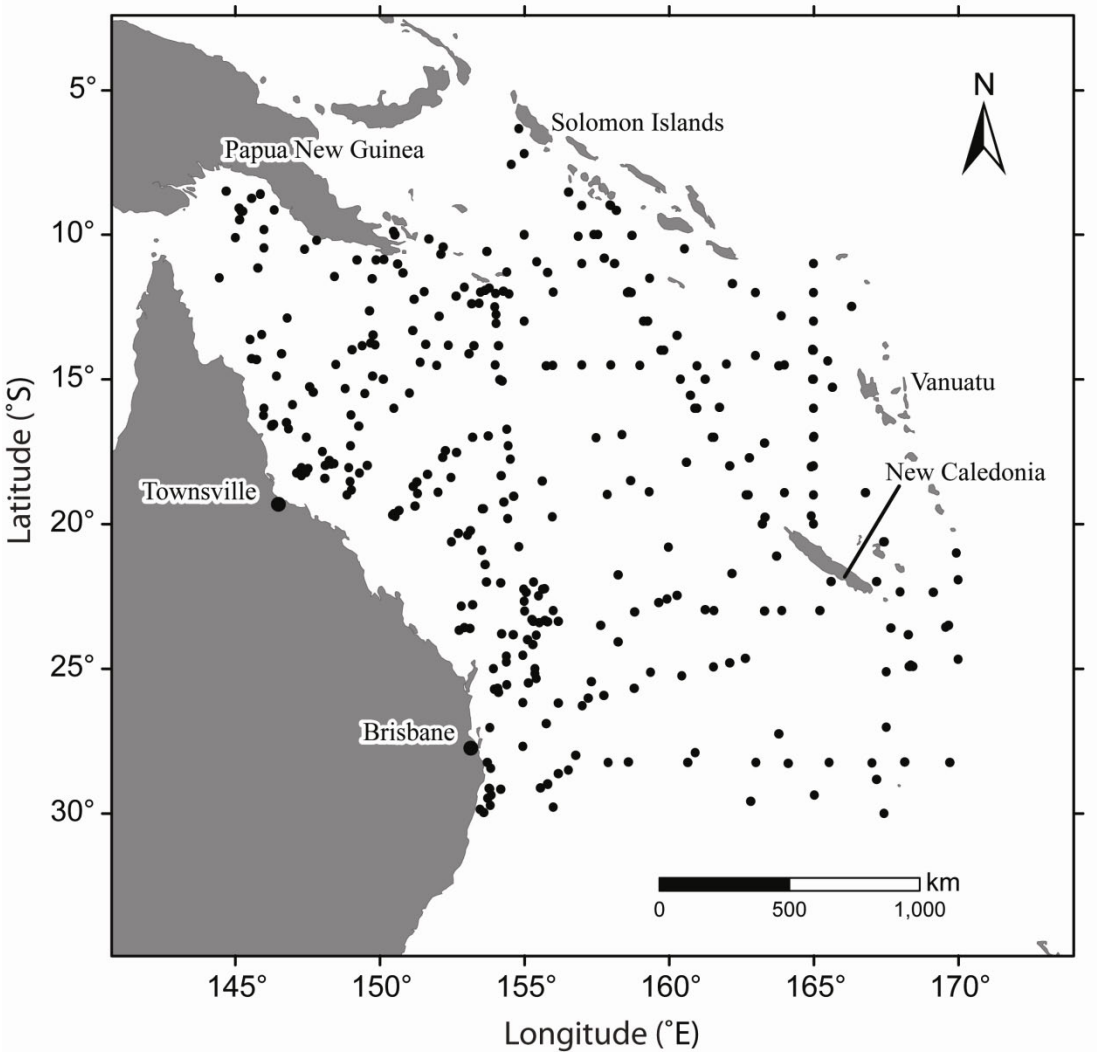


**Figure 6.2.1. Distribution of World Ocean Database (WOD) CTD profiles that were used for the MLD analysis.**

Around 5-10% of the WOD data were removed because they were located outside the study site. After visual inspection of the remaining profiles, about 20% of the CTD files were eliminated from the analysis since these profiles were not deep enough to capture the MLD. A further ~40% were removed due to low vertical resolution (measurement

frequency lower than every 10 m) in the upper ocean. In addition, to avoid an overrepresentation of areas in which multiple measurements were taken within a few days, only a limited, randomly selected number of profiles were evaluated in locations with clustered data. Altogether, 383 SST and SSS profiles were employed to determine the MLD using both the gradient and threshold method (Figure 6.2.1; see section 3.2.1.2). The threshold method was tested and compared closely with the gradient method to determine the suitability of the threshold method for the Coral Sea area. After a visual inspection of several representative temperature, salinity and density profiles, $\Delta T$ = 0.2°C, $\Delta S$ = 0.03 psu and $\Delta\rho$ = 0.03 kg/m$^3$ were used for the isothermal layer depth (ILD, section 3.2.1.1) and MLD, respectively, for the threshold method, which agrees well with previous findings of most accurate threshold values (cf. de Boyer Montégut *et al.*, 2004).

To obtain an accurate estimation of the MLD and ILD, threshold values for temperature ($\Delta T$) and salinity ($\Delta S$) have to take into account the possible presence of temperature and/or salinity inversions. Here, the ILD (and isohaline layer depth) was determined as the depth where temperature (salinity) has either decreased or increased by the given increment.

### 6.2.2 Argo

For the first time, detailed studies of the mixed layer behaviour and mid-depth circulation are made possible due to the deployment of numerous Argo floats both in global oceans and regional seas such as the Coral Sea. Since 1999, more than 3000 Argo floats have been deployed across the world, with an expected lifetime of around 4-5 years for each individual Argo float (Roemmich and Owens, 2000). To maintain Argo's target of a global network of 3,000 active floats, which was first achieved in late 2007 (Roemmich and Gilson, 2009), about 750 additional floats have to be set up worldwide to substitute floats that terminated or were lost. These free-drifting floats are parked at a preprogrammed pressure (usually 1000 dbar, but some also at their maximum depth of around 2000 m) from which, at predetermined intervals (typically 10 days), they will first descend to around 2000 m (2000 dbar) depth (unless already located there) before rising to the surface, transmit data, and descend to the parking position (Roemmich and Owens, 2000). Measurements of temperature and salinity are taken during the ascent with a CTD

sensor module (Kako and Kubota, 2007). The Argo program is unique in that all collected data are made publicly available by the International Argo Project and the national programmes that contribute to it (www.argo.ucsd.edu, argo.jcommops.org; cf. Gould *et al.*, 2004). The accuracy for temperature and uncorrected salinity is ±0.005°C and ±0.01 psu, respectively, whereas depth errors are ±5 m (Argo Science Team, 2000). Real-time salinity data are sometimes affected by a mostly small sensor drift (Wong *et al.*, 2003). As a result, a delayed-mode correction is applied to further reduce errors in salinity and depth measurements.

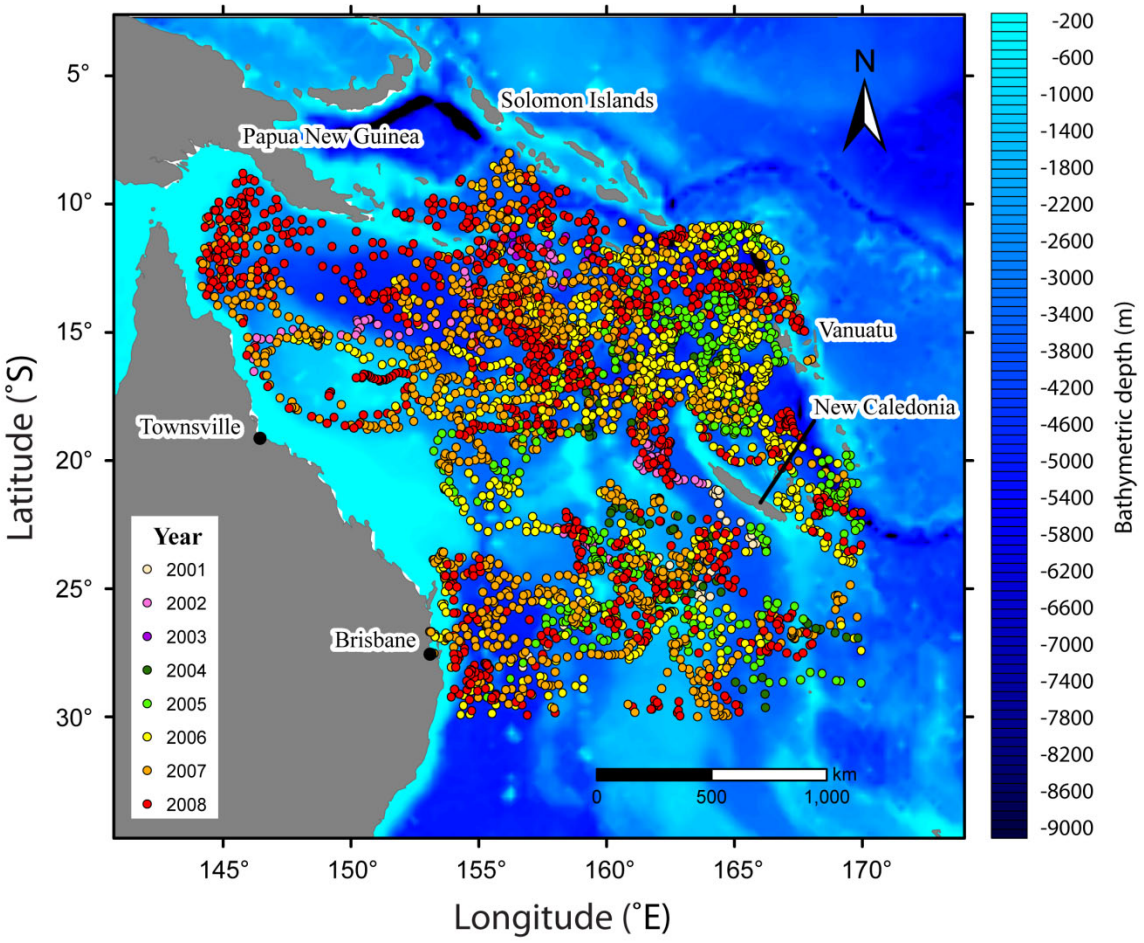


**Figure 6.2.2. Geographical position of Argo floats within the Coral Sea by year (www.argo.ucsd.edu, argo.jcommops.org). The deployment of Argo floats within the Coral Sea began in the southeast in mid-2001 and, since then, the frequency and spread of measurements have been significantly augmented and are now taken throughout most of the study area.**

Numerous Argo floats were also deposited within and nearby the Coral Sea region (Figure 6.2.2), with 38 active floats as of 31 December 2008. Some of these floats, which contain temperature and salinity profiles at relatively coarse vertical resolution (5-10 m), are used to investigate the MLD variability, similarly to the procedure applied for the WOD CTD profiles (cf. section 6.2.1). To estimate the most appropriate value for the Coral Sea region, four different threshold values have been evaluated for both the ILD ($\Delta T = \pm 0.1°C, \pm 0.15°C, \pm 0.2°C, \pm 0.25°C$) and the MLD ($\Delta\rho = 0.025$ kg/m$^3$, 0.03 kg/m$^3$, 0.035 kg/m$^3$, 0.04 kg/m$^3$), with the threshold reference depth set at 10 m. In addition, similar to previous studies (e.g. Thomson and Fine, 2003), all profiles were visually inspected to obtain a reference MLD ($MLD_{ref}$) and ILD ($ILD_{ref}$). The MLDs and ILDs obtained with the threshold method were compared closely with their respective $MLD_{ref}$ and $ILD_{ref}$, to determine the suitability of the threshold methods for the Coral Sea area. CTD profiles in which the MLD were not well-defined (absence of vertical homogeneity due to restructuring) were excluded from the MLD analysis (cf. Ohno *et al.*, 2009). Altogether, MLDs were calculated for 1306 Argo profiles.

The MLDs obtained from Argo floats may be considered less accurate compared to the WOD-derived MLD as a result of lower vertical resolution (measurements taken every 5-20 m, generally). Nonetheless, these floats are very valuable since they can provide a clearer picture of the seasonality and short-term variability of the MLD due to their repeated salinity and temperature measurements over the last few years, some of which are from relatively constant locations. Due to their relatively deep parking depth, however, Argo floats can only remain operational when the water depth exceeds 2000 km, implying that no active floats operate within the GBR lagoon.

### 6.2.3 CARS

The CSIRO Atlas of Regional Seas (CARS) is a digital high-resolution climatology of seasonal ocean water properties, CARS2006 encompassing the entire southern hemisphere and equatorial regions (http://www.marine.csiro.au/~dunn/cars2006/). During 2009, a new version (CARS2009) was released, which covers the global ocean but, at this stage, only includes salinity and temperature fields. Throughout the thesis, CARS is referring to CARS2006.

CARS is providing historic mean fields and average seasonal cycles of temperature, salinity, MLD, nitrate, oxygen, phosphate and silicate (Ridgway *et al.*, 2002; Condie and Dunn, 2006). To create CARS, all available historical measurements have been gathered, with the data derived from various research sources including WOD, WOCE and Argo. Prior to creating the atlas, all data was screened for duplicates and erroneous parameters (Ridgway *et al.*, 2002).

CARS does not provide information for any given year since not enough data is available to resolve any one year. Instead, the atlas represents a multi-decadal average of all parameters, with all available oceanographic data being averaged by ignoring the year of collection of each observation and retaining only the day-of-year - and then fit a mean and mean-seasonal-cycle at each point. In the western equatorial Pacific and the Gulf of Carpentaria, adjustments were applied for interannual (e.g. ENSO) signals. Any such signals will affect the maps, both by these signals being aliased into spatial structure or seasonal cycles, and by biasing towards the interannual anomaly of data-rich periods.

### 6.2.4 Ocean Heat Content

The ocean heat content (OHC) has been obtained as well, using the following formula:

$$Q = \int_{z=D}^{z=0} \rho \cdot c_p \cdot (T - T_{ref}) \cdot dz$$

where $c_p$ is the specific heat capacity of seawater (4000 J $kg^{-1}$ $C^{-1}$), $\rho$ is density, T is temperature, and z is the depth range of the OHC integration. The reference temperature $T_{ref}$ was arbitrarily set to zero, with the OHC equation then simplifying to:

$$Q = \int_{z_{ref}=250\,m}^{z=0} \rho \cdot c_p \cdot T_{(z)} \cdot dz$$

The OHC was computed to a depth of 250 m to ensure that the maximum depth of surface oceanic mixing is captured by the OHC calculation.

### 6.2.5 Satellite Data – Giovanni

To complement the Argo data, and for later verification purposes of the model output, satellite-derived SST data is presented in section 6.3.4. The monthly averaged satellite data was obtained through the Giovanni online data system, developed and maintained by the NASA (National Aeronautics and Space Administration) Goddard Earth Sciences Data and Information Services Center (Acker and Leptoukh, 2007). Giovanni facilitates the visualisation, analysis and access of remote sensing data sets.

The SST data presented in section 6.3.4 are monthly mean SST (11 micron day) data derived from MODIS-Terra (Moderate Resolution Imaging Spectroradiometer on NASA's Terra satellite), with 1/12° data available for the entire 2000/02/01 - 2010/10/01 period. For every month (e.g. every January), the monthly SSTs were averaged over the entire period available (e.g. January 2001, January 2002,…., January 2010):

$\bar{y}_i = \frac{1}{n}\sum_{t=1}^{n} y_{i,t}$ where $y_{i,t}$ is the mean SST of month(i) of year(t), and $\bar{y}_i$ is the overall mean of a given month(i) over all available years(n).

In some instances, the monthly Giovanni data did not have full coverage, including several months in 2009 (i.e. January-August). For these cases, a MATLAB script was written to ensure that every grid cell was divided by the number of years(n) available for that grid (cf. appendix A2).

## 6.3 Results

### 6.3.1 WOD CTD Profiles

The MLD of the Coral Sea displays significant seasonal variability (Figure 6.3.1). Generally, the winter mixed layer is much deeper than summer mixed layer due to reduced heat flux and increased wind stress (Messié and Radenac, 2006), both resulting in increased mixing because of reduced upper surface stratification and increased momentum. In summer, the MLD is rather shallow and homogeneous throughout the Coral Sea, whereas in winter, a strong MLD gradient is obvious, with the MLD increasing towards the south.

The MLD also shows significant dependence on latitude (Figure 6.3.2). Throughout the year, but especially during austral winter months, subtropical mixed layers (south of

20°S) tend to be significantly thicker than concurrent low latitude mixed layers. As a result, the range in subtropical MLDs can be twice as large (10–240 m) compared to the tropical region (10-120 m), which is characterised by relatively warm SSTs throughout the year.

Numerous locations displayed fossil layers, secondary pycnoclines, which are a result of restratification of the upper ocean after prolonged deep sea surface mixing due to elevated wind stress (Kara *et al.*, 2003), such as during a storm event. Once the wind strength is weakening, or the sea surface is warming, a more shallow MLD and ILD is formed above another uniform mixed layer (Kara *et al.*, 2003).

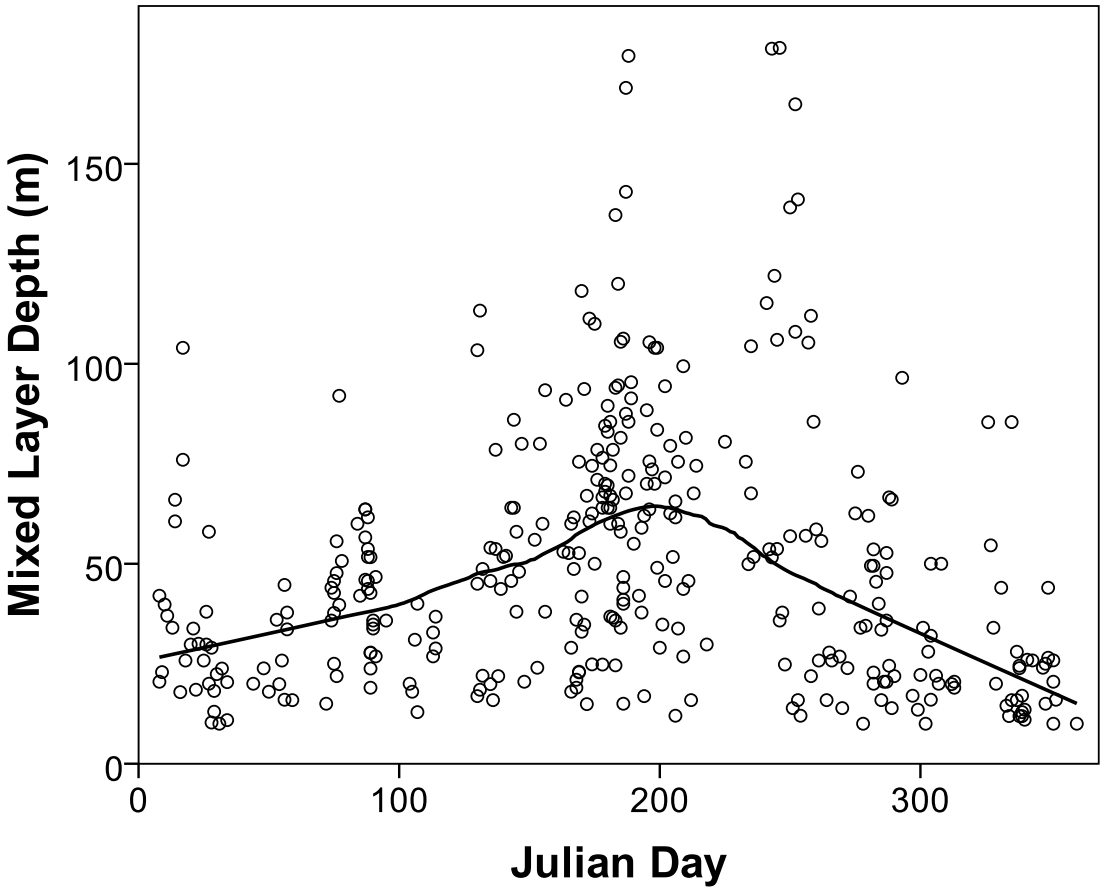


**Figure 6.3.1. Mixed layer depth seasonality within the Coral Sea based on WOD data.**

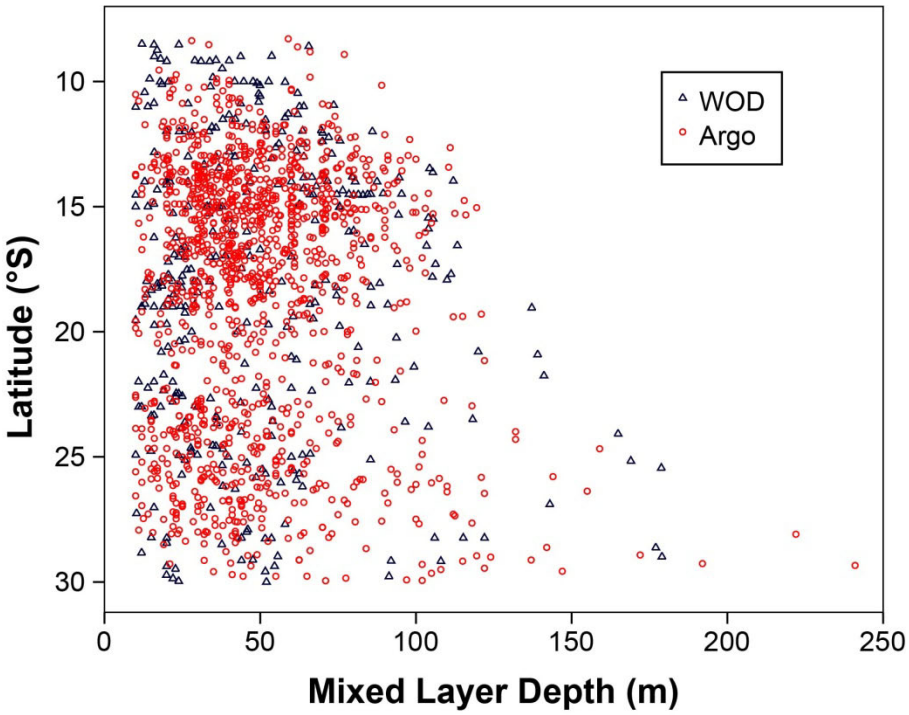


**Figure 6.3.2. Latitudinal variation of the mixed layer depth within the Coral Sea. The data is derived from the World Ocean Database (WOD, blue triangles) and the Argo project (red circles).**

## 6.3.2 Seasonality - Argo Profiles

### *6.3.2.1 Sea Surface Patterns*

As a result of seasonal changes in solar radiation and the position of the ITCZ, sea surface temperature (SST) displays strong seasonal cycling in both tropical and sub-tropical regions (Figure 6.3.3A), with gradually cooler SSTs towards the south (Figure 6.3.4). Sea surface density (SSD), which is strongly negatively correlated to temperature ($R^2$ = -0.96) exhibits a very distinct seasonal pattern as well (Figure 6.3.3C).

There are also two distinct sea surface salinity (SSS) groups discernible, with tropical SSS ranging from about 34.0 to 35.4 psu and extra-tropical SSS showing higher values, ranging from around 35.2 to 36.0 psu (Figure 6.3.3B). The northern half of the Coral Sea displays some SSS seasonality, with lowest values occurring during the summer month, which is most likely attributable to precipitation during the austral summer wet season. Conversely, a seasonal pattern is absent in the higher latitudes, which can only partially be ascribed to a change in the geographical location of the southerly Argo floats.

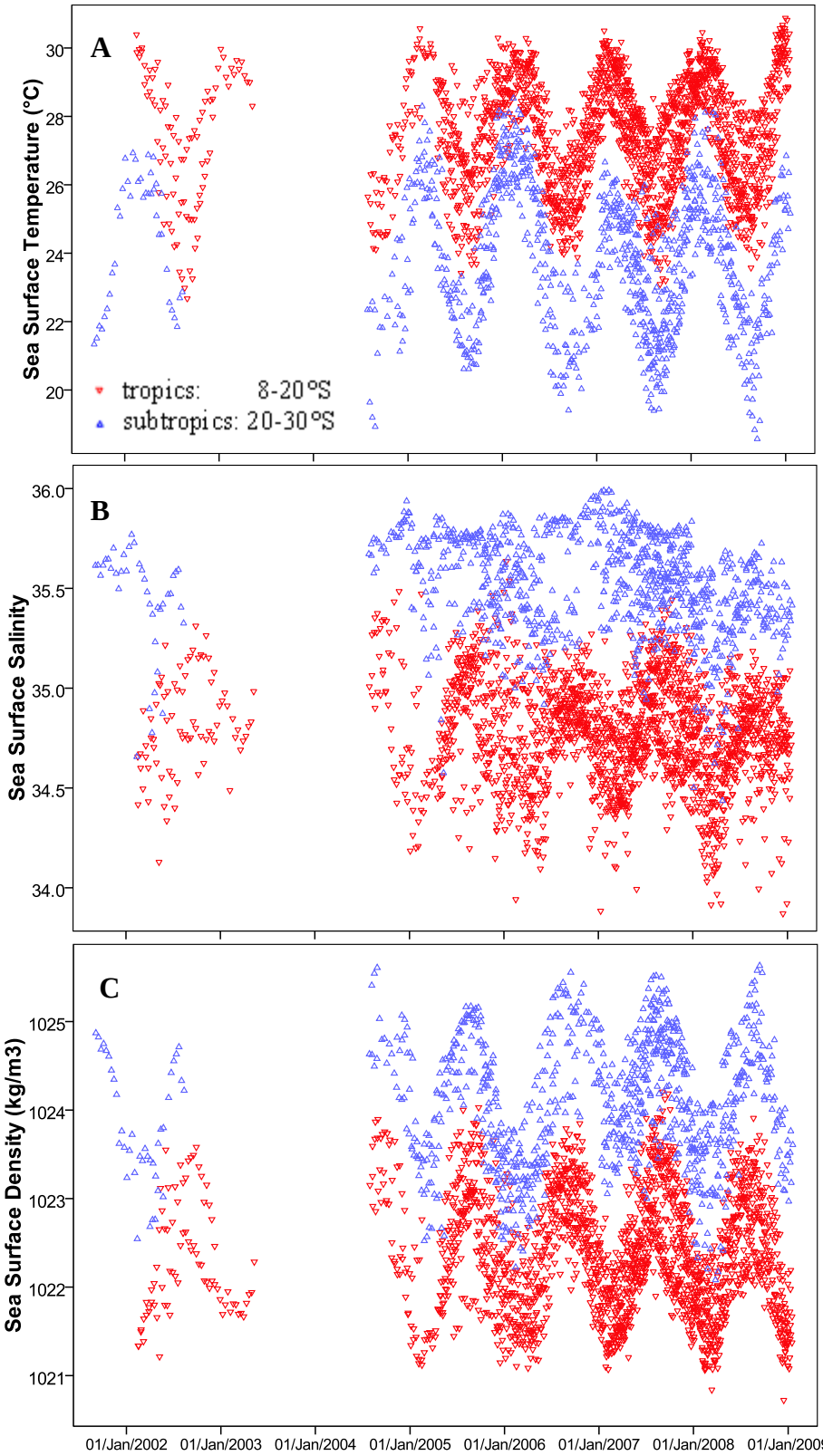


**Figure 6.3.3. Seasonal variability of A) sea surface temperature, B) sea surface salinity and C) sea surface density in the tropical and subtropical Coral Sea.**

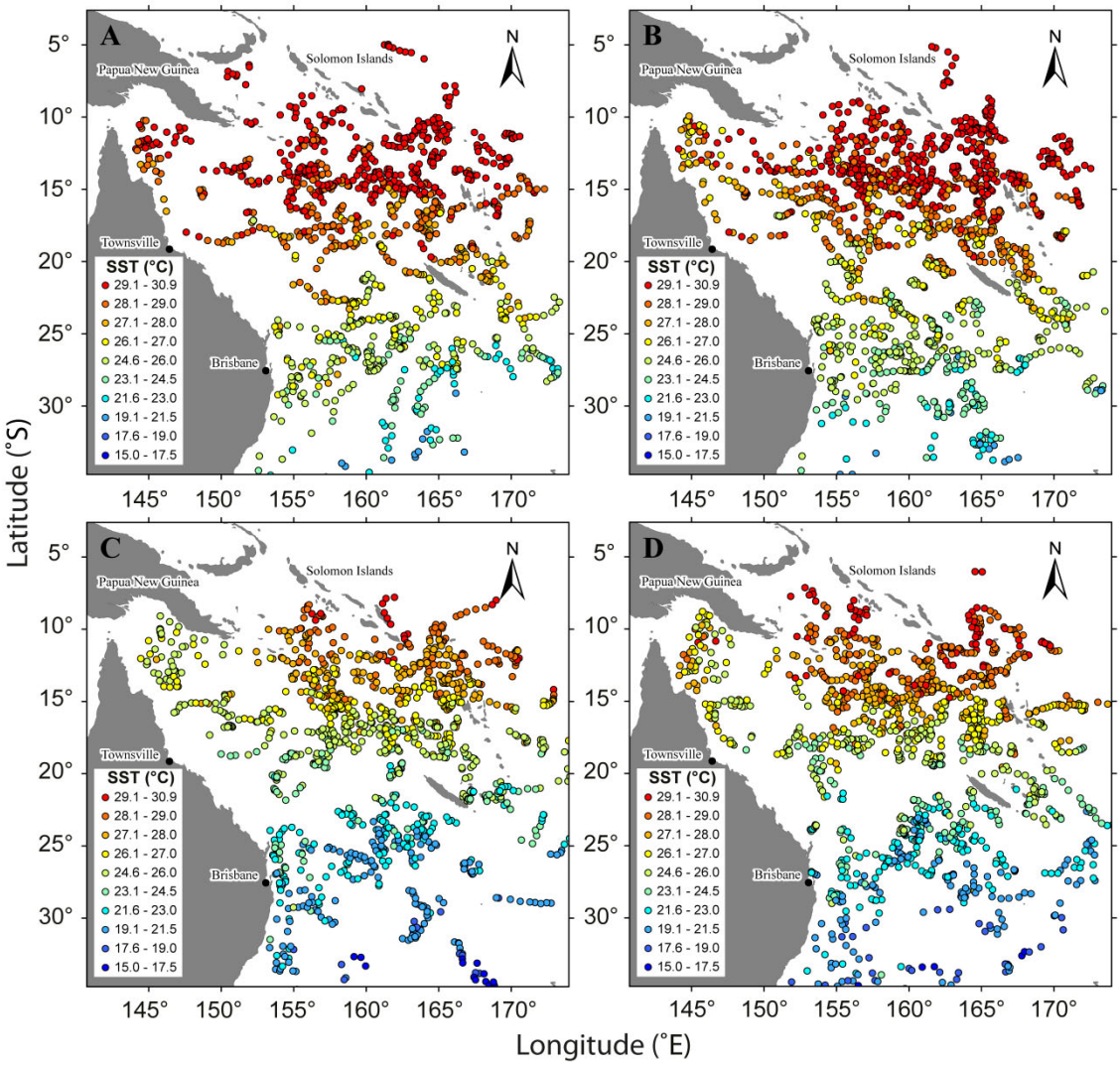


**Figure 6.3.4. Spatial distribution of sea surface temperature (SST) during A) summer, B) autumn, C) winter and D) spring. The SST data has been obtained from Argo floats and represent temperatures in the upper 10 m.**

### *6.3.2.2 Tropical vs Extra-Tropical MLD Seasonality*

A clear seasonality in the MLD is evident throughout the Coral Sea, although the seasonal variation is much more noticeable in higher latitudes (Figure 6.3.5) due to greater seasonal fluctuations of sea surface heating (Figure 6.3.3A) and wind stress (Messié and Radenac, 2006), both features facilitating increased mixing in the upper ocean. Mixed layers increase significantly towards the winter month in all regions (Figure 6.3.6). The deepening occurs due to a combination of a cooling upper ocean and elevated wind stress (predominantly southeasterly trade winds) during austral winter

(Messié and Radenac, 2006). Conversely, mixed (and isothermal) layers are shallower in summer throughout the Coral Sea, generally 10-50 m, as a result of increased sea surface heating and relatively weak wind stress. Tropical MLDs typically range from about 50 m to 100 m in winter, whereas higher latitude MLDs generally exceed 100 m and can occasionally surpass 200 m. The seasonal deepening towards austral winter is also evident in pre-Argo data (Figure 6.4.7).

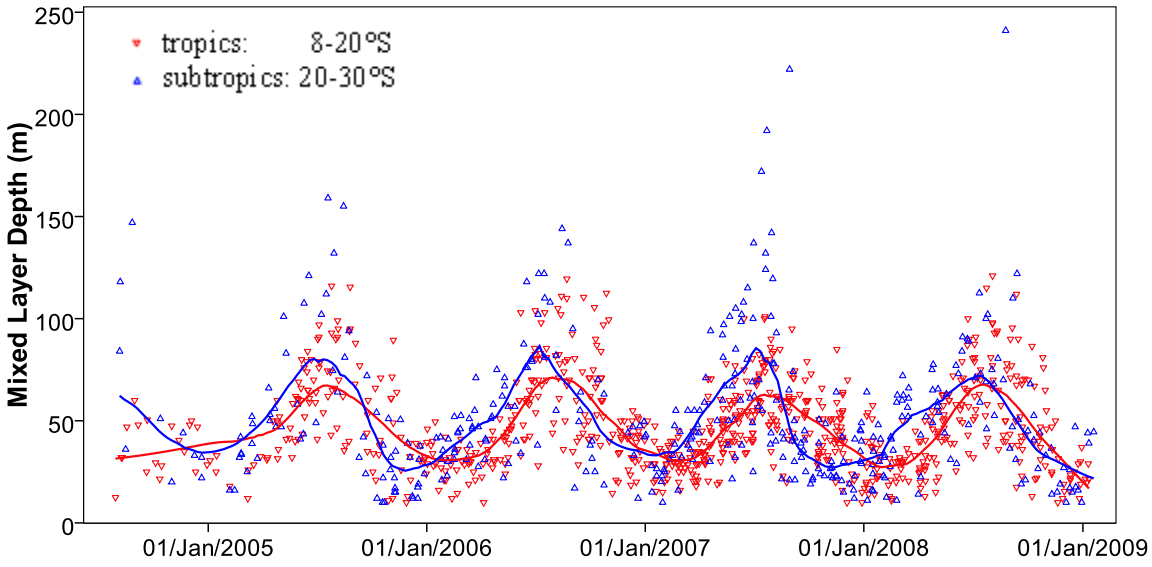


**Figure 6.3.5. Evolution of the mixed layer depth over a 4.5 year period as derived with the gradient method. A strong seasonality is evident in the northern (8-20°S, red triangles) and southern (20-30°S, blue triangles) regions of the Coral Sea.**

Regionally, the deepest mixed layers are located in the southwest Coral Sea (Figure 6.3.6). In addition, the same area also displays some of the deepest summer MLDs, while shallow summer mixed layers are also observed. A similarly high variability has also been noted by Condie and Dunn (2006), who linked it to the changing position of the EAC. In contrast, however, their summer MLDs tend to be less than 40 m in the southwest, a depth which many Argo mixed layers exceed.

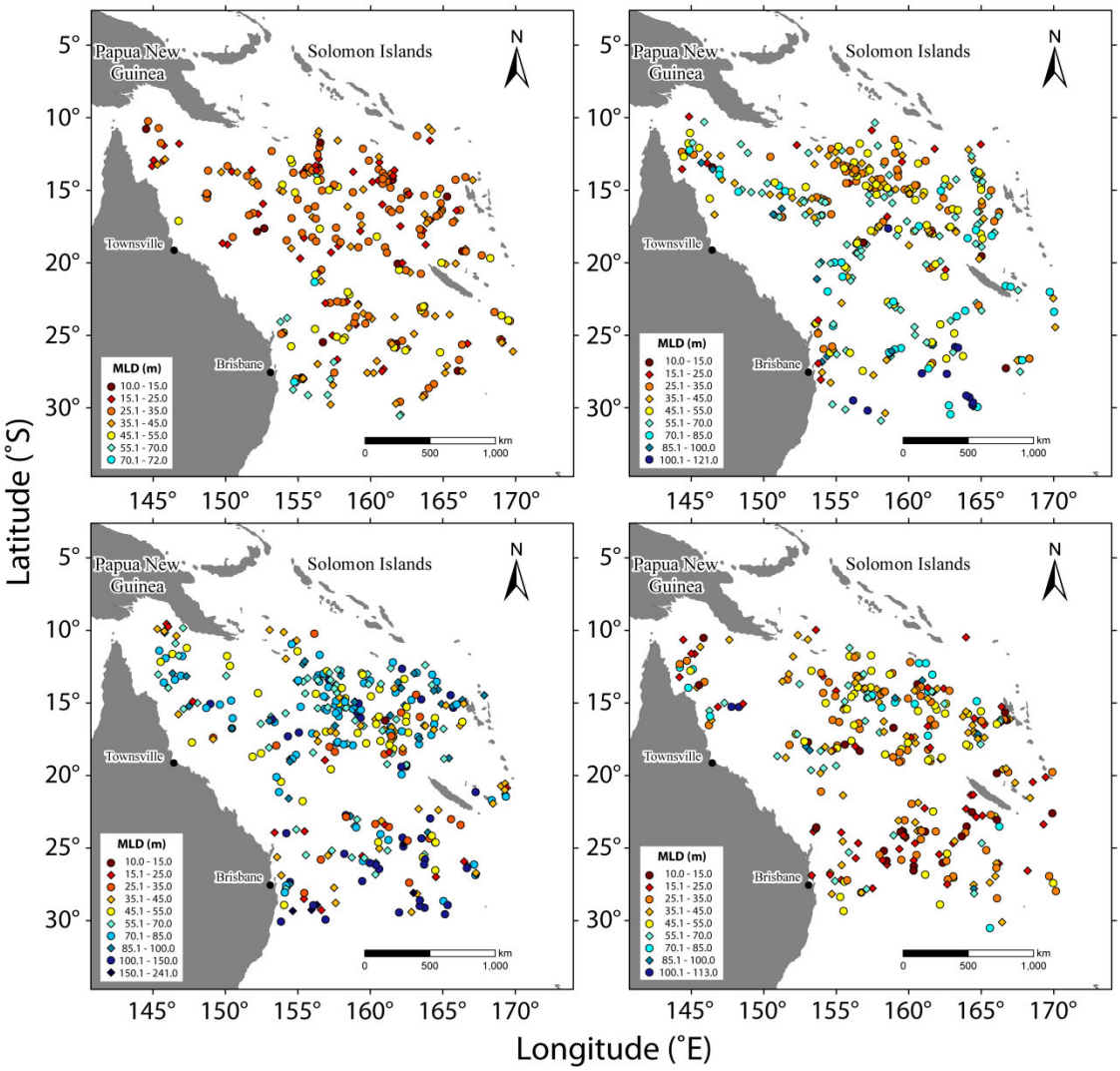


**Figure 6.3.6. Seasonal variation of the mixed layer depth (MLD) for January-March (top left), April-June (top right), July-September (bottom left) and October-December (bottom right).**

#### *6.3.2.3 Barrier Layers*

The vast majority (88%) of Argo profiles examined do not display signs of a significant barrier layer being present, such that there is no area with persistent barrier layers within the Coral Sea. With the potential exception of the southwest Coral Sea (south of 24°S and west of 157°E), where barrier layers are only observed during the cooler months, temporary barrier layer are not linked to a specific season (Figure 6.3.7). Rather, they could appear any time of the year. Considering the Argo data availability, the region seemingly least likely to contain barrier layers is located between 15°S and 19°S along a longitudinal transect west of 162°, a location roughly attributable to the North Caledonia Jet (cf. section 5.3.1). However, north and east of that transect, the likelihood of a barrier layer formation appears to increase, which is most likely linked to greater monsoonal activity and total average rainfall in that region (Figure 6.3.8). Throughout the year, relatively high rainfall rates are noted in the north-eastern Coral Sea, frequently resulting in a lowering of salinity in the upper ocean. As a consequence of persistent precipitation, a shallower halocline may be induced, encouraging the formation of a temporary barrier layer.

There is a minor tendency towards the thickest barrier layers occurring during the cooler months (Figure 6.3.7A). This can be attributed to the, on average, deeper isothermal layers during austral winter, rather than to geographical location (Figure 6.3.7B), SST, SSS or average temperature within the mixed layer.

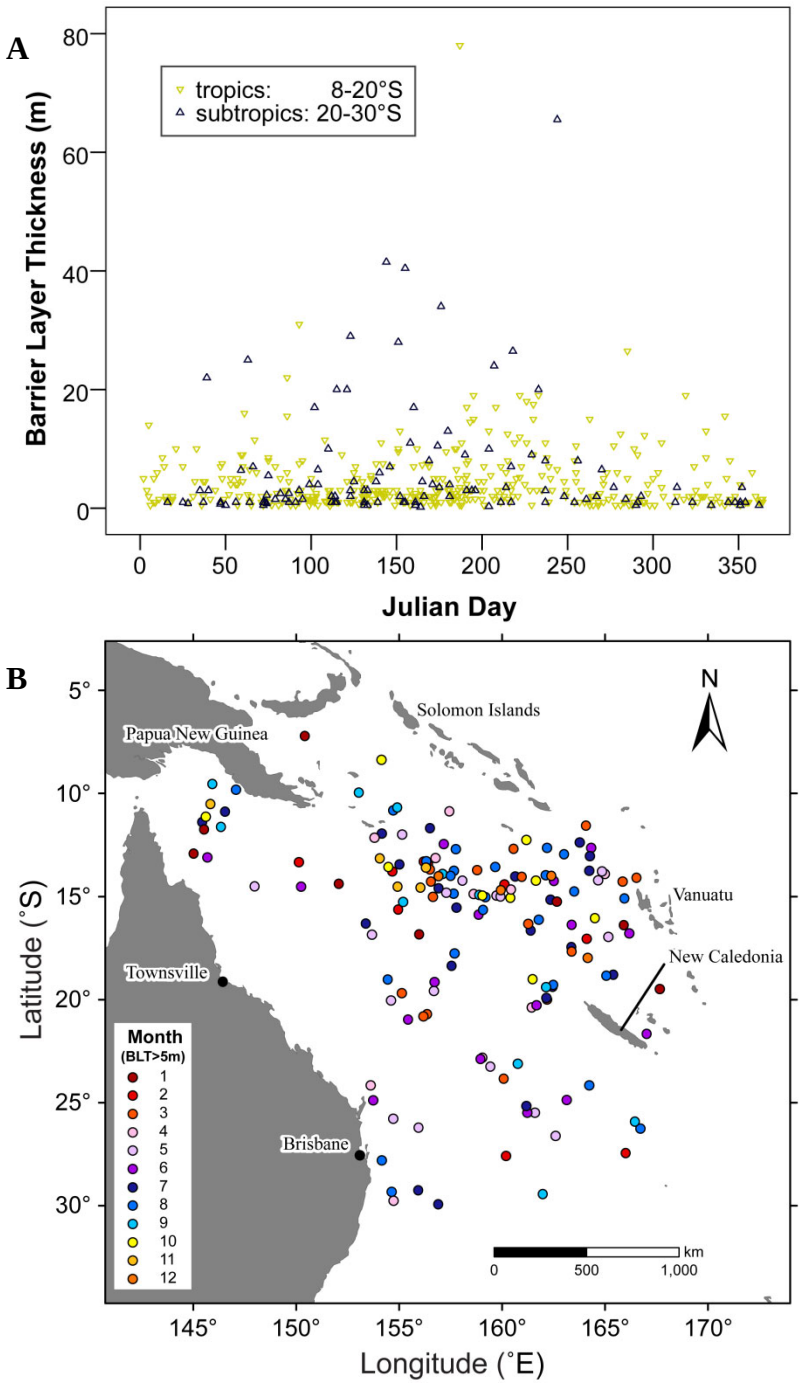


**Figure 6.3.7. Barrier layer thickness (BLT) with respect to A) month and B) geographical location. In Figure B, only the BLTs exceeding 5 m are displayed. BLTs in excess of 10 m predominantly occur during the cooler months (March-September). Geographically, barrier layers can be formed throughout the Coral Sea at any time of the year.**

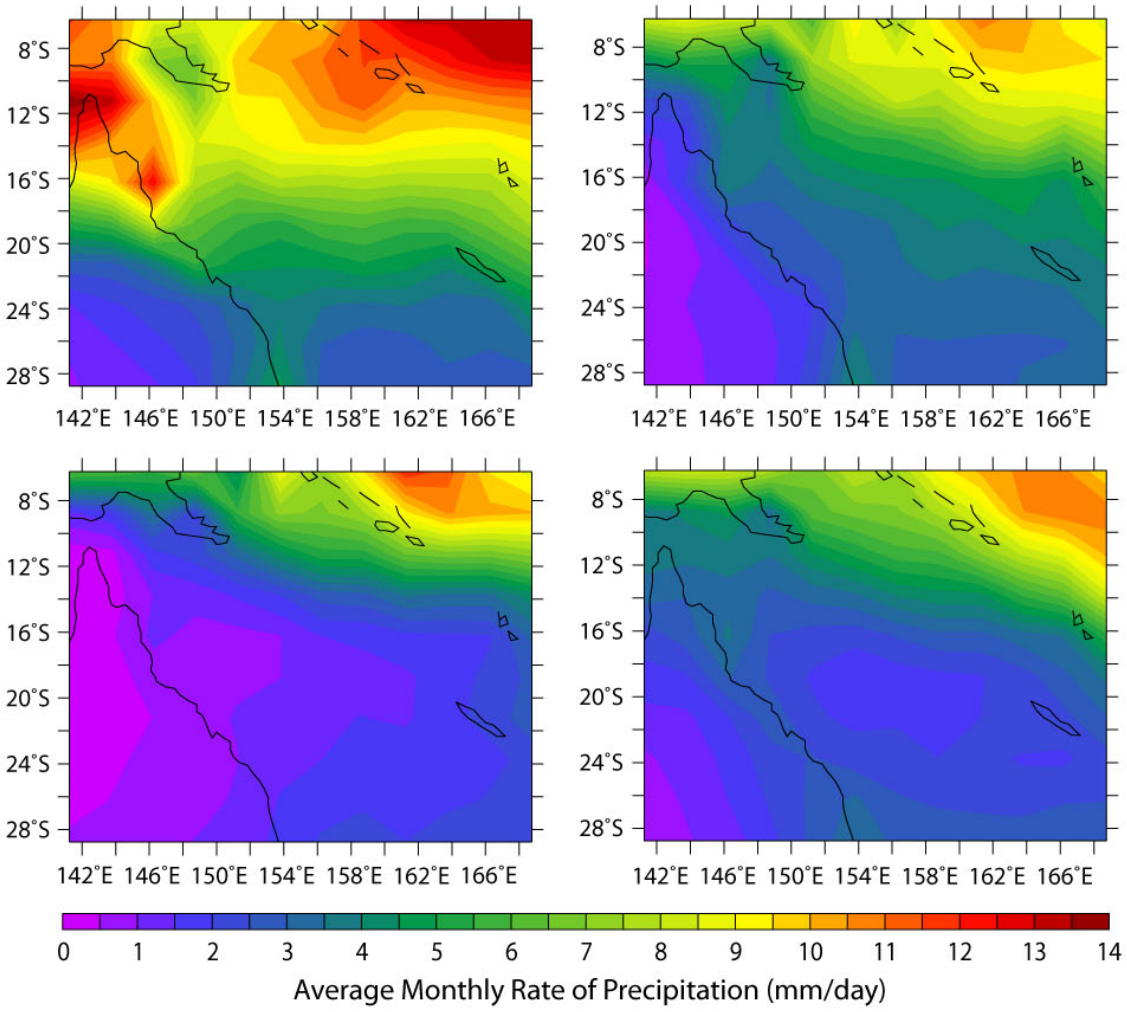


**Figure 6.3.8. Seasonal mean precipitation rates (in mm/day) for summer (top left), autumn (top right), winter (bottom left) and spring (bottom right). The CMAP Precipitation data is provided by the NOAA/OAR/ESRL PSD, Boulder, Colorado, USA (data freely accessible at http://www.cdc.noaa.gov/data/gridded/data.cmap.html).**

#### *6.3.2.4 Temperature and Salinity Inversions*

Even though temperature inversions appear to be very rare within the Coral Sea, salinity inversions (i.e. decrease in salinity with depth) inversions are relatively common and occur year-round, although most of the inversions are clustered within the south-eastern part of the Coral Sea (Figure 6.3.9). Salinity inversions in the southeast appear to be quite long-lasting as several Argo floats (mainly 5900572, 5900870, 5900871 and 5901511) displayed salinity inversions over prolonged and continuous periods. Compensated layers (i.e. layer of near-homogeneous density between a relatively shallow

thermocline and a deeper halocline) are, however, rarely observed. That is, the decline in density due to a salinity inversion is not enough to offset the increase in density due to the gradual decrease in temperature. In the presence of a compensated layer, an MLD estimation solely based on a density criterion would lead to an overestimation of the MLD. This is comparable to the inverse occurrence (barrier layer), where an MLD inference based on temperature alone would also result in an MLD overestimation. Although density within the compensated layer is quasi-homogeneous (and comparable to density within the MLD above the compensated layer), both salinity and temperature are fluctuating due to the absence of convective overturning (cf. de Boyer Montégut *et al.*, 2004). Since a compensated layer occurrence is rare within the Coral Sea, MLD estimations based on density are appropriate. Conversely, MLD estimations based solely on temperature (i.e. ILD) have to be used cautiously due to the quite frequent occurrence (12%) of barrier layers within the Coral Sea, which result in ILDs that are significantly deeper than the MLDs.

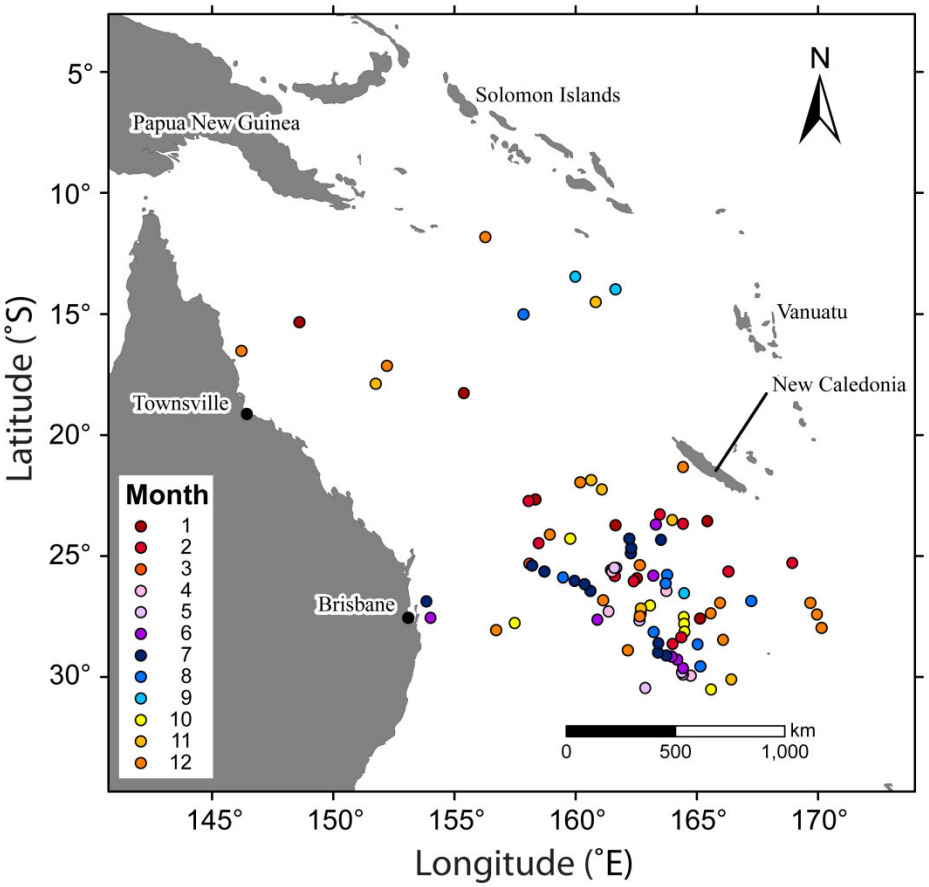


**Figure 6.3.9. Locations within the Coral Sea where salinity inversions are observed.**

### *6.3.2.5 Seasonal Variation of Ocean Heat Content*

The seasonal variability of ocean heat content (OHC), which was computed to a depth of 250 m, is shown in Figure 6.3.10. The seasonality of the OHC, which is relatively strongly correlated to both SST ($R^2$ = 0.70, P<0.001) and SSS ($R^2$ = -0.64, P<0.001), is not as obvious as for the sea surface parameters and MLD. Average OHC is consistently greater in the tropics compared to the subtropics. The annual maximum OHC appears to be slightly offset in the two regions, with highest the OHC being observed around February in higher latitudes (south of 20°S), and 1-2 months earlier in the tropical regions. This can be ascribed to the seasonal movement of the sun, with a maximum in surface heating in the tropical Coral Sea preceding the summer solstice by a few weeks. Conversely, tropical MLD appears to lag behind subtropical MLD by a few weeks (Figure 6.3.5), while SST does not show any significant sign of temporal offset between the two regions. Although solar and wind forcing have a very significant impact on the mixed layer, the offset MLD seasonality observed here is most likely attributable to a combination of relatively low Argo data availability in the southern Coral Sea, giving greater significance to extreme values, and high spatial MLD variability concomitant with low observation coverage at any given time throughout the Coral Sea.

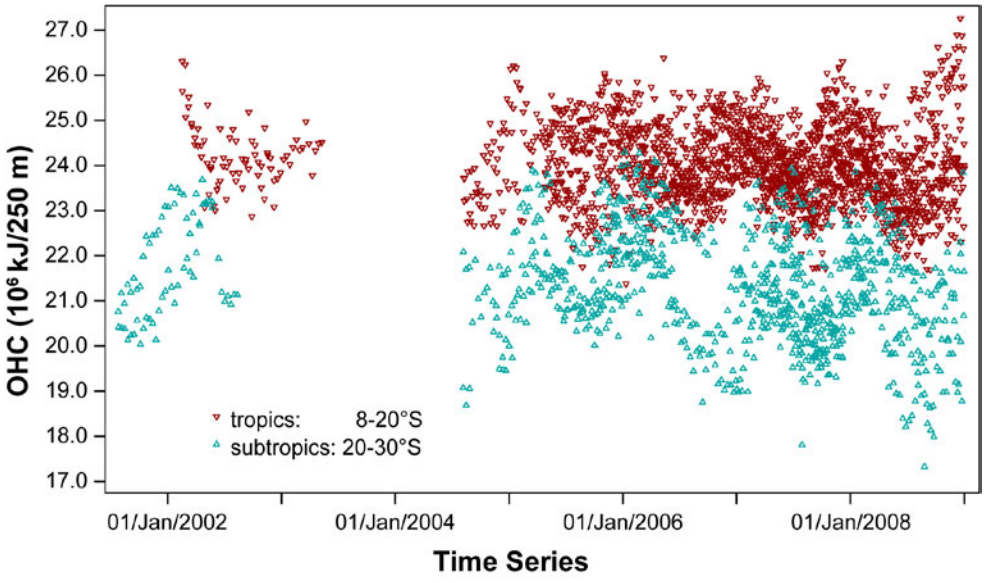


**Figure 6.3.10. Normalised ocean heat content (OHC) for the individual Argo profiles. The OHC was integrated to a depth of 250 m to ensure that all mixed layer depths were captured by the OHC calculation. The 1-year gap from mid-2003 to mid-2004 results from no active Argo float being present within the Coral Sea during that period.**

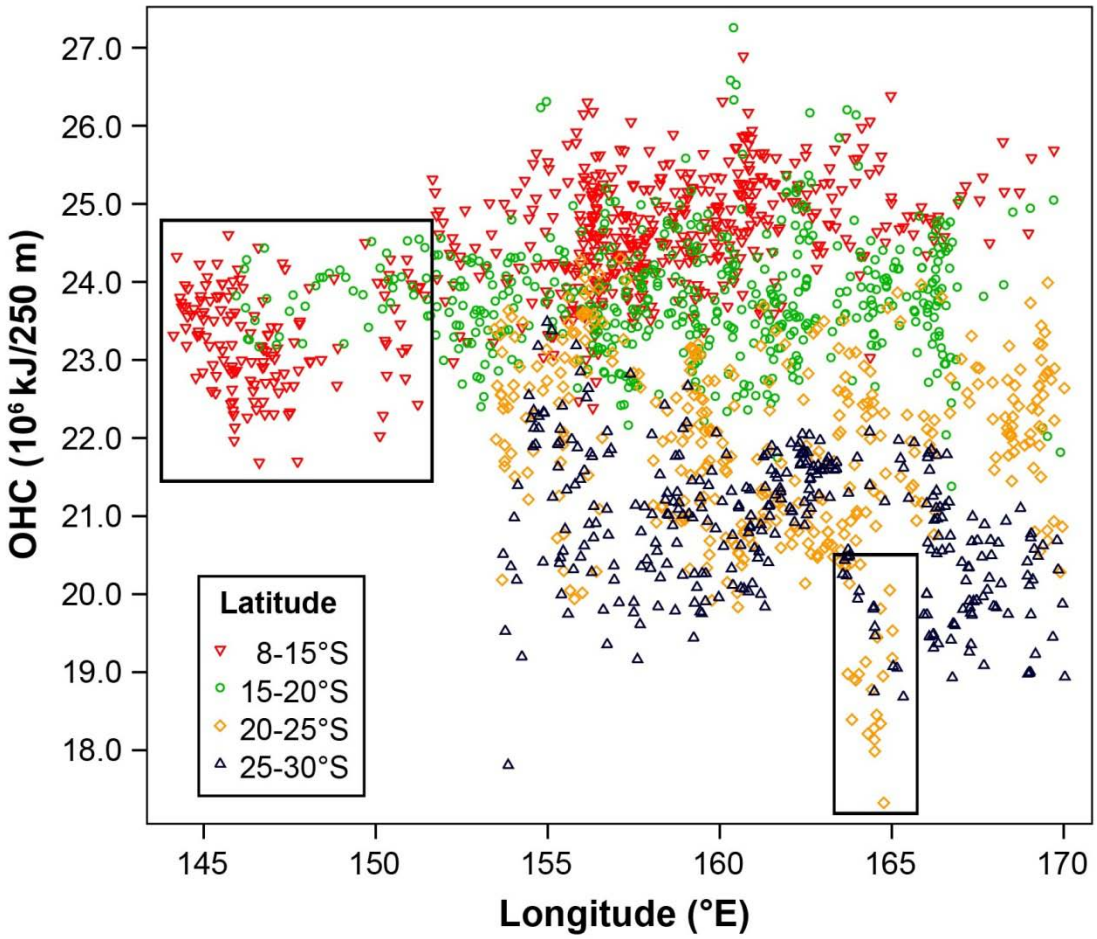


**Figure 6.3.11. Longitudinal pattern of ocean heat content (OHC), with the colour scheme denoting the latitudinal provenance. There are two regions within the Coral Sea where the otherwise very strong positive relationship between OHC and latitudinal location is not as evident: the Gulf of Papua (north of 15°S in the upper left box) and southwest of New Caledonia (around 23-25°S, lower right box).**

Although, in general, there is a strong link between OHC and the latitudinal position of the data, there are regions within the Coral Sea where the positive relationship between OHC and latitudinal location is not as evident (Figure 6.3.11). The spatial variability of the observed ocean heat content did reveal the strong influence of regional currents, most notably relatively low OHC in the north-western Coral Sea due to the Hiri current (Figure 6.3.12). Within the Gulf of Papua (north of 15°S and west of 148°E), both SST and OHC are decreased substantially by the clockwise movement of the Hiri current (cf. Figure

5.3.1), which transports relatively cool water masses northwards (Figure 6.3.12). The relatively low temperature in the north-western Coral Sea is also clearly evident in the upmost 75 m temperature fields of CARS2009 (CSIRO Atlas of Regional Seas, v. 2009), a global high-resolution climatology of seasonal ocean water properties (Ridgway *et al.*, 2002).

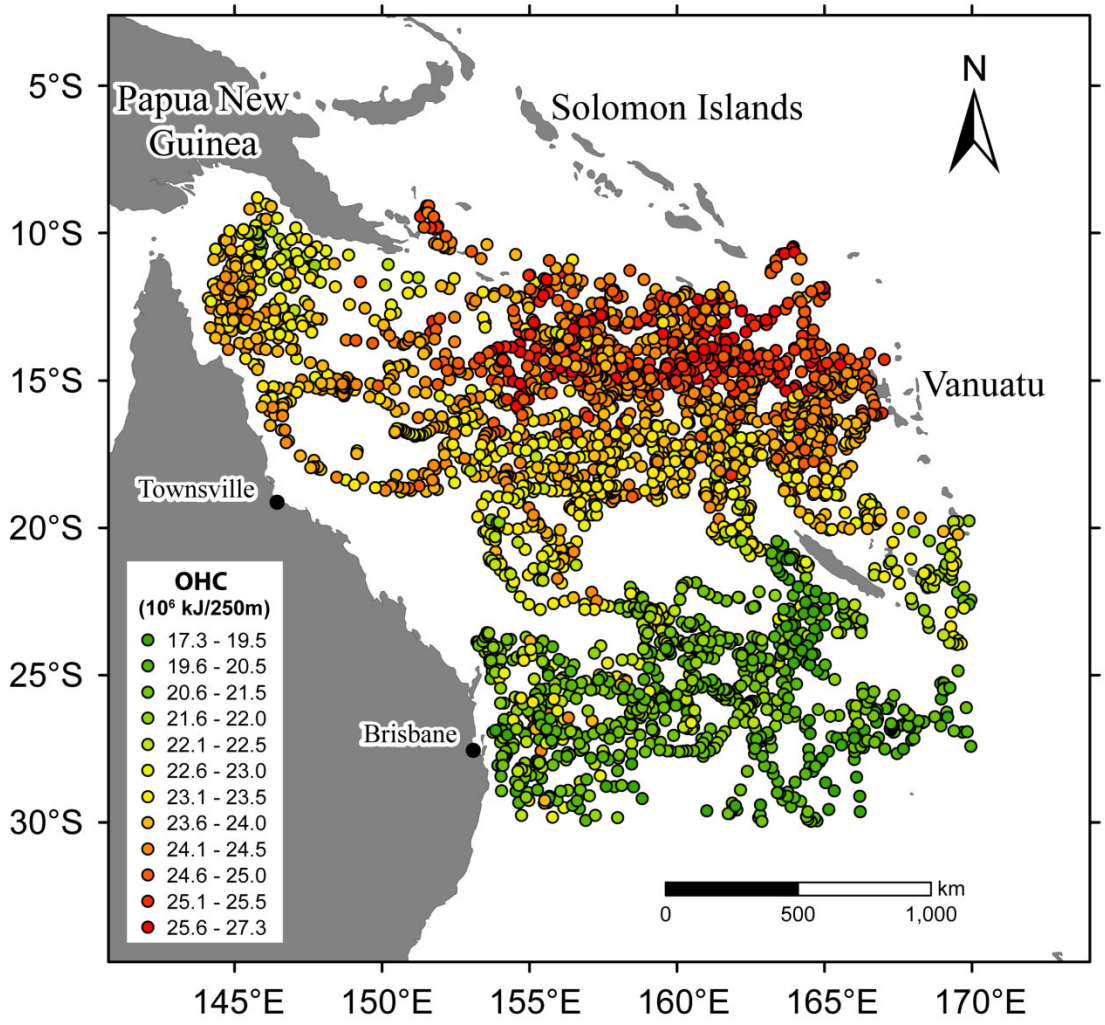


**Figure 6.3.12. Geographical position of Argo floats within the Coral Sea. The colour scheme of the Argo data is denoting ocean heat content (OHC). Locations are only displayed for CTD profiles that encompass the entire top 250 m of water.**

Another region with relatively low OHC is located southwest of New Caledonia. It is possible that the eddy-rich nature of the southern Coral Sea, associated with the Tasman front (Sokolov and Rintoul, 2000), resulted in these temporarily low OHC values. In

addition, the North Caledonia Jet may transport cooler water mass northwards along the west coast of New Caledonia.

In relation to the MLD, the long-term monitoring of the OHC is important due to their close connectivity. A change in OHC would likely result in an alteration of the mixed layer if wind stress remains unchanged. In turn, a decrease in MLD would induce a warmer upper ocean (within the mixed layer), concomitant with a decrease in OHC below the MLD. Within the Coral Sea, no significant long-term trends in OHC and MLD are discernible based on current Argo data alone. If the OHC of the Coral Sea increases in the future, which is expected to occur in many other regions around the world due to global warming, and in the absence of increased wind stress, the upper ocean would become more highly stratified, resulting in a shallowing of the MLD. According to a study by Yeh *et al.* (2009), we can expect the Coral Sea MLD to decrease by up to 20% by the end the 21$^{st}$ century relative to the pre-industrial MLD conditions, assuming a doubling of atmospheric $CO_2$ levels. This, in turn, would have significant impacts on biogeochemistry (e.g. nutrient supply and chlorophyll distribution) and the ocean-atmosphere interaction (e.g. evaporation, circulation).

## 6.3.3 CARS 2006

### *6.3.3.1 Annual Means and Seasonality of SST and MLD*

Figures 6.3.13 and 6.3.14 exemplify the pattern of the mean annual Coral Sea surface temperature and mixed layer depth, respectively. Whereas there is a clear latitudinal gradient in mean SST (Figure 6.3.13), with average temperatures being about 7°C lower in the extratropics, there is no obvious spatial trend discernible in the mean annual MLD field, although there is some tendency towards higher MLDs in the southern Coral Sea as well as near the equator (Figure 6.3.14).

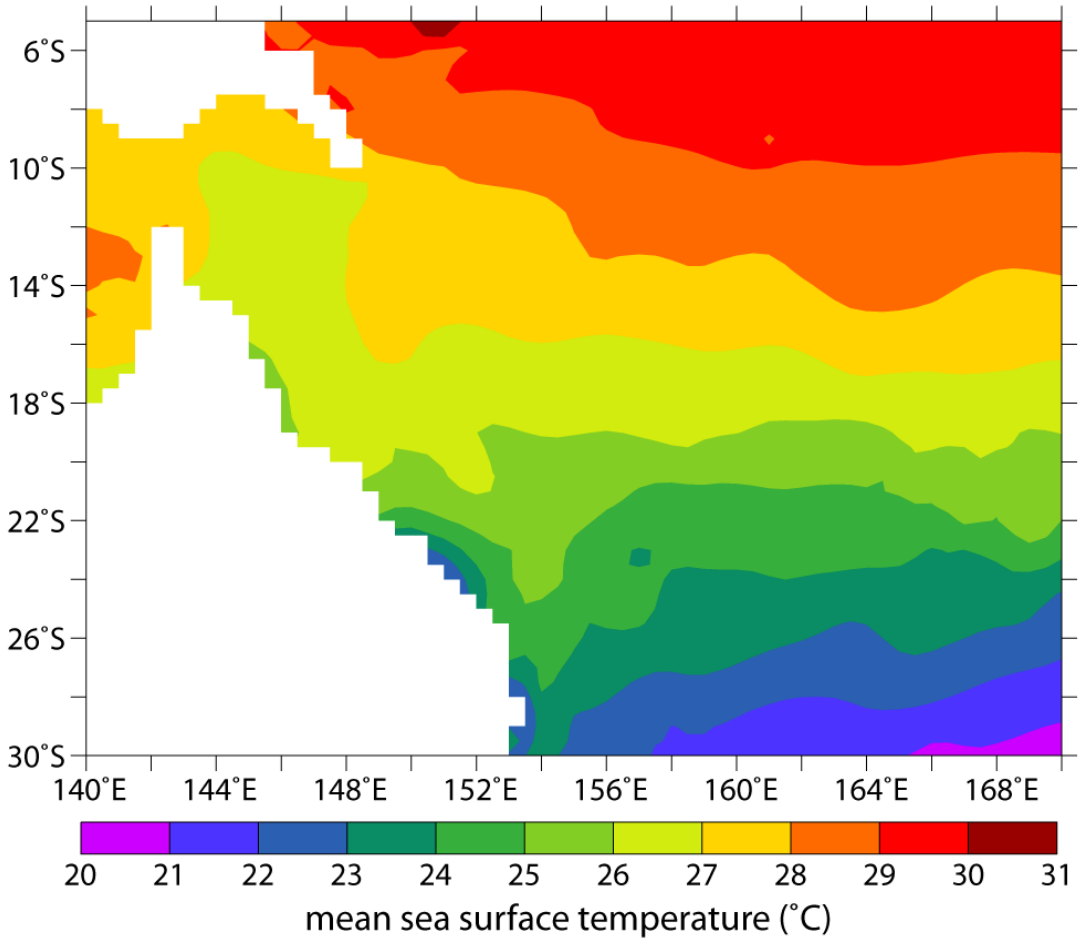


**Figure 6.3.13. Mean annual sea surface temperature (ºC) field within the Coral Sea.**

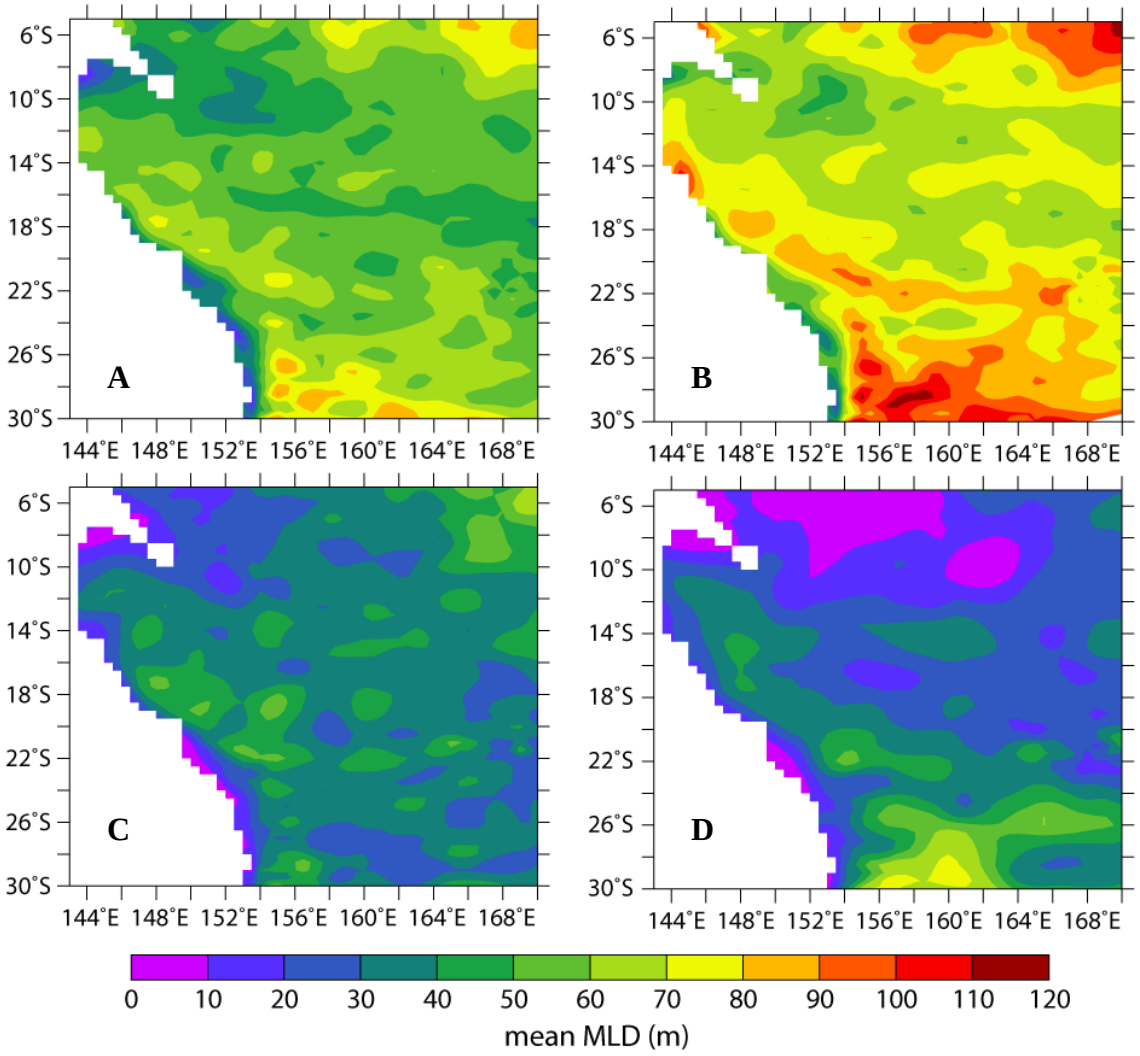


**Figure 6.3.14. Mean annual mixed layer depth (m) field within the Coral Sea, with MLD being determined as the depth where A) T= $T_{10m}$-0.5°C, B) T=$T_{10m}$-1°C, C) dT/dz > 0.015°C/m and D) dρ/dz > 0.004 kg/m$^4$.**

Variability in solar and latent heat fluxes greatly influence seasonal temperature changes in the topmost 100 m (Figure 6.3.15). Solar heating induces increased vertical temperature stratification during summer (Figure 6.3.15A), suppressing vertical mixing and thus instigating a shallowing of the MLD. Conversely, LHF is most dominant during winter months as a result of stronger trade winds, which both enhance evaporative cooling and mixing of the upper ocean.

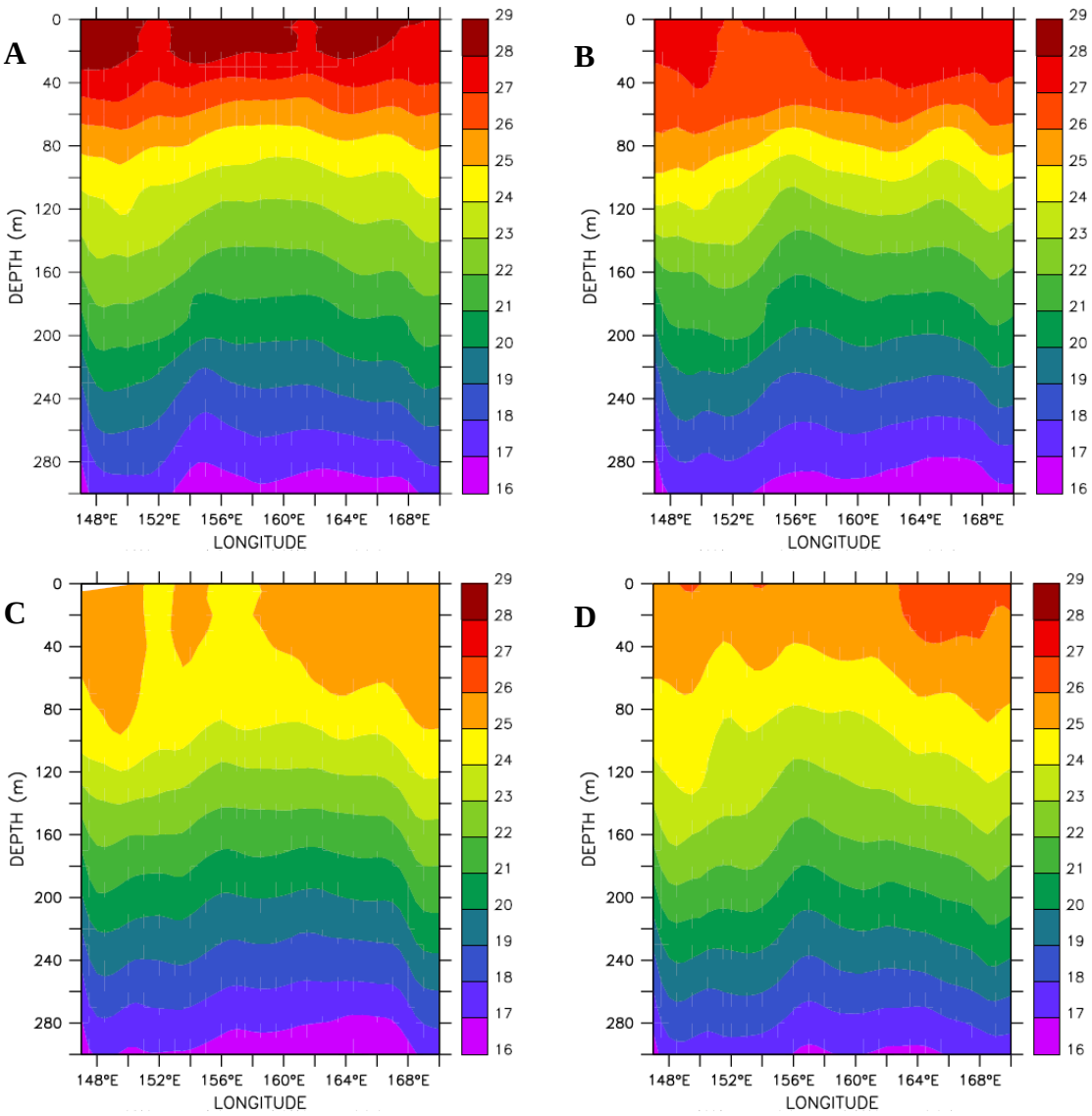


**Figure 6.3.15. Longitudinal variation of temperature (ºC) in the upper 300 m at 17°S in austral A) summer, B) autumn, C) winter and D) spring.**

Latitudinally, temperature in the upper ocean displays much greater variability in the subtropics compared to the tropics (Figure 6.3.16) since both solar heat fluxes and evaporative cooling vary more substantially in the southern regions (Chou *et al.*, 2005).

During summer and early autumn, significant warming is evident in the upper 40-100 m of the Coral Sea (Figure 6.3.17), causing a shallowing of the thermocline as a result of reduced stirring of the upper ocean water column. Although a temperature increase towards summer is marked throughout the Coral Sea (see also Figure 6.3.18), it is more

prevalent in the southern regions of the Coral Sea as a result of greater seasonality in heat fluxes.

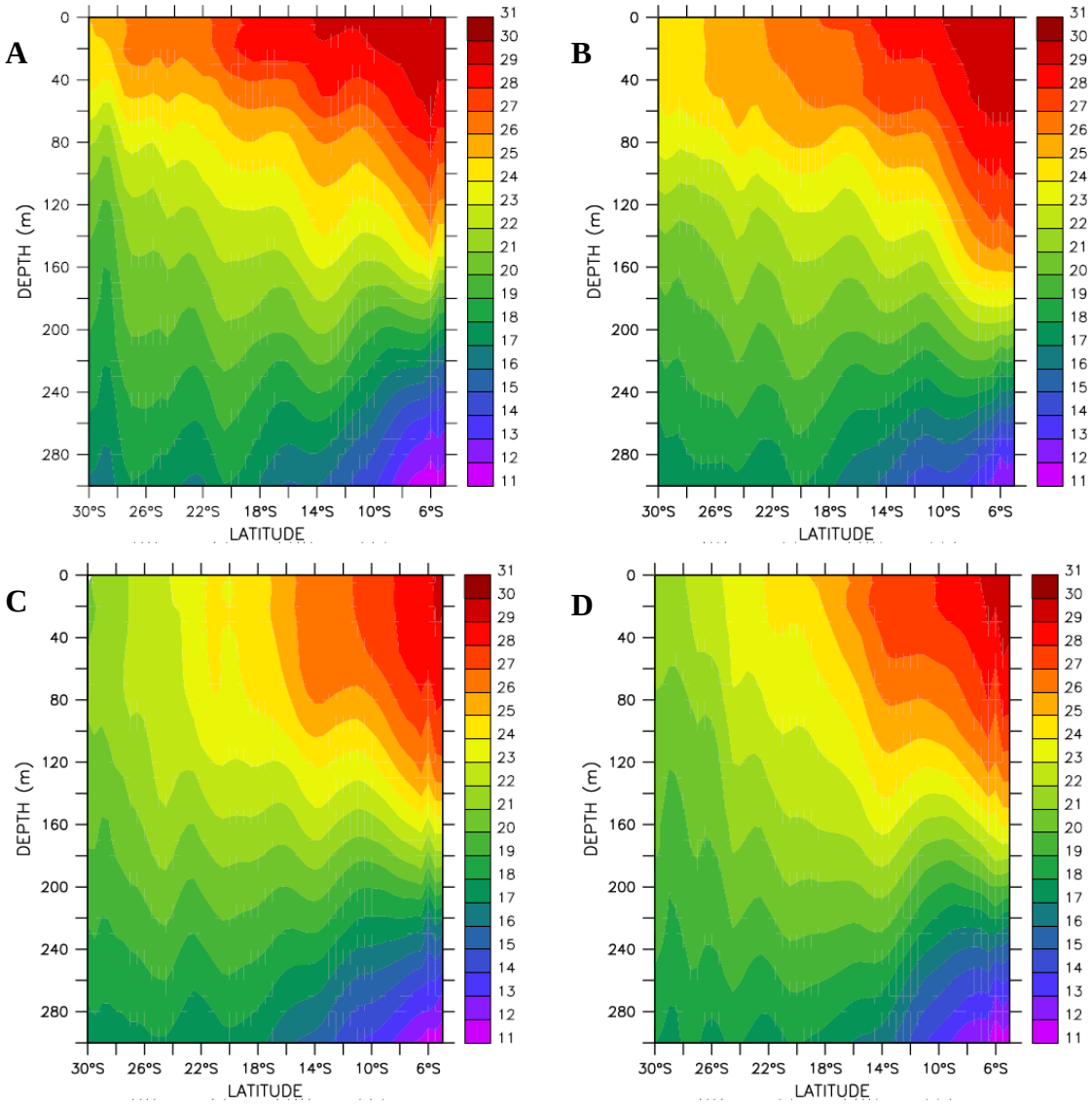


**Figure 6.3.16. Latitudinal variation of temperature (ºC) in the upper 300 m at 155°E in austral A) summer, B) autumn, C) winter and D) spring.**

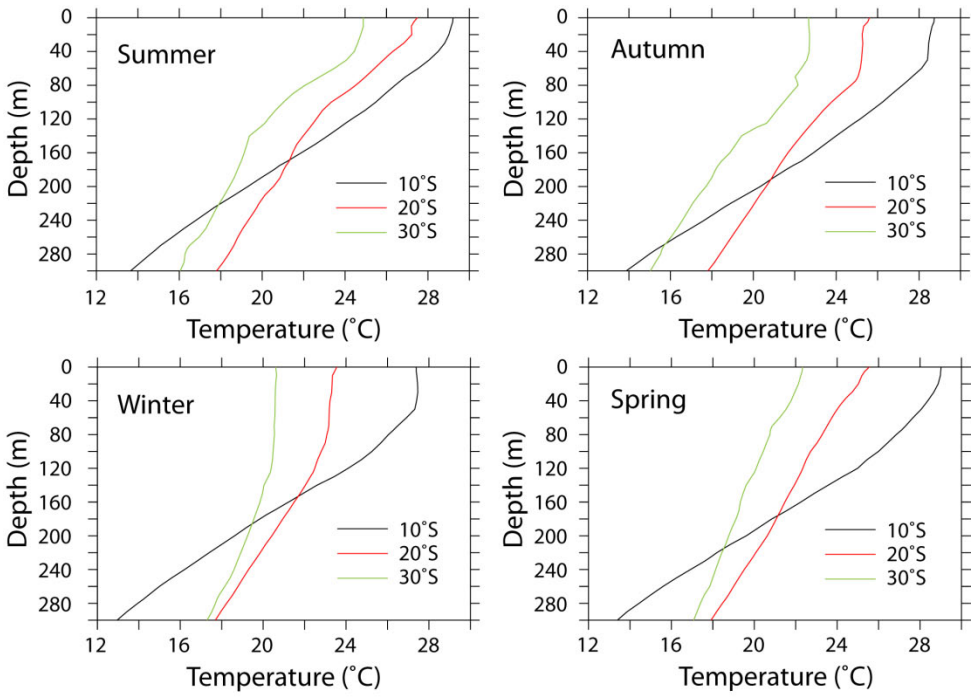


**Figure 6.3.17. Latitudinal variation of mean seasonal temperature (ºC) profiles in the upper 300 m at 156°E. Temperature profiles are shown for three different latitudes.**

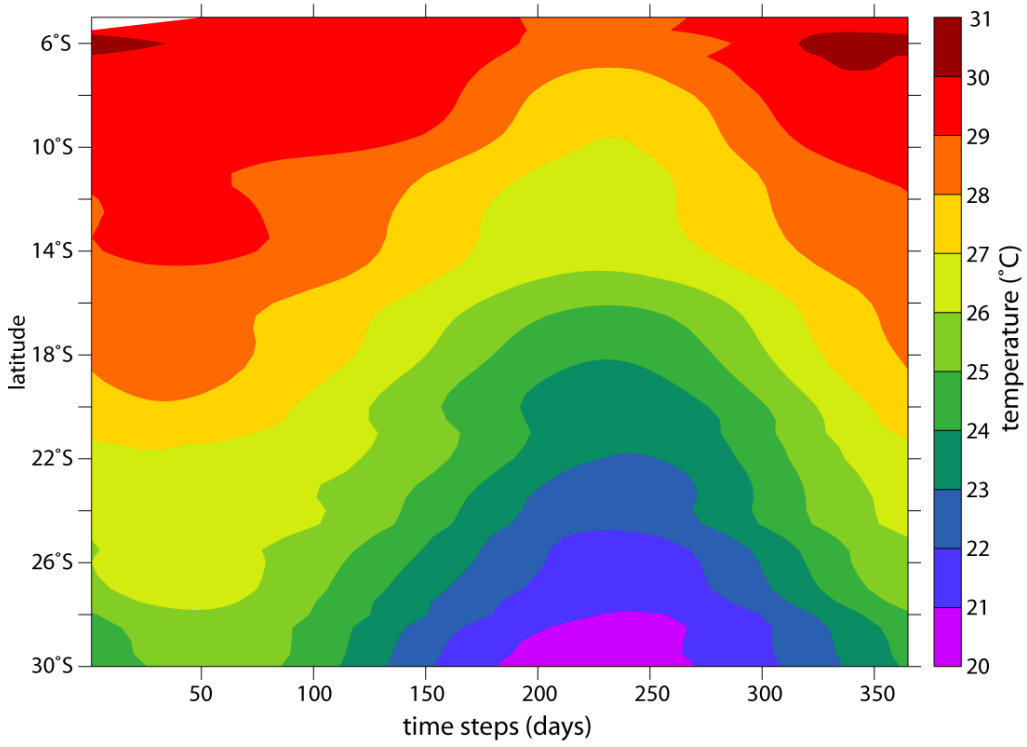


**Figure 6.3.18. Hovmöller plot of latitudinal SST (ºC) seasonality at 155°E. Output is given daily from January 1st (left) to December 31st (right).**

The east-west gradient of temperature at 12.5°S (Figure 6.3.19) could be a result of the all-year inflow of warm tropical waters (i.e. SEC) into the north-eastern Coral Sea, resulting in only minor seasonal temperature fluctuation along the path of the SEC.

Figure 6.3.20 displays the maximum MLDs within the Coral Sea for four different MLD determination methods. It should be noted here that Figures 6.3.20A-C show the ILD as opposed to MLD since the threshold (Figures 6.3.20A and B) and gradient (Figure 6.3.20C) methods are solely based on temperature. In the following paragraphs, they will all be referred to as MLDs, however. In addition, ILDs in Figure 6.3.20B will always be deeper than those in Figure 6.3.20A since both are based on the threshold method with the same reference temperature, but the former ILD having a larger prescribed ΔT (1°C vs 0.5°C). In both cases, the reference temperature is set at 10 m ($T=T_{10m}$-0.5°C and $T=T_{10m}$-1°C) to avoid strong diurnal variability in the first few metres of the ocean.

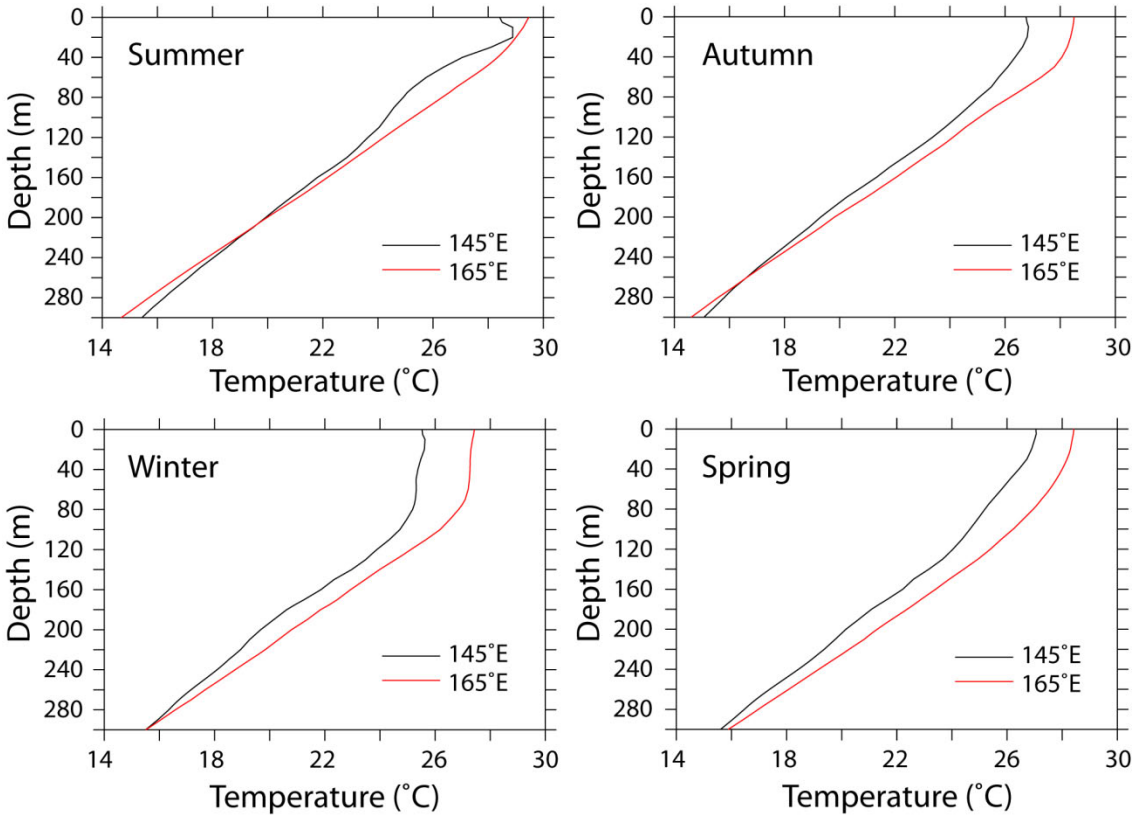


**Figure 6.3.19. Longitudinal variation of mean seasonal temperature (ºC) profiles in the upper 300 m at 12.5°S. The profiles are shown for two different longitudes.**

In Figure 6.3.20C, in which the MLD is determined using the gradient method (dT/dz > 0.015°C/m), the deepest MLDs, generally attributed to enhanced mixing in winter, are located in the region of 18-23°S and 152-157°E, with the deepest mixed layer (120 m) occurring at the end of August (figure not shown). Whereas the typical gradient towards greater maximum MLDs in higher latitudes is absent in Figure 6.3.20C, the expected pattern is visible for the three other MLD fields. All three maps show deeper MLDs towards the south, with the maximum MLD (220 m) being found at the southern border of the Coral Sea (Figure 6.3.20B).

The distribution of the minimum MLD appears to be relatively homogenous within the Coral Sea (Figure 6.3.21). Although there is no clear north-south trend, there is some tendency towards deeper (40-90m) MLDs towards the equatorial Pacific Ocean (outside of the Coral Sea, north of 8°S), as well as at the outer edges of the continental shelf in the southern Coral Sea. The latter is likely linked to local downwelling, the strength of which is positively correlated to MLD. Overall, however, the MLDs are comparatively homogeneous throughout the Coral Sea, with Figure 6.3.21D (based on the gradient method applied on density, $d\rho/dz > 0.004$ kg/m$^4$) displaying the shallowest minimum MLD field (0-30m).

The latitudinal and longitudinal MLD patterns are shown in more detail in Figures 6.4.22 and 6.4.23, respectively. Throughout the Coral Sea, and independently of which method was used to obtain the MLD, the shallowest mixed layers are observed in summer, although comparatively thin mixed layers can occur at low latitudes all year round (Figure 6.3.22). Similar to the results obtained from the Argo dataset alone (Figure 6.3.5), the deepest MLDs generally occur during the cooler winter months. Furthermore, since more extensive cooling of the upper ocean and wind mixing in the subtropics (south of 20°S) induces the deepest mixed layers within the study area, the seasonal variability of the MLD is more pronounced in the southern Coral Sea. The longitudinal MLD pattern is relatively homogenous throughout the Coral Sea, with MLD differences normally not exceeding 50 m (Figure 6.3.23). Since zonal SST is relatively uniform, longitudinal variations in MLD are mainly attributable to localised upwelling or downwelling, and shifts in subsurface currents.

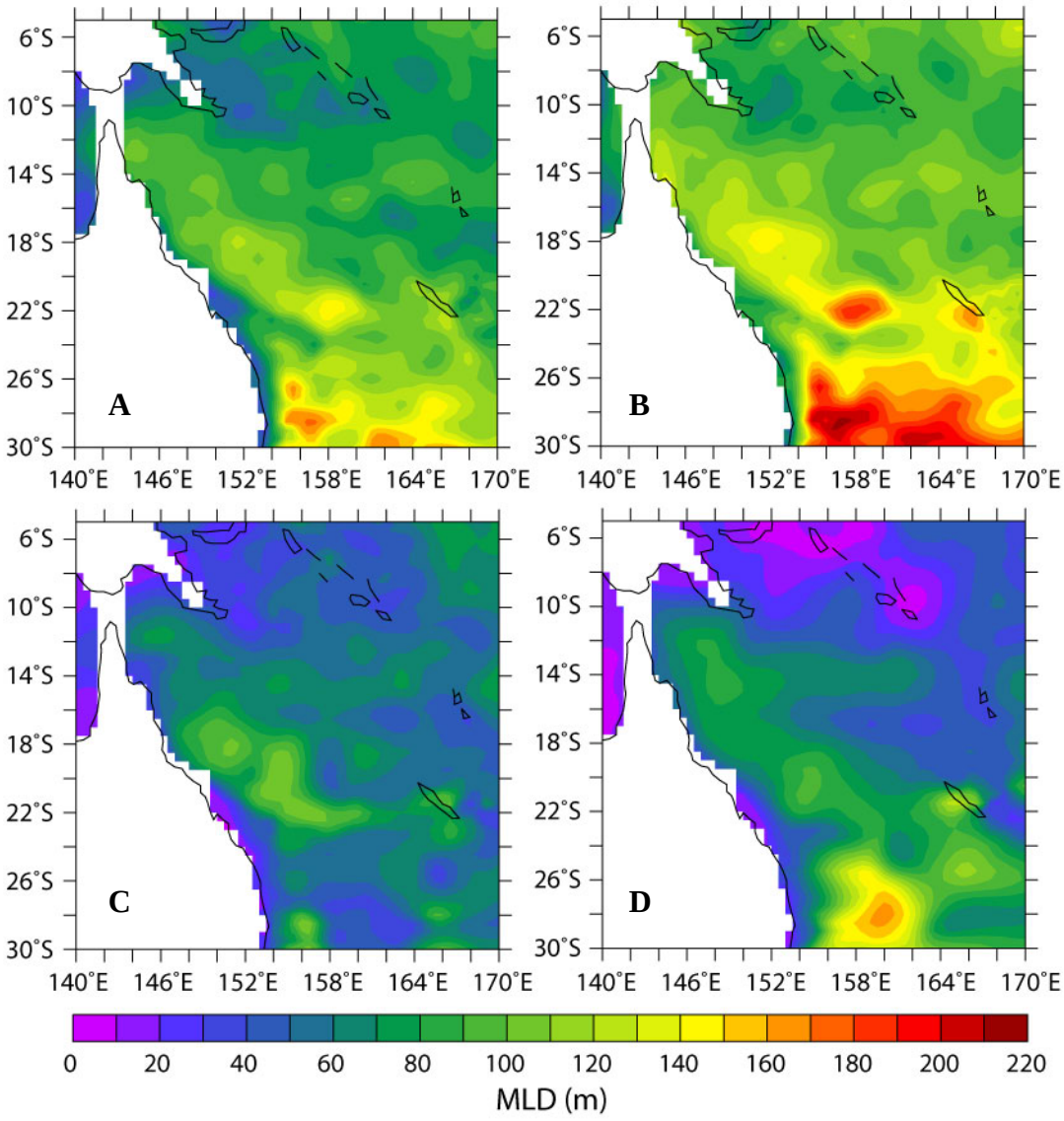


**Figure 6.3.20. Maximum mixed layer depth (m) within the Coral Sea, with MLD being determined as the depth where A) T= $T_{10m}$-0.5°C, B) T=$T_{10m}$-1°C, C) dT/dz > 0.015°C/m and D) dρ/dz > 0.004 kg/m$^4$.**

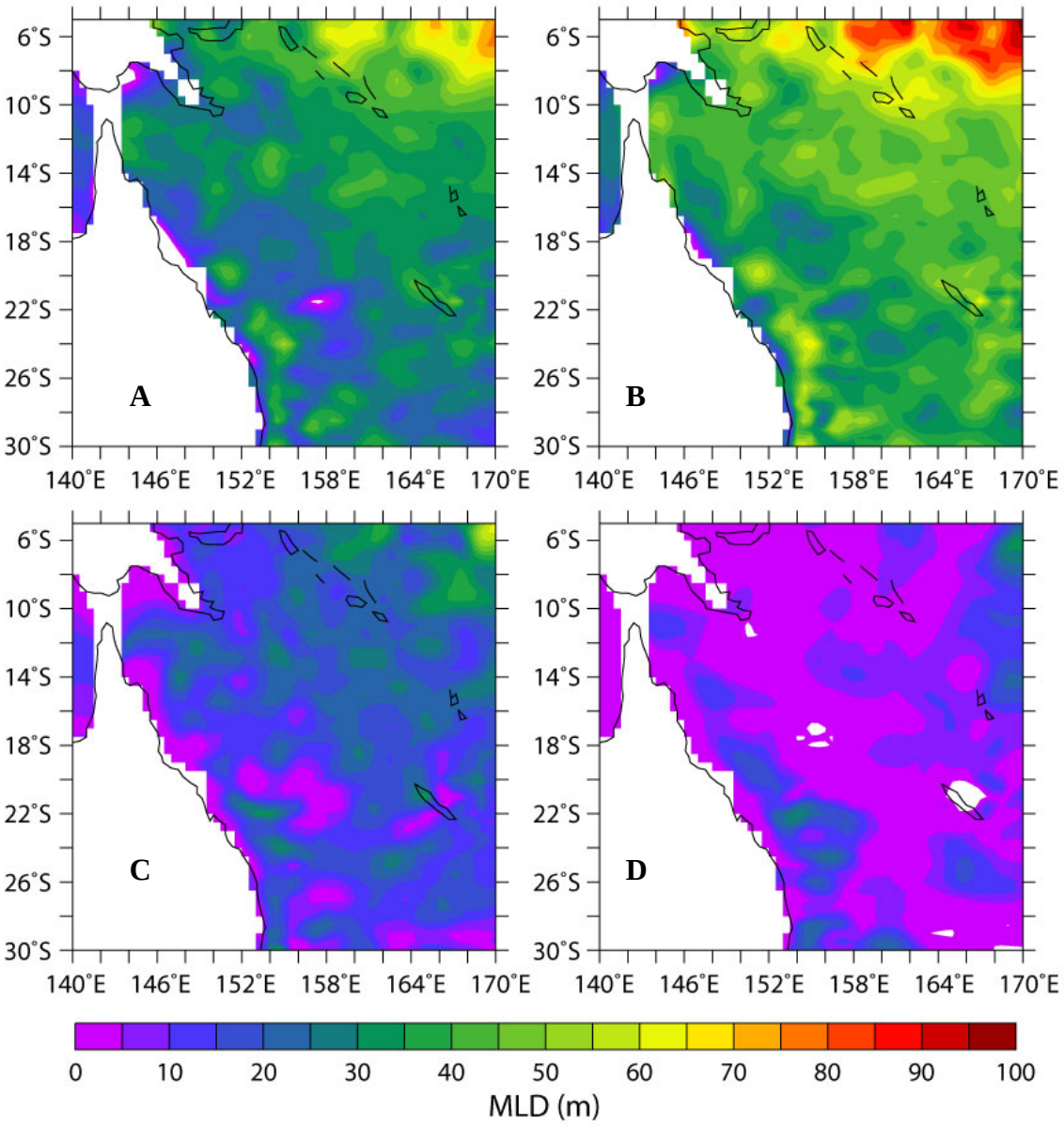


**Figure 6.3.21. Minimum mixed layer depth (m) within the Coral Sea, with MLD being determined as the depth where A) T= $T_{10m}$-0.5°C, B) T=$T_{10m}$-1°C, C) dT/dz > 0.015°C/m and D) dρ/dz > 0.004 kg/m$^4$. Negative MLD estimates were omitted.**

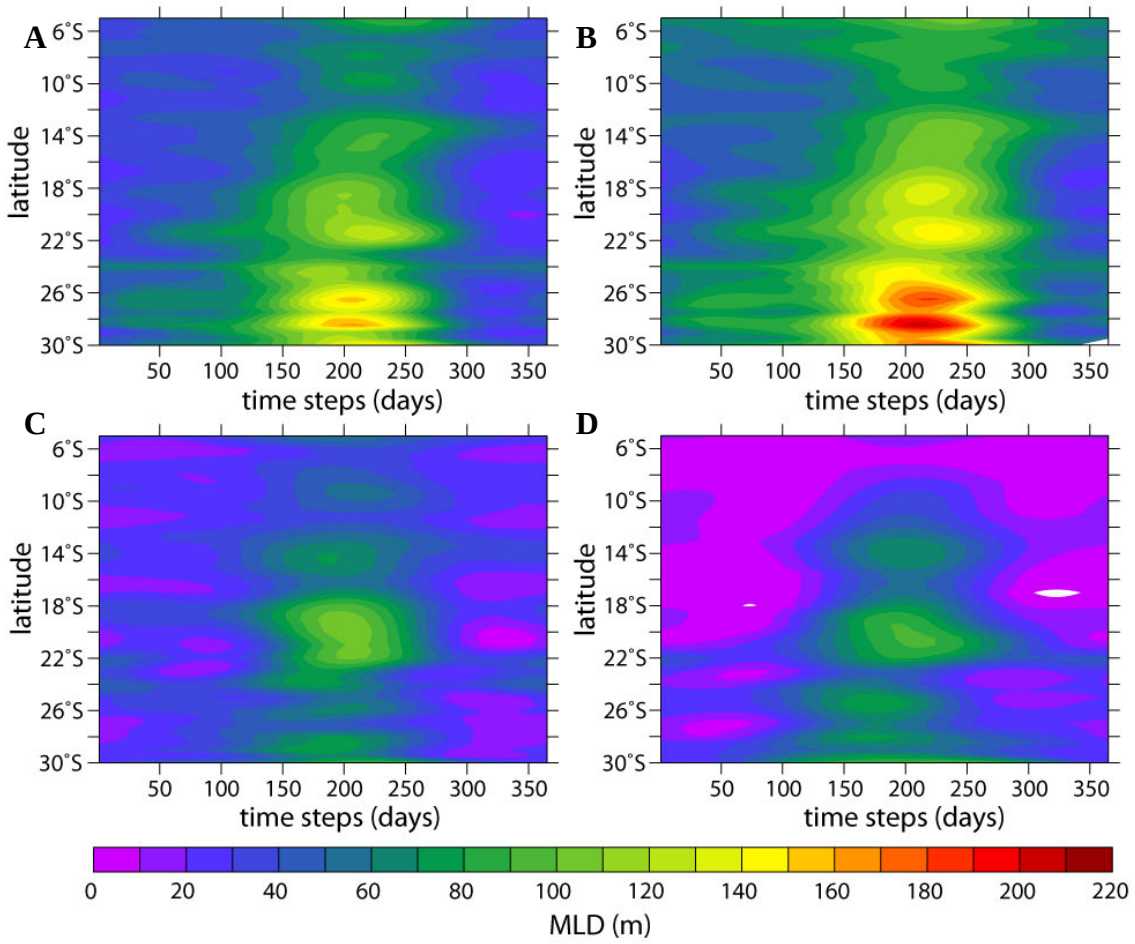


**Figure 6.3.22. Hovmöller plot of latitudinal MLD (m) seasonality at 155°E, with MLD being determined as the depth where A) T= $T_{10m}$-0.5°C, B) T=$T_{10m}$-1°C, C) dT/dz > 0.015°C/m and D) dσ/dz > 0.004 kg/m$^4$. Output is given daily from January 1$^{st}$ (left) to December 31$^{st}$ (right). Negative MLD estimations were excluded.**

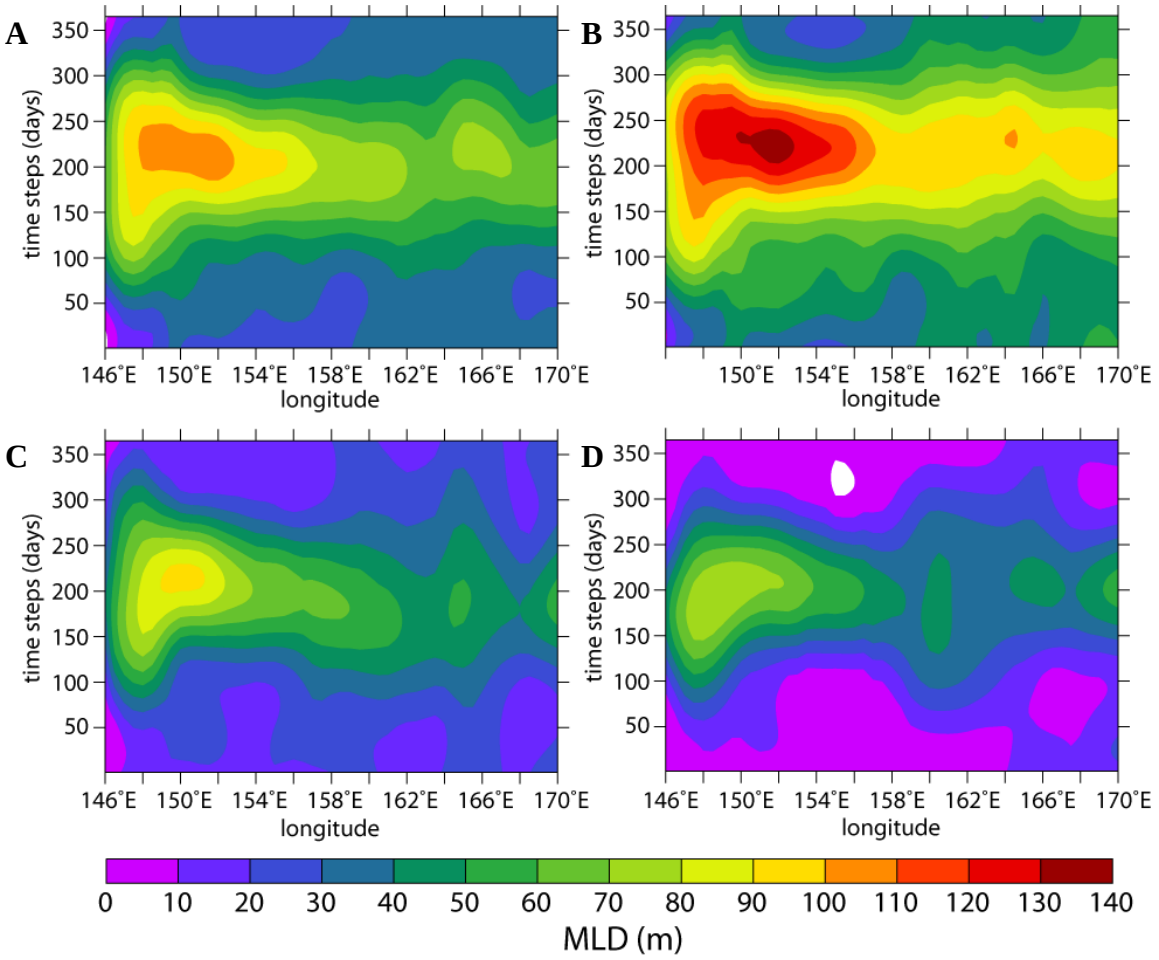


**Figure 6.3.23. Hovmöller plot of longitudinal MLD (m) seasonality at 17°S, with MLD definitions as in Figure 6.3.22. Negative MLD estimates were ignored.**

## 6.3.4 Satellite-derived SST

Although Argo floats represent a significant improvement in the coverage and sampling of the oceans globally, Argo is nonetheless only covering a very small percentage at any given time. Thus, to complement the Argo data, and for subsequent verification purposes of the model output (cf. section 8.4 onwards), satellite-derived SST data is briefly presented here.

Figure 6.3.24 displays the monthly means of SST (11 micron day) data derived from MODIS-Terra, with 1/12° data available for the entire 2000/02/01 - 2010/10/01 period. The SST patterns clearly show the impact of the major Coral Sea currents, with the Hiri current moving relatively cool surface waters clockwise northwards into the Gulf of Papua. These currents are thus distorting the latitudinal SST gradient, as indicated by the

Argo data as well (cf. Figure 6.3.4). In contrast to the Argo data, the presence of the EAC is evident, with the EAC transporting warm water southward along the coast throughout the year. Unlike Argo floats, satellites are not impeded by bathymetry or currents, allowing for data collection in both shallow (<1000 m) locations and areas outside of dominant flow.

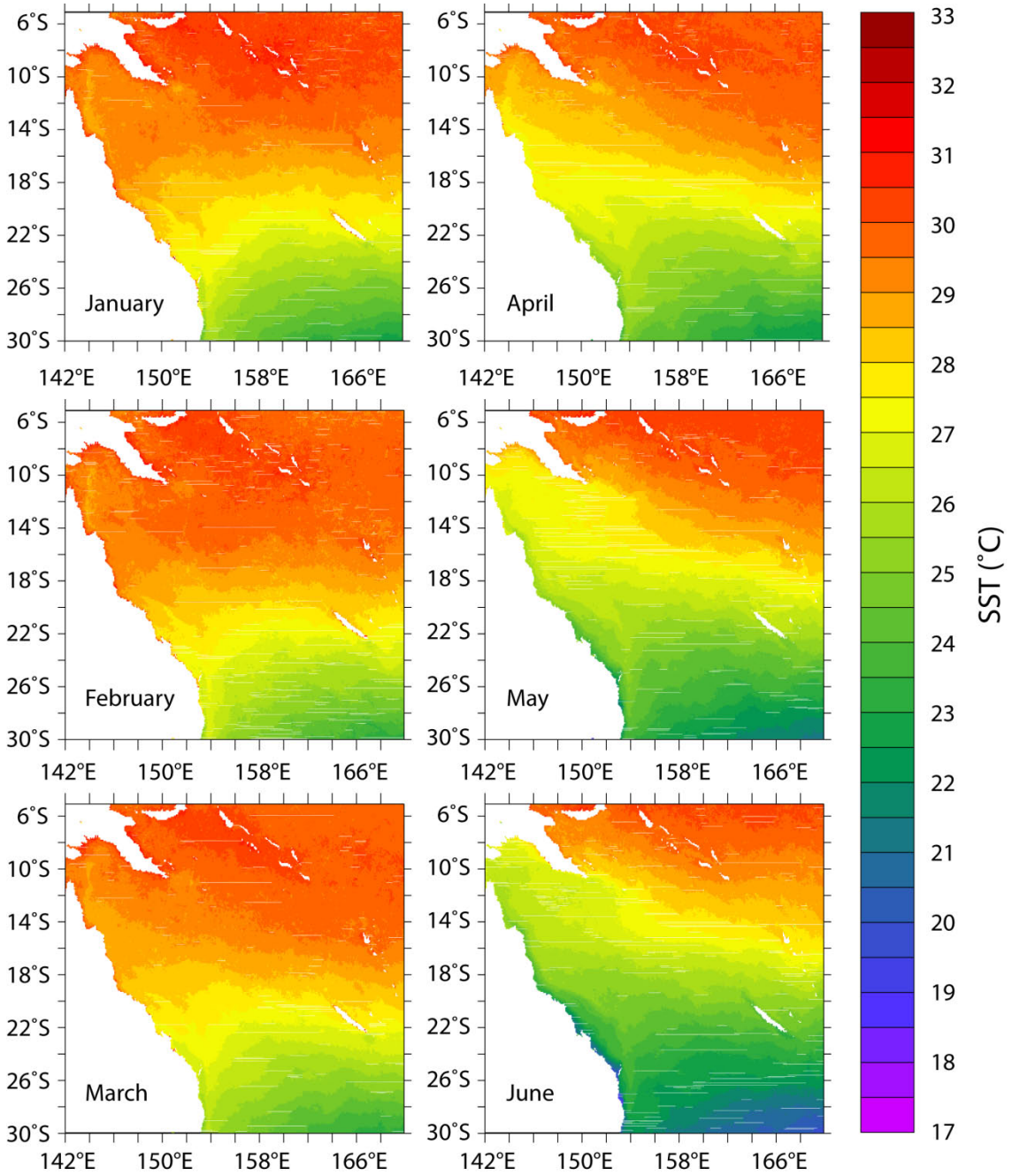


**Figure 6.3.24. Monthly mean sea surface temperature (SST, 11 micron day) derived from MODIS-Terra. All available satellite data from 2000/02/01 to 2010/10/01 are included.**

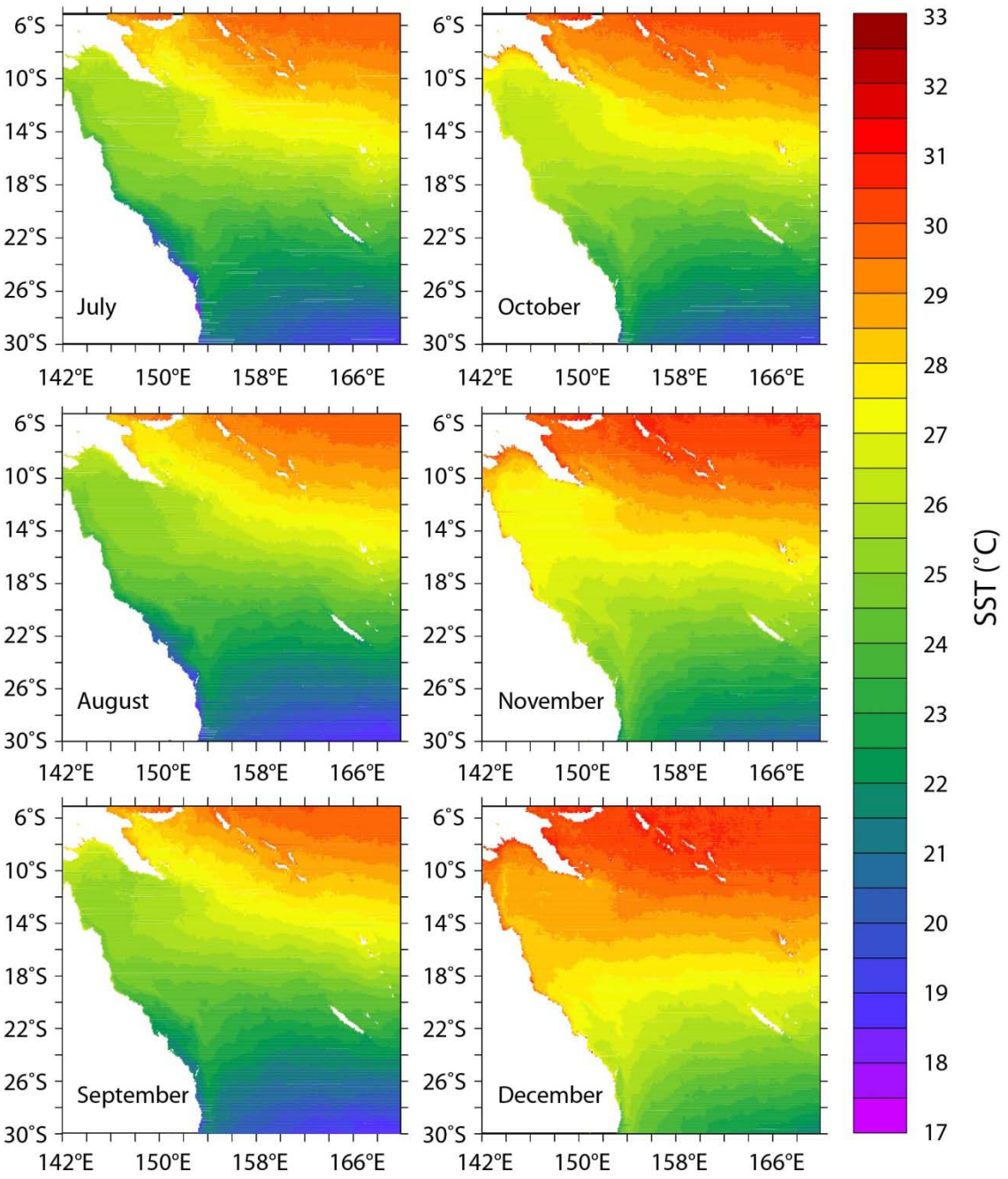


**Figure 6.3.24 continued.**

## 6.4 Discussion

### 6.4.1 Reliability of Argo Profiles

Recently, there have been some concerns in regard to the accuracy and consistency or Argo float data (Willis *et al.*, 2007). Normally, satellite altimetry and OHT derived from Argo floats are closely correlated with each other (Roemmich and Owens, 2000). However, for the 2003-2005 period, several OHT studies (e.g. Lyman *et al.*, 2006) show a cooling trend, which disagrees with the satellite altimetry for those years (cf. http://sealevel.colorado.edu/current/sl_ib_ns_global.jpg). Nevertheless, with the exception of Argo float 5901162 (which has been grey-listed by the Argo team, but was not confirmed as having been impacted by faulty measurements), none of the Argo floats used in this study is believed to be affected by this temperature bias.

### 6.4.2 Argo Profile Distribution

Although care was taken to maximise the coverage of the Coral Sea when selecting the 42 Argo floats to be used for this project, due to the free-floating nature of Argo floats some bias could not be avoided. Several regions of the Coral Sea (including the continental coast of Queensland, the Queensland Plateau in the northwest, and the Bellona plateau in the central Coral Sea) are characterised by relatively shallow topography (<1000 m). As a result, Argo floats, with their deep parking depth of 1000-2000 m, very rarely entered these areas (cf. Figure 6.2.2). If an Argo floats is blown into shallow waters while they are at the surface transmitting data back to the satellites, they ground out and are often lost (Josh Willis, pers. comm.).

Most floats that entered or passed through the Coral Sea were either deposited in the eastern Coral Sea or in the West Pacific (Figure 6.4.1), and were carried deeper into the Coral Sea by the dominant currents (e.g. South Equatorial Current; Choukroun *et al.*, 2010). Consequently, CTD profiles of the early years are mainly from the eastern part of the Coral Sea. In later years, as the amount of new floats used for this study was gradually reduced (Figure 6.4.2), the bulk of profiles are positioned in the western Coral Sea. The majority of floats (52%) used in this research were deployed into the Pacific or Coral Sea in 2004/2005.

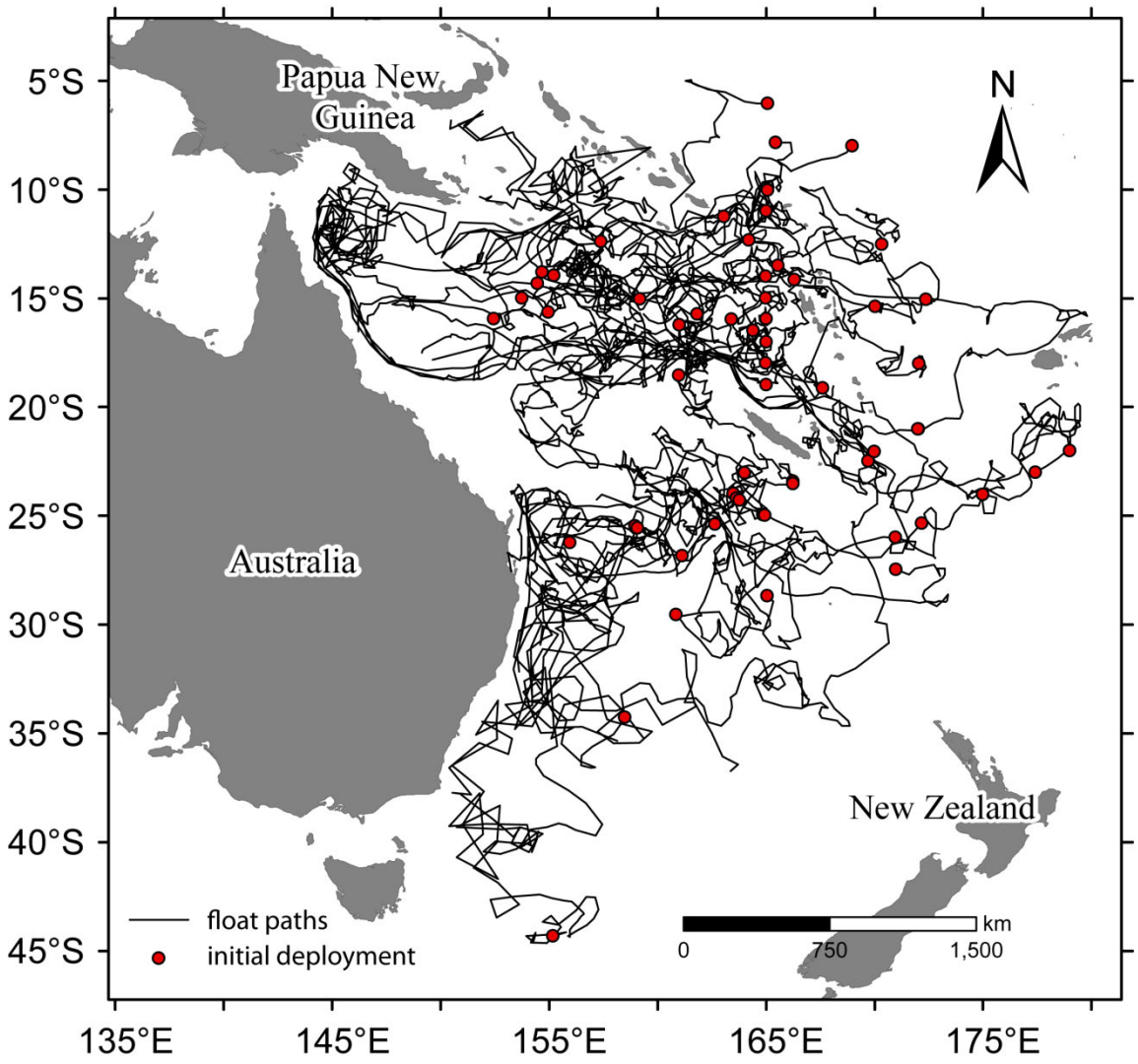


**Figure 6.4.1. Paths of the Argo floats deposited within or near the Coral Sea. Depositions east of the Coral Sea were commonly transported into the Coral Sea by the South Equatorial Current. Subsequently, most floats moved northwards into the Gulf of Papua by the Hiri current, while other floats stopped functioning after being stranded in shallow waters. Additional floats were deposited within the Tasman Sea, and moved northwards towards the southern Coral Sea border (the eddy-rich Tasman front region).**

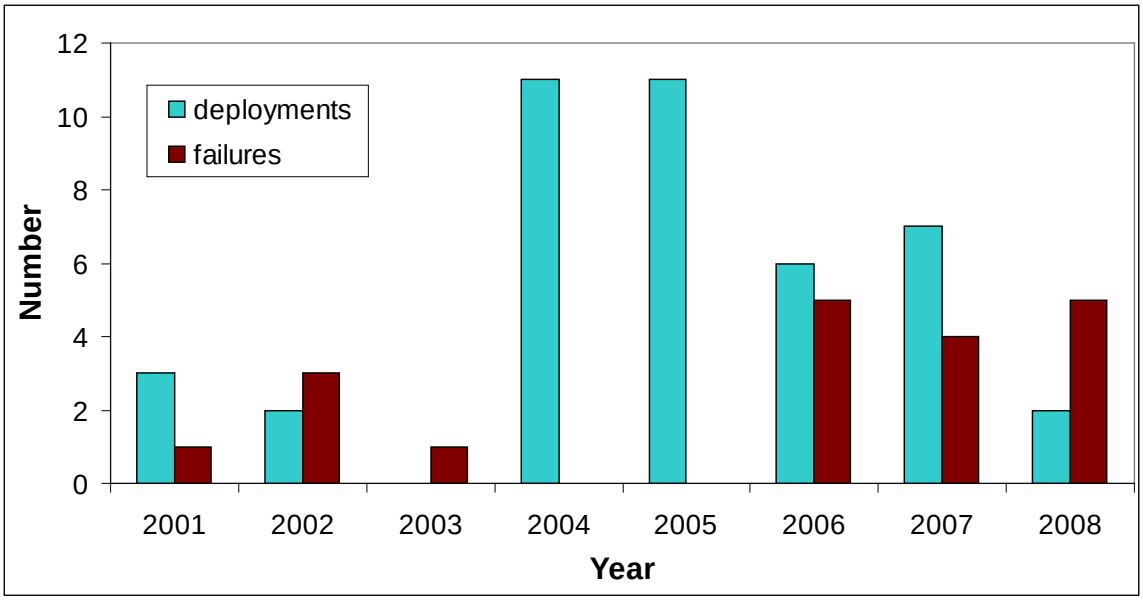


**Figure 6.4.2. Number of new Argo floats used (per year of float deployment) and the total amount of used floats that failed each year. Number of new deployments and failures of Argo floats per year within or nearby the Coral Sea.**

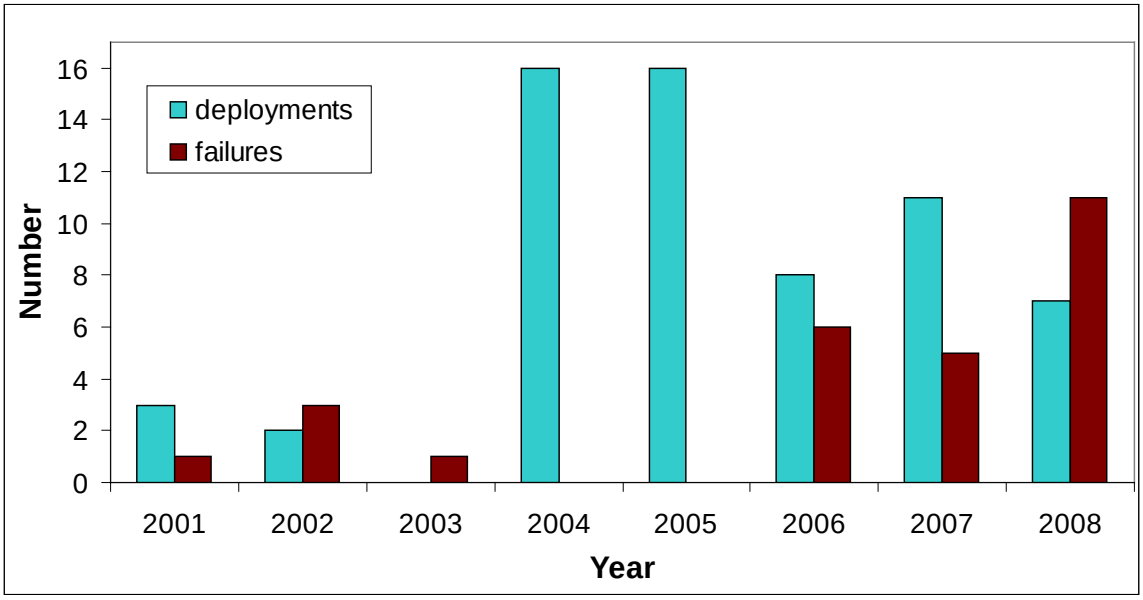


**Figure 6.4.3. Total number of new deployments and failures of Argo floats per year within or nearby the Coral Sea.**

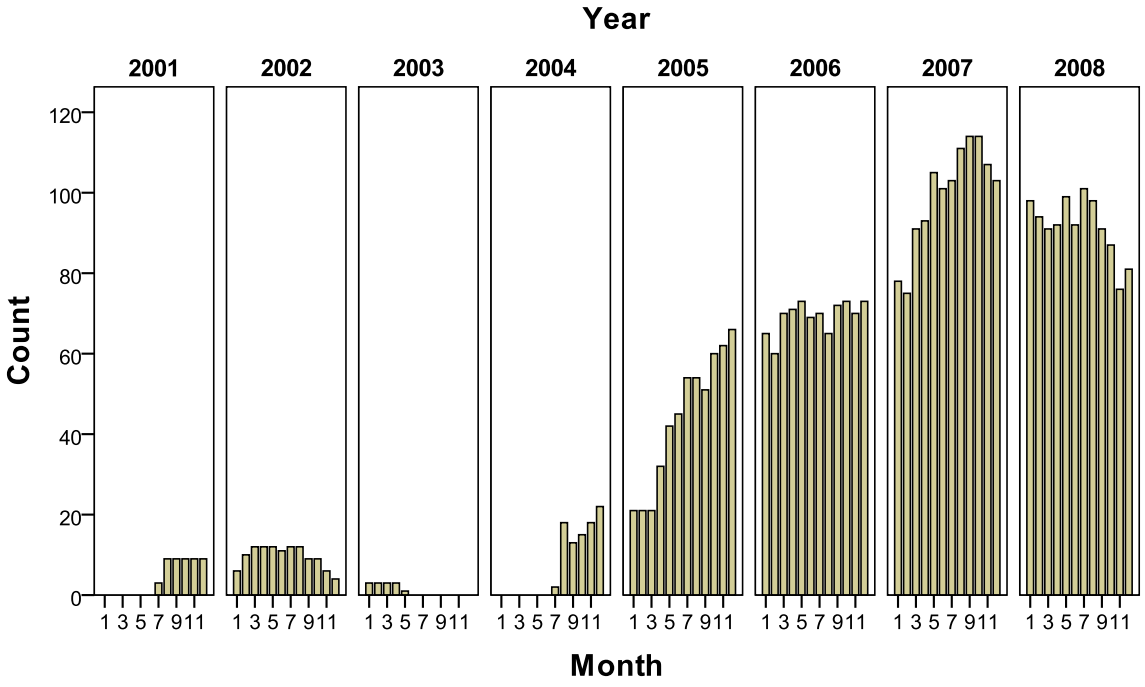


**Figure 6.4.4. Distribution of total number of Argo CTD profiles available within the Coral Sea prior to 2009 (excluding some Argo floats deployed in 2008). On average, each Argo float provides three CTD profiles per month (every ten days).**

Both the number and quality of Argo floats available improved dramatically over time. Prior to 2004, only five Argo floats were deployed within or near the Coral Sea (Figure 6.4.3); and even though a float's current life expectancy is around four years, these early floats had a maximum life of 15 months, resulting in a 1-year gap from mid-2003 to mid-2004 during which no Argo CTD measurements were taken (Figure 6.4.4). After mid-2004, the life of individual floats generally exceeded three years, with many floats (45%) deployed in the Coral Sea and its vicinity in 2004 and 2005 still being operational as of April 2009.

Figure 6.4.5, which illustrates the number of CTD profiles available over time from the 42 Argo floats used, displays a trend towards lower CTD profiles from mid-2007. This decline is partially a reflection of the gradual failure of the Argo floats utilised (cf. Figure 6.4.2), rather than an indication of fewer Argo floats being available in the Coral Sea. About 40% of available Argo floats have been used for this project, of which 62% were still operational as of April 2009.

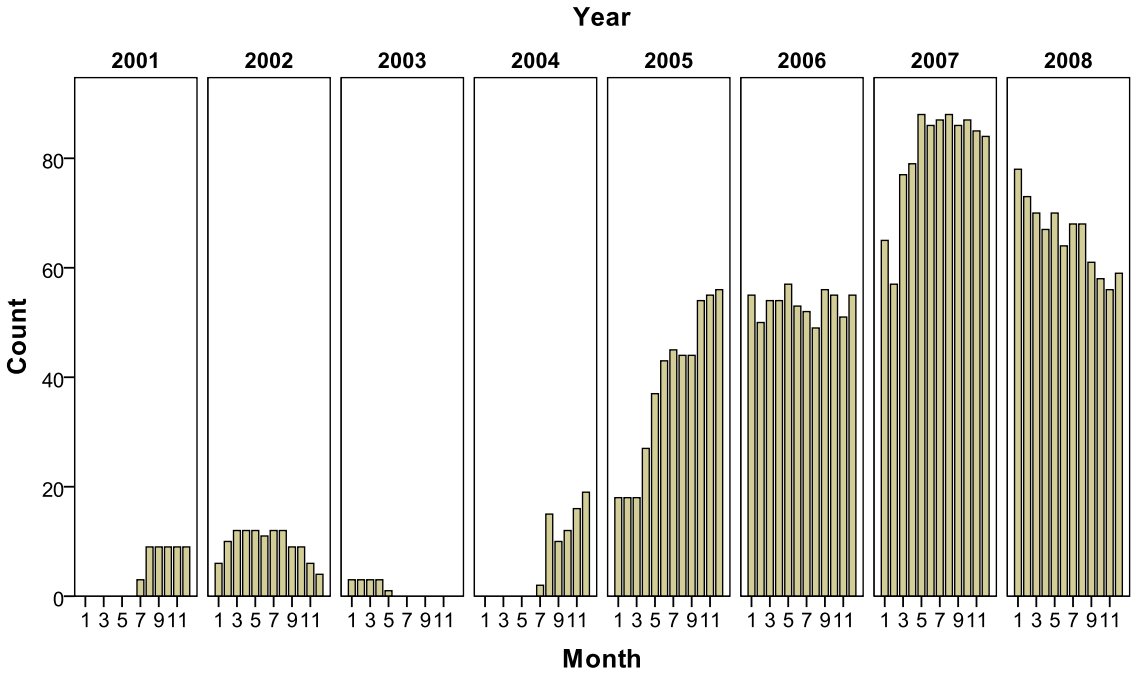


**Figure 6.4.5. Distribution of number of Argo CTD profiles used per month in this study for the MLD analysis. The trend towards lower CTD profiles from mid-2007 does not reflect a decrease in the total number of available profiles. Rather, it is indicative of the gradual demise of the Argo floats used in this study (see also Figure 6.4.2), with most of these floats having been deployed in 2004 and 2005. The mean running time of Argo floats utilised in this project is 31.5 months, with the mean running time for newer floats being significantly higher (>30 months) than floats deployed before 2004 (8 months).**

### 6.4.3 Sampling Trend - Argo versus WOD

The first CTD measurements within the Coral Sea were undertaken in 1982, although the earliest profiles have a relatively low data precision (i.e. the precision of the salinity data is given to two decimal points only). Before 2001, however, data collection was very sparse and often repeated and clustered in small areas (e.g. nearby Brisbane, around New Caledonia and along the Townsville trough. Since their introduction into the Coral Sea in 2001, Argo floats have produced at least as many CTD profiles as all shipboard CTD profiles stored in the World Ocean Database (WOD) over the previous two decades. As a result, more detailed mixed layer analysis is now possible, with the Argo data displaying a much clearer seasonal signal than the pre-Argo period (Figure 6.4.6).

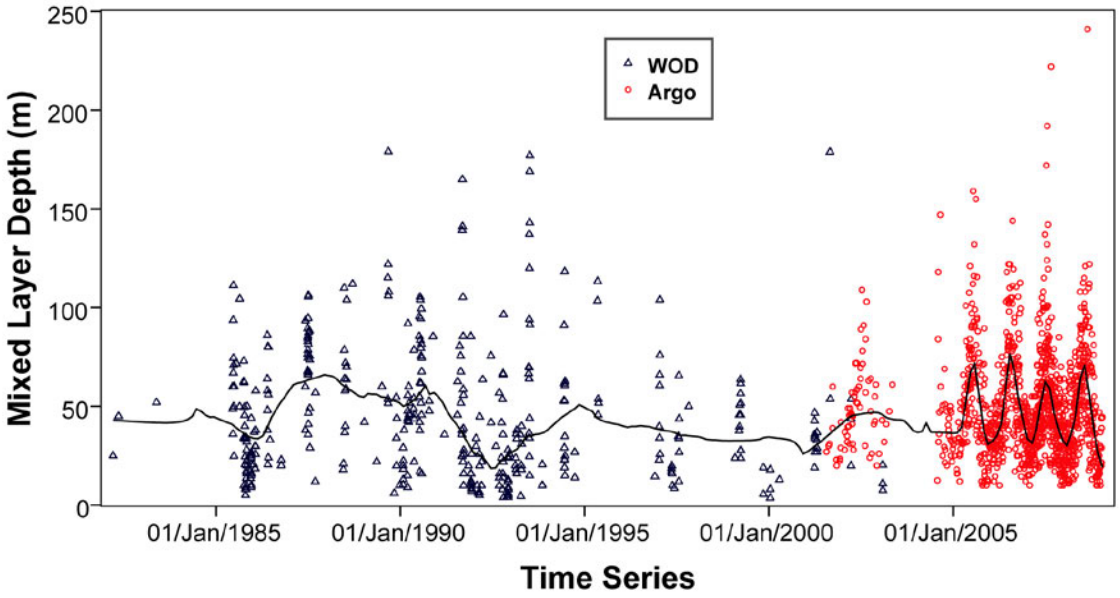


**Figure 6.4.6. Temporal trend of the mixed layer depth (derived with the gradient method) within the Coral Sea since 1982. This figure exemplifies how the post-2003 introduction of Argo floats within the Coral Sea augments the seasonal resolution of MLD variability. Pre-2001 MLDs were derived from CTD profiles of the World Ocean Database (WOD). The 2001-2003 period contains data from both WOD and Argo.**

While the mean observed MLDs agree closely between Argo- and WOD-derived MLDs from January to July, there is a trend evident towards comparatively lower WOD-MLDs from August to December (Figure 6.4.7). This can be ascribed to a combination of scarcity of WOD CTD profiles deep enough to capture thicker mixed layers, and the relative paucity of WOD CTD profiles in general.

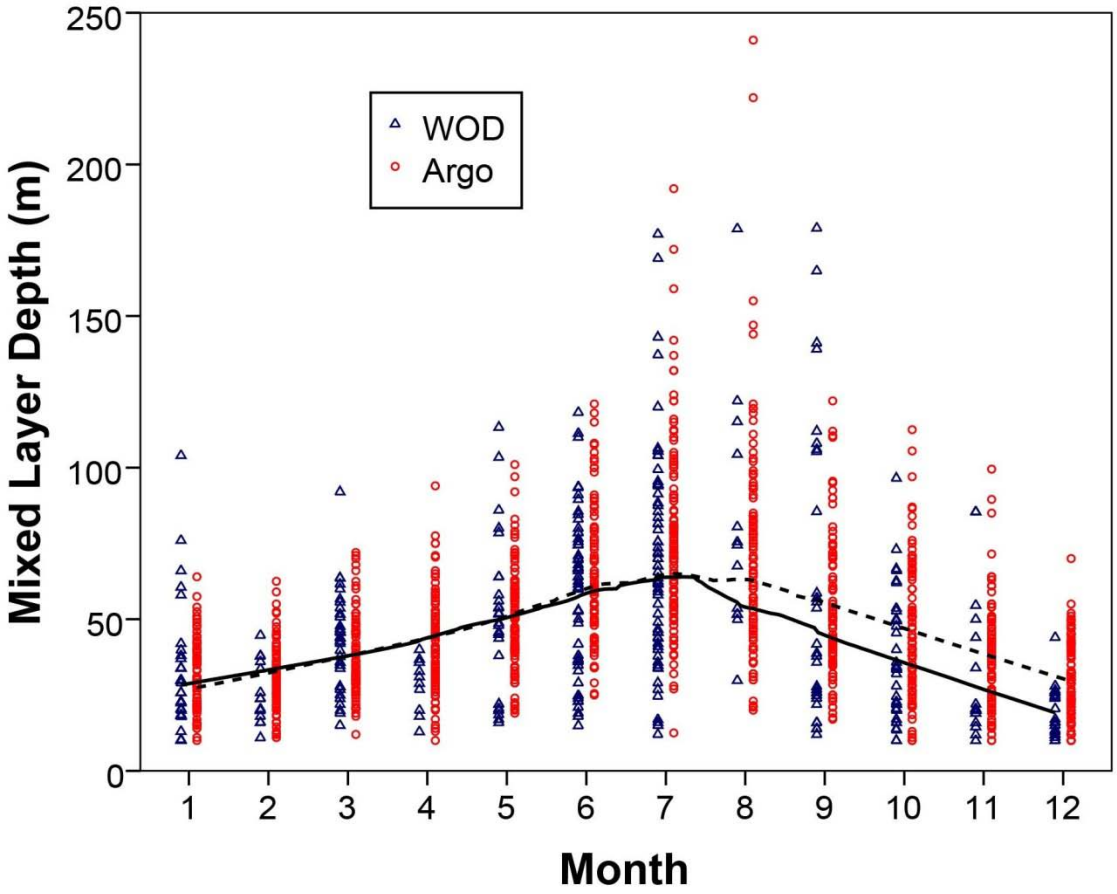


**Figure 6.4.7. Monthly observations of WOD and Argo mixed layer depths ($MLD_{ref}$). For clarity, data are shown in monthly groups, slightly offset, rather than in Julian days. A trend towards deeper winter mixed layers is evident in both datasets. The line of best fit (solid-black for WOD, dashed-grey for Argo) was created using the Loess method.**

### 6.4.4 Suitability of the Threshold Method

Within the Coral Sea, there is some trend evident that the values suggested by de Boyer Montégut *et al.* (2004) commonly results in an overestimation of the actual ILD (Figure 6.4.8B). Conversely, the MLD displays a slight tendency to being underestimated rather than overvalued (Figure 6.4.8A), especially for relatively shallow MLDs. To determine the most accurate threshold value, four values have been applied to both temperature and density profiles.

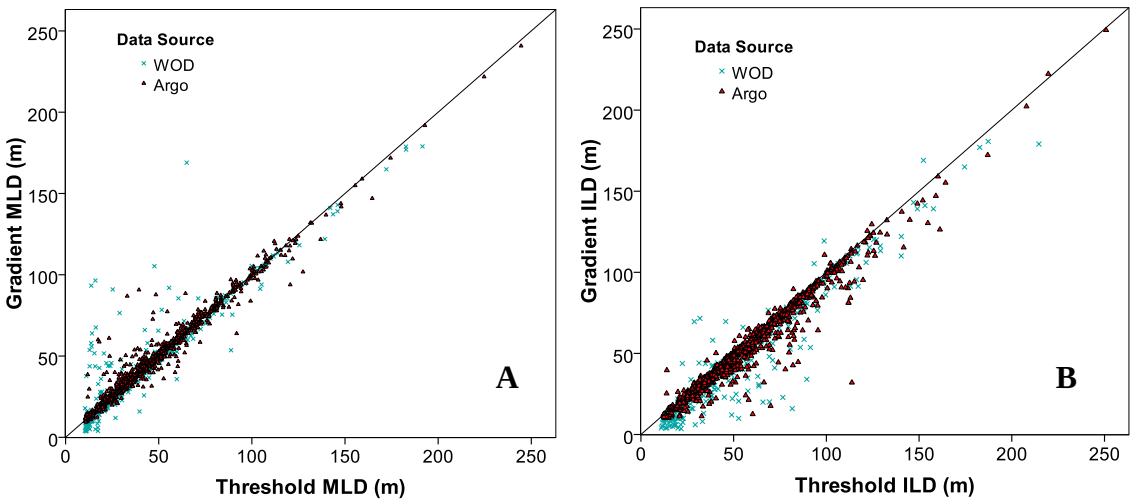


**Figure 6.4.8. Intercomparison of A) MLDs and B) ILDs obtained with the threshold (x-axis) and gradient method (y-axis). Threshold values suggested by de Boyer Montégut *et al.* (2004) were used ($\Delta\rho$ = 0.035 kg/m$^3$ and $\Delta T$ = 0.2°C). Whereas the MLDs based on the threshold and gradient method (A) are roughly equally distributed along either side of the diagonal axis, the two methods show a significant bias towards too deep ILD values (B) when the threshold method is applied.**

The statistical analysis of the MLDs and ILDs, derived from the four different threshold values, is shown in Table 6.4.1. In general, the MLDs (0.03 kg/m$^3$) and ILDs (0.2°C) obtained using the threshold method with values proposed by de Boyer Montégut *et al*. (2004) compare quite well with the reference MLDs (± 3 m) and ILDs (±5 m). In the case of the MLD, however, a threshold value of 0.035 kg/m$^3$ appears to be more accurate in determining the estimated MLD (Table 6.4.1b), based on the lowest standard deviation ($\sigma$ = 6.43), highest correlation (r = 0.97) and lowest mean difference (2.44). The statistical results for the ILD are more complex (Table 6.4.1a). The lowest standard deviation ($\sigma$ = 5.96) and highest correlation (r = 0.98) are attributable to $\Delta T$ = 0.2°C, whereas the lowest mean difference (2.79) is linked to $\Delta T$ = 0.1°C. There are advantages and disadvantages to both threshold values. Whereas threshold values in excess of 0.1°C have a tendency to overestimate the ILD, resulting in higher mean differences, $\Delta T$ = 0.1°C is less suitable for temperature profiles affected by restructuring (e.g. diurnal variability reaching depths in excess of 10 m). A threshold value of 0.1°C (and to a certain extent $\Delta T$ = 0.15°C) is predisposed to significantly underestimate the ILD when

the isothermal layer is not well defined, consequently exhibiting a lower correlation ($r = 0.96$) and a higher standard deviation ($\sigma = 8.041$). Overall, assuming that the temperature profiles are not thoroughly pre-screened and profiles with poorly defined isothermal layers removed, a threshold value of 0.2°C for temperature profiles is the most appropriate for this region. A similar analysis of salinity profiles indicates that a threshold value of 0.02 psu most accurately predicts the isohaline layer depth.

**Table 6.4.1. Mean differences, standard deviation for paired differences (in parentheses), as well as Pearson correlations between a) isothermal layer depths (ILD) and b) mixed layer depths (MLD) as obtained by visual inspection ($ILD_{ref}$ and $MLD_{ref}$) and with four different threshold values.**

a)

| ILD (m) | $ILD_{ref}$ | 0.1 | 0.15 | 0.2 |
|---|---|---|---|---|
| **0.1** | 2.79 (8.04) / 0.96 | | - | - |
| **0.15** | 3.16 (7.08) / 0.97 | 1.90 (2.80) / 1.00 | | - |
| **0.2** | 3.93 (5.96) / 0.98 | 3.46 (6.82) / 0.97 | 1.57 (4.73) / 0.99 | |
| **0.25** | 5.09 (6.90) / 0.97 | 4.79 (7.62) / 0.96 | 2.90 (5.53) / 0.98 | 1.32 (2.00) / 1.00 |

b)

| MLD ($kg/m^3$) | $MLD_{ref}$ | 0.025 | 0.03 | 0.04 |
|---|---|---|---|---|
| **0.025** | 3.15 (8.13) / 0.95 | | - | - |
| **0.03** | 2.6 (7.18) / 0.96 | 0.99 (2.34) / 1.00 | | - |
| **0.035** | 2.44 (6.43) / 0.97 | 1.79 (5.40) / 0.98 | 0.80 (3.79) / 0.99 | |
| **0.04** | 2.51 (7.73) / 0.96 | 2.46 (8.49) / 0.95 | 1.48 (7.16) / 0.97 | 0.68 (3.51) / 0.99 |

Factors which impact on the accuracy of the threshold method include heavy precipitation, and the strong diurnal variability in wind mixing and temperature in localised areas. Their influence sporadically extends beyond the reference depth, forming a temporary mixing layer (region in which mixing is currently active; cf. Brainerd and Gregg, 1995) which may be mistaken for the mixed layer. Even though a reference depth of 10 m is chosen to avoid the short-term variability, sometimes an underestimation of the MLD occurs due to diurnal solar heating or heavy precipitation affecting depths down

to 15-20 m. For these profiles, the MLD (and ILD) is much more accurately determined by choosing 20 m (or 15 m, if appropriate) as the reference depth. This reference depth, however, cannot be chosen universally since at least summer mixed layers, at least, are frequently shallower than 20 m and can even be as shallow as ~10 m, in which case the method with a reference depth of 10 m would unavoidably result in an overestimation of the MLD and ILD.

## 6.5 Summary – Physical Oceanography

An evaluation of four different threshold values for both temperature and density profiles revealed the extent of suitability of the threshold method for the Coral Sea. Due to the general absence of compensating and barrier layers, the threshold method predicts the ILD ($\Delta T = \pm 0.2°C$) and MLD ($\Delta\rho = 0.035$ kg/m$^3$) reasonably well in this region. Discrepancies mainly occur when short-term sea surface variability (e.g. diurnal heat flux or intense rainfall) extends beyond 10 m depth, or when the ILD and/or MLD are not well defined due to restructuring of the upper ocean.

Analysis of 7.5 years worth of CTD data derived from Argo floats displays a strong seasonality in the MLD throughout the Coral Sea. As a result of larger seasonal variation in temperature and wind stress, MLDs in higher latitudes (20-30°S) exhibit a greater seasonality (10-150 m) compared to those of the tropical area of the Coral Sea (10-90 m). While summer mixed layers are relatively homogeneously shallow (10-50 m) throughout the Coral Sea, winter mixed layers in higher latitudes tend to be significantly deeper (70-140 m) compared to tropical regions (40-90 m).

Multi-decadal MLD trends are not discernible in the WOD and Argo MLD dataset. This absence of evidence of a multi-decadal MLD change may be due to the lower data coverage prior to the Argo project rather than a genuine signal that the mean monthly MLD within the Coral Sea remained constant over the last few decades.

Although not commonly detected in the Argo profiles, barrier layers are formed throughout the year and can be observed anywhere within the Coral Sea. The north-eastern Coral Sea has the highest barrier layer density, which is most likely linked to high precipitation rates during all seasons. Salinity inversions, in turn, are mainly found in the southeast, a turbulent region affected by the eddy-rich Tasman front.

The OHC of the top 250 m displays a latitudinal gradient in most regions. The north-western Coral Sea, a zone affected by the clockwise moving Hiri current, is the main area displaying a strong influence on Argo data by a current, with cooler water mass being transported northwards. Conversely, there are few effects evident by the EAC due to the shallow continental shelf inhibiting movement of Argo floats along the path of the EAC.

The Argo floats program represents a significant advancement for marine studies. Procuring near-continuous CTD data within the Coral Sea since mid-2001, Argo will enable more detailed studies on long-term variability and trends of the MLD and its associated impact on the photic zone and the Great Barrier Reef. At this stage, however, the available CTD data is not sufficient yet to verify whether the upper ocean within the Coral Sea is affected by increases in heat content and/or a thinning of the MLD, both of which is expected to occur in many regions.

# 7 Geochemical Patterns within the Coral Sea

To this date, there has been surprisingly little effort to monitor the changes in biogeochemistry within the Coral Sea. The aim of this chapter is to gain insights into current patterns, and determine seasonal and longer trends in carbon chemistry within the Coral Sea. Here, all available observational marine carbon data (chiefly $fCO_2$ and $p$H) is presented and analysed, with the data reviewed in this chapter derived from various observational sources, including the World Ocean Database and the Carbon Dioxide Information Analysis Center.

## 7.1 Introduction

Although the ocean as a sink for anthropogenic $CO_2$ from the atmosphere has received a lot of attention and has been studied throughout the major ocean basins, not many ship cruises have measured $CO_2$ levels in the Coral Sea. One notable exception is the study by Suzuki *et al.* (2001), in which the $CO_2$ fugacity in the Great Barrier Reef region was examined. They found that $fCO_2$ within the GBR lagoon displayed significantly higher levels, presumably due to $CO_2$ release by calcification of corals, coralline macroalgae and planktonic organisms (cf. section 4.5.1), than in the open ocean.

The present study involves the collection of all available Coral Sea $fCO_2$-related data in literature and online databases, and their analysis for seasonal and long-term trends in changes in sea surface $fCO_2$. A further aim is to evaluate whether the Coral Sea currently acts as a sink of atmospheric $CO_2$.

### 7.1.1 Atmospheric $CO_2$

Observations of atmospheric $CO_2$ content are essential to determine the state and trends of the oceanic carbon cycle. The atmospheric $CO_2$ concentration ultimately also controls the extent and direction of $CO_2$ uptake by the world's oceans.

Atmospheric $CO_2$ has been directly monitored since early 1958, with the longest - and still ongoing - time series available from the station in Mauna Loa, Hawaii (e.g. Keeling *et al.*, 1995). Due to the large ratio of (atmospheric $CO_2$ fluxes)/(atmospheric $CO_2$ reservoir), $CO_2$ has a relatively short residence time (6-8 years) in the atmosphere

(Sarmiento and Gruber, 2006: p. 392) and is comparatively well-mixed throughout the atmosphere. This residence time is not to be confused with the time (>>400 years; cf. Figure 10.2.3 of Sarmiento and Gruber, 2006) required for the atmosphere to adjust to a new equilibrium, or to return to its initial state, if the equilibrium is perturbed, as is currently the case with anthropogenic $CO_2$.

Some regional differences are occurring due to a 6-month lag of the sea-air exchange of $CO_2$ (Sarmiento and Gruber, 2006: p. 300). As a result, the atmospheric $CO_2$ concentrations in the southern hemisphere tend to be slightly lower than in the northern hemisphere (cf. Fan *et al.*, 1999: Fig. 1), the source of most anthropogenic $CO_2$. The atmospheric $CO_2$ concentration also displays seasonal cycling due to atmospheric $CO_2$-drawdown as a result of seasonal variability in photosynthesis of terrestrial biota (Doney *et al.*, 2006), with minima in atmospheric $CO_2$ concentration generally occurring in late summer/early autumn and maxima in late winter/early spring (Pearman and Beardsmore, 1984; Thoning *et al.*, 1989; Tans *et al.*, 1990: Fig. 4). The amplitude of the seasonal variability in atmospheric $CO_2$ greatly depends on the latitude and hemisphere, with more pronounced seasonality being noted in the northern hemisphere (as a result of greater landmass) and low seasonality at mid-latitudes in the southern hemisphere (Thoning *et al.*, 1989; Francey *et al.*, 1995; Keeling *et al.*, 1995; Manning *et al.*, 2003). Thoning *et al*. (1989) determined a mean seasonality of 6.77 ± 0.32 ppm at Mauna Loa from 1974 to 1985, with the amplitude increasing by about 0.05 ppm each year. Pearman and Beardsmore (1984), in turn, measured a seasonal amplitude of around 1.2 ppmv in the mid-troposphere over the Australian and New Zealand region from 1972 to 1981, with highest $CO_2$ concentrations occurring in October and minima during April.

## 7.2 Methods

### 7.2.1 Data Sources

Most of the physical and geochemical sea surface data used in this study was obtained from the Carbon Dioxide Information Analysis Center (CDIAC), with some additional data (mainly *p*H) deriving from the World Ocean Database (WOD, http://www.nodc.noaa.gov) and from the Japanese Oceanographic Data Center (JODC, http://www.jodc.go.jp).

### 7.2.2 CO2SYS

Most of the WOD data had a very limited number of carbonate system parameters. However, some WOD profiles included *p*H, total alkalinity (TA) and/or total dissolved inorganic $CO_2$ ($tCO_2$, which is the sum of dissolved $CO_2$, bicarbonate and carbonate). In such cases, the freely available CO2SYS program (Lewis and Wallace, 1998) was used to obtain the missing carbonate system parameters such as $fCO_2$ and $pCO_2$. CO2SYS requires temperature and salinity, as well as at least two of the following geochemical parameters to be able to calculate the missing values: $tCO_2$, *p*H, TA, $fCO_2$ and $pCO_2$. CO2SYS also provides estimates for saturation state ($\Omega$) of aragonite and calcite.

CO2SYS can be used for both single and batch inputs. For this study, the single input option was initially employed to investigate the relative importance and influence of the various carbonate system parameters on changes in marine chemistry. The batch-input mode, in turn, was utilised to obtain the missing carbonate system parameters.

To successfully run CO2SYS in the batch mode, the program requests the input to be given in a specific order and saved as a comma-separated values (csv) file. The following data fields (in that order) are always required for each sample of the input file:

- ID fields
- salinity [PSS]
- total phosphate [µmol/kg] (often 0 µmol/kg)
- total silicate [µmol/kg] (often 0 µmol/kg)
- input temperature [°C]
- input pressure [dbar] (normally 0 dbar)
- output temperature [°C] (usually chosen to be equal the input temperature)
- output pressure [dbar] (normally 0 dbar)
- 1$^{st}$ known $CO_2$ system parameter
- 2$^{nd}$ known $CO_2$ system parameter

The two known $CO_2$ system parameters also follow a specific order:

- TA [µmol/kg] (always first if used)
- $tCO_2$ [µmol/kg]
- *p*H
- $fCO_2$ (or $pCO_2$) [µatm] (always last if used)

In general, $fCO_2$ and $pCO_2$ are comparable to each other. However, unlike $pCO_2$, $fCO_2$ is also taking into account the non-ideality of $CO_2$ as a gas (Le Borgne *et al.*, 2002). Consequently, $fCO_2$ tends to be lower than $pCO_2$ by about 1-1.5 µatm (or by 0.3-0.4%) in equatorial surface waters (Le Borgne *et al.*, 2002).

### 7.2.3 $CO_2$ Solubility

In cases where the only available geochemical parameter is the mole fraction of $CO_2$ ($xCO_2$), the following equation was used to obtain $pCO_2$:

$$pCO_2sw = xCO_2 \cdot p_{atm} \cdot (1 - pH_2O)$$

where $xCO_2$ is the mole fraction of $CO_2$ in water, $p_{atm}$ is pressure [atm] and $pH_2O$ is the partial pressure of water vapour. $pH_2O$, if not measured, can be obtained using both temperature [K] and salinity [PSS]:

$$pH_2O = e^{(24.4543-6745.09/T-0.000544\times S)\times(T/100)\text{^}(-4.8489)}$$

The solubility of $CO_2$ can be calculated using Henry's Law [$F = s\cdot(\Delta pCO_2)_{sea-air}$], where s is the solubility coefficient of $CO_2$ in seawater (mol $kg^{-1}$ $atm^{-1}$):

$$s = (T/100)^{23.3585} \cdot e^{(9345.17/T-60.2409+S\cdot(0.023517-0.00023656\cdot T+0.0047036\cdot(T/100)^2))} \quad (1)$$

where T is temperature in Kelvin (K) and S is salinity in practical salinity scale (PSS) (Weiss, 1974). K is sometimes also referred to as Henry's Constant (H).

### 7.2.4 $fCO_2$

The change in partial pressure of $CO_2$ ($pCO_2$) is a function of change in temperature, salinity, total alkalinity and $tCO_2$, and can thus be described with the following thermodynamic equation:

$$dpCO_2 = \left(\frac{\partial pCO_2}{\partial T}\right)dT + \left(\frac{\partial pCO_2}{\partial tCO_2}\right)dtCO_2 + \left(\frac{\partial pCO_2}{\partial TA}\right)dTA + \left(\frac{\partial pCO_2}{\partial S}\right)dS$$

where $pCO_2$ = partial pressure of $CO_2$ in seawater; T = temperature, $tCO_2$ = total $CO_2$ concentration in seawater; TA = total alkalinity in seawater; and S = salinity. The change in fugacity of $CO_2$ ($fCO_2$) can be described with an analogous equation. The exact association of all the above parameters is varying both in space and time.

To inter-compare the seasonal and spatial variability of $fCO_2$ derived from multiple years, all $fCO_2$ data was normalised to the year 2001. This was achieved by linking observed atmospheric $fCO_2$ data from the Coral Sea from a given month and year to the respective atmospheric $CO_2$ value at Cape Ferguson, Queensland, Australia (19.28°S, 147.06°E, 2 m above MSL). Since the atmosphere behaves nearly as an ideal gas, $fCO_2$ (μatm) can be considered equivalent to $CO_2$ (ppmv).

The atmospheric $CO_2$ concentration data from Cape Ferguson, gathered by Commonwealth Scientific and Industrial Research Organisation (CSIRO), is derived from the GLOBALVIEW-$CO_2$ database (2006). $CO_2$ measurements at Cape Ferguson were undertaken since July 1991 (Steele *et al.*, 2007), with interpolated $CO_2$atm going back to 1979, and the data are freely accessible (via anonymous FTP to ftp.cmdl.noaa.gov, Path: ccg/co2/GLOBALVIEW). The average annual increase of atmospheric $CO_2$ at Cape Ferguson has been 1.67 ppmv since 1979.

The value of each (ocean and atmosphere) pair of Coral Sea $fCO_2$ measurements was increased by the difference of that year and month's Cape Ferguson value relative to the 2001 value of atmospheric $CO_2$ of the month of interest:

$$fCO_{2\,\mathrm{Coral(2001\text{-}month)}} = fCO_{2\mathrm{Coral(year\text{-}month)}} + [\,fCO_{2\mathrm{Cape(2001\text{-}month)}} - fCO_{2\,\mathrm{Cape(year\text{-}month)}}\,]$$

where $fCO_{2\mathrm{Cape(2001\text{-}month)}}$ and $fCO_{2\mathrm{Cape(year\text{-}month)}}$ refer to the average Cape Ferguson $CO_2$ value of the month (and year) of interest.

## 7.3 Results - Coral Sea Geochemistry

### 7.3.1 *p*H characteristics

*p*H data within the Coral Sea is relatively scarce, with WOD containing the largest dataset. Its Coral Sea *p*H data is mainly concentrated offshore in the open ocean (Figure 7.3.1), with very little *p*H data available on the Queensland continental shelf (mainly nearby the city of Brisbane).

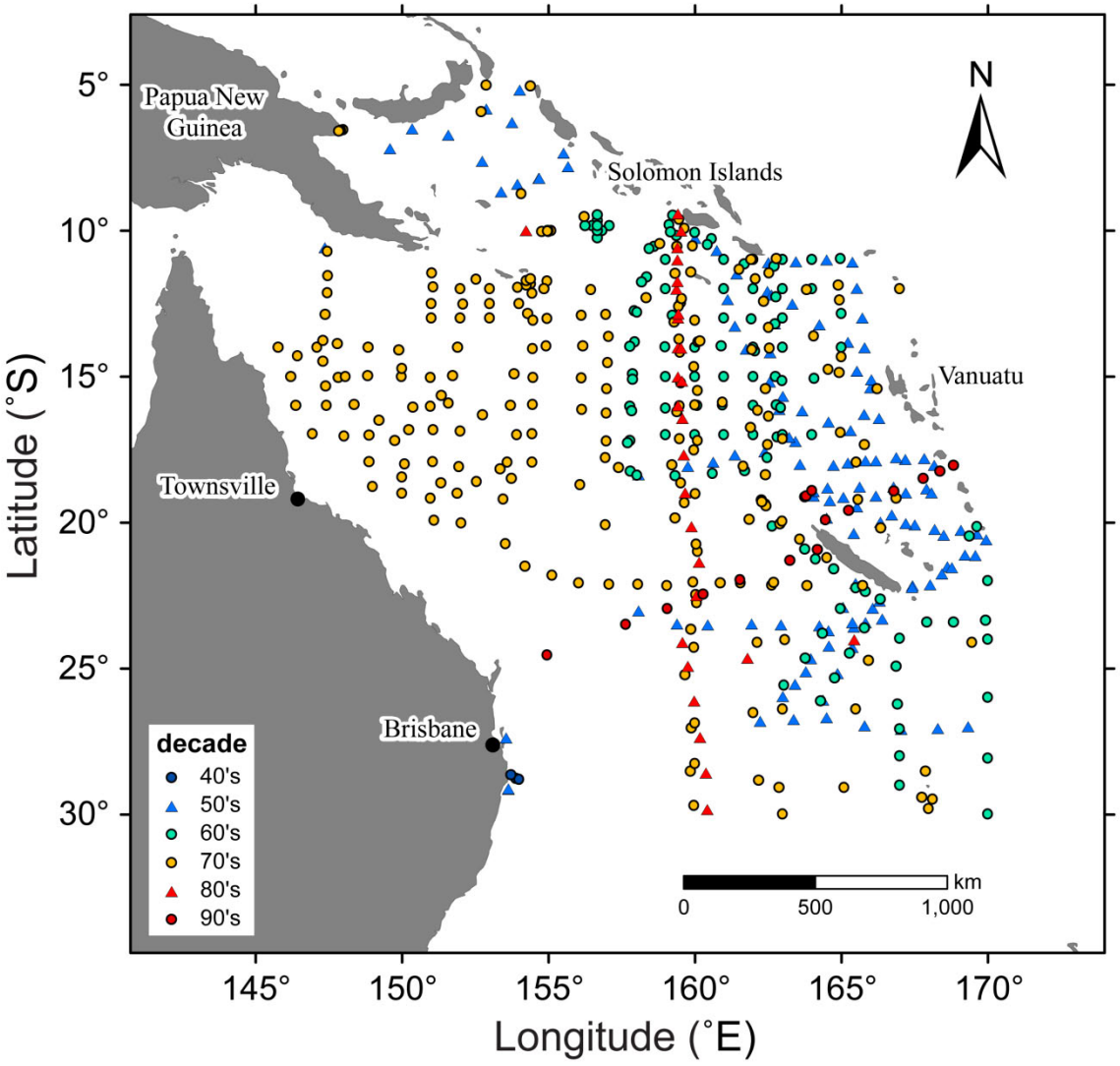


**Figure 7.3.1. Spatial distribution of *p*H measurements within the Coral Sea and Solomon Sea. All available surface data was included, with the data obtained from the World Ocean Database. The colour scheme relates to the decade the data was gathered.**

The first available *p*H data derive from the year 1942. Since then, sampling was undertaken very sporadically (Figure 7.3.2). Early measurements were mainly gathered in the eastern Coral Sea and the Solomon Sea, with a gradual shift of sampling focus towards the western Coral Sea during the 1970s (Figure 7.3.1). The vast majority (79.7%) of *p*H measurements were not supplemented with any additional geochemical parameters. The remaining 20.3% contain total alkalinity and/or $tCO_2$, in which case the missing $CO_2$-related parameters were obtained with the CO2SYS program (see also appendix A3 for a sensitivity analysis).

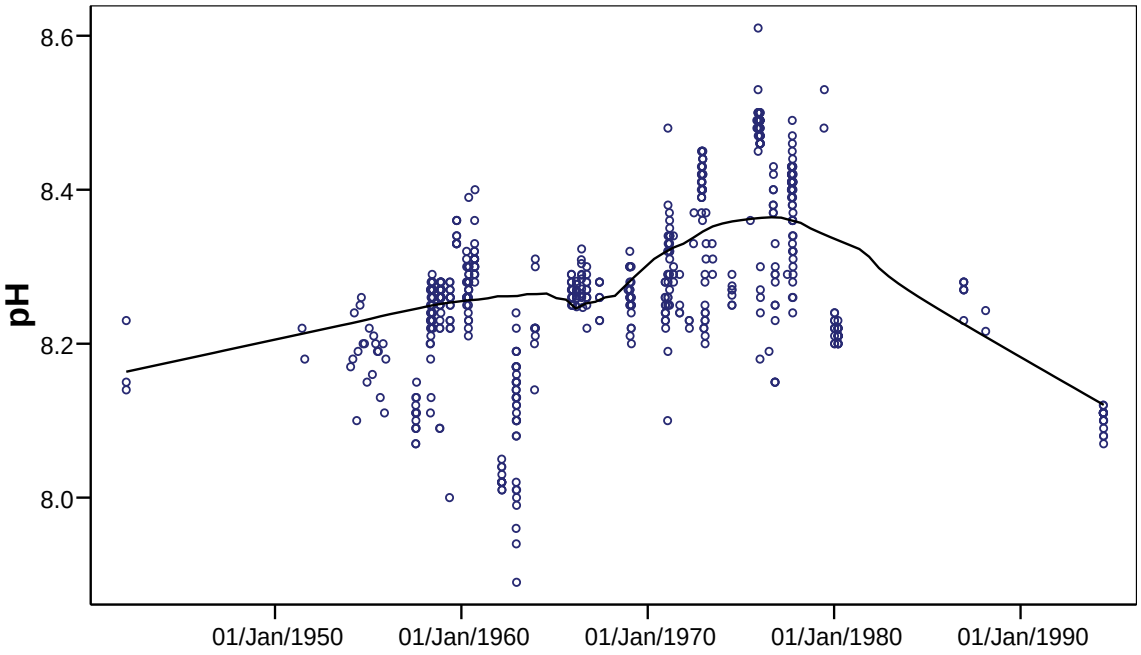


**Figure 7.3.2. Temporal trend of *p*H sampling undertaken within or in close proximity of the Coral Sea since 1942.**

There is a clear trend towards higher *p*H visible towards the western Coral Sea in Figure 7.3.3. Interestingly, this trend seems to contradict a relatively recent publication (Pelejero *et al.*, 2005: Fig. 1), in which present mean annual surface *p*H displays a clear tendency towards lower *p*H westward. All decades showing a spatial trend in WOD *p*H exhibit either a decline eastward, or northward into the Solomon Sea.

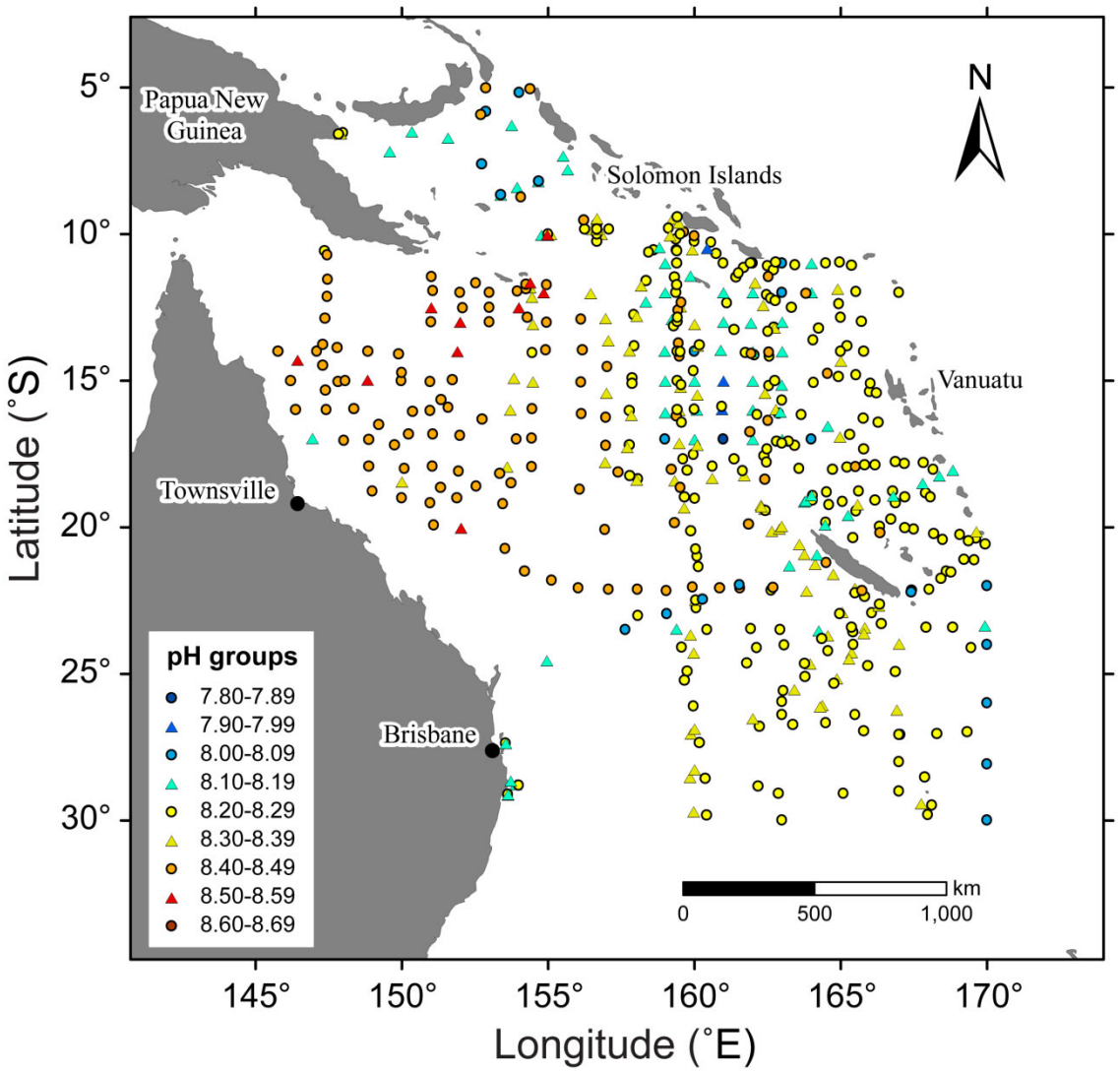


**Figure 7.3.3. Spatial distribution of *p*H data, with the colour scheme denoting the range of *p*H values.**

Within the Coral Sea, the available *p*H does not display any correlation with latitude, nor does the data demonstrate a diurnal rhythm. There is, however, a relatively clear seasonal signal evident (Figure 7.3.4), with highest *p*H values registered during austral summer. Nevertheless, minimum *p*H values show a bimodal signal, with austral spring and autumn displaying higher minimum values than winter and summer. The greatest data spread is observed during summer (December-January), which could be linked to greater primary productivity (increasing *p*H) and higher temperatures (lowering *p*H).

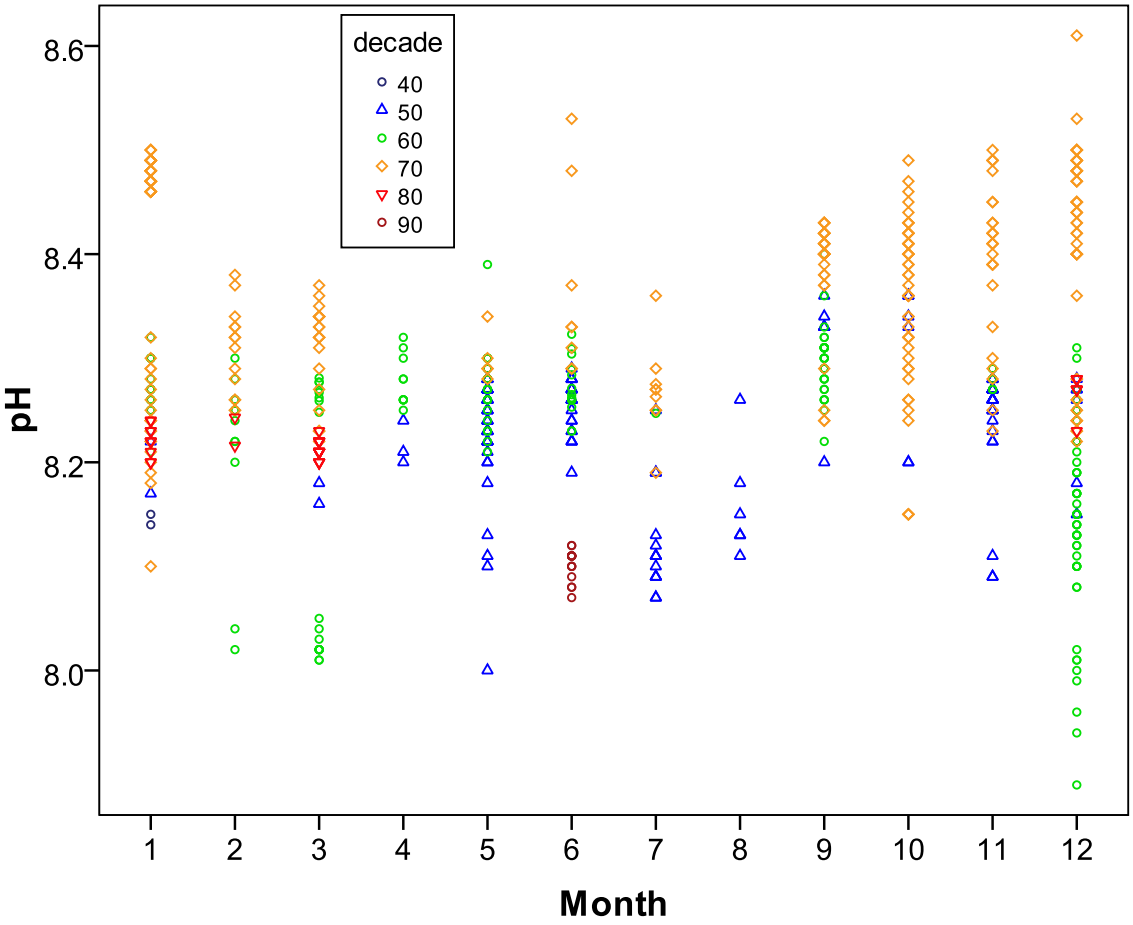


**Figure 7.3.4. Seasonality of *p*H. Colour scheme as in Figure 7.3.1.**

## 7.3.2 Temporal Distribution and Proportions of Carbonate Species

Within the Coral Sea, the output from CO2SYS based on observational WOD data (with *p*H varying from 8.07 to 8.36) indicates that around 0.23-0.55% of $tCO_2$ remains as $CO_2^*$ ($CO_{2aq}$ + $H_2CO_3$), while most dissociates into $HCO_3^-$ (78-88%) and $CO_3^{2-}$ (12-22%). These values differ a little from the carbonate species distribution found at *p*H of 8.2 ($CO_2^*$ < 1%, $HCO_3^-$ ~ 90% and $CO_3^{2-}$ ~ 9%) (cf. Kleypas *et al.*, 1999a; Wolf-Gladrow *et al.*, 1999). *p*H within the Coral Sea frequently reaches 8.3, resulting in higher proportions of $CO_3^{2-}$ and a lower fraction of $HCO_3^-$. Independent of whether the carbonate species distribution has been calculated using *p*H-tAlk or *p*H-$tCO_2$ as predictor variables, $CO_2^*$ displays the strongest correlation with *p*H ($R^2$ = 0.95). $CO_2^*$ exhibits a minor quadratic relationship with *p*H, with 0.45-0.55% of $tCO_2$ being converted to $CO_2^*$

at *p*H values of ~8.1, and 0.25-0.35% of $tCO_2$ remaining as $CO_2^*$ at *p*H values exceeding 8.2 (Figure 7.3.5).

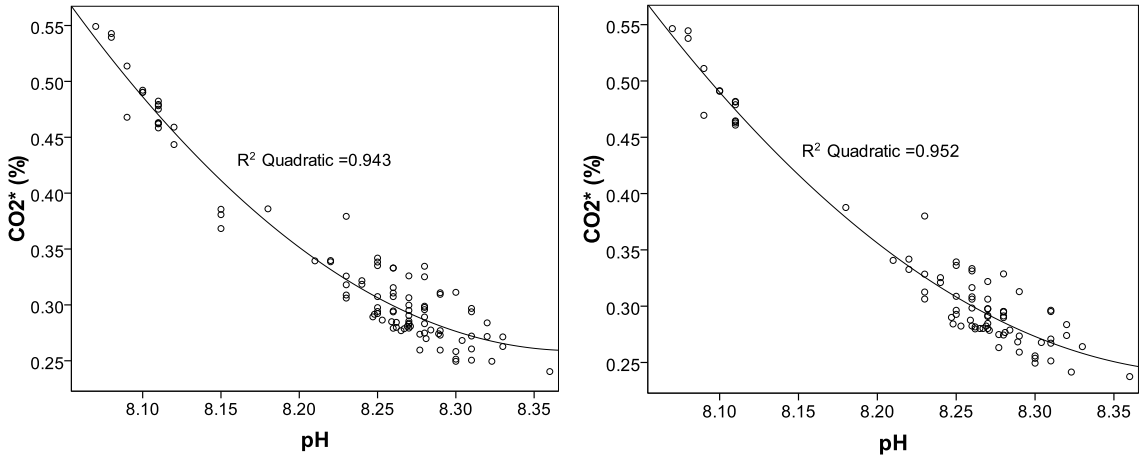


**Figure 7.3.5. Relationship between *p*H and percentage of DIC species remaining as $CO_2^*$ ($CO_{2aq}$ + $H_2CO_3$), with a) *p*H-tAlk and b) *p*H-$tCO_2$ used as predictor variables. As *p*H declines, the oceanic $CO_2$ content is expected to increase.**

There were only six years for which sufficient data was available to derive the time-dependent carbonate species distribution and $fCO_2$ (Figure 7.3.6). Most measurements containing *p*H (the most commonly measured chemical parameter) did not include any additional parameters required for the carbonate species derivation. In addition, early data from 1958 very frequently did not include salinity and temperature, resulting in their removal from further analysis.

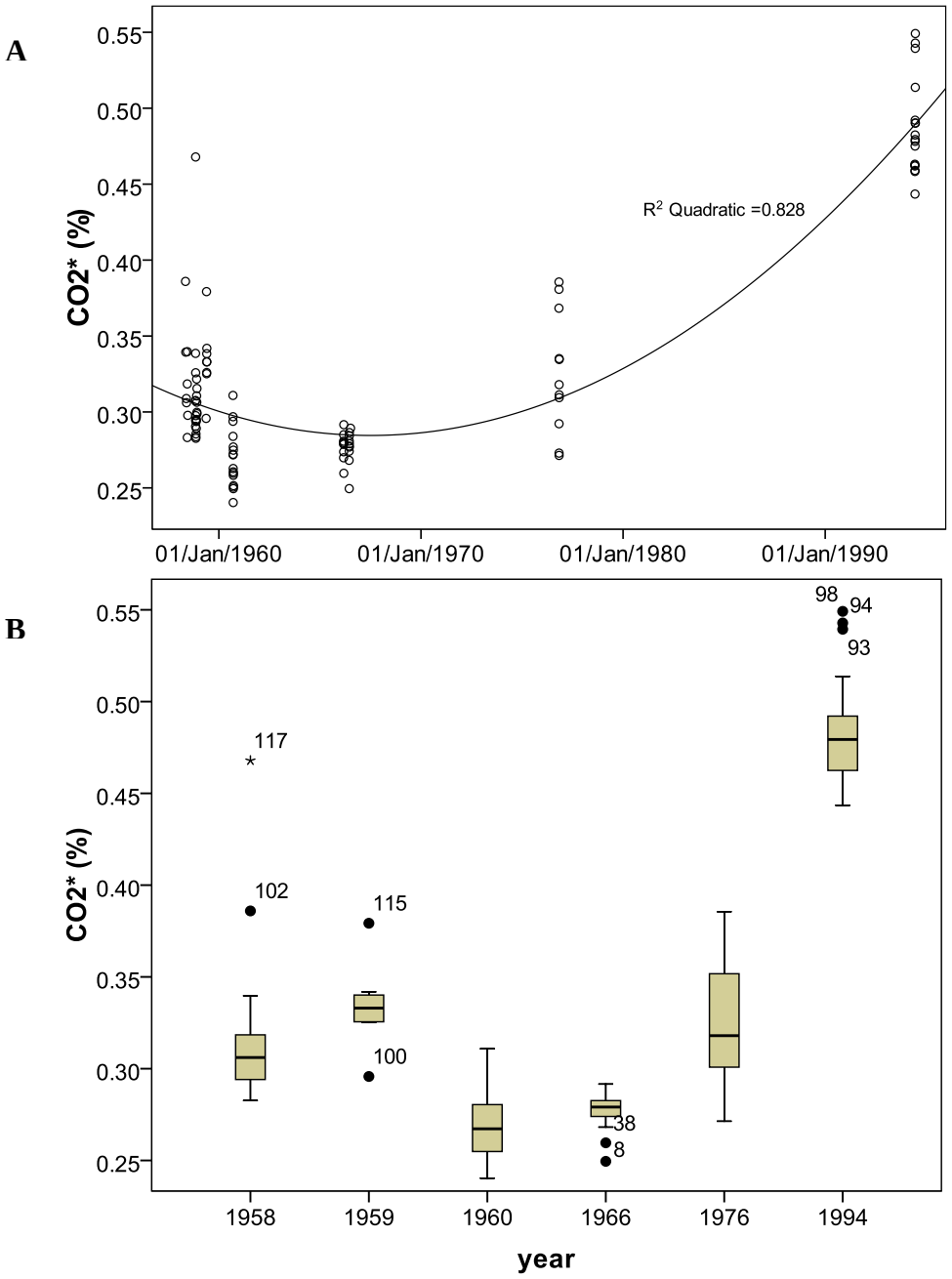


**Figure 7.3.6. A) Scatterplot and B) boxplot of percentage of $CO_2^*$, calculated using CO2SYS for the six available years for which chemical data was obtainable for at least 2 different carbon parameters. $CO_2^*$ [%] was derived using *p*H and total alkalinity as predictor variables. In B), each box represents values between the 1st ($x_{25}$) and 3rd ($x_{75}$) quartile, with the horizontal line designating the median value. Any data with a distance greater than the interquartile range ($IQR_{75-25}$ = 3rd – 1st quartile) is labelled an outlier. All remaining values that are not considered outliers are contained by the whiskers (connected to the box by vertical lines). Note that B) only displays years for which data is available.**

### 7.3.3 Seasonal and Spatial $fCO_2$ Variability

Direct measurements of $fCO_2$ within the Coral Sea are rare (Figure 7.3.7) and can be ascribed to only a handful of individual ship cruises, with the first direct measurements going back to December 1983 (Figure 7.3.7B). Several routes have been duplicated however, with measurements being taken in four successive years (1984-1987) along (26.0°S, 155.7°E) (21.4°S, 170.0°E), and two successive years (1995-1996) along (13°S, 156°E) (5°S, 153.56°E), for example.

There is a relatively clear long-term trend towards higher $fCO_2$ values in the Coral Sea since the 1980s, with an average increase of 1.41 ± 0.04 µatm/year from 1983 to 2001. This yearly rate of increase in oceanic $fCO_2$ compares very well with the global trend of mean sea surface $fCO_2$ (1.5 µatm/year, Takahashi *et al.*, 2009) and mean atmospheric $fCO_2$ (1.43 µatm/year, Conway *et al.*, 1994), whereas atmospheric $fCO_2$ at Cape Ferguson displays a somewhat higher rate (1.55 µatm/year) over the 1983-2001 period.

No obvious spatial patterns or long-term trends emerge in relation to $\Delta fCO_2$sea-air (difference between oceanic and atmospheric $fCO_2$, Figure 7.3.8). It appears that, throughout the study site, the Coral Sea can act either as a sink or a source at any location, with the possible exception of the Torres Strait in the north-western Coral Sea. The Torres Strait is characterised by very shallow topography (<20 m; Harris *et al.*, 2005), extensive mixing (Wolanski *et al.*, 1995) and high SSTs (Saint-Cast and Condie, 2006). During the ship cruise measurements of $fCO_2$ within the Torres Strait, typical SSTs were 26.5°C in winter (June1999) and 29.1°C in late autumn (November 1995). During November, $\Delta fCO_2$sea-air was consistently highly positive (>15.0 µatm), with $\Delta fCO_2$sea-air increasing westward towards the Gulf of Carpentaria. A similar east-west trend was also found in June: whereas in the western Torres Strait (west of 142.5°E), $\Delta fCO_2$sea-air remained strongly positive (>10.0 µatm), $\Delta fCO_2$sea-air was commonly near-zero, or even negative (>-6.0 µatm) towards the Gulf of Papua. Therefore, the Torres Strait appears to generally act as a strong source of $CO_2$ to the atmosphere throughout the year, with only the eastern Torres Strait displaying near-neutral patterns during the cooler months.

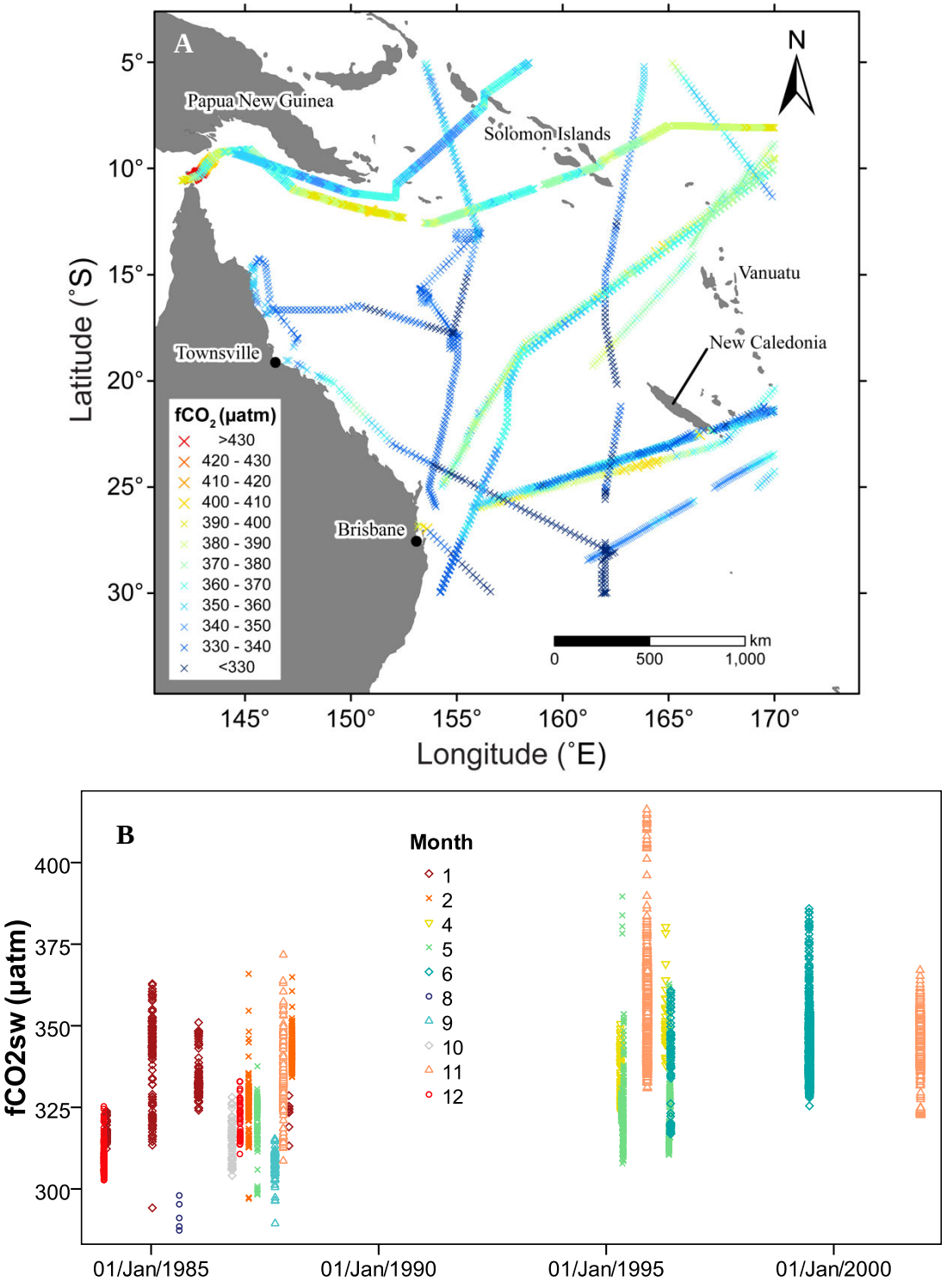


**Figure 7.3.7. A) Geographical and B) temporal distribution of seawater *f*$CO_2$ within the Coral Sea. Note that, to allow for spatial data intercomparison, *f*$CO_2$ in Figure 7.3.7A was normalised to the year 2001 using the atmospheric $CO_2$ time series of Cape Ferguson (ftp.cmdl.noaa.gov). The *f*$CO_2$ data is derived from NOAA, JODC and CDIAC.**

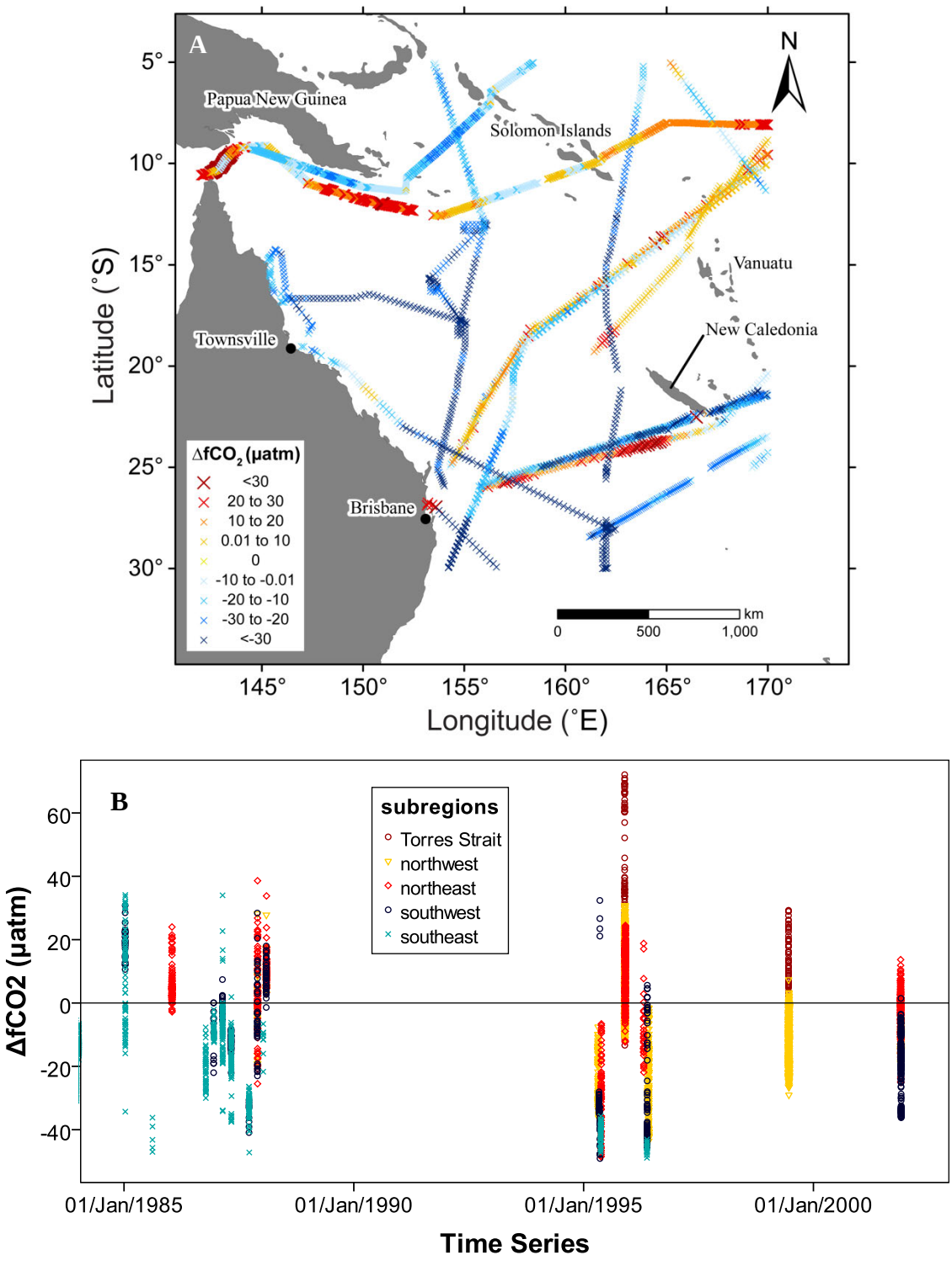


**Figure 7.3.8. A) Spatial and B) temporal distribution of the difference between oceanic and atmospheric $fCO_2$ ($\Delta fCO_2$sea-air), with negative values implying an uptake of atmospheric $CO_2$ by the Coral Sea. Data sources are NOAA, JODC and CDIAC. South-north and east-west borders at 20°S and 160°E, respectively, and Torres Strait data east of 145°E.**

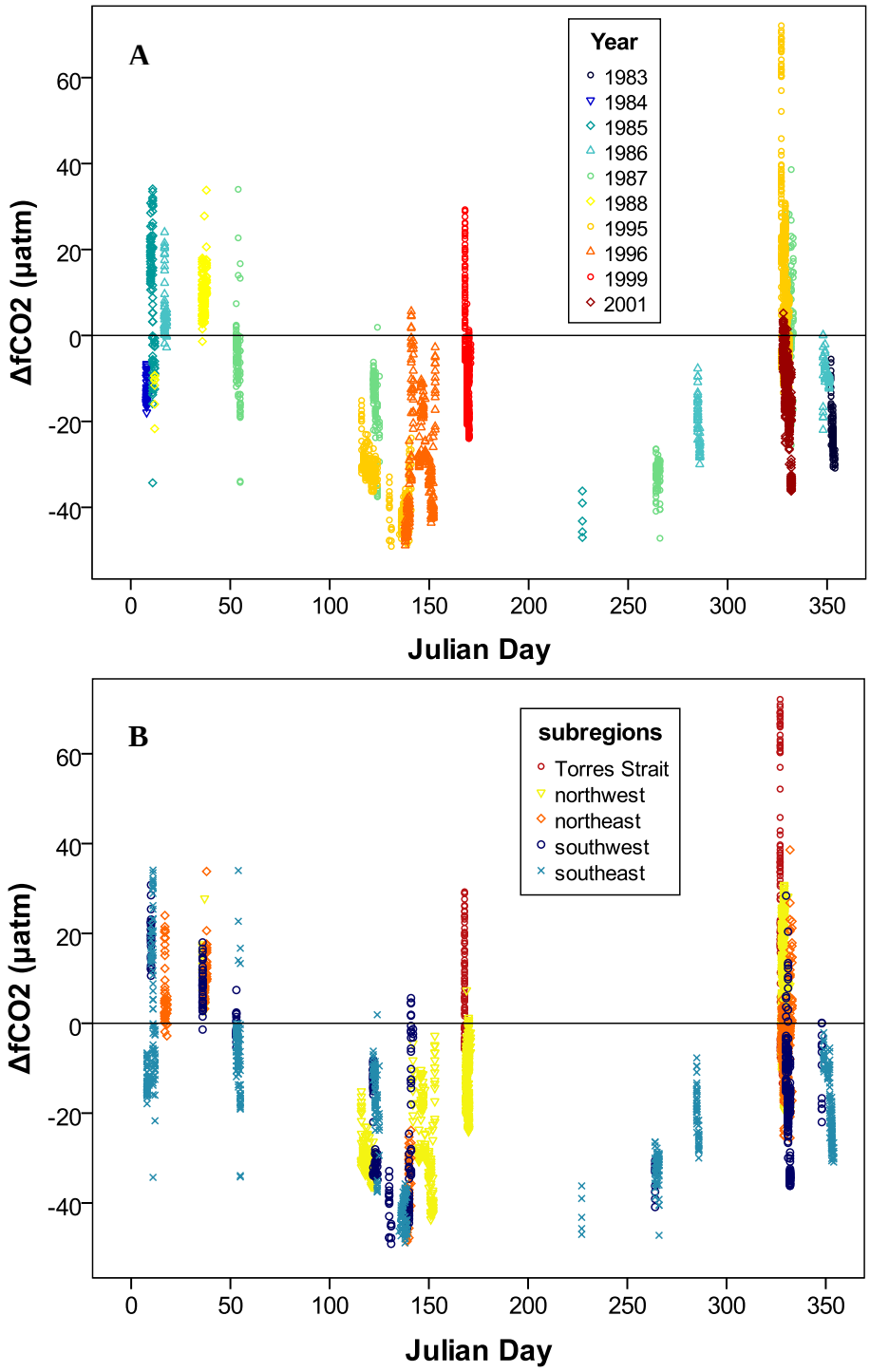


**Figure 7.3.9. Seasonality of Δ$fCO_2$sea-air. The colour scheme is denoting A) the year and B) the region (south-north and east-west borders at 20°S and 160°E, respectively, and Torres Strait data east of 145°E) the data was gathered in.**

Within the Coral Sea, most physical and chemical parameters display both seasonal and regional variability, which can have a significant effect on $fCO_2$, depending both on the extent of variability and combination of parameters that fluctuate concurrently.

Although the seasonal signal of $fCO_2$ is not entirely consistent, $\Delta fCO_2$sea-air (Figure 7.3.9) and $fCO_2$sea exhibit quite a strong seasonality, with the higher austral summer $fCO_2$sea values signalling increased outgassing of $CO_2$ into the atmosphere during the warmer months. The highest $fCO_2$sea (>400 μatm) values were observed during November 1995 (Figure 7.3.7B), coinciding with a weak La Niña. A La Niña event usually coincides with warmer than usual SSTs within the Coral Sea, which would be expected to result in increased oceanic $fCO_2$.

Besides atmospheric $fCO_2$, changes in temperature most significantly impact on $fCO_2$ variability ($R^2 = 0.39$, $P < 0.001$), with a 1°C change resulting in a $fCO_2$ alteration of around 13.1-15.6 μatm. Consequently, a relatively strong seasonal signal is expected. The effect of temperature variability on $fCO_2$ declines with decreasing *p*H. Besides temperature, $tCO_2$ has the most considerable influence on $fCO_2$ (Takahashi *et al.*, 1993). Conversely, salinity changes have a minor impact on $fCO_2$.

The diurnal timing of $fCO_2$ measurements, which often is considered important due to diurnal changes in numerous $CO_2$ system parameters such as temperature and photosynthesis (Frankignoulle and Borges, 2001; Shirayama and Thornton, 2005), also does not appear to impact significantly on $fCO_2$. Nevertheless, the highest $fCO_2$ values (>405 μatm), associated with the Torres Strait (Figure 7.3.7A), do coincide with the cooler night-time. However, since $fCO_2$ measurements in the Gulf of Carpentaria (collected just prior to the Torres Strait data during daytime) are even higher, the $fCO_2$ pattern within the Torres Strait is more likely attributable to location rather than diurnal variability.

$CO_2$ uptake ultimately not only depends on the difference between oceanic and atmospheric $CO_2$ levels but also on the solubility of $CO_2$ in the ocean. The solubility of $CO_2$ decreases exponentially with temperature (Figure 7.3.10A). As a result, $CO_2$ solubility changes seasonally, with the solubility increasing towards cooler months (Figure 7.3.10B). Salinity has only a minor influence on the solubility of $CO_2$, with increases in salinity inducing small declines in solubility. In the long-term, the solubility

of $CO_2$ does not appear to have changed significantly between 1983 and 2001 (Figure 7.3.11).

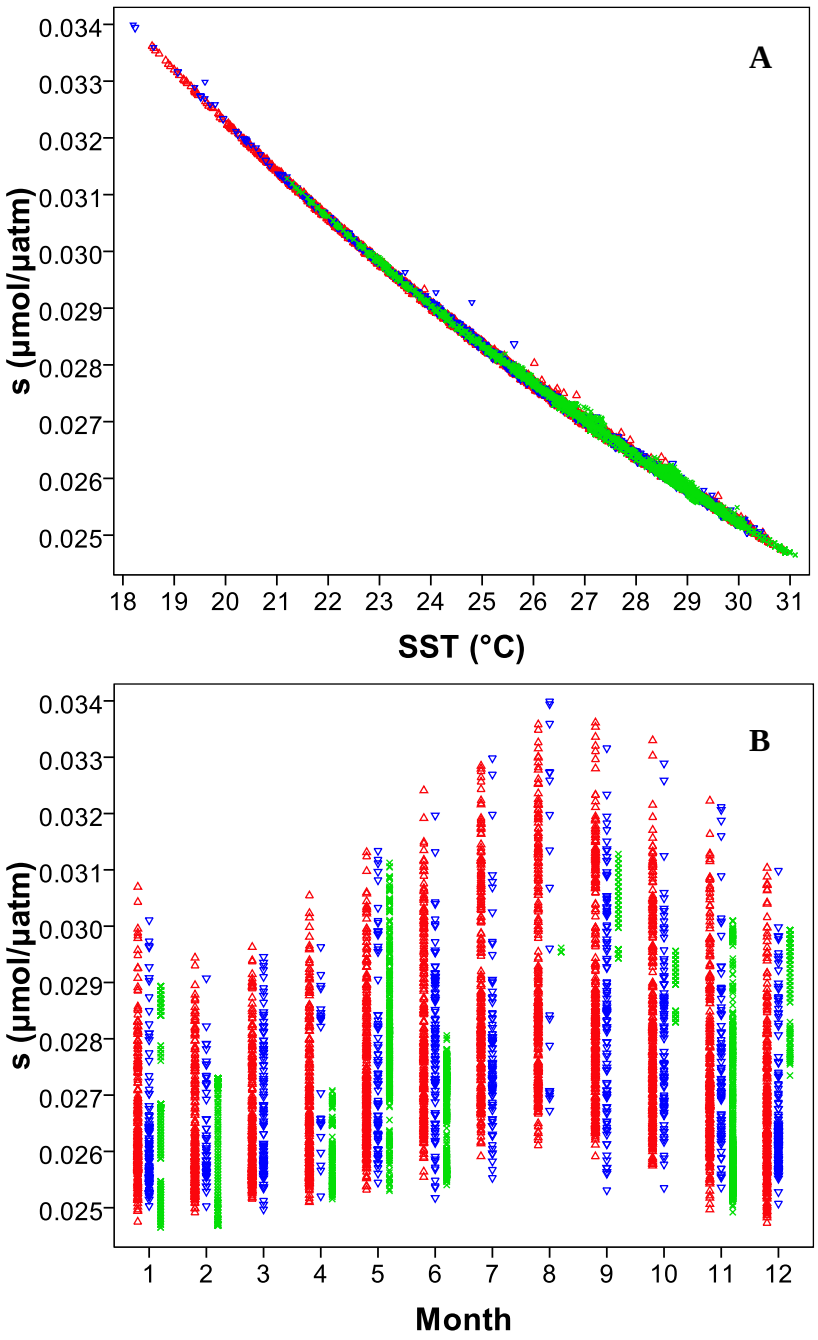


**Figure 7.3.10. Change in $CO_2$ solubility (s) with A) temperature and B) season. The solubility of $CO_2$, obtained with the constants of Weiss (1974), is strongly temperature dependent, with salinity changes only having a minor impact on solubility. SST and SSS data sources are Argo (red), WOD (blue), and others (green – JODC, CDIAC). For further details on the derivation of the $CO_2$ solubility, cf. equation (1) (section 7.2.3).**

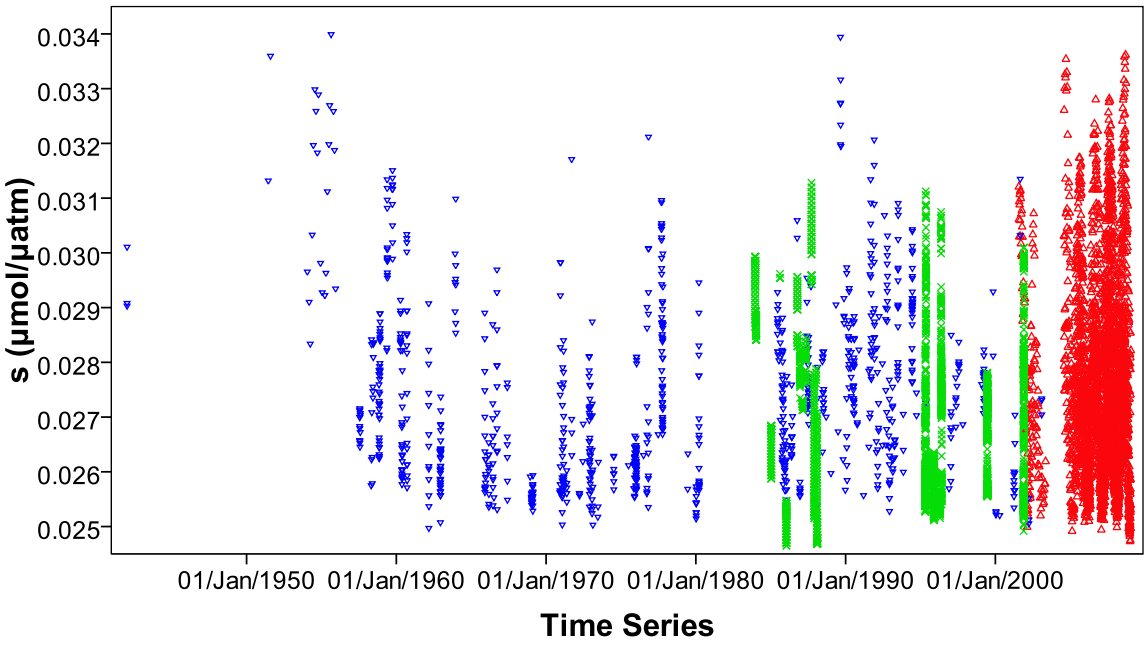


**Figure 7.3.11. Change in $CO_2$ solubility (s) with time. $CO_2$ solubility does not appear to have significantly changed between 1983 and 2001. SST and SSS data sources are Argo (red), WOD (blue), and others (green – JODC, CDIAC). For further details on the derivation of the $CO_2$ solubility, cf. equation (1) (section 7.2.3).**

## 7.3.4 Predictability of $fCO_2$ in the Absence of Geochemical Data

The seawater $fCO_2$ data shown in Figure 7.3.12 was utilised to investigate the predictability of seawater $fCO_2$ in the absence of any other carbon parameter. If solely SST and SSS are used as predictor variables, $fCO_2$ within the Coral Sea can be described with the following linear regression ($R^2 = 0.38$, $P < 0.001$):

$$fCO_2 = (5.326 \pm 0.124) \cdot SST + (2.595 \pm 0.505) \cdot SSS + (102.9 \pm 19.9) \quad (2)$$

The prediction can be significantly improved if the data's location (i.e. longitude and latitude) is taken into account as well ($R^2 = 0.59$, $P < 0.001$, Figure 7.3.13A):

$$fCO_2 = (5.371 \pm 0.144) \cdot SST + (13.831 \pm 0.491) \cdot SSS + (0.803 \pm 0.051) \cdot latitude - (0.954 \pm 0.027) \cdot longitude - (128.2 \pm 17.3) \quad (3)$$

However, the latter regression equation still does not take into account that $fCO_2$ is expected to display a trend towards higher values over time, which is not evident in Figure 7.3.13A. If the observation date (e.g. 20001231 for December 31 2000) is

incorporated as well, the predictive skill is augmented slightly ($R^2$ = 0.65, P < 0.001, Figure 7.3.13B):

$$fCO_2 = (6.077 \pm 0.137) \cdot SST + (16.284 \pm 0.467) \cdot SSS + (0.457 \pm 0.050) \cdot latitude - (0.78 \pm 0.026) \cdot longitude + (3.011 \cdot 10^{-8} \pm 0.118 \cdot 10^{-8}) \cdot date - (657.4 \pm 26.3) \quad (4)$$

A further improvement was achieved when incorporating the linearised relationship between $fCO_2$ and month to take into account that $fCO_2$ varies seasonally ($R^2$ = 0.71, P < 0.001, Figure 7.3.13C):

$$fCO_2 = (3.807 \pm 0.144) \cdot SST + (15.808 \pm 0.423) \cdot SSS + (1.1 \pm 0.050) \cdot latitude - (0.865 \pm 0.024) \cdot longitude + (3.723 \cdot 10^{-8} \pm 0.109 \cdot 10^{-8}) \cdot date + (0.572 \pm 0.019) \cdot (month - 6.5)^2 - (655.5 \pm 23.7) \quad (5)$$

A removal of the Torres Strait sea surface data, which do not display strong cross-correlations with $fCO_2$ (cf. Figure 7.3.12), produces a slight improvement in the 1st ($R^2$ = 0.45, P < 0.001), 3rd ($R^2$ = 0.69, P < 0.001, equation 6) and 4th ($R^2$ = 0.75, P < 0.001, equation 7) regression, whereas no predictive skill enhancement was achieved for the 2nd regression. The absence of a skill increase for the 2nd regression can be ascribed to the strong relationship between Torres Strait data and longitude (as evident by the strong reduction of the longitude coefficient), such that the incorporation of 'data location' offsets the removal of Torres Strait data. Figure 7.3.14 illustrates predicted oceanic $fCO_2$ for the following regression equations, which were obtained by ignoring all Torres Strait data:

$$fCO_2 = (6.039 \pm 0.121) \cdot SST + (17.193 \pm 0.448) \cdot SSS + (0.407 \pm 0.043) \cdot latitude - (0.451 \pm 0.025) \cdot longitude + (3.529 \cdot 10^{-8} \pm 0.103 \cdot 10^{-8}) \cdot date - (809.0 \pm 24.4) \quad (6)$$

$$fCO_2 = (4.072 \pm 0.124) \cdot SST + (16.995 \pm 0.400) \cdot SSS + (0.997 \pm 0.043) \cdot latitude - (0.587 \pm 0.022) \cdot longitude + (4.084 \cdot 10^{-8} \pm 0.093 \cdot 10^{-8}) \cdot date + (0.52 \pm 0.016) \cdot (month - 6.5)^2 - (796.9 \pm 21.8) \quad (7)$$

Figure 7.3.15 compares the observed $fCO_2$ (from Figure 7.3.7) with the predicted $fCO_2$ based on the 6th regression equation. Figure 7.3.15 clearly shows that the 6th regression equation is not applicable to the Torres Strait data. Although a regional subdivision may increase the predictive skill (by applying regression equations tailored to the subregions), the close agreement of observed and predicted $fCO_2$ values, and the absence of any strong deviations in Figure 7.3.15 (with the possible exception of the

southwest Coral Sea), does not warrant it at this stage. Thus, the equation was then applied to all available datasets containing the required parameters (SST, latitude, etc.), including Argo data. The temporal evolution of the resultant $fCO_2$ values, as well as of the observed $fCO_2$ levels, was plotted in Figure 7.3.16.

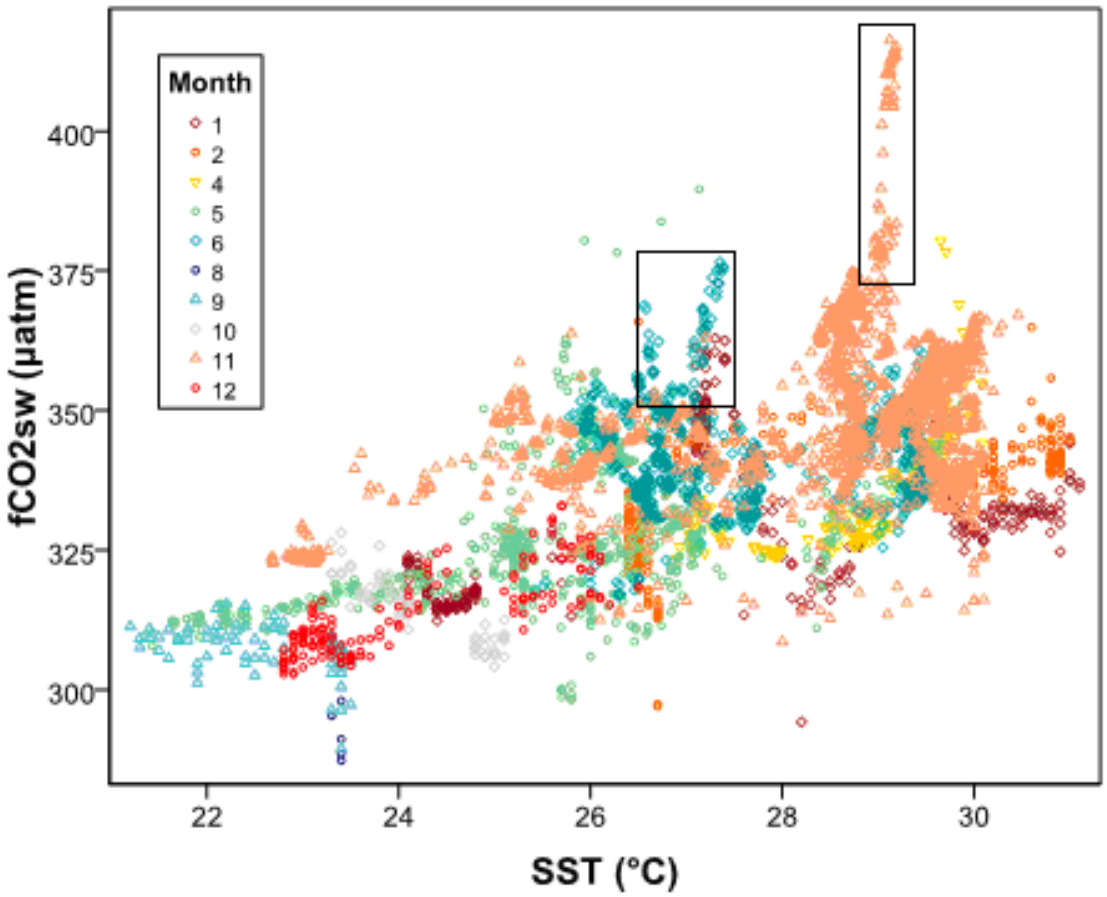


**Figure 7.3.12. Correlation between seawater $fCO_2$ and sea surface temperature ($R^2$ = 0.39). The boxed data (November values, top right, and June values, centre) derive from the Torres Strait.**

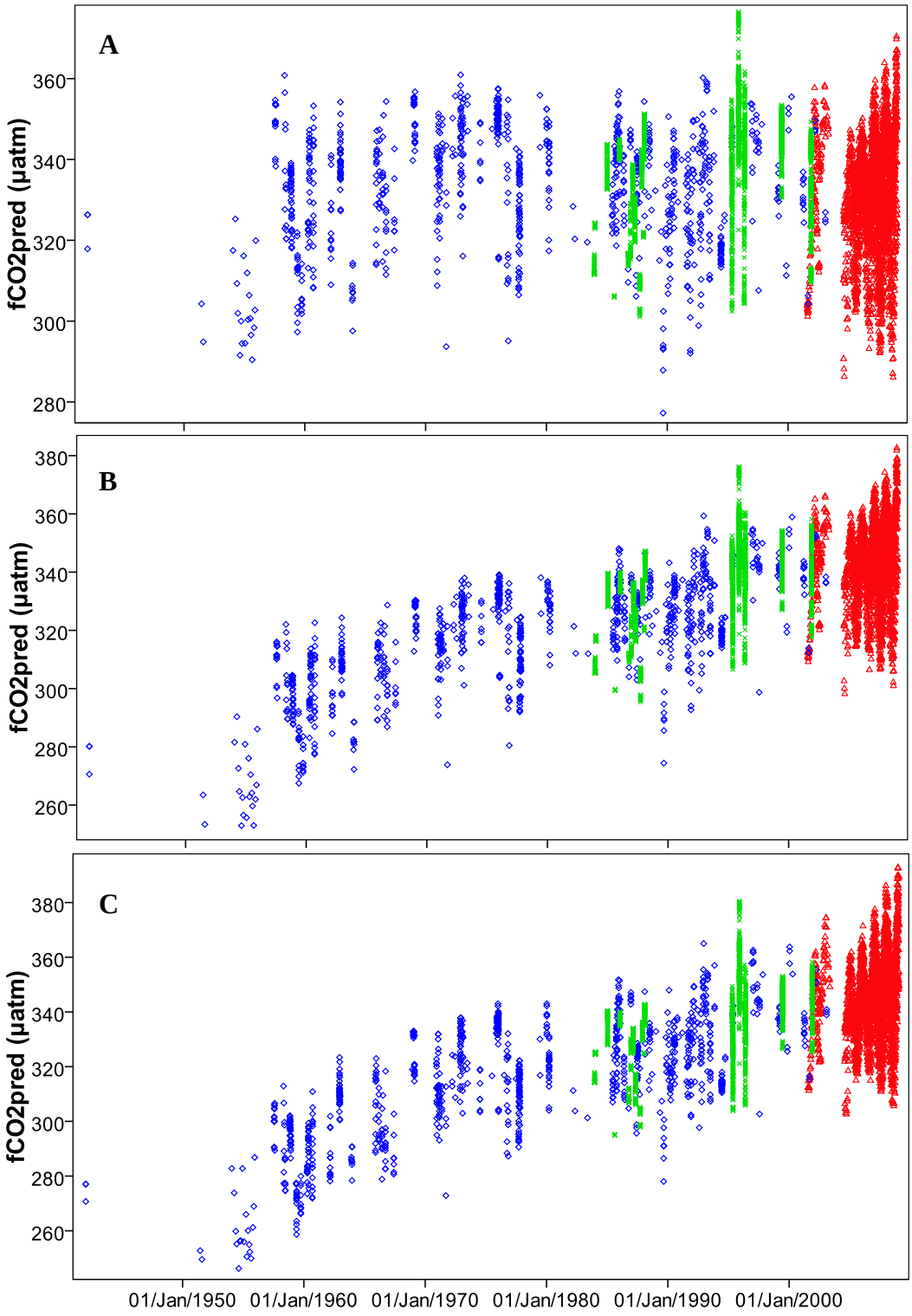


**Figure 7.3.13. Change of predicted seawater $fCO_2$ based on A) SST, SSS and location (2nd regression equation), as well as B) the date of the measurement (3rd regression equation), and C) the month of the data collection (4th regression equation). Data sources are Argo (red triangles), WOD (blue diamonds) and others (green crosses).**

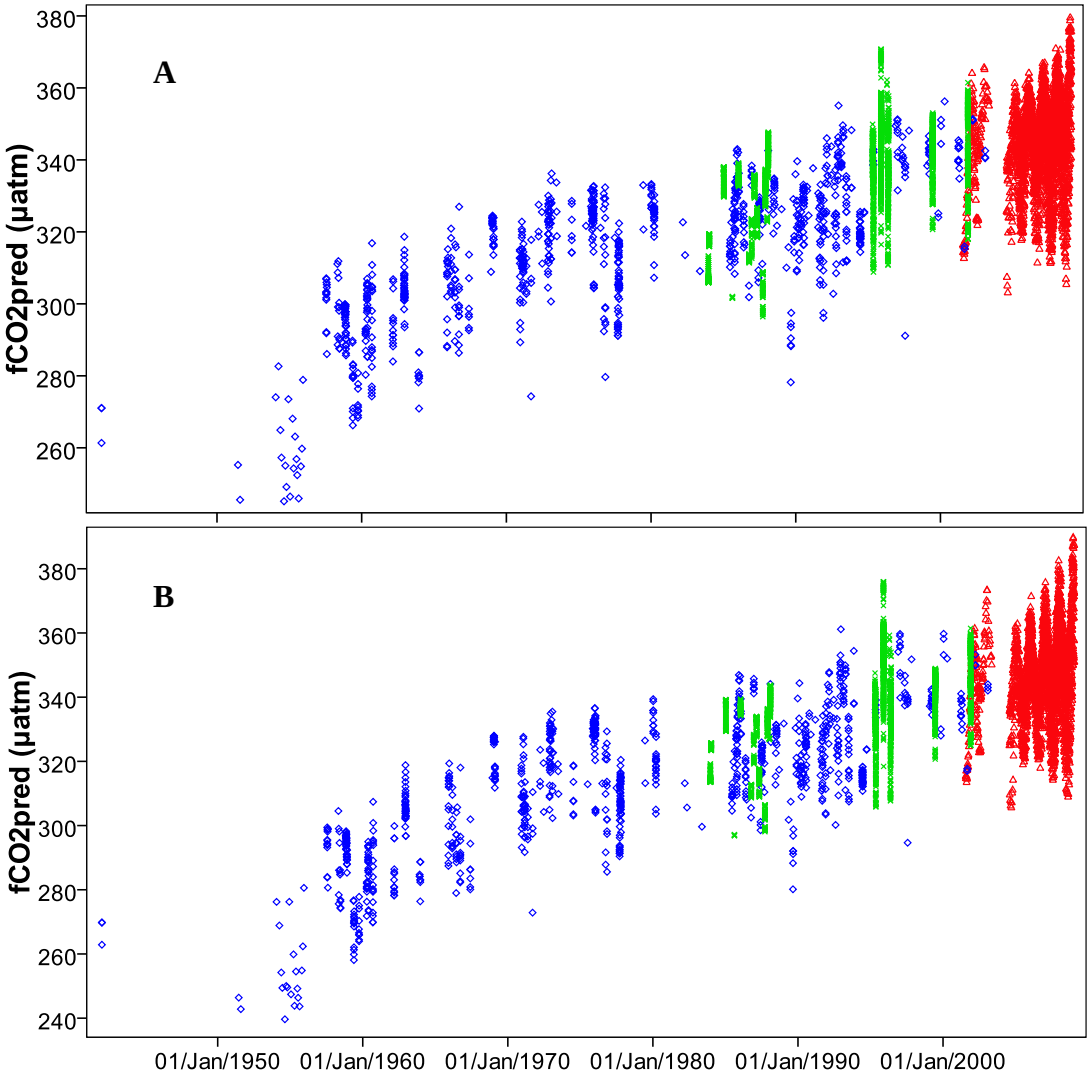


**Figure 7.3.14. Change of predicted seawater $fCO_2$ with removed Torres Strait data based on A) SST, SSS, location and the date of the measurement (5$^{th}$ regression equation), as well as B) the month of the data collection (6$^{th}$ regression equation). Data sources are Argo (red triangles), WOD (blue diamonds) and others (green crosses).**

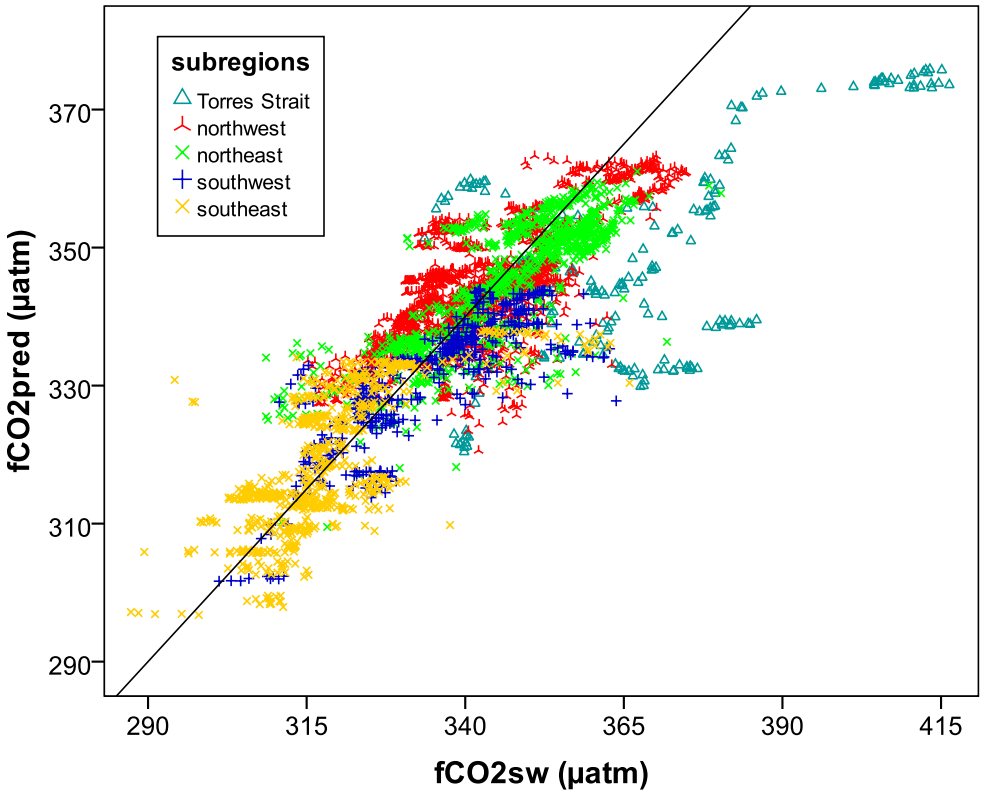


**Figure 7.3.15. Observed (fCO2sw) vs predicted (fCO2pred) $fCO_2$ levels, with the colour scheme denoting the area of data collection. The south-north and east-west borders are at 20°S and 160°E, respectively, and Torres Strait data east of 145°E. A line was plotted where fCO2sw equals fCO2pred.**

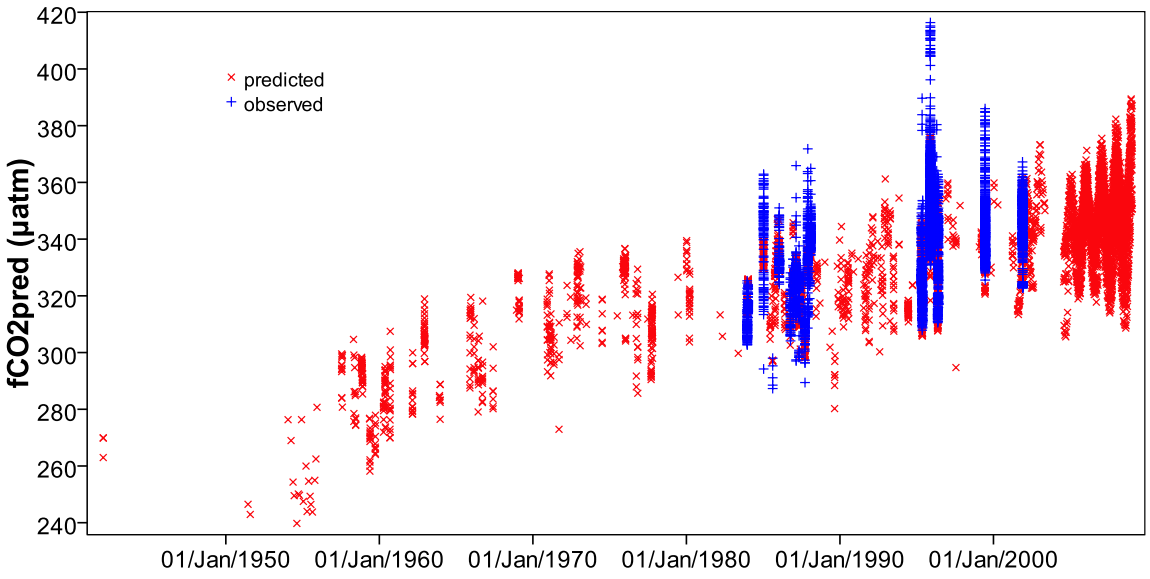


**Figure 7.3.16. Temporal distribution of observational (blue) and predicted (red) *f*$CO_2$. Data from the WOD and Argo have been included for the *f*$CO_2$ estimation.**

Clearly, a better accuracy is desirable for $fCO_2$ estimation. However, to improve seawater $fCO_2$ predictions, other parameters besides physical sea surface data are required. A possibility would be the incorporation of vertical water motion (i.e. up- and downwelling) in the absence of chemical data. This, however, is beyond the scope of the thesis and might be a suitable project for future studies.

Ideally, in the absence of direct $fCO_2$ measurements, other geochemical parameters (e.g. TA, *p*H, $tCO_2$) related to the carbon cycle would have been monitored, in which case a program like CO2SYS could then be used to more accurately determine past and present $fCO_2$ within the Coral Sea.

### 7.3.5 Long-term Changes in the Carbon Chemistry

Long-term changes in carbon chemistry are difficult to discern due to the scarcity of the Coral Sea dataset. Both $CO_2^*$ [%] and $fCO_2$ show a minor tendency towards higher values in the mid-90s. However, in both cases, these data coincide with ENSO events. *p*H initially appears to display a trend towards increasing values until 1980, with a temporary shift towards lower values in 1963, but seems to decrease from the late 1980s, with the latter trend mainly based on low values measured in the mid-1990s. The high values of $CO_2^*$ [%], and low values of *p*H, overlap with the strong El Niño of 1994/1995. As El Niño events usually coincide with cooler than average Coral Sea SSTs, both $fCO_2$ and $CO_2^*$ [%] would be expected to decline, concomitant with an increase in *p*H (appendix A3.1). Thus, unless the cooling is driven by deeper mixing bringing cool but $CO_2$-rich waters to the surface, it is unlikely that the El Niño events induced the shifts during austral summer of 1994/1995. Conversely, the highest $fCO_2$ values were measured during a weak La Niña. As discussed earlier (cf. section 7.3.3), the 1995/1996 La Niña may have contributed to higher $fCO_2$ values. However, to be able to evaluate whether long-term climate change, multi-decadal variability (e.g. IPO), interannual (i.e. ENSO) climate signals, or simply scarce, random sampling produced the long-term chemistry patterns presented here, a much larger and spatially more homogenous dataset is required.

## 7.4 Summary - Geochemistry

Within the Coral Sea, no consistent long-term trends in *p*H are discernible since *p*H has been measured very sporadically since 1942. However, both $fCO_2$ and *p*H exhibit some annual seasonality. $fCO_2$sea values tend to increase towards summer, which is linked to the positive relationship between fugacity and SST. As a result, the Coral Sea's capacity to act as a sink of atmospheric $CO_2$ is reduced during summer and the region is thus more likely to act as a source of $CO_2$ to the atmosphere compared to winter. Consequently, the Coral Sea appears to be in a net near-neutral $CO_2$ flux state, with the potential exception of the Torres Strait, which appears to be a strong source of $CO_2$ throughout the year. Unexpectedly, no diurnal influence was observed in the available Coral Sea $fCO_2$ data, the levels of which are normally expected to increase at night due to increased respiration and reduced photosynthesis. $\Delta fCO_2$ (the difference between oceanic and atmospheric $fCO_2$) does not appear to have changed since 1983, the year of the first Coral Sea $fCO_2$ measurement. Conversely, there is a trend evident towards higher $fCO_2$sea over time, consistent with - and comparable to - the increase in atmospheric $fCO_2$ over the same period. These results indicate that the Coral Sea has not changed its behaviour in regard to $CO_2$ uptake since the early 1980s.

An investigation into the capability of $fCO_2$sea estimation in the absence of any chemistry data revealed that regression equations based on SST, SSS, location (latitude and longitude) as well as the date and month (of the observation) delivers the most accurate approximation ($R^2$ = 0.75) for $fCO_2$sea, although there appears to be an underestimation for older samples. The Torres Strait region exhibits a very distinct relationship, with $fCO_2$sea strongly linked to the longitudinal position rather than SST. It is also the only region within the Coral Sea that typically acts as a source of $CO_2$ to the atmosphere.

Due to the absence of a large geochemical dataset to resolve long-term, seasonal and spatial patterns within the Coral Sea, a significant increase in sampling endeavours (ship cruises, stationary instruments,…) is highly desirable. Meanwhile, high resolution numerical models may provide more detailed answers to past, present and future geochemical changes within the Coral Sea.

# 8 Observational versus Model Patterns in Ocean Physics and Geochemistry

Due to the discontinuous and scarce nature of the observational carbon dataset, no statistically significant evaluation of the impact of timescales exceeding seasonal variability on carbon chemistry can be made based on observational data alone. In consequence, a regional high-resolution coupled model (ROMS-PISCES) was chosen to simulate the seasonal and climate variability of the physical and chemical parameters within the Coral Sea. In this chapter, physical and chemical model output for three different atmospheric $CO_2$ levels is presented to determine large-scale patterns and long-term changes in the various parameters of interest. In addition, a short segment is dedicated to the inter-comparison of model results and observational data.

After a short introduction to the history of numerical modelling (section 8.1), a brief summary of ROMS-PISCES is given in sections 8.2.1 and 8.2.2. A review of the complete documentation and mathematical basis of the numerical models is well beyond the scope of this thesis. However, comprehensive websites can be found at https://www.myroms.org/wiki/index.php/Documentation_Portal (ROMS-Rutgers) and http://roms.mpl.ird.fr/documentation.html (ROMS-Agrif and PISCES). A summary is attached in appendix A4.

## 8.1 History of Numerical Modelling - Early Developments

Prediction and evaluation of large-scale, complex environmental Earth systems have a long history. At the beginning of the 20$^{th}$ century, Vilhelm Bjerknes (1862-1951), a Norwegian physicist and meteorologist, developed seven so-called ‘primitive equations’ of motion and state to approximate global atmospheric flow (Bjerknes, 1904), and these nonlinear differential equations have been widely used for scientific weather forecasting with atmospheric climate models.

The first numerical weather prediction (NWP) system was developed by mathematician Lewis Fry Richardson (1881-1953) in 1922 (Richardson, 1922). He simplified Bjerknes’ ‘primitive equations’ (and added atmospheric dust as an 8$^{th}$ variable), applied finite difference solutions of differential equations and divided space

into grid cells. However, at the time, his technique was too computationally expensive to be of practical use before the availability of digital computers in the 1940s.

The first barotropic numerical weather prediction model was developed at the Institute for Advanced Study (IAS) in Princeton, with the first simulations being produced in 1950 (Charney *et al.*, 1950) using ENIAC (Electronic numerical integrator and calculator), the world's first electronic computer (Platzman, 1979). Four years later, the Royal Swedish Air Force Weather Service became the first organisation to generate operational real-time numerical weather forecasts, with output being made three times a week using a barotropic model developed by the Institute of Meteorology at the University in Stockholm (MISU), of which the meteorologist Carl-Gustav Rossby was the founding director (Persson, 2005).

From the 1960s, as computer power grew and numerical models became more sophisticated, barotropic and baroclinic equations were replaced by the more accurate 'primitive equations' of Bjerknes and Richardson (Shuman, 1989). The first numerical climate (general circulation) simulation was produced in 1963 (Smagorinsky *et al.*, 1965), followed by the development of the first 3-dimensional global ocean model in 1967 (Bryan and Cox, 1967). This first ocean circulation model, built at the Geophysical Fluid Dynamics Laboratory (GFDL, now located in New Jersey, USA), mainly considered wind stress and thermodynamic forcing. The numerical schemes developed by Michael Cox and Kirk Bryan to solve the equations of motion describing flow on a sphere led to the 3-dimensional Modular Ocean Model (MOM) (Griffies *et al.*, 2000), which is still widely used by ocean and atmosphere modellers.

In the subsequent years, the first fully coupled ocean-atmosphere models were created (Manabe, 1969; Manabe and Bryan, 1969). In their 1969 publication, meteorologist Syukoro Manabe and oceanographer Kirk Bryan demonstrated the importance of ocean heat transport in determining global climate (Manabe and Bryan, 1969). As computing technology progressed, and climate modelling techniques improved, many coupled general circulation models (GCMs) gradually evolved from asynchronous and coarse-grid model simulations into synchronously producing output at higher resolutions (Meehl, 1990). Semi-lagrangian methods and data assimilation (Navon, 2009) were introduced to numerical modelling in the 1980s.

A significant advance in computational capability was the massively parallel processing (MPP) developments in the 1990s (Foster *et al.*, 1996), which enabled much more efficient and faster numerical model simulations. MPP is a type of computing that uses central processing units (CPUs) in parallel to execute a single computer program.

More recently, the coupling of several components to form Earth system models has become very widespread, with biogeochemical modules, for example, now commonly added to ocean-atmosphere GCMs. However, as a result, global simulations remain very computationally expensive. To reduce operational cost, and at the same time increase spatial resolution, regional climate models are now commonly employed to investigate the attributes of relatively small-scale areas (e.g. equatorial Pacific, Coral Sea and Great Barrier Reef). One commonly used high-resolution ocean model is the Regional Ocean Model System (ROMS) model.

## 8.2 Model Description

The following two sections provide a brief synopsis of the mathematical basis of the numerical models (ROMS-Agrif and PISCES) employed in this study.

### 8.2.1 ROMS

Two models have been used in this study to investigate the physical and biogeochemical attributes of the Coral Sea. The physical properties of the Coral Sea are explored using ROMS-Agrif (Adaptive Grid Refinement In Fortran; Penven *et al.*, 2006), the IRD version of the Regional Ocean Model System (ROMS) model, originally developed at Rutgers University (http://www.myroms.org/). ROMS is a split-explicit, free-surface, terrain-following ocean model that is solving the ‘primitive equations’ with the Boussinesq approximation and hydrostatic vertical momentum balance (Haidvogel *et al.*, 2000; Marchesiello *et al.*, 2001; 2003; Shchepetkin and McWilliams, 2003; 2005). The present version (ROMS-Agrif) has been tested previously for areas within the Pacific Ocean (e.g. Penven *et al.*, 2006), including coastal areas around New Caledonia.

## 8.2.2 PISCES

The ocean biogeochemistry is investigated by coupling the Pelagic Interaction Scheme for Carbon and Ecosystem Studies (PISCES; Figure 8.2.1) model (Bopp *et al.*, 2003; 2005) to ROMS, the two models running simultaneously. PISCES, derived from the ecosystem model HAMOCC5 (Hamburg Model of Carbon Cycle version 5; cf. Aumont *et al.*, 2003), is simulating the marine carbon cycle, as well as the main nutrients (Fe, N, P and Si) and biological productivity.

The original PISCES contains a total of 24 prognostic variables (Table 8.2.1), including nutrients ($PO_4^{3-}$, $NO_3^-$, Fe, $SiO_3$ and $NH_4$), four plankton groups (nanophytoplankton, diatoms, micro- and mesozooplankton) and three non-living parameters, dissolved inorganic carbon (DIC), dissolved organic matter (DOM), as well as two size classes of sinking particles, referred to as big and small particulate organic matter (bPOM and sPOM, respectively).

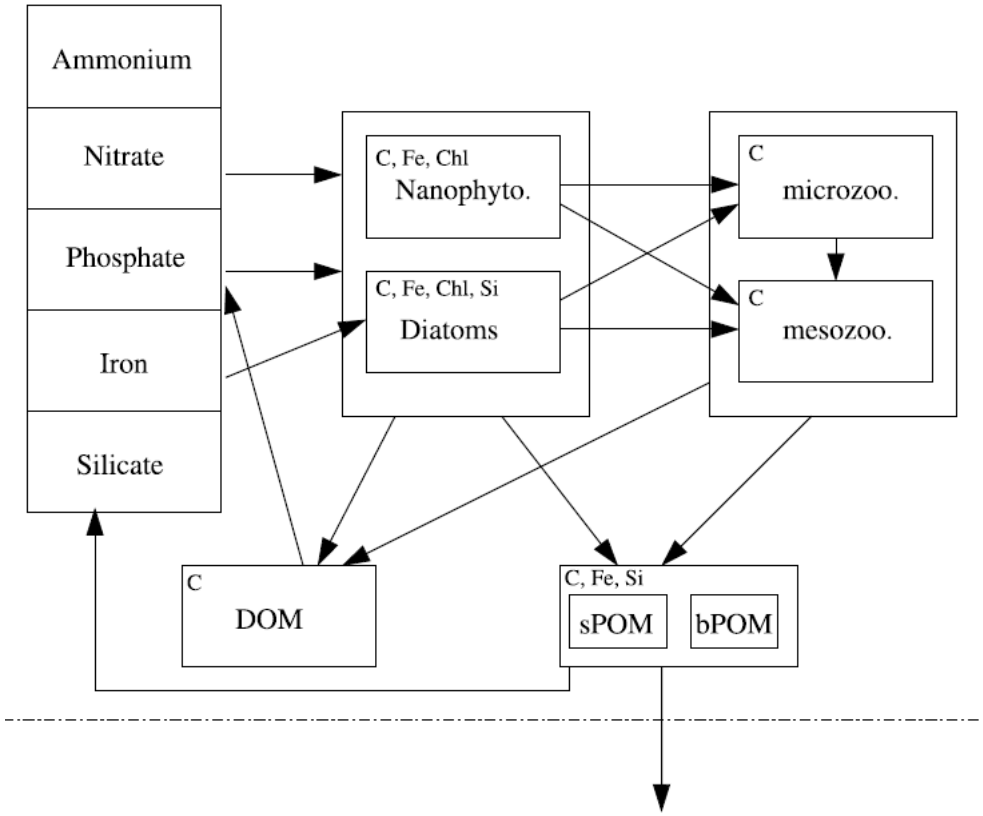


**Figure 8.2.1. Basic structure of the PISCES biogeochemical model. The explicitly modelled nutrients are listed in the upper left corner of the boxes (figure from Aumont and Bopp, 2006).**

To simplify the biogeochemical model, many parameters and interactions had to be ignored, or their interactions simplified. As C, N and P (and $O_2$) are not explicitly modelled, a constant Redfield ratio ($O_2$:$C_{org}$:N:P = 172:122:16:1 for marine phytoplankton organic matter; (cf. Takahashi *et al.*, 1985) is imposed (Aumont and Bopp, 2006). That is to say, the above nutrients are not allowed to vary independently in PISCES. Conversely, iron, silicon and calcite are explicitly modelled, thus allowing for their ratios to vary.

More recently, additional prognostic parameters related to the carbon cycle have been incorporated into PISCES (Table 8.2.2). Atmospheric $pCO_2$ is set as an external adjustable constant and, therefore, does not display spatial or temporal variability (i.e. $pCO_2$atm is invariable during the course of a simulation). Parameters not included in PISCES are benthic biota, as well as aragonite-related variables. Consequently, $CaCO_3$ and the saturation state of $CaCO_3$ only refer to the calcitic polymorph. Half of the grazed calcite shells are exported with the biological pump, with the remainder designated to dissolve in the guts of zooplankton.

Another model limitation is that several minor constituents co-determining alkalinity are ignored, i.e. only carbonate ($CO_3^{2-}$ and $HCO_3^-$), borate ($B(OH)_4^-$) and water ($H^+$, $OH^-$) alkalinity are used to obtain total alkalinity. However, this is considered to be a very good approximation for *p*H values exceeding 8 (cf. Zeebe and Wolf-Gladrow, 2001).

**Table 8.2.1. Original 24 prognostic parameters in PISCES.**

| Category | Component | Unit |
|---|---|---|
| phytoplankton | nanophytoplankton | µmol C/l |
| | diatoms | µmol C/l |
| zooplankton | microzooplankton | µmol C/l |
| | mesozooplankton | µmol C/l |
| chlorophyll | chlorophyll in nanophytoplankton | mg Chl/$m^3$ |
| | chlorophyll in microzooplankton | mg Chl/$m^3$ |
| nutrients | ammonium ($NH_4^+$) | µmol N/l |
| | phosphate ($PO_4^{3-}$) | µmol P/l |
| | dissolved iron (Fe) | µmol Fe/l |
| | nitrate ($NO_3^-$) | µmol N/l |
| | silicate ($SiO_3$) | µmol Si/l |
| dissolved oxygen | dissolved oxygen | µmol/l |
| biogenic silica ($SiO_2$) | $SiO_2$ | µmol Si/l |
| diatoms silicon (Si) | Si | µmol Si/l |
| iron | iron in big particles | µmol Fe/l |
| | iron in small particles | µmol Fe/l |
| | iron in nanophytoplankton | µmol Fe/l |
| | iron in diatoms | µmol Fe/l |
| total alkalinity | total alkalinity | µmol C/l |
| dissolved inorganic carbon (DIC) | DIC | µmol C/l |
| calcite ($CaCO_3$ ) | $CaCO_3$ | µmol C/l |
| non-living compartments | semi-labile dissolved organic matter (DOM) | µmol C/l |
| | small particulate organic matter (sPOM) | µmol C/l |
| | big particulate organic matter (bPOM) | µmol C/l |

**Table 8.2.2. Recently included prognostic parameters in PISCES.**

| | | |
|---|---|---|
| carbonate ($CO_3^{2-}$) | $CO_3^{2-}$ | mol/l |
| saturation state of $CO_3^{2-}$ | $\Omega_{calcite}$ | mol/l |
| primary production | nanophytoplankton | mol $C/m^3/s$ |
| | diatoms | mol $C/m^3/s$ |
| iron production | nanophytoplankton | mol $Fe/m^3/s$ |
| | diatoms | mol $Fe/m^3/s$ |
| flux | DIC | mol $C/m^2/s$ |
| | $O_2$ | mol $O/m^2/s$ |
| export | organic matter | mol $C/m^2/s$ |
| | Fe export from nano | mol $Fe/m^2/s$ |
| | Fe export from diatoms | mol $Fe/m^2/s$ |
| | Si export from diatoms | mol $Si/m^2/s$ |
| | calcite | mol $C/m^2/s$ |
| $\Delta pCO_2$ | $\Delta pCO_2$ | µatm |
| gas transfer | gas transfer | mol $C/m^2/s/\mu atm$ |

## 8.3 Methodology

Before ROMS-PISCES can be compiled and run, several preprocessing files have to be invoked to establish the physical and biogechemical forcing within and at the boundaries of the Coral Sea. The Comprehensive Ocean-Atmosphere Data Set (COADS) (e.g. Woodruff *et al.*, 1987; da Silva *et al.*, 1994), which contains the most complete observational sea surface dataset since 1854, is frequently used to provide boundary conditions in long-term integrations of ocean and atmosphere general circulation models (GCMs) (da Silva *et al.*, 1994). Data parameters incorporated in COADS include zonal and meridional wind components, air temperature, SST, sea level pressure (SLP), dew point depression, cloudiness and 'present weather' (da Silva *et al.*, 1994). The physical results presented in this chapter are mainly based on COADS forcing, with the exception of wind forcing which is derived from Quikscat. Quikscat contains satellite-derived wind data, which has a higher resolution (1/4°) compared to COADS (1°). In addition, Quikscat data is newer (1999 onwards) than COADS (1984-2000).

Observational datasets such as the World Ocean Atlas 2005 (WOA05) have a relatively low resolution and therefore large errors compared to the model derived output.

Consequently, the lateral boundary conditions and the initial conditions are given by the results of another numerical model (ORCA). Included climatologies are salinity, potential temperature, momentum in u and v components, and free surface. Biological forcing comprises nitrate, phosphate, silicon, oxygen, DIC, total alkalinity, DOC and iron. The addition of dust forcing is important since dust contains a substantial amount of iron, which can significantly enhance phytoplankton growth and, thus, alter the carbon cycle (cf. Winckler *et al.*, 2008).

After creating all forcing and climatology netcdf files, and compiling the model, ROMS-PISCES was run over a period of 11 model years to ensure that the model has achieved its equilibrium state (cf. appendix A4.5). Throughout the simulation, the data for every $5^{th}$ day was saved into monthly output files, which were later concatenated into yearly files if necessary. Here, only results from the last ($11^{th}$) year are presented. In the following sections, output of physical oceanography as well as ROMS-derived biochemistry (i.e. chlorophyll) is solely based on the more realistic open-boundary scenario, whereas PISCES-derived parameters are displayed for both open- and closed-boundary model runs.

## 8.4 Physical Coral Sea Characteristics

### 8.4.1 Sea Surface Temperature

Sea surface temperature (SST) within the Coral Sea exhibits a strong north-south gradient in the model, with SSTs increasing towards low latitudes (Figure 8.4.1A). However, SSTs do not increase homogenously along the entire east-west section owing to the presence of several large-scale current systems. Warmer water, associated with the Eastern Australian Current (EAC), flows southwards along the Queensland coast, resulting in southwestern Coral Sea SSTs that are up to 5° warmer than in the absence of the EAC. Similarly, the northwestern Hiri current moves slightly cooler water mass clockwise to the north around the Gulf of Papua. Consequently, the ocean heat content within the Gulf of Papua would be significantly lower compared to similar latitudes further east from the Gulf of Papua (cf. section 6.3.2.5).

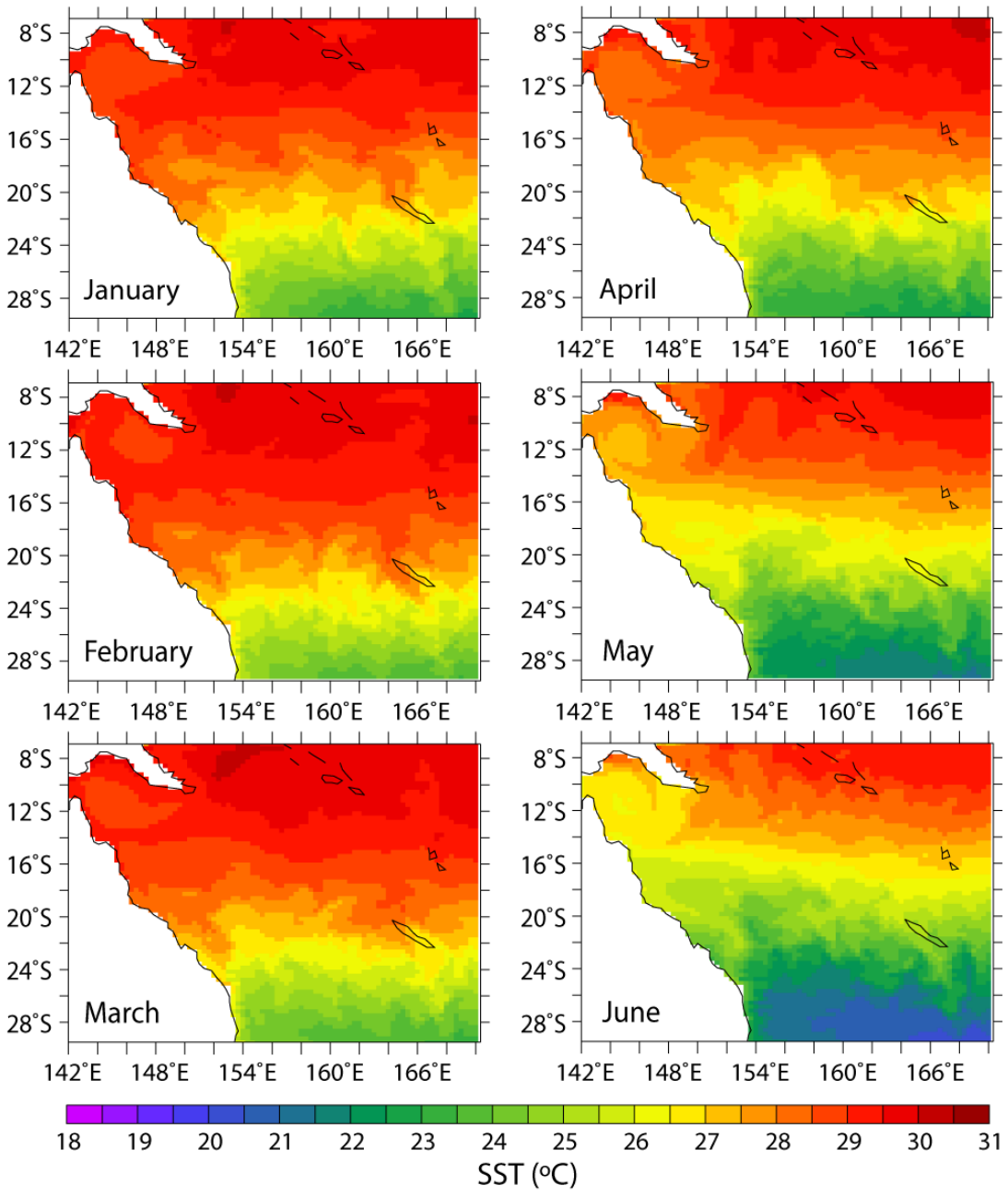


**Figure 8.4.1. Monthly averages of sea surface temperature (SST) within the Coral Sea based on ROMS-PISCES with open boundaries. A clear latitudinal gradient in SST is evident throughout the year, with the average SST decreasing towards the high latitude.**

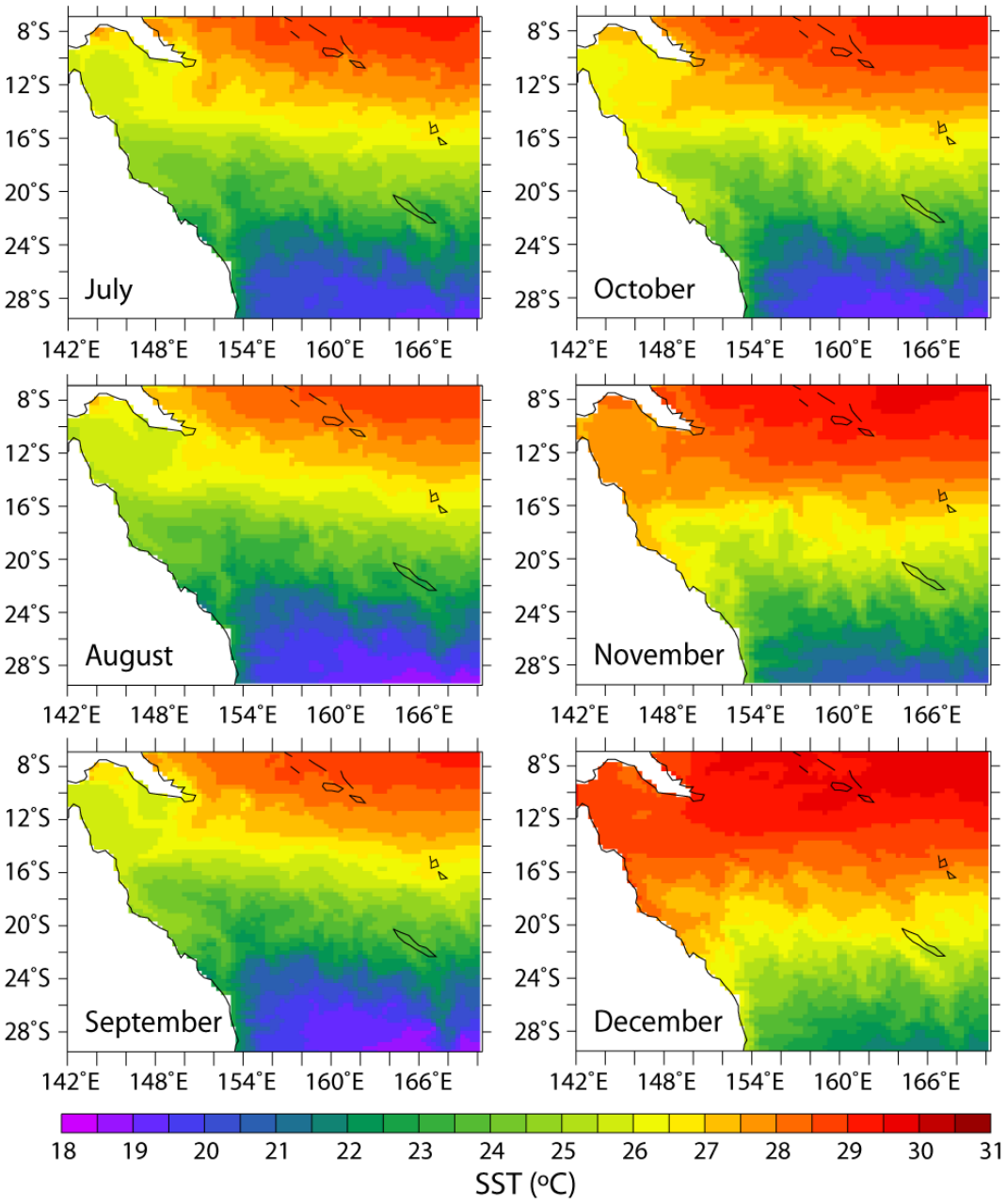


**Figure 8.4.1 continued.**

## 8.4.2 Mixed Layer Depth

From the temperature and salinity profiles provided by ROMS-PISCES, the mixed layer depth (MLD) has been deduced from the density profiles using a threshold value of 0.03 kg/m$^3$ and a reference depth of 10 m, similar to the procedure used in section 6.2. The MATLAB script used to convert salinity and density into density and ultimately into a MLD, is provided in appendix A4.6.

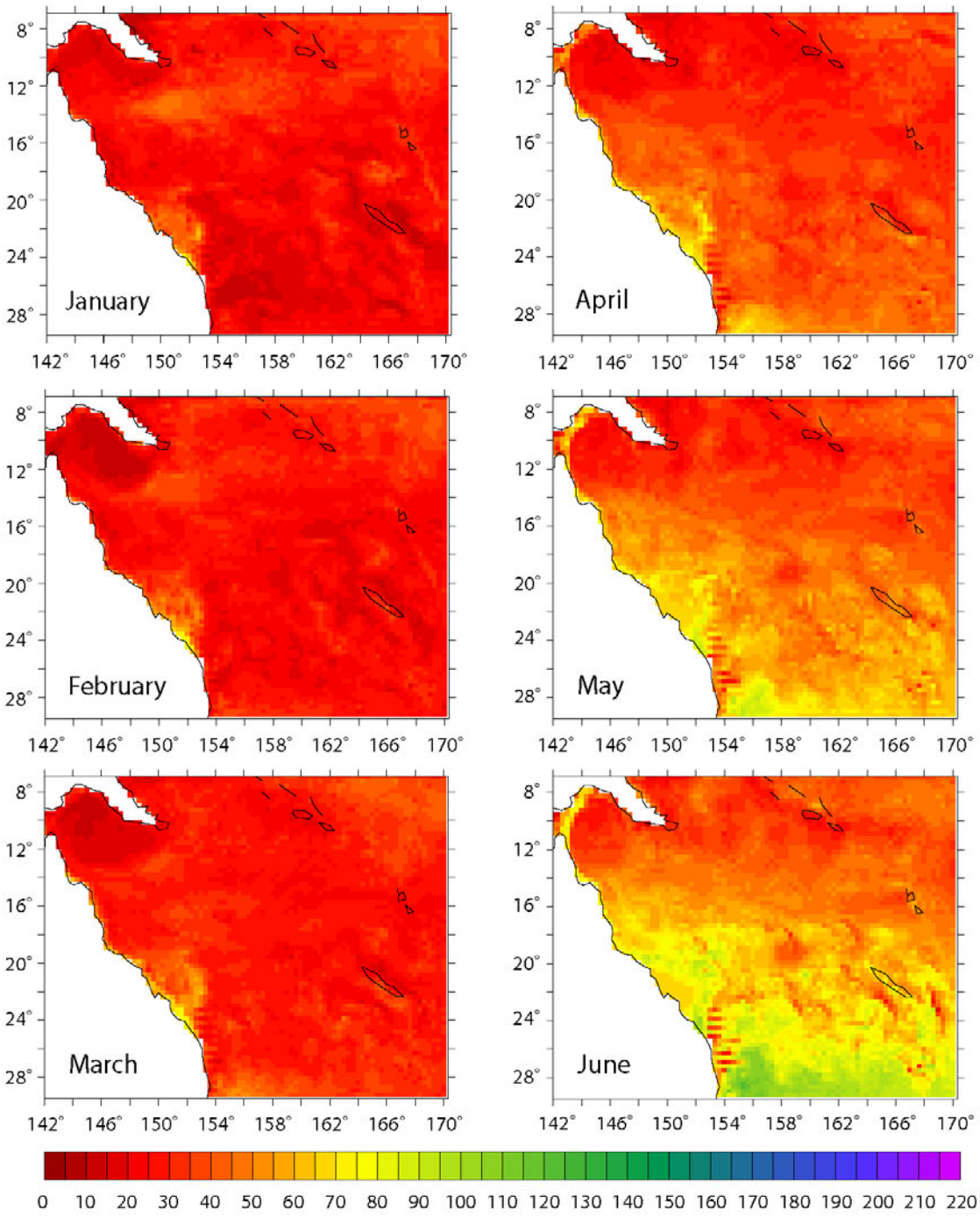


**Figure 8.4.2. Monthly averages of the mixed layer depth (MLD) field within the Coral Sea based on ROMS-PISCES with open boundaries. The mixed layer increases from relatively homogenously shallow (~20 m) depth during austral summer, to values exceeding 100 m during the cooler months. During winter, a strong latitudinal gradient in MLD is present, with the average MLD decreasing in depth towards the low latitude.**

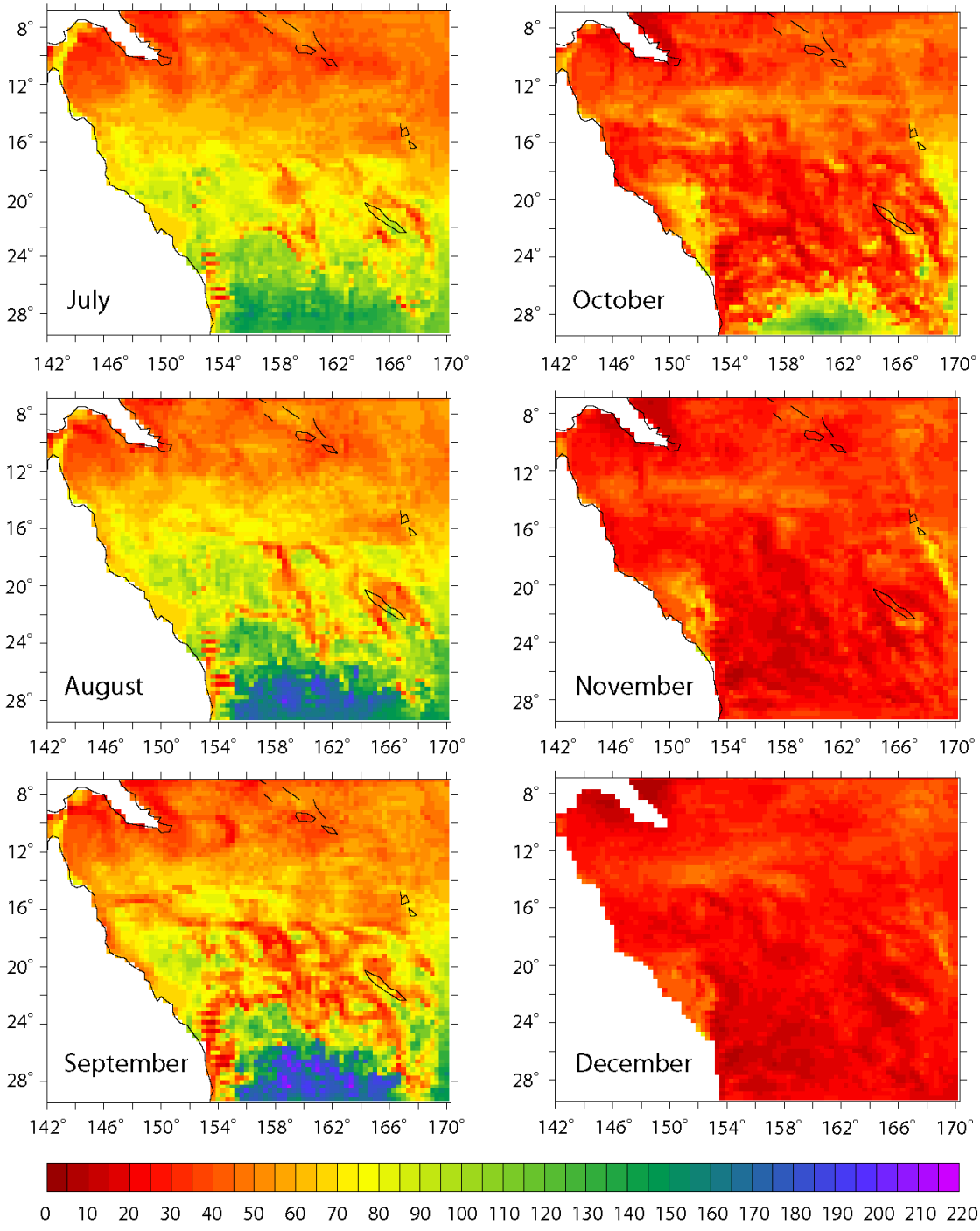


**Figure 8.4.2 continued.**

Figure 8.4.2 shows the seasonality of the modelled MLD. Comparable to the behaviour of the observed MLD variability (cf. section 6.3.2.2), the simulated MLD increases from relatively homogenously shallow (~20 m) depth during austral summer, to values exceeding 100 m during the cooler months. During winter, a strong latitudinal gradient in MLD is present, with the average MLD decreasing in depth towards the low latitude. The larger range in annual MLD variability in the southern Coral Sea is visualised in Figure 8.4.3.

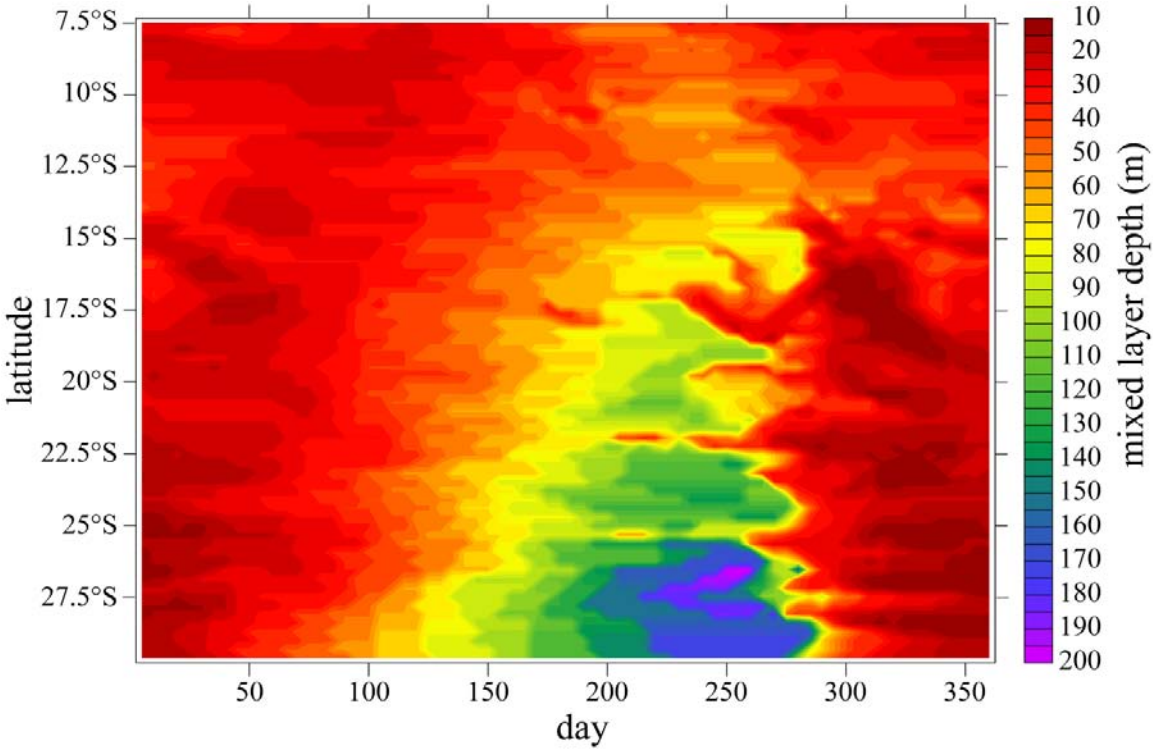


**Figure 8.4.3. Seasonal evolution of the ROMS-derived mixed layer depth (MLD) field in the Coral Sea in a latitudinal transect at 157°E. The transect begins at 7°S and ends at 29.5°S. The time indices are displayed in 3-day time steps over a one-year period (360 days) from January 2$^{nd}$ to December 29$^{th}$. At low latitudes, the MLD is consistently shallower than 70 m whereas at high latitudes, the MLD varies seasonally, with a deepening occurring during the austral winter. Consequently, a zonal gradient of the MLD is formed in winter, with a deeper mixed layer occurring at higher latitudes, whereas in summer, the MLD is homogeneous throughout the Coral Sea.**

### 8.4.3 Modelled vs Observed Physical Attributes

The results from the numerical model ROMS closely agrees with the Argo-observed seasonal and regional patterns of temperature and mixed layer within the Coral Sea. Both observed and modelled MLDs are shallow (<70 m) throughout the Coral Sea during austral summer and are deepening towards the cooler winter months. This mixed layer thickening is more evident in the higher latitudes, with the maximum observed winter MLDs exceeding 200 m in both Argo and ROMS.

There is a clear latitudinal gradient in temperature throughout the year in both datasets. However, as a result of the substantially greater spatial coverage in ROMS, the influence of the dominant currents (SEC, EAC and Hiri current) are more evident in the modelling output, with cooler water moving northwards due to the Hiri current and warmer water southward with the EAC. Although this current-induced temperature variability is not as apparent in the Argo dataset (cf. Figure 6.3.4), an investigation of the spatial variability of the observed ocean heat content did reveal the strong influence of the regional currents, most notably a relatively low OHC in the north-western Coral Sea due to the Hiri current (cf. Figure 6.3.12). The main reason for the Hiri current showing greater presence and influence compared to the EAC in the observational dataset is owed to the Coral Sea bathymetry: while there are numerous Argo floats that travelled northward (due to the Hiri current) through a comparatively deep channel (Townsville and Queensland troughs), floats initially moving southwards with the EAC tended to get stranded on the shallow Coral Sea Plateau. Therefore, there are few Argo data available that recorded properties of the EAC, including the southward stream of relatively warm water mass. If, for example, ocean gliders were employed in the region affected by the EAC, patterns very similar to those visible in the ROMS output would be expected.

Remote sensing allows for much greater spatial coverage than Argo floats. In section 6.3.4, monthly SST data was presented that were derived from NASA's MODIS-Terra satellite. That satellite data is used to estimate the accuracy of the ROMS SST data, with the difference between the two data sets shown in Figure 8.4.4 (cf. appendix A2.2 for the method). The agreement is generally quite good, especially considering the strong SST variability on interannual (ENSO) and longer timescales (IPO), with ROMS not differing from the mean observations by more than 2.9°C. In the tropical Coral Sea (north of

20°S), the consistency is best (<1.0°C difference in general) throughout all seasons. ROMS may potentially slightly underestimate the SSTs associated with the SEC, albeit generally by less than 0.5°. The greatest dissimilarity is observed in the southwest Coral Sea, partially associated with the EAC. Compared to the satellite observations over the last decade, the ROMS-simulated EAC appears to be located closer to east coast of Australia, resulting in a potential SST overestimation near the coast (except during austral summer) and an SST underestimation further offshore throughout the year.

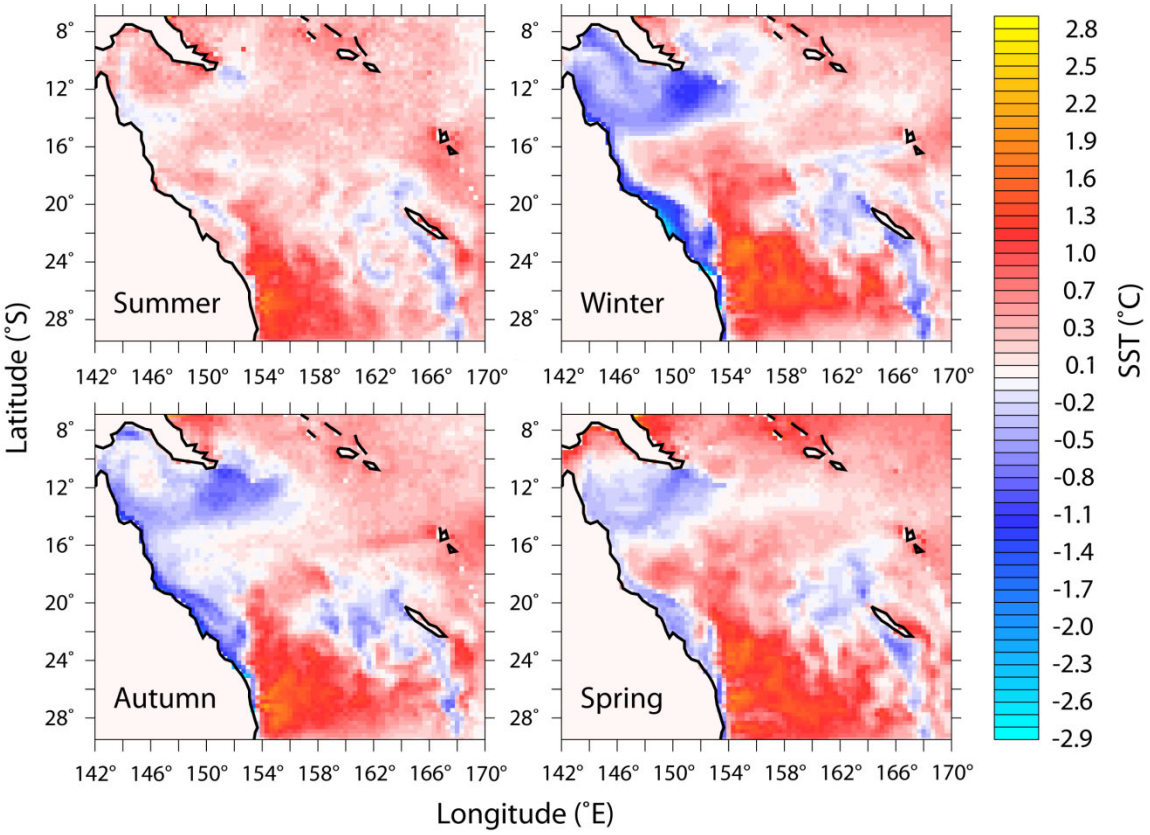


**Figure 8.4.4. Difference between seasonal sea surface temperature (SST) as derived from the NASA's MODIS-Terra satellite and ROMS. The satellite data is based on measurements between February 2000 and October 2010 (Figure 8.4.5). Negative values imply that the ROMS SST is higher than observed by satellite over that decade. These differences are small relative to the observed mean SSTs within the Coral Sea (e.g. Figure 8.4.5), but interannual variations may be more significant (see below).**

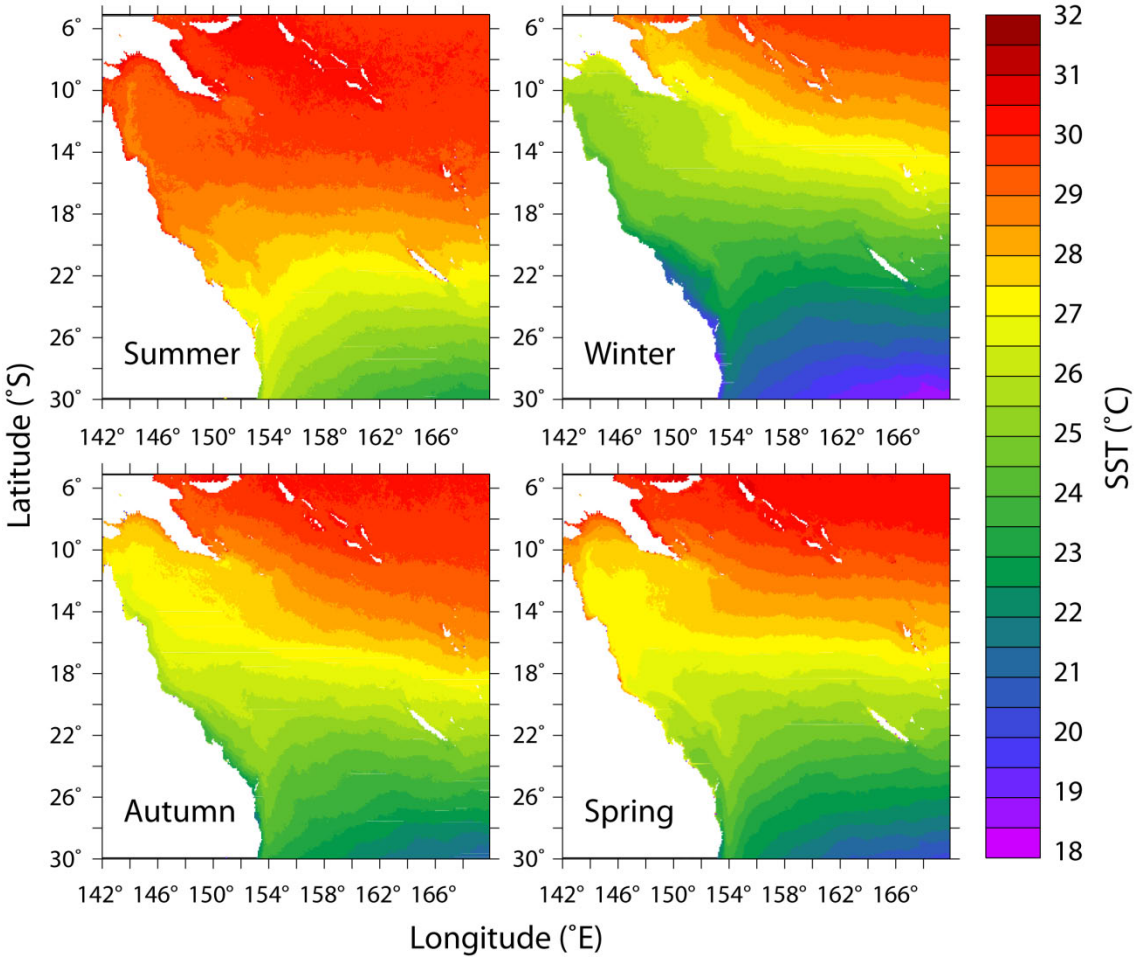


**Figure 8.4.5. Seasonal mean sea surface temperature (SST, 11 micron day) obtained from MODIS-Terra, with all data from 2000/02/01 to 2010/10/01 included.**

A closer analysis of the interannual SST variability within the Coral Sea shows the significant impact of climate signals such as ENSO. In Figure 8.4.6, the mean monthly difference between satellite data and ROMS is shown for July, the month that shows the greatest differences between the two datasets. The equivalent data is also shown for January (Figure 8.4.7), a month known to be strongly influenced by ENSO events.

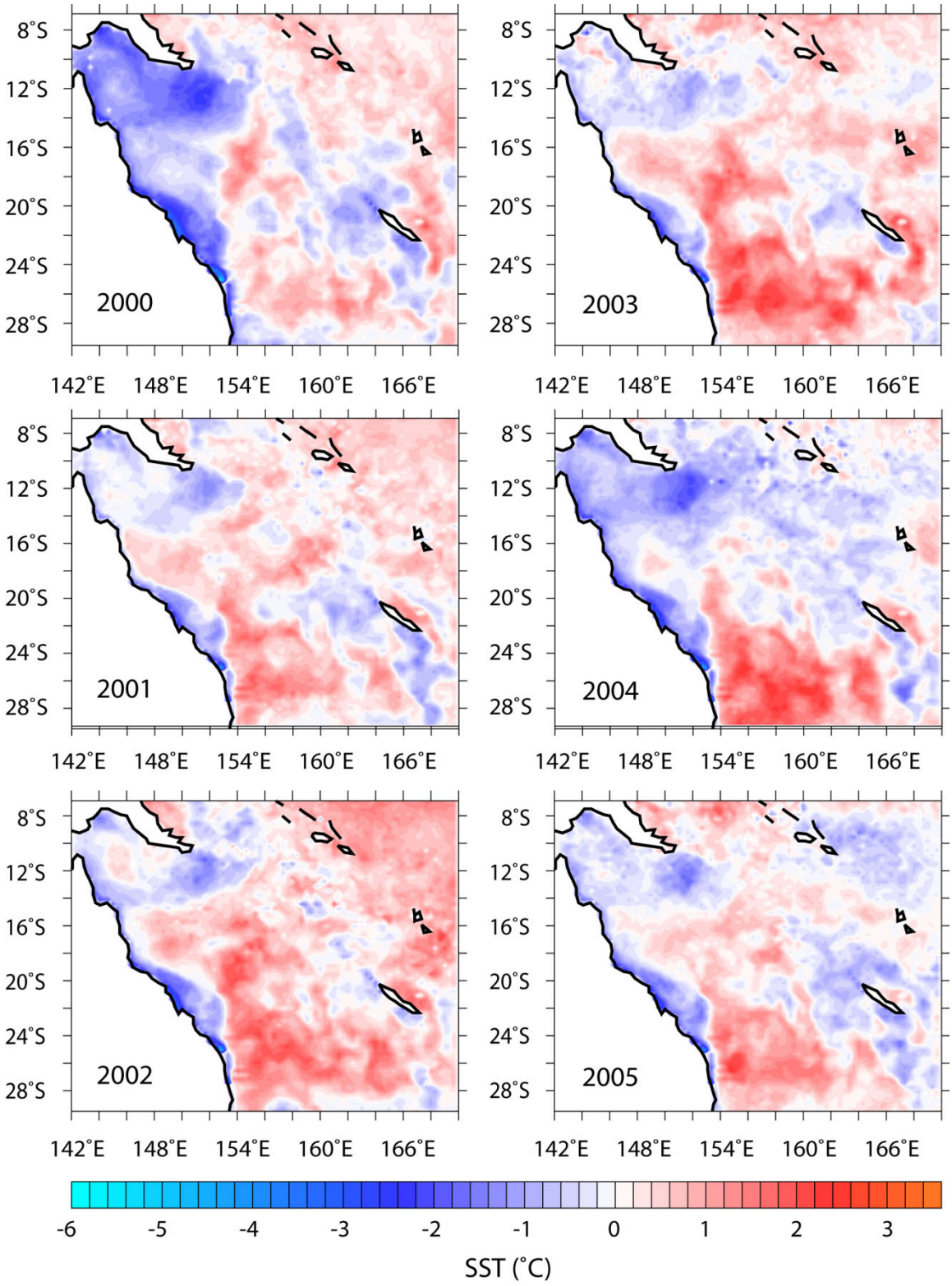


**Figure 8.4.6. Mean difference between satellite-observed and ROMS-modelled sea surface temperature (SST) for July, with negative values indicating regions where ROMS exceeds the satellite SST values.**

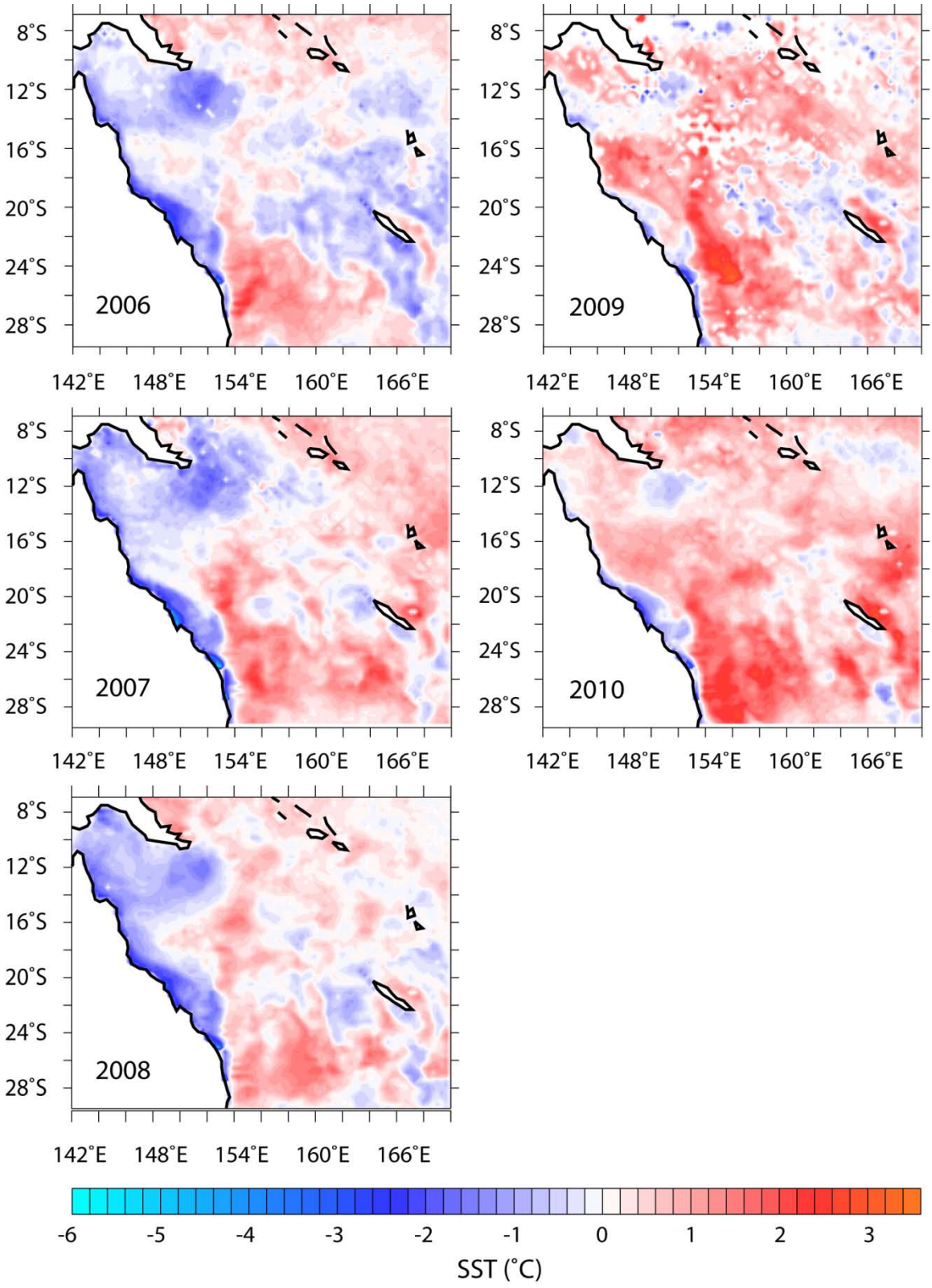


**Figure 8.4.6 continued.**

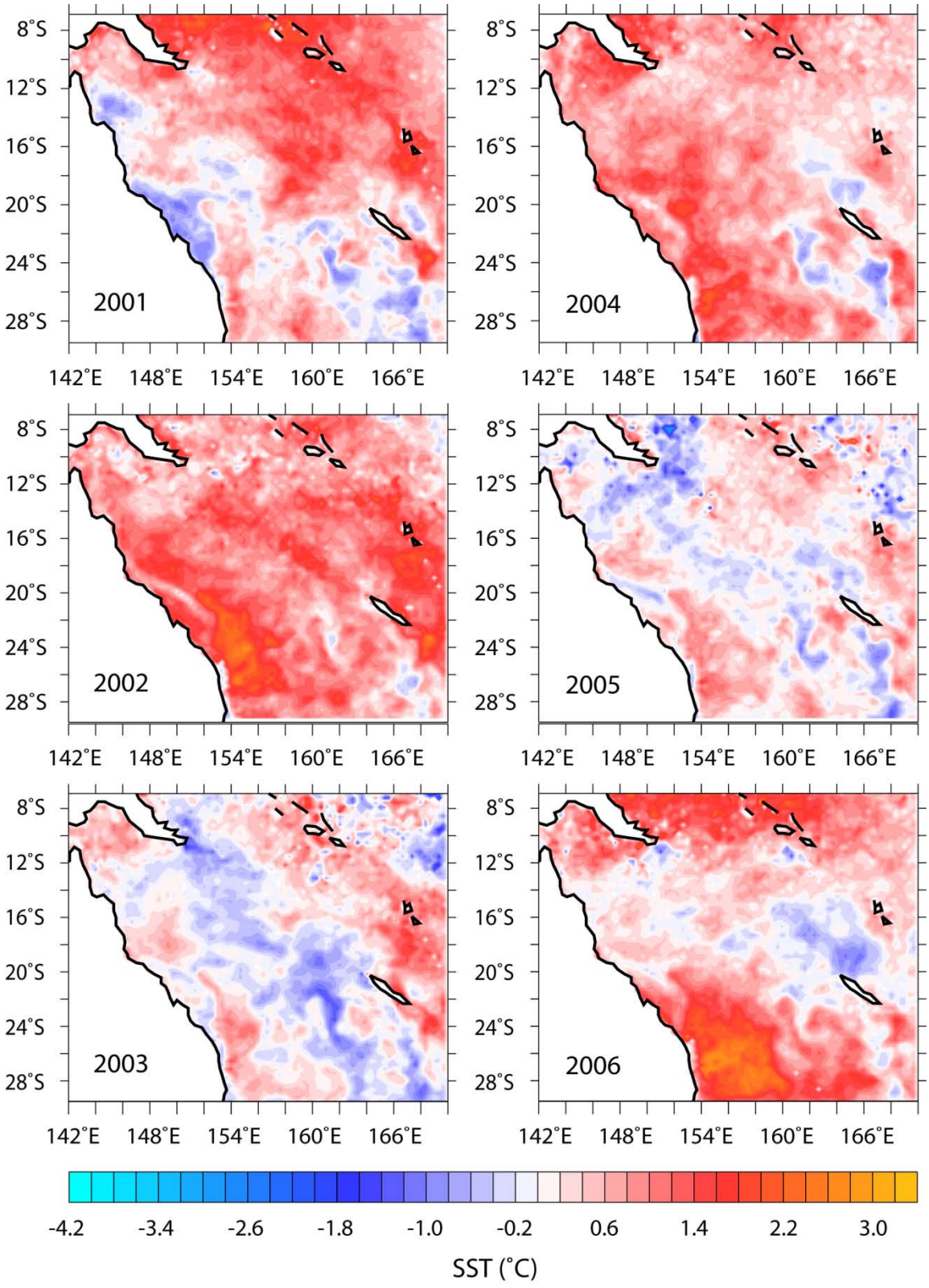


**Figure 8.4.7. As in Figure 8.4.6 but for January.**

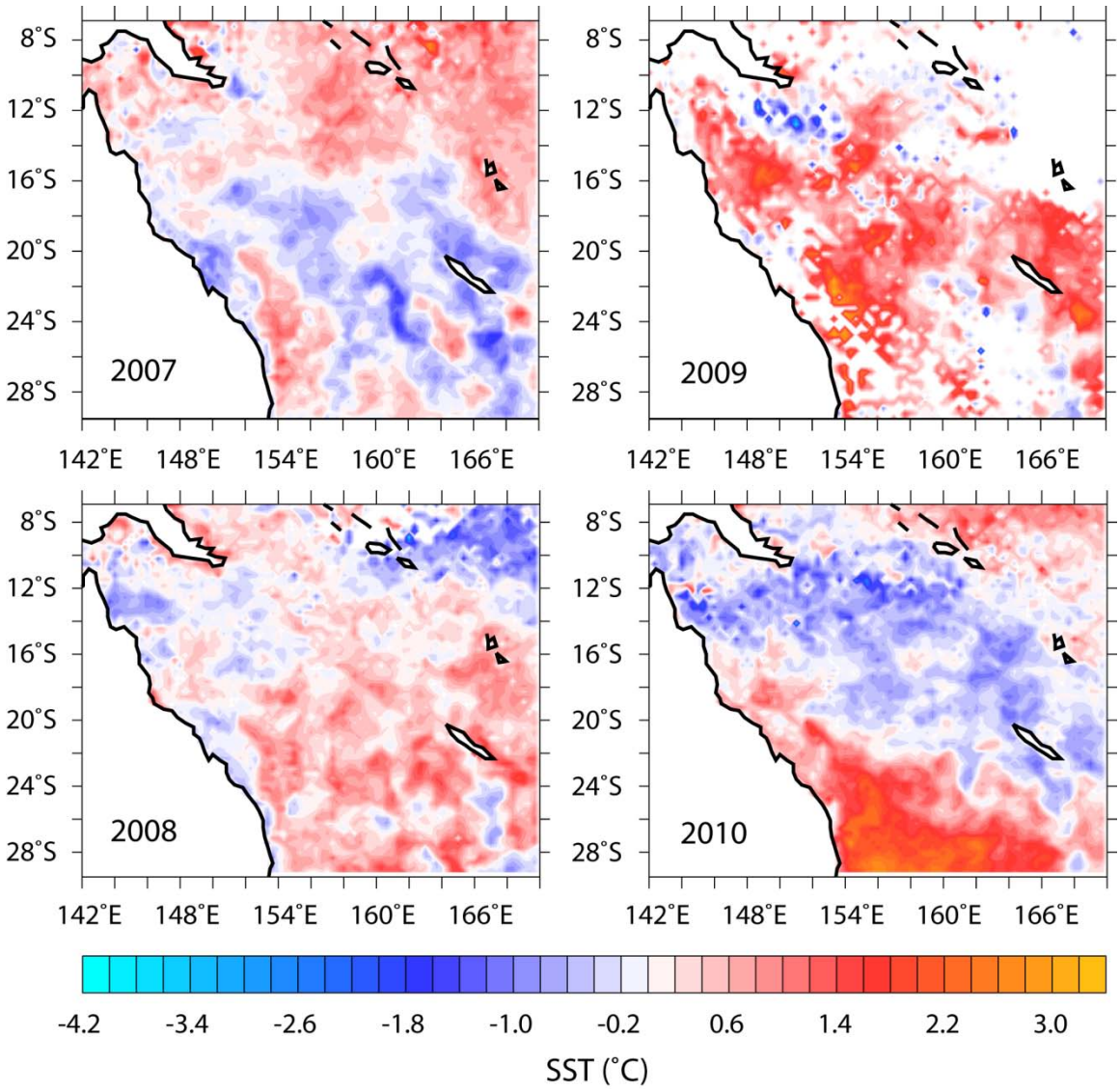


**Figure 8.4.7 continued.**

For July, there are few regions that show a consistent bias. Although the modelled SST in the Gulf of Papua tends to be higher than observed by satellite since 2000, the reverse is observed in the two most recent years (2009 and 2010) throughout most of the northwestern Coral Sea. Similarly, the seemingly overestimated model-SSTs on Queensland's continental shelf agree also quite well with the observations during the last two years. Regions where the bias is consistent throughout the decade include the southeast of Papua New Guinea (SST overestimation) and the south-southwestern Coral Sea (SST underestimation).

In January, ROMS tends to underestimate SSTs throughout most of the Coral Sea compared to prevalent satellite SSTs from 2001, most notably in the year 2002. Interestingly, the difference-patterns observed during weak La Niña years (January 2003, 2005 and 2007) closely resemble each other, with the SSTs being overestimated by ROMS through a northwest-southeast corridor. Also notably, the agreement between ROMS and satellite data is best during these years. In addition, the same pattern of increased accord is also seen for the months of July preceeding austral summers characterised by weak La Niñas (July 2002, 2004 and 2006). With the onset of an ENSO event generally occurring mid-year, these results may indicate that the ROMS SST is slightly biased towards a weak La Niña state. Ideally, if detailed interannual SST forcing fields are not available, the SST forcing should be closest to a neutral ENSO state.

To what exact extent these differences are associated with climate and short-term variability, rather than modelling accuracy, is difficult to evaluate due to detailed observational SST fields only being available for the most recent years. The last decade is characterised by weak to neutral ENSO events. Due to this absence of strong ENSO events (with the exception of 2010; cf. SOI in Figure 8.4.8) since 2000, and the relatively short time span of satellite data (~11 years), it cannot be verified whether the SST biases observed here would persist during major ENSO events. Previous studies (e.g. Quinn *et al.*, 1998; Cravatte *et al.*, 2009) that incorporated multi-decadal data indicate interannual and decadal SST changes clearly in excess of 0.5°. Considering that the ROMS SST presented here was simulated without considering interannual and multi-decadal climate variability, and mean Coral Sea SSTs tend to vary quite significantly due to, for example, ENSO events, the agreement between ROMS and the observations can be considered quite reasonable.

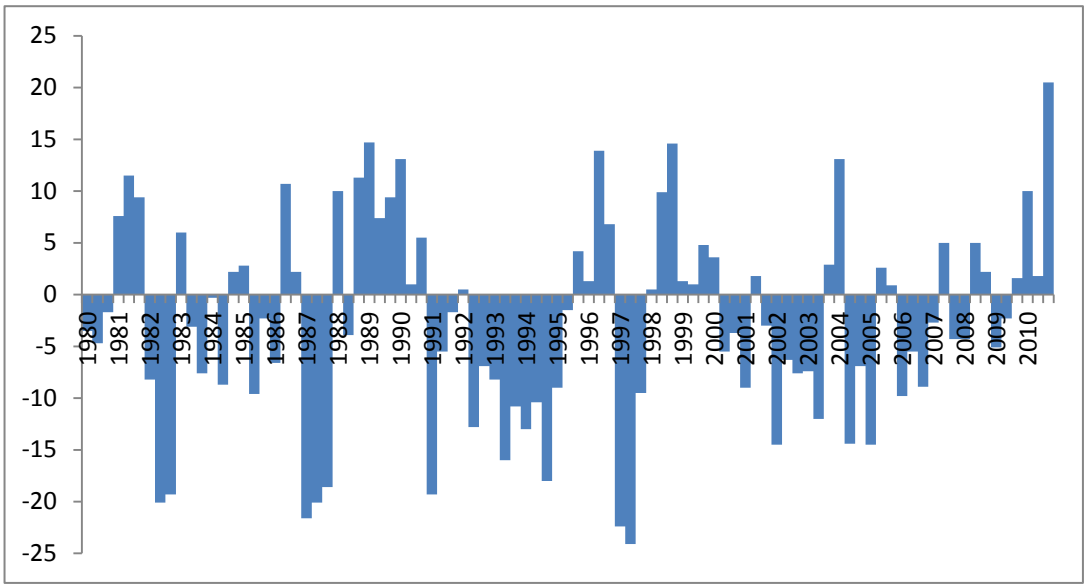


**Figure 8.4.8. The Southern Oscillation Index (SOI) for May-July since 1980. The SOI measures the difference in sea level pressure between Tahiti and Darwin. El Niño (La Niña) events are linked to negative (positive) SOI values.**

## 8.5 Ocean Biochemistry

### 8.5.1 Chlorophyll

The forcing for chlorophyll-a (Chl-a) in ROMS is obtained from SeaWifs observations, the same data source as presented in Figure 5.4.1. ROMS underestimates near-coastal Chl-a, which is expected not only due to its limited capability to represent the coastal region accurately but also, more importantly in this instance, because benthic diatoms and other micro-algae were not included into the ROMS code.

More problematic, due to the vast area affected, are the relatively high offshore chlorophyll levels modelled – generally 0.3-0.6 mg/m$^3$ (Figure 8.5.1). Based on satellite Chl-a data, chlorophyll levels within the Coral Sea are generally very low, normally not exceeding 0.2 mg/m$^3$ (Figure 5.4.1). Mesozooplankton, a closely linked parameter (ROMS keeps the chlorophyll/phytoplankton ratio constant), is likely overestimated as well, whereas the diatom and microzooplankton distributions appear reasonable.

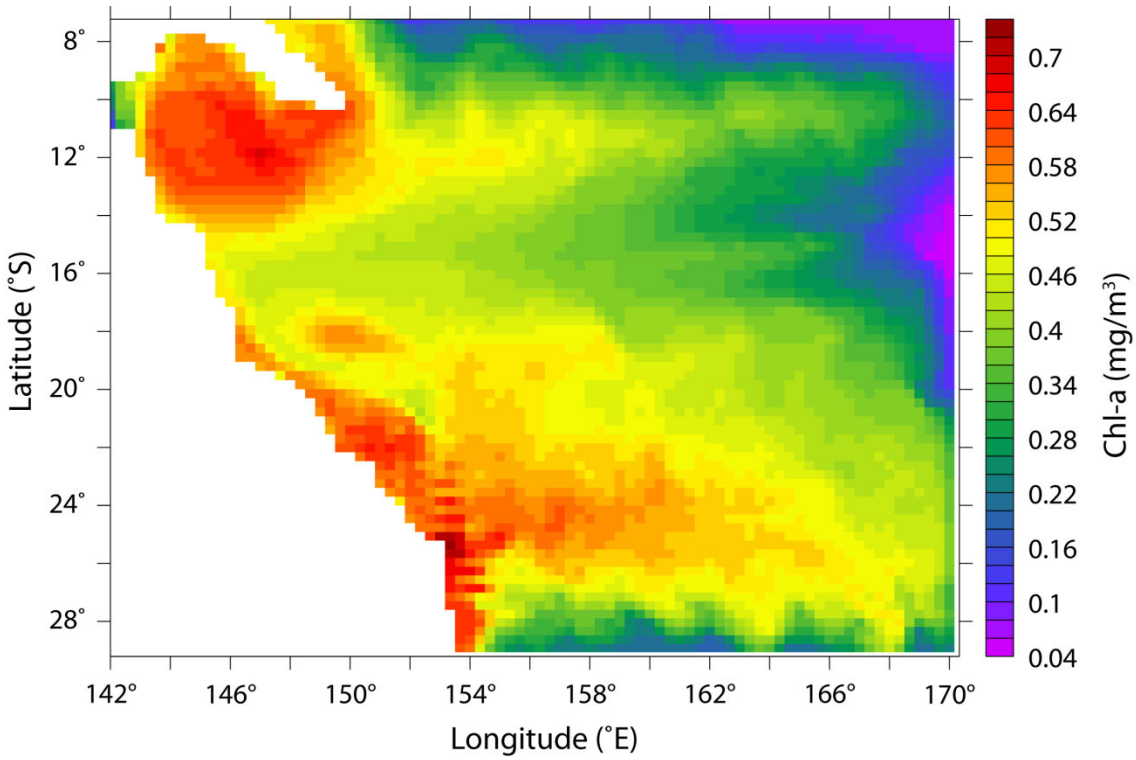


**Figure 8.5.1. Mean chlorophyll-a (Chl-a) for a 1-year model period. Chl-a represents the total Chl-a calculated by ROMS, i.e. chlorophyll produced by non-benthic organisms (i.e. phyto- and zooplankton).**

Regions where observations and modelling Chl-a output more closely agree are situated near the model boundaries (i.e. in the southern, eastern and northern Coral Sea), as well as within the surface region of the SEC. This signals that boundary conditions are appropriate for Chl-a, with the high modelled Chl-a values being a result of the model parameterisation within the Coral Sea. This is also supported by the Chl-a output produced from a closed-boundary run, which produces even higher Chl-a concentrations, especially north of 18°S and east of 150°E, and along the boundaries.

To eliminate the possibility that the high chlorophyll levels are a product of the 10-year spin-up rather than the model parameterisation, model output from the 6$^{th}$ (spin-up) and 11$^{th}$ year were compared (from the open-boundary runs). The agreement between the two model years (±0.05 mg/m$^3$ in general), and the absence of a trend or bias between the two years, indicate that little would be gained from using a longer spin-up period.

Given these problems, modelled chlorophyll does not appear to be a good proxy for real chlorophyll, and therefore the model's related predictive capacity to estimate productivity and carbon fluxes is limited.

### 8.5.2 $CO_2$

Model $CO_2$ patterns vary significantly depending on the chosen model parameterisation. For the present-day scenarios, ROMS-PISCES was forced with an atmospheric $pCO_2$ value of 380 µatm, corresponding to the present-day $pCO_2$ concentration (Figure 8.5.2). The Coral Sea appears to be mostly a sink of $CO_2$ when all borders are kept open (Figure 8.5.3). Only the Gulf of Papua – which is associated with the Hiri current and a warm, shallow ocean - demonstrates a weak seasonal $CO_2$ efflux during austral summer.

Conversely, during model runs with closed boundaries, a more varied pattern emerges, with a general trend of higher efflux in the lower latitudes being present (Figure 8.5.4). Although the north-south trend is expected owing to the $CO_2$-temperature relationship, surprisingly, the strongest high-latitude $CO_2$ sinks appear to be connected to austral spring and summer rather than the cooler winter months.

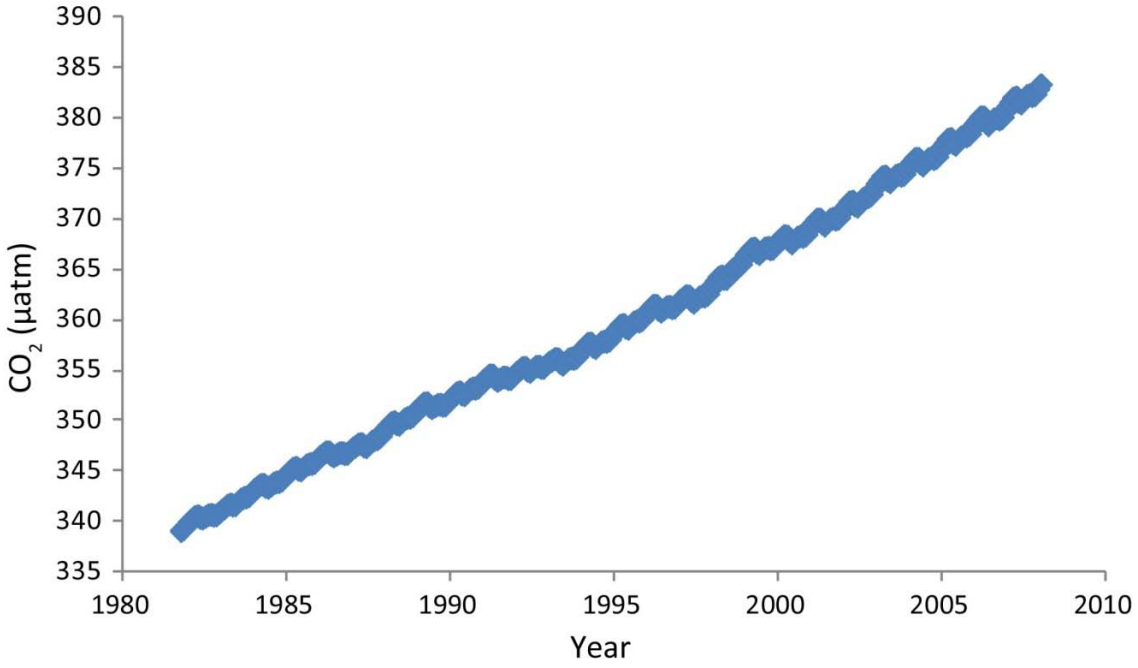


**Figure 8.5.2. Evolution of atmospheric $CO_2$ collected at American Samoa (data from Keeling *et al.*, 2008).**

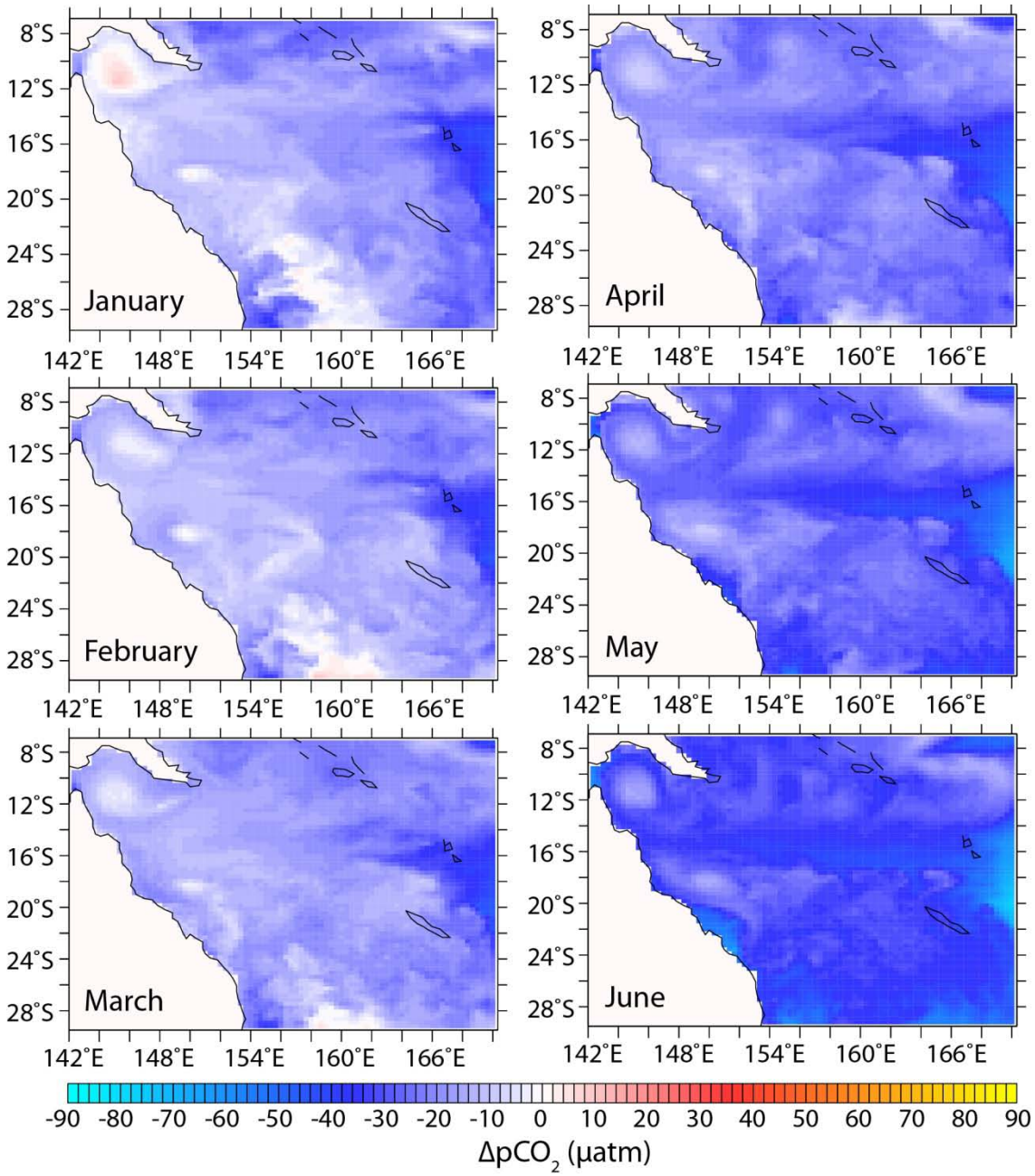


**Figure 8.5.3. Monthly averages of the difference between oceanic and atmospheric *p*$CO_2$ (Δ*p*$CO_2$ ocean-atm) within the Coral Sea based on ROMS-PISCES with open boundaries. Negative (blue) values imply a $CO_2$ flux into the ocean as a result of atmospheric $CO_2$ exceeding the oceanic $CO_2$ level.**

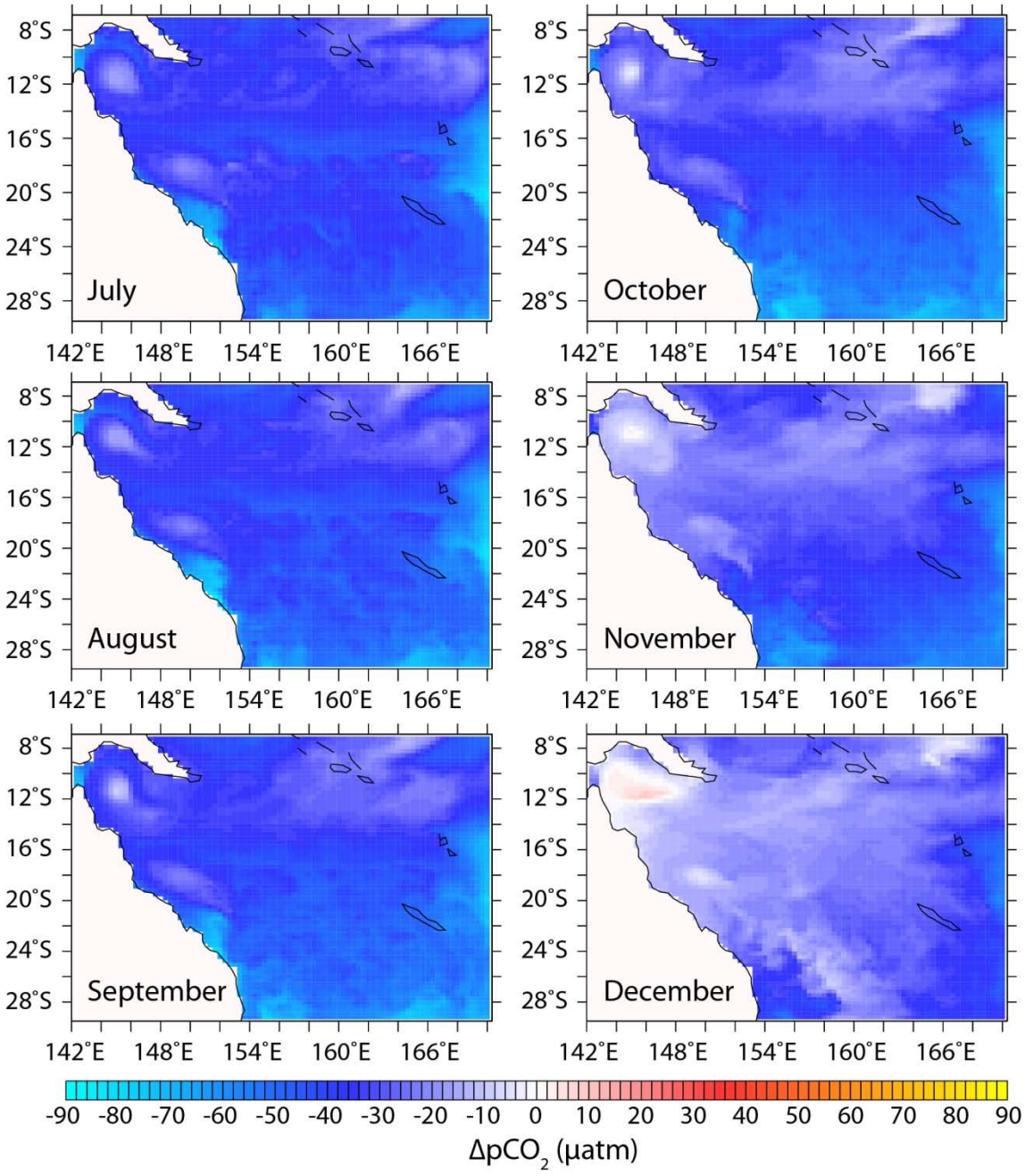


**Figure 8.5.3 continued.**

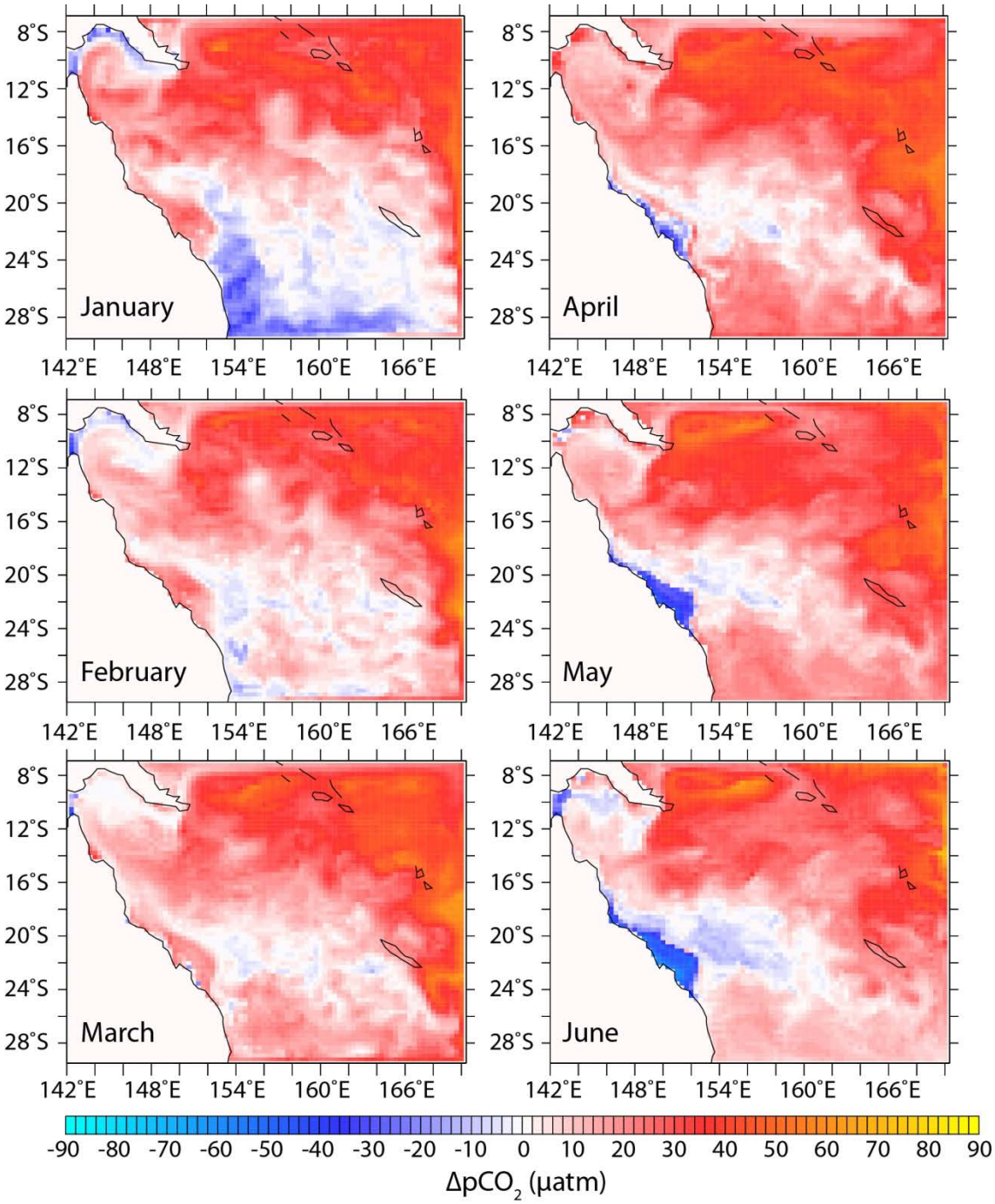


**Figure 8.5.4. As in Figure 8.5.3 with closed boundaries.**

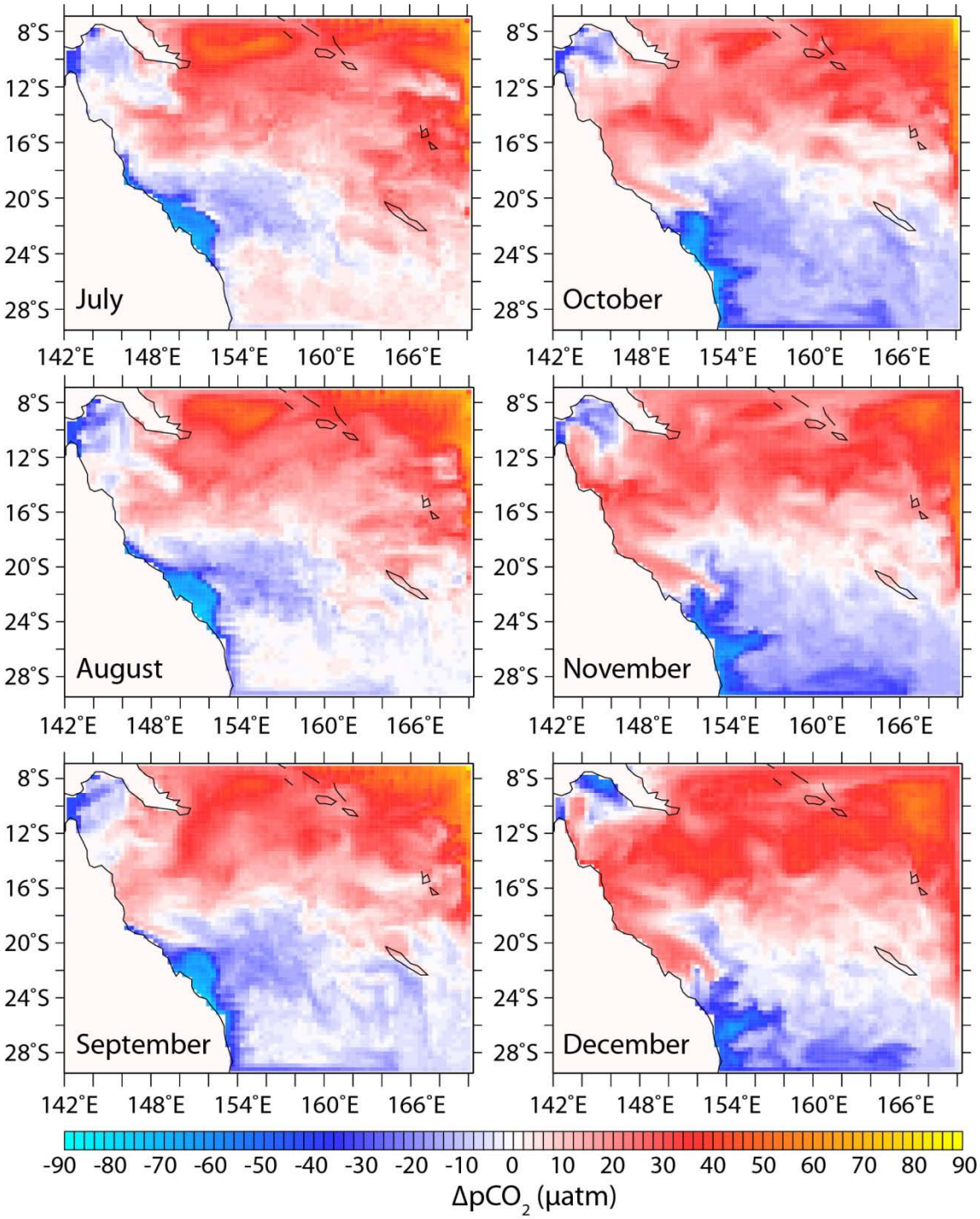


**Figure 8.5.4 continued.**

In both scenarios, the strongest $CO_2$ influx is linked to the shallow Queensland continental shelf area. A possible explanation is the lower oligotrophic state of near-coastal regions, with increased primary productivity potentially resulting in a lowering of

sea surface $CO_2$ levels. Due to the general absence of observational data on shallow shelf regions, it was not possible to verify whether the obtained numerical output closely reflects the actual geochemical patterns. However, two ship cruises through the Torres Strait do indicate that, at least in the northwest, $CO_2$ levels in warm, shallow regions should be higher than in the open Coral Sea, a feature not recreated by the model.

There are two model features that negatively impact on the accuracy of ROMS-PISCES in shallow and near-coastal regions. Firstly, the absence of benthic parameters in the model code signifies that $CO_2$-producing corals and other organisms are not represented. Secondly, the minimum depth was set at 75 m due to model constraints. That is, a maximum depth of 75 m was assigned to regions where the bathymetry is shallower than 75 m. Possible effects might include cooler temperatures throughout the water column (due to distribution of the heat content over a larger area) and consequently lower $pCO_2$ (since $CO_2$ is more soluble in cooler water).

The unexpectedly large difference between open- versus closed-boundary model $\Delta CO_2$ fields, and particularly the very low $\Delta CO_2$ values in the open-system scenario, may be linked to the usage of historical forcing fields. To try to compensate for the possibly artificially low $\Delta pCO_2$ in the open-system model (Figure 8.5.3), the open-boundary $\Delta pCO_2$ field was shifted by +40 μatm to have a comparable distribution about 0 to the closed-boundary results (Figure 8.5.5). This method also helped to determine whether the $\Delta pCO_2$ fields for open- versus closed-boundary model outputs have spatial patterns more similar than Figures 8.5.3 and 8.5.4 suggest. The data shift improved the comparison between the two model scenarios. The cooler months (July-November) of the shifted open-system model data now more clearly show the expected decline in $\Delta CO_2$ with increasing latitude due to the negative relationship between oceanic $CO_2$ and temperature. Another highlighted feature in the shifted output is the incoming SEC (April-August), moving relatively $CO_2$-poor water westwards. This attribute is absent in the closed-boundary scenario since currents such as the SEC and EAC are not allowed to move freely across the model boundaries, affecting all surface oceanographic parameters.

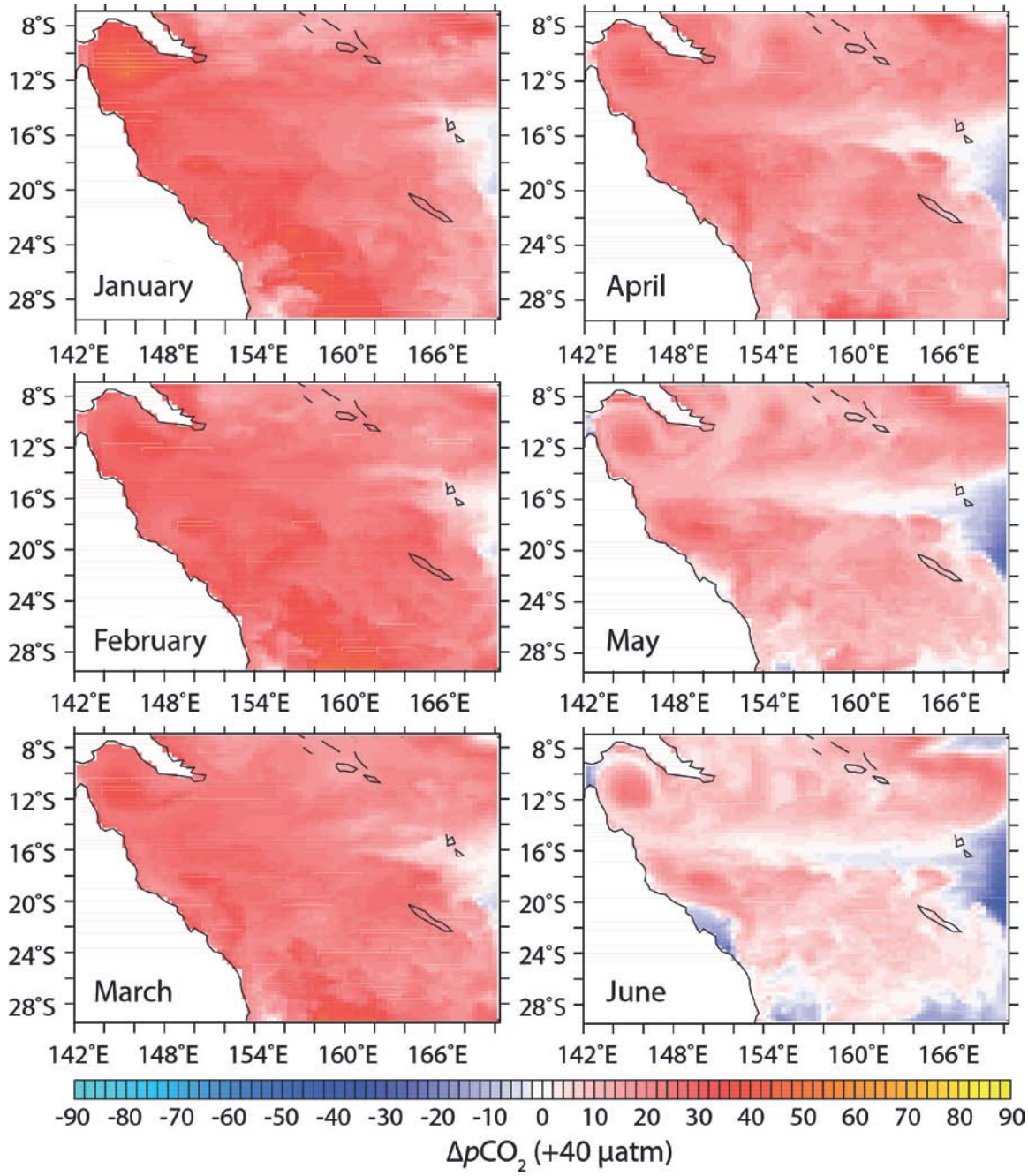


**Figure 8.5.5. Monthly averages of the difference between oceanic and atmospheric $pCO_2$ ($\Delta pCO_2$ ocean-atm), shifted by +40 µatm, based on ROMS-PISCES with open boundaries.**

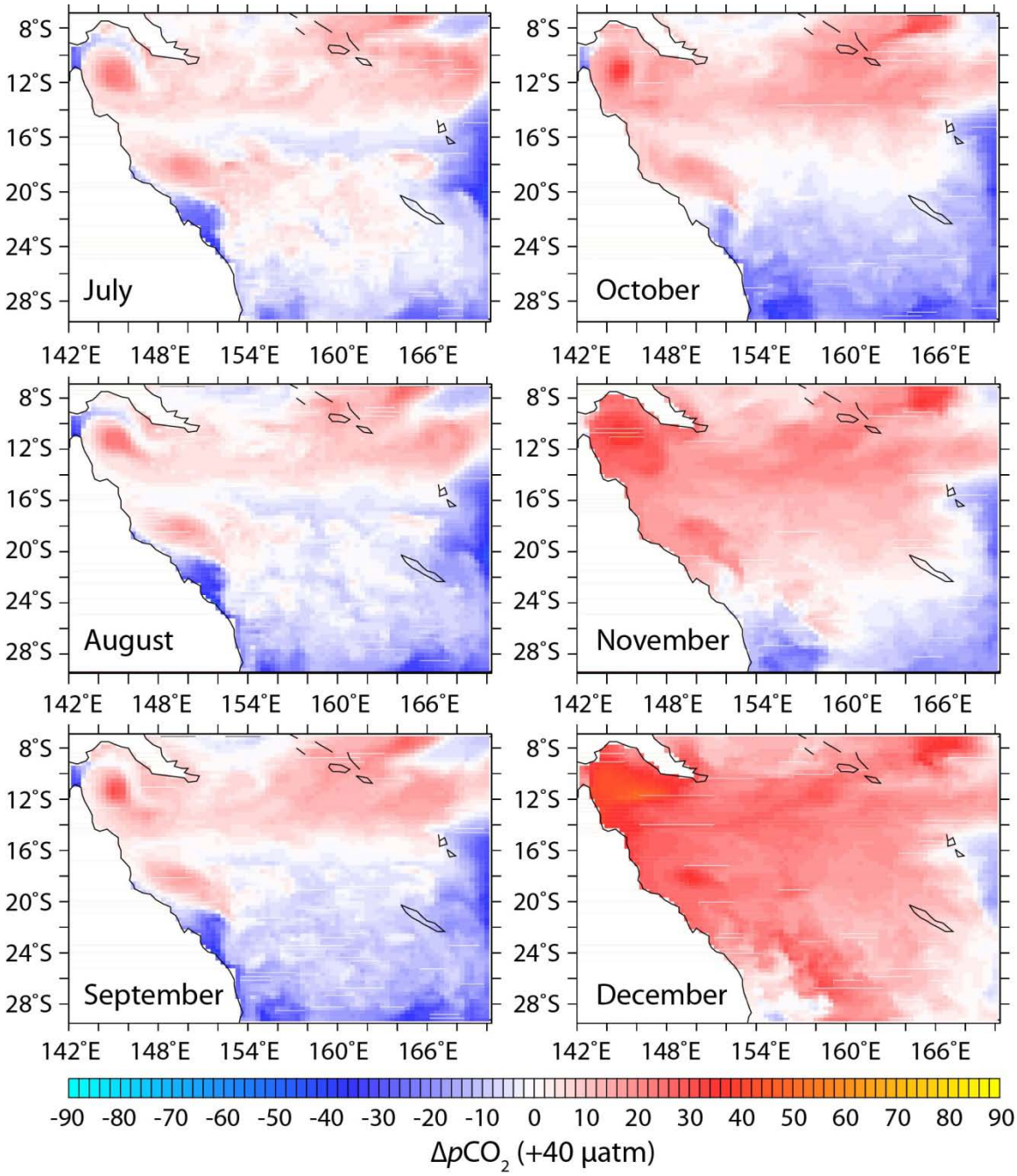


**Figure 8.5.5 continued.**

The partial success in obtaining expected $\Delta CO_2$ patterns by shifting the open-boundary $\Delta CO_2$ may also indicate that open-boundary model runs rely heavily on forcing fields (especially temperature) to match the period equivalent of the input atmospheric $CO_2$ (380 µatm for present-day scenarios in this study, representing a post-2000 value). That is, the mean seasonal fields used for the model forcing most likely best correspond

to a period which precedes the time when observed atmospheric $CO_2$ value surpassed 380 µatm by a few decades. The ORCA-derived forcing fields were, in turn, mainly obtained from observational WOA05 fields predominantly derived from in situ data collected in the second half of the 20$^{th}$ century. The 'improvement' in the visual results by shifting $\Delta CO_2$ by +40 µatm (Figure 8.5.5) indicates that atmospheric $CO_2$ may have been set too high for PISCES to accurately represent the carbon parameters. If an atmospheric $CO_2$ value of ~340 µatm had been used, corresponding to observed atmospheric $CO_2$ in the early 1980s (Figure 8.5.2), this may have produced open-boundary model output that more closely matched expectations. However, problems with the summer months in the open-system model remain.

The summer period (December-March) of the open-boundary model run exhibits the most unexpected result, due to the absence of both a latitudinal $\Delta CO_2$ gradient and visible impact by the major Coral Sea currents (including the SEC, EAC and Hiri current). Their nonexistence may indicate insufficient connection between marine temperature and oceanic $CO_2$ (among other parameters) in PISCES, resulting in $CO_2$ patterns that are not strongly correlated to the temperature field. Alternately, PISCES does not adequately model the open system case. Unfortunately, due to time constraints and the model code complexity, it was not possible to determine which parameters caused these potentially spurious results.

### 8.5.3 *p*H

Simulated *p*H patterns also vary depending on the chosen model parameterisation. With open-boundary model runs, *p*H exhibits a seasonal increase mid-year owing to cooler SSTs towards austral winter (Figure 8.5.6), with a seasonal amplitude of ~0.05 units. The influence of the Southern Equatorial Current (SEC) is quite clearly evident, especially during the cooler months, with waters associated with the SEC and its divergent flows (Hiri current to the north and EAC to the south) being characterised by higher *p*H levels.

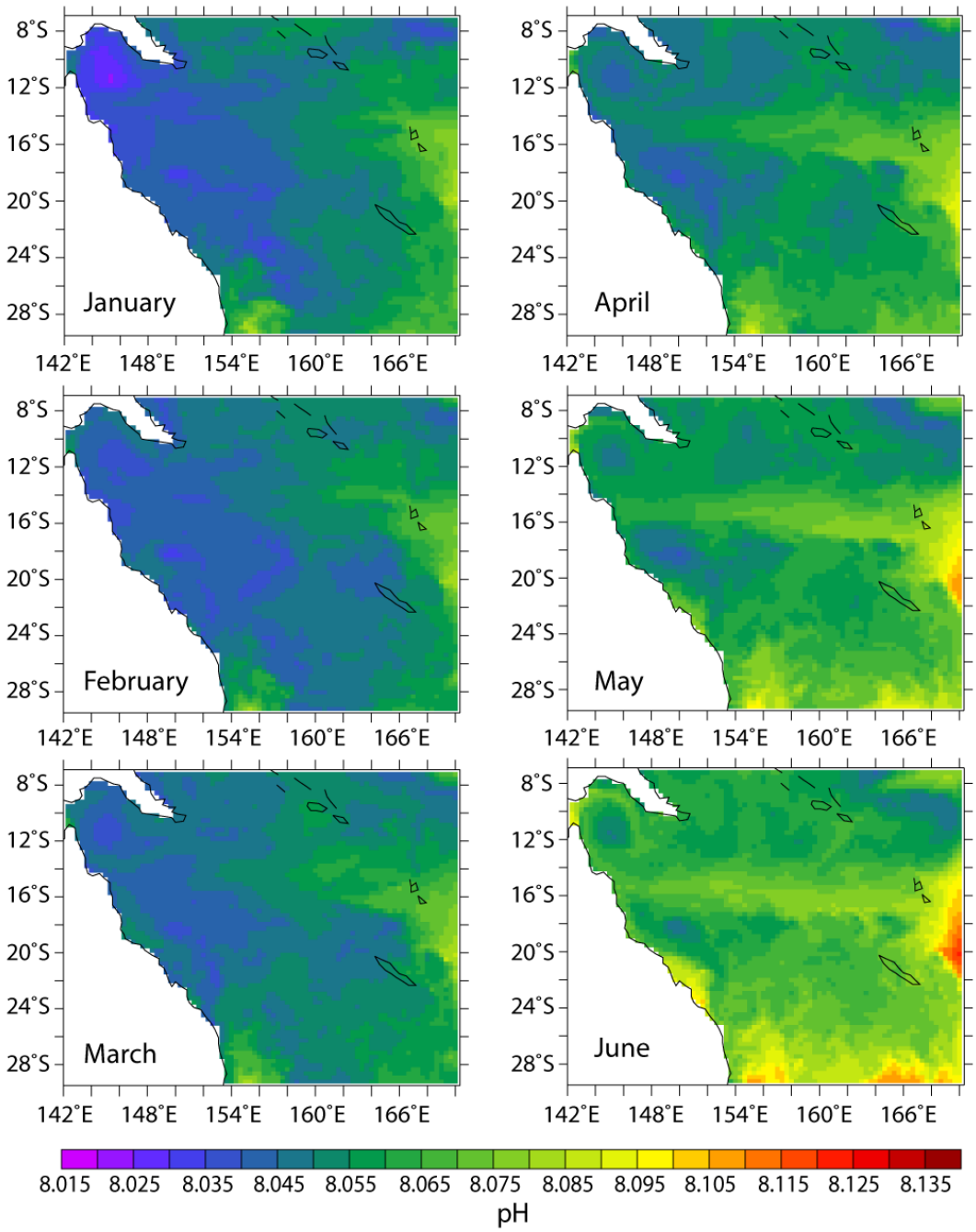


**Figure 8.5.6. Monthly averages of the *p*H field within the Coral Sea based on ROMS-PISCES with open boundaries. As a result of cooler SSTs towards austral winter, *p*H displays a seasonal increase mid-year. A strong boundary effect is evident, especially at the eastern and southern border.**

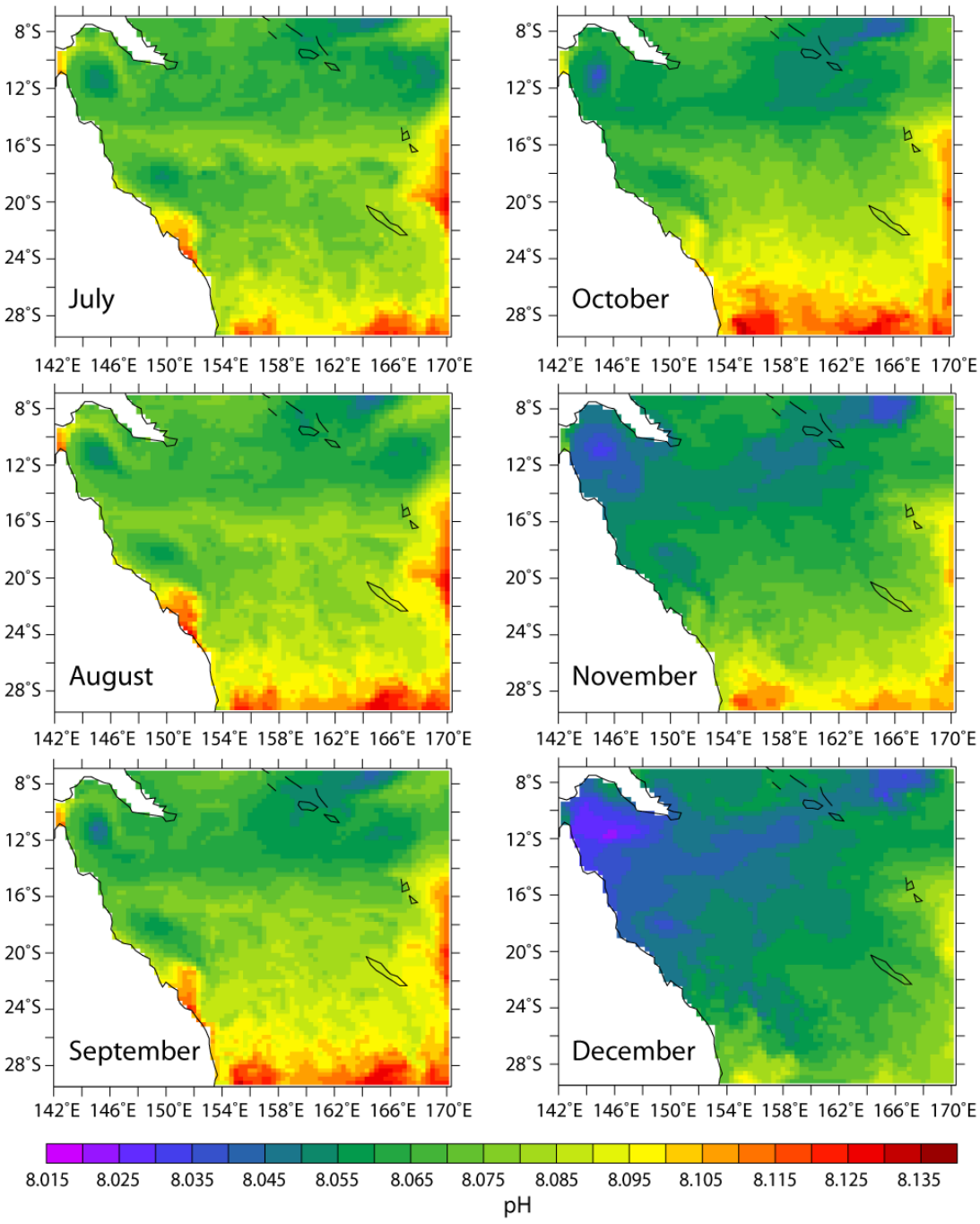


**Figure 8.5.6 continued.**

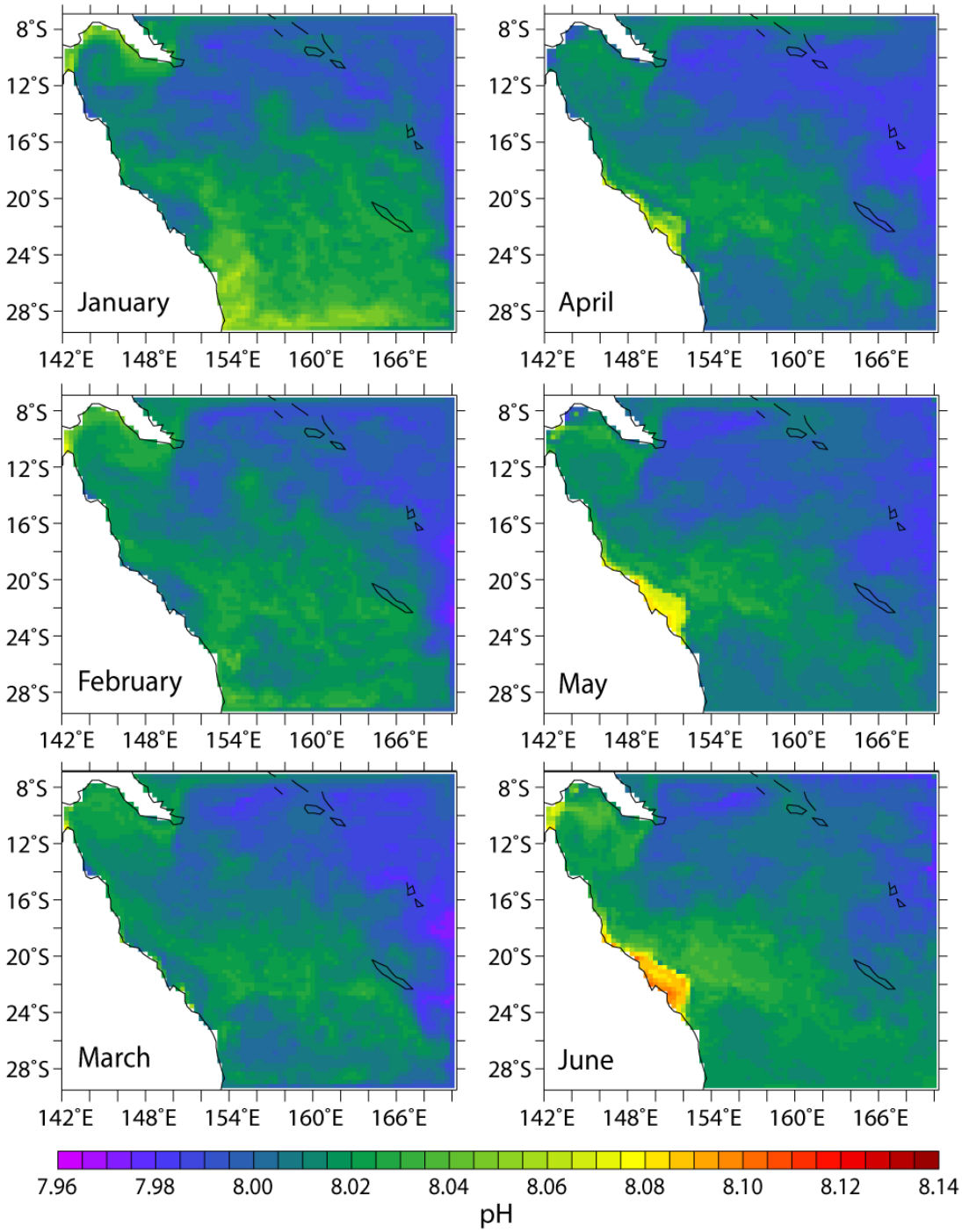


**Figure 8.5.7. Monthly averages of the *p*H field within the Coral Sea based on ROMS-PISCES with closed boundaries. Throughout the model year, a north-south gradient in *p*H is evident, with consistently higher values being observed in the cooler high-latitudes. The negative relationship between temperature and *p*H is also evident seasonally, with *p*H increasing mid-year in both the open ocean and near coastal areas. It is possible that the more distinct increase in near-coastal areas is due to stronger upper ocean cooling.**

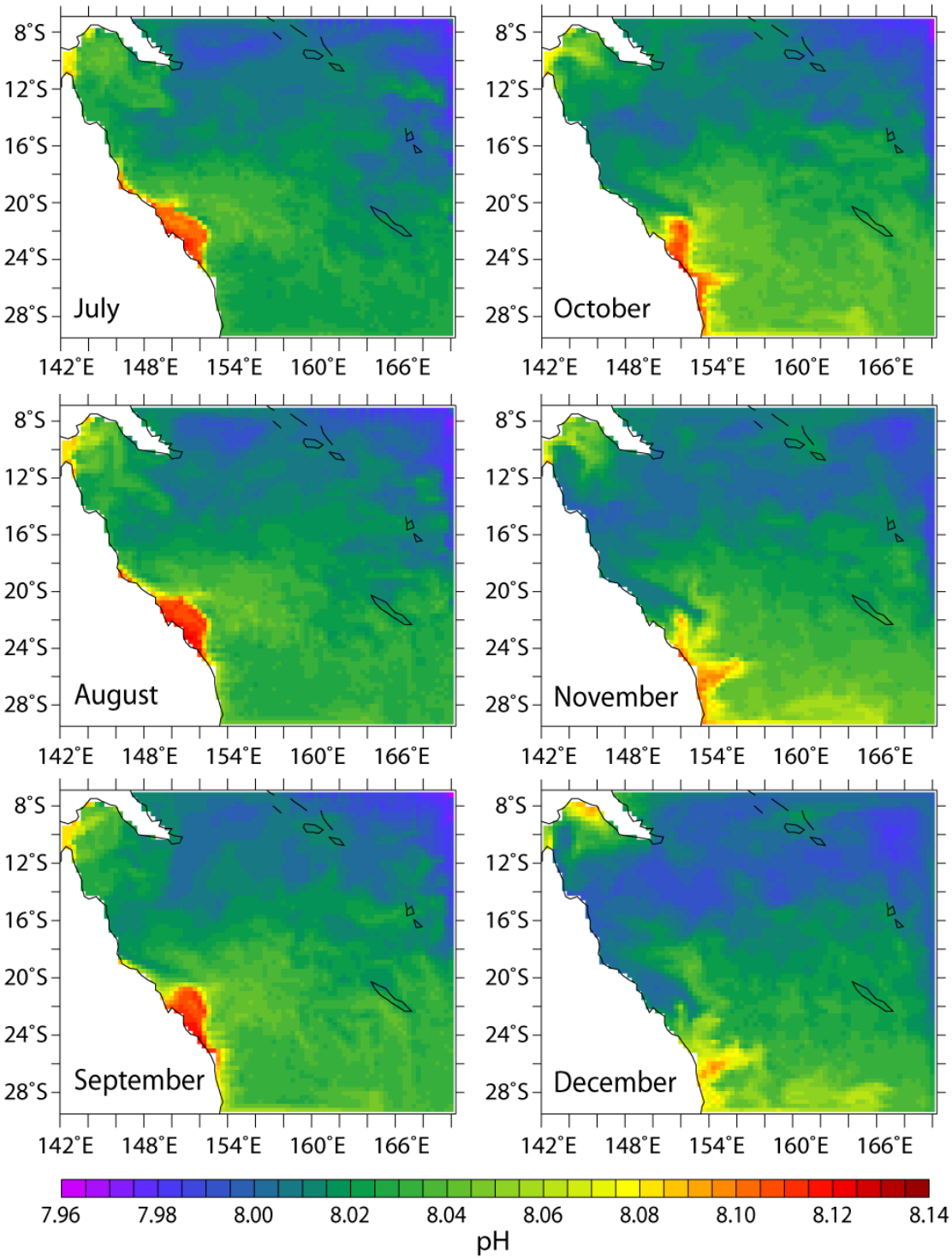


**Figure 8.5.7 continued.**

Whereas there is no strong north-south trend in *p*H in open-boundary simulations, the closed-boundary model output displays a tendency of gradually increasing *p*H towards the cooler high-latitudes (Figure 8.5.7). In addition, the impact of the SEC and associated currents on *p*H levels is minor since closed-boundary simulations do not allow entrance of the SEC from the Pacific.

Both open- and closed-boundary *p*H levels are relatively low compared to observed *p*H, with both simulations reaching maximum mean monthly values of 8.14 units, a value generally exceeded by the WOD *p*H data.

## 8.6 Future Climate Scenarios

Two different IPCC scenarios for predicted atmospheric $pCO_2$ were used to determine likely changes in the biogeochemistry of the Coral Sea during the 21st century. At present, the atmospheric $pCO_2$ concentration is around 380 µatm. It is forecast that $pCO_2$atm will increase to 650-1000 µatm by the end of the 21$^{st}$ century (Houghton *et al.*, 2001). To investigate how future rises in atmospheric $pCO_2$ might impact on the Coral Sea, ROMS-PISCES was forced with atmospheric $pCO_2$ ranging from 380 µatm to 1000 µatm. It has to be noted here that, even though atmospheric $pCO_2$ was increased, the model was forced with the current physical fields (e.g. temperature and wind stress) for the future climate scenarios such that potential future changes in physical oceanography were not taken into account. This further limits the accuracy and usefulness of the biogeochemical forecast since parameters such as wind stress and SST have a significant impact on the carbon cycle.

An increase of atmospheric $pCO_2$ from 380 µatm to 650 µatm results in a decrease of sea surface *p*H by 0.14-0.21 units within the Coral Sea in the model simulation (Figure 8.6.1). *p*H is further reduced if a final atmospheric $CO_2$ concentration of 1000 µatm is assumed. In the latter scenario, a *p*H decline of 0.28-0.36 units is expected. These values agree well with previous estimates (0.2 to 0.4 *p*H units by 2100) (Haugan and Drange, 1996; Brewer, 1997; Gattuso *et al.*, 1998; Wong and Matear, 1998; Wolf-Gladrow *et al.*, 1999; Langdon *et al.*, 2000; Caldeira and Wickett, 2005; Kleypas *et al.*, 2006; Blackford and Gilbert, 2007).

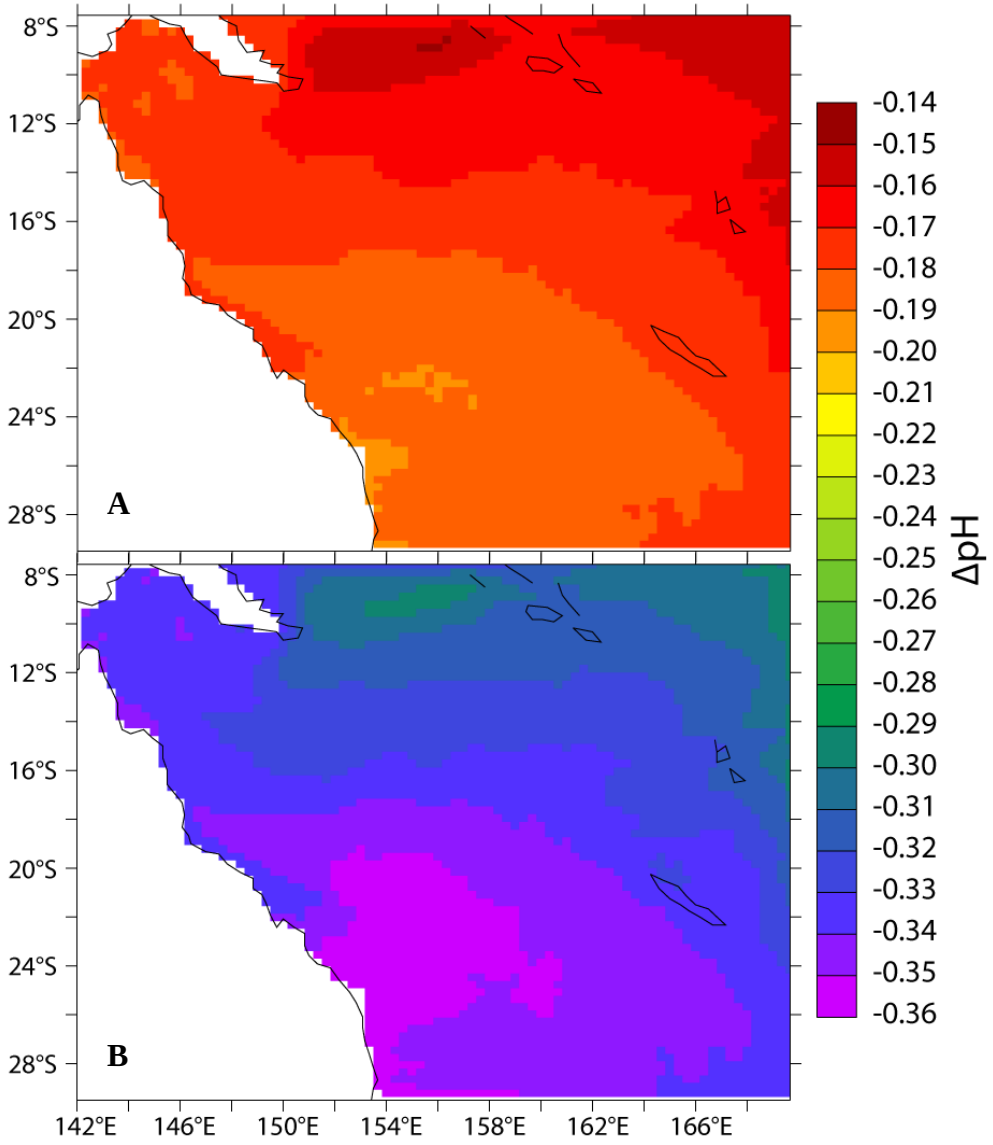


**Figure 8.6.1. Predicted change in yearly averages of *p*H for an increase of atmospheric $pCO_2$ from 380 µatm to A) 650 µatm and B) 1000 µatm. *p*H for both scenarios decreases throughout the study area, with greatest declines occurring in the southwest. If sea surface temperatures in the Coral Sea will increase in future, it would exacerbate the trend towards lower *p*H levels. Possible future changes in marine physics were, however, not incorporated in the simulations.**

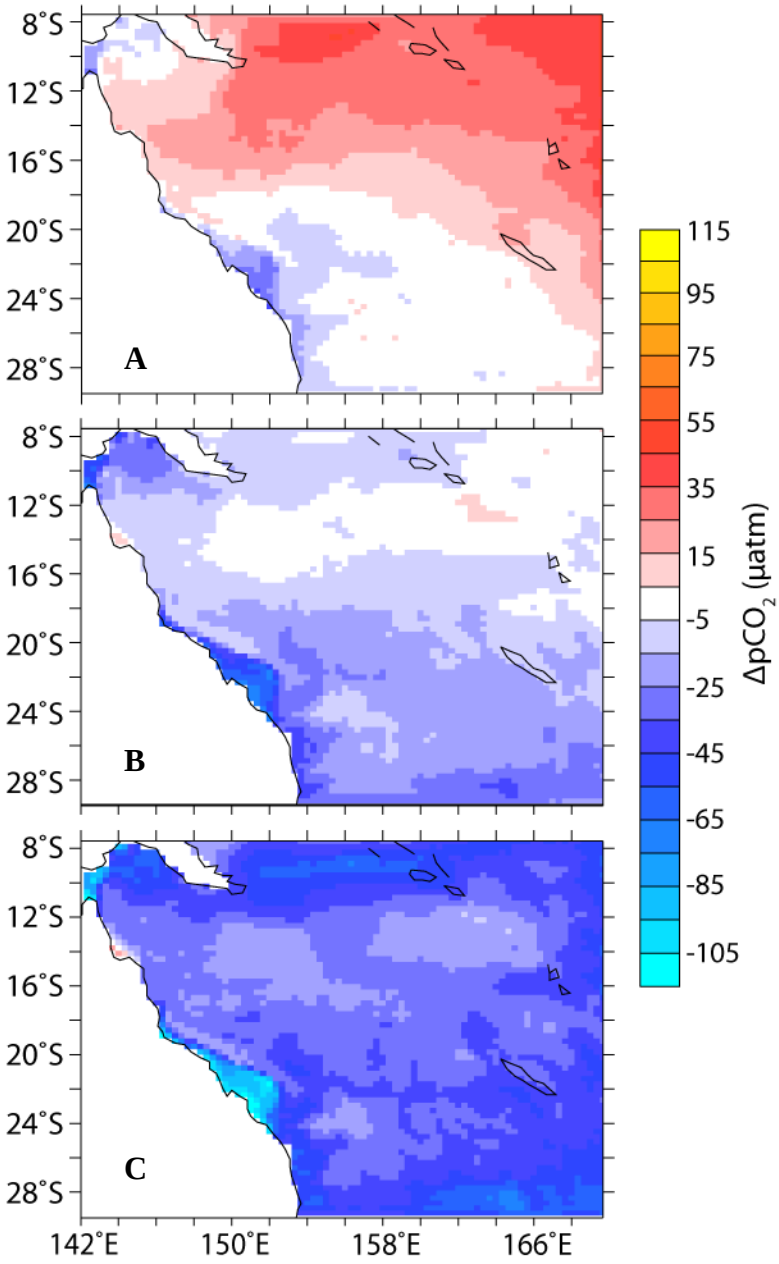


**Figure 8.6.2. Yearly average of $\Delta pCO_2$ (ocean-atmosphere) within the Coral Sea for atmospheric $pCO_2$ levels of A) 380 µatm, B) 650 µatm and C) 1000 µatm. Presently, the tropical ocean constitutes a source of $CO_2$ to the atmosphere as a result of high sea surface temperatures (SSTs), whereas the subtropics act as a seasonal sink during the cooler months. With increasing $pCO_2$atm, the Coral Sea progressively develops into a net sink in all regions, albeit not during all seasons, due to higher atmospheric $CO_2$ levels.**

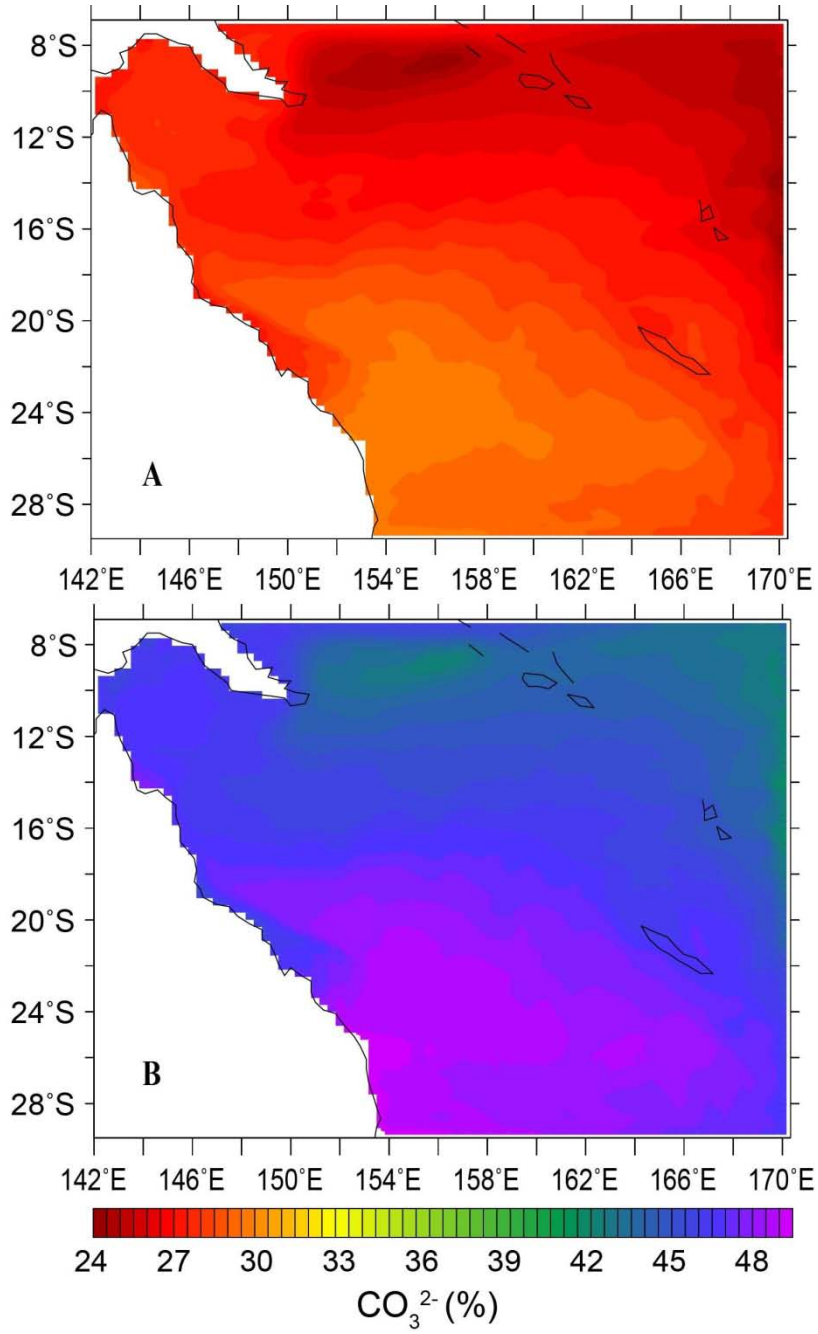


**Figure 8.6.3. Predicted change in yearly average of sea surface $CO_3^{2-}$, expressed as a percentage decline relative to present day $CO_3^{2-}$ levels, for an increase in atmospheric $pCO_2$ from 380 µatm to A) 650 µatm and B) 1000 µatm. $CO_3^{2-}$ for both scenarios decreases throughout the study area, with greatest declines occurring in the southwest.**

The difference between atmospheric and oceanic $pCO_2$ ($\Delta pCO_2$oc-atm), in turn, would mostly increase by 0-50 μatm, resulting in the Coral Sea changing from a source of $pCO_2$ in the equatorial region, and from a seasonal source in the subtropical area (mainly during late summer and autumn), to a predominant sink in the entire Coral Sea (Figure 8.6.2). Concurrent with increased ocean acidification and $pCO_2$, the saturation state of aragonite and calcite will decline significantly, which would have wide-reaching effects on the coral calcification rates and the general health, and structural strength, of calcifying organisms. Assuming that the ocean's $[Ca^{2+}]$ will remain unchanged in future, we have to expect that the $CaCO_3$ saturation state of the surface ocean will decline by 24-50%, based on a similar decrease in $CO_3^{2-}$ (Figure 8.6.3).

It has to be noted here, however, that these future scenarios are solely based on increased $pCO_2$atm. That is, the model was run with current physical data fields such that the simulations did not take into account that the future Coral Sea may become warmer and the mixed layers shallower. Such physical changes would have widespread impacts on the carbon cycle, including higher $pCO_2$, lower $CO_2$ solubility, a reduction in the biological pump, and a general tendency towards reduced $CO_2$ uptake by the Coral Sea. According to simulations by GFDL's climate model version 2.1 (CM2.1; Gnanadesikan *et al.*, 2006), a long-term decline in the Coral Sea MLD of up to 10 m can be expected over the 21st century, with the mixed layer shallowing throughout the Coral Sea (Figure 8.6.4C). On decadal and shorter time-scales, the MLD may become deeper in some regions due to conducive climate patterns (e.g. ENSO) and/or meteorological conditions (e.g. cyclones) (Figure 8.6.4A and B). Seasonally, the MLD is forecast to decline most during the cooler months, with the greatest change occurring in the southern Coral Sea, along the Queensland continental shelf edge and within the GBR (Figure 8.6.5).

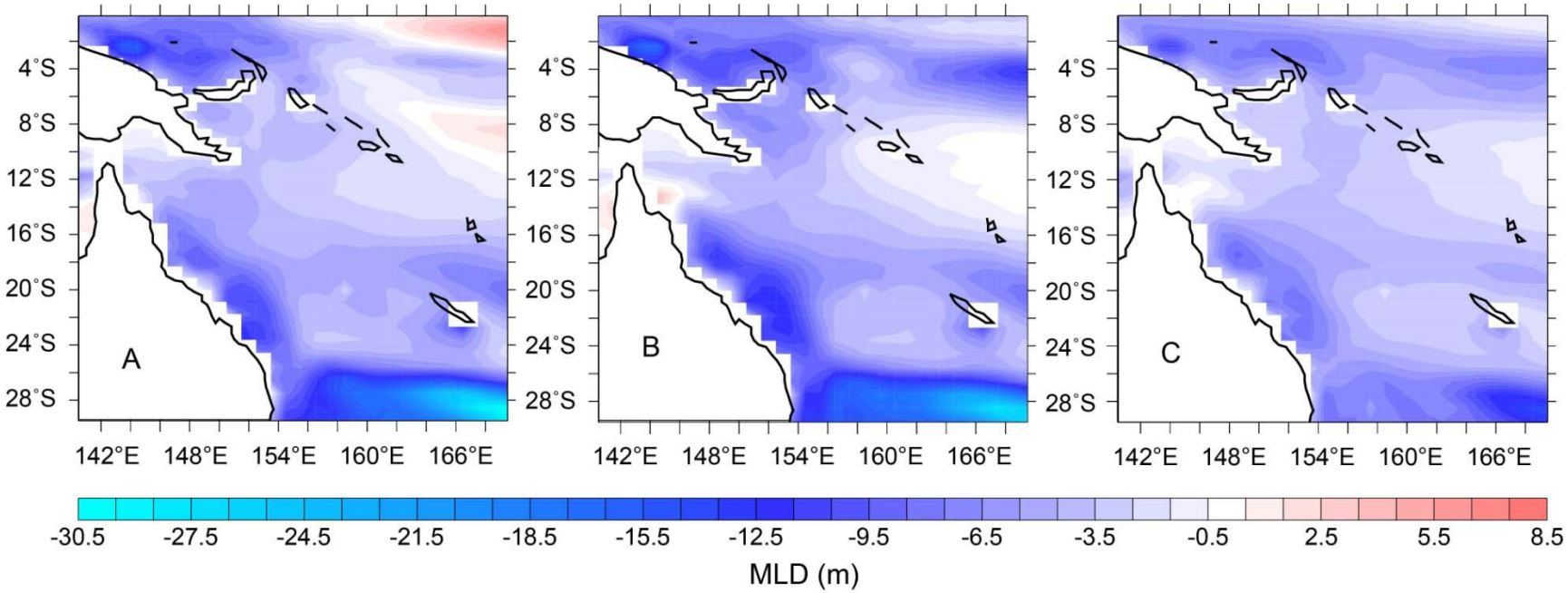


**Figure 8.6.4. Change in mixed layer depth (MLD) between A) 1991-2000 and 2091-2100, B) 1861-1870 and 2091-2100 and C) 1861-2000 and 2001-2100. Negative values imply a decline in the MLD. The MLD is derived from GFDL's climate model version 2.1 (CM2.1), using the K-profile parameterisation (KPP) mixed layer scheme of Large *et al*. (1994; see also Gnanadesikan *et al.*, 2006).**

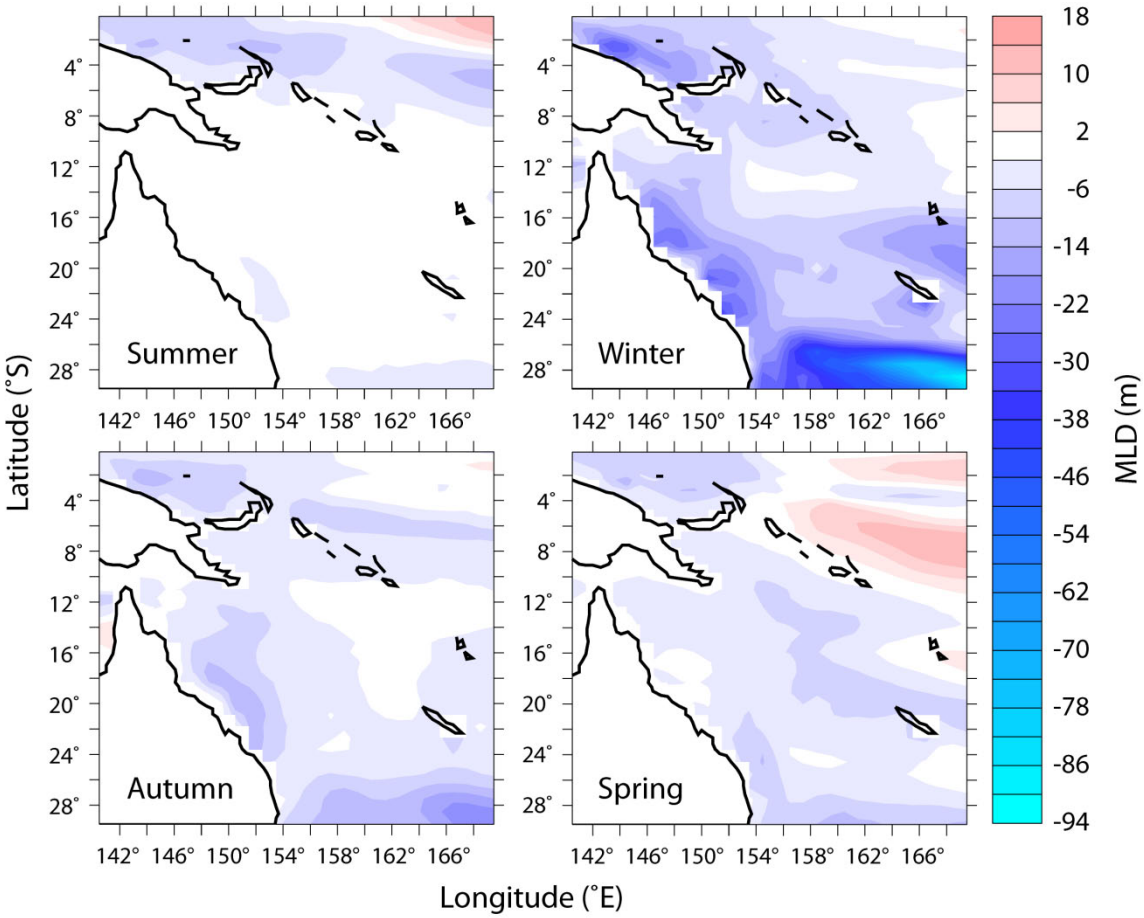


**Figure 8.6.5. Seasonal change in mixed layer depth (MLD) between 1991-2000 and 2091-2100. Negative values imply a decline in the MLD. For further description see Figure 8.6.4.**

## 8.7 Model Limitations

The conclusions that can be drawn from the models require careful appraisal of the model limitations. In this instance, the closed-boundary scenarios by PISCES are deemed more suitable for future steady state analysis due to the absence of available[1] forcing files for the boundary area. That is, the same forcing files were used for the future climate model scenarios (section 8.6) as for the current ocean conditions. Consequently, biogeochemical values near the boundary remain at modern values in open-boundary simulations, whereas closed-boundary scenarios appear to be able to more freely adapt to future steady states.

[1] Forcing files for future scenario model runs were not provided with ROMS-PISCES.

However, surprisingly, the PISCES closed-boundary scenarios for the present sea state also appear to correspond more closely to observations and expected patterns than the open-boundary scenarios. It is possible that boundary fluxes for momentum and tracers may not have been specified appropriately in PISCES, resulting in the near-boundary values being artificially forced by the open-boundary model. In addition, simulations with open boundaries possibly require much more than a 10-year spin-up to obtain equilibrium in all biogeochemical parameters modelled by PISCES, although no evidence was found that a longer spin-up is necessary.

The apparent superiority of closed-boundary scenarios does not apply to biochemical output obtained by ROMS, where the open-boundary chlorophyll concentration, albeit still too high, more closely corresponds to observations compared to the closed-boundary model output. Similarly, only temperature fields from open-boundary simulations accurately mirror the impact of the SEC and EAC within the Coral Sea.

Normally, open-boundary scenarios are expected to provide more accurate model output due to the more realistic representation of physical oceanography (e.g. the SEC moving into the Coral Sea from the east, and the EAC leaving the study area from the southwest). Thus, the behaviour of ROMS (more accurate open-boundary output) fits expectations more closely than PISCES. ROMS has been extensively tested by the ROMS-PISCES developers, whereas the coupling of PISCES to ROMS is a relatively new endeavour.

### 8.7.1 Errors and Omissions

The following is a brief summary of additional issues observed, or features not included, in the model runs:

- Due to an unresolved problem in the code, ROMS consistently outputs the euphotic layer as being zero meters deep. There is potential that this problem may relate to poor or compromised results for modelled chlorophyll and phytoplankton.
- Nitrate occasionally has values below zero at the northern boundary. This remains another unresolved computational issue.
- River inflow has not been enabled. Although river runoff is not that important for most of the Coral Sea , it would have quite a significant impact on the nutrient and

salinity levels in the Gulf of Papua (and to a certain extent on the QLD continental shelf).

## 8.8 Summary - Modelling

The spatial and seasonal data fields of the investigated parameters (SST, MLD, $fCO_2$, $p$H) obtained with the coupled regional model ROMS-PISCES exhibit comparable patterns to those based on observational data. SST displays a strong latitudinal gradient throughout the year, whereas the mixed layer changes seasonally from a spatially homogenous pattern during austral summer to deeper winter MLDs that increase towards the south. $pCO_2$, in turn, increases towards summer and lower latitudes due to the positive relationship between fugacity and SST. Consequently, the capacity of the Coral Sea to act as a sink of atmospheric $CO_2$ is reduced during summer and is thus more likely to act as a source of $CO_2$ during the warmer season. Based on the significant differences between open- and closed-boundary model outputs, it is not evident, however, whether the Coral Sea is generally a source or a sink of $CO_2$. One notable difference between model and observational results is the relatively low Torres Strait $pCO_2$ levels obtained with PISCES (cf. Figures 8.5.3 and 8.5.4). Observations indicate that this region should be characterised by one of the highest $fCO_2$ levels, with the area acting as a source of $CO_2$ throughout most of the year. It is likely that the numerical model struggles to accurately represent shallow and near-coastal regions, thus potentially producing results which can differ quite significantly from observations.

Several future scenarios for atmospheric $pCO_2$ levels were used to determine likely changes in the geochemistry of the Coral Sea during the 21$^{st}$ century. The projected increase of atmospheric $CO_2$ from 380 ppmv to 650-1000 ppmv causes the Coral Sea to change from a predominant sink of atmospheric $CO_2$ to a seasonal source in the numerical model. At the same time, sea surface $p$H is declining by 0.15-0.38 units. In addition, the $CO_3^{2-}$ concentration is reduced by 24-50%, which suggests a comparable decrease of the $CaCO_3$ saturation state in the upper ocean. This could have wide-reaching effects on the general health, and structural strength, of calcifying organisms, with calcification rates expected to decline - and dissolution rates anticipated to increase - in the future.

Since no forcing file for future physical oceanography steady states was readily available for ROMS-PISCES, simulations from another model (GFDL's climate model version 2.1) were utilised to investigate how the MLD will most likely change over time within the Coral Sea. The mean MLD of the 21$^{st}$ century is forecast to become shallower by up to 10 m compared to the mean MLD of the previous decades, with much more significant MLD decreases expected on seasonal and interannual timescales.

# 9 Conclusions

Several research gaps were highlighted earlier in the thesis, including the lack of studies specifically focussing on the Coral Sea. One purpose of the thesis was to evaluate the seasonal to long-term variability of the mixed layer within the Coral Sea, in addition to finding the most appropriate method to determine the MLD. Furthermore, this research aimed to find spatial and temporal patterns of marine geochemistry, including whether the Coral Sea is currently a source or a sink of atmospheric $CO_2$. Since a low data availability was anticipated, a coupled regional model (ROMS-PISCES) was chosen to complement the observational data. The model's performance was to be evaluated by comparing the numerical output with the observational results; the model would then be used for projection of future changes in MLD and carbon chemistry due to anthropogenic greenhouse warming and $CO_2$ emissions.

Observational data derived from Argo and the World Ocean Database (WOD) display a distinct seasonality in the mixed layer depth (MLD) throughout the Coral Sea. The annual MLD fluctuations were generally more pronounced in higher latitudes as a result of greater seasonality in sea surface temperature and wind stress. While summer mixed layers are relatively homogeneously shallow throughout the Coral Sea, winter mixed layers in higher latitudes tend to be significantly deeper compared to tropical regions, with MLDs often clearly exceeding 100 m. The same seasonal and spatial patterns were also obtained with the coupled regional model ROMS-PISCES. Due to the scarcity of available observational data prior to the introduction of Argo profiles into the Coral Sea in 2001, no long-term changes in sea surface temperature (SST) and MLD can be detected. More observational data, at better coverage and over a longer period, is required to investigate whether MLDs are indeed thinning within the Coral Sea.

Barrier layers, which inhibit mixing of nutrient- and $CO_2$-rich deep ocean water with the surface mixed layer, do not commonly occur within the Coral Sea. The north-eastern Coral Sea has the highest barrier layer density, which is most likely linked to high precipitation rates during all seasons. Salinity inversions are, in turn, mainly found in the southeast, a turbulent region affected by the eddy-rich Tasman front.

Similar to the mixed layers, observational geochemistry also displays some annual seasonality in the Coral Sea. During the cooler months, the Coral Sea appears to

predominantly take up atmospheric $CO_2$. However, marine $fCO_2$ ($fCO_2$sea) values tend to increase towards austral summer, which is linked to the positive relationship between fugacity and SST. Consequently, the region's capacity to act as a sink of atmospheric $CO_2$ is reduced during the warmer months, with an increased likelihood of $CO_2$ evasion to the atmosphere. Accordingly, the Coral Sea appears to be in a net near-neutral $CO_2$ flux state when the seasonality is taken into account. The only region that exhibits more consistent $CO_2$ flux behaviour is the Torres Strait, which generally appears to be a strong source of $CO_2$ to the atmosphere. Although $fCO_2$sea was measured very sporadically since 1983, there is a long-term trend towards increasing $fCO_2$sea values evident, with an estimated average yearly increase of 1.41 ± 0.04 μatm/year from 1983 to 2001. This rate of increase corresponds well with the observed growth in atmospheric $fCO_2$ over the same period. Although *p*H exhibits some seasonality, no long-term trend is observed due to a scarcity of data. Similar to MLDs, future more widespread coverage of geochemical measurements may reveal long-term trends in the carbon cycle that are currently imperceptible.

The output from ROMS-PISCES displays distinct seasonal, spatial and long-term changes in geochemistry. For the simulation representing current $CO_2$ levels (380 ppmv), seasonal and spatial $fCO_2$sea and $\Delta fCO_2$ (difference between oceanic and atmospheric $fCO_2$) patterns in general agree well with the observational data. However, modelled $fCO_2$ (and accordingly $\Delta fCO_2$) in near-coastal regions appears to be too low compared to observational data. This is attributed to the numerical model's difficulty in accurately representing shallow near-coastal regions of complex topography. However, it is also possible that the coupled model's numerical code does not take into account that the geochemistry and biological processes of near-coastal regions greatly differ from the offshore ocean. Notably, ROMS-PISCES does not include the interaction with shallow carbonate sediments or the benthic biological carbon cycle. Further model versions may be able to be improved by not only incorporating additional parameters, but also by putting better constraints on the existing variables used.

Two ROMS-PISCES simulations were run to forecast the geochemical pattern for atmospheric $CO_2$ levels of 650 ppmv and 1000 ppmv. Such an increase, predicted to be reached towards the end of the 21$^{st}$ century, will result in a decrease of sea surface *p*H by

0.14-0.38 units. Simultaneously, the Coral Sea may be changing from a seasonal source of atmospheric $CO_2$ to a predominant sink, as projected by the numerical model. However, the simulations did not take into account possible changes in physical attributes. That is, even for future scenarios, the numerical model was forced by present-day physical oceanographic attributes. Since most published studies are anticipating warmer SSTs and shallower MLDs in future, the consequential reduced $CO_2$ solubility would partially counteract the ocean's increased tendency for $CO_2$ uptake due to higher atmospheric $CO_2$ levels. Parallel with increased ocean $fCO_2$, the $CO_3^{2-}$ concentration will be reduced by 25-50%, with a similar decline expected for the saturation state of aragonite and calcite. Such a substantial change in saturation state will have a significant impact on the general health of calcifying organisms within the Coral Sea. Calcification rates will most likely decline in future, and dissolution and erosion rates will increase.

Since no forcing file for future physical oceanography scenarios was readily available for ROMS-PISCES, numerical output for future MLD trends has been obtained from a second model (GFDL's climate model version 2.1). Relative to the 1861-2000 period, the MLD is expected to decline by up to 10 m throughout the Coral Sea over the 21$^{st}$ century. On decadal and shorter time-scales, the mixed layer thinning may approach 100 m in the southern Coral Sea while some regions may experience a temporary deepening as a result of favourable climate patterns (ENSO, IPO, etc.) and/or meteorological conditions (e.g. cyclones). Seasonally, the MLD is forecast to decrease most during the cooler months, with the greatest change occurring in the southern Coral Sea, along the Queensland continental shelf edge and within the GBR.

This surface mixed layer thinning would have a very significant – and complex – impact on marine physics, carbonate chemistry and some biological processes. A shallowing of the MLD is usually accompanied by a warmer and more highly stratified upper ocean, inhibiting mixing with the nutrient-rich deeper water bodies. Lower nutrient levels would reduce primary productivity (and therefore lower the $CO_2$ consumption and carbon export to deep water). Warmer Coral Sea mixed layers, in turn, would increase its $fCO_2$ levels, reducing the regional ocean's capability to uptake atmospheric $CO_2$ and at the same time more likely becoming a source of $CO_2$. There are many more factors and interactions that would have to be taken into account to more accurately predict the

impact of mixed layer thinning and rising atmospheric $CO_2$ on biological productivity. Changes in marine carbonate equilibria could have far-reaching effects on organisms that are reliant on calcification and are susceptible to dissolution in water with lowered carbonate ion activity. Due to the complexity and severity of this issue, it is essential that more research aim at monitoring the physical and geochemical state and trends within the Coral Sea to obtain a more accurate and detailed view of how global warming and higher atmospheric $CO_2$ levels will impact on the Coral Sea.

# REFERENCES


Achituv, Y. and Dubinsky, Z. (1990) Evolution and zoogeography of coral reefs. In *Ecosystems of the world 25: coral reefs* (Ed. Z. Dubinsky), Elsevier, Amsterdam, pp. 1-9.

AchutaRao, K. M., Ishii, M., Santer, B. D., Gleckler, P. J., Taylor, K. E., Barnett, T. P., Pierce, D. W., Stouffer, R. J. and Wigley, T. M. L. (2007) Simulated and observed variability in ocean temperature and heat content. *PNAS*, 0611375104.

Acker, J. G. and Leptoukh, G. (2007) Online Analysis Enhances Use of NASA Earth Science Data. *Eos Trans. AGU*, 88(2), 10.1029/2007EO020003.

Acreman, D. M. (2005) The impact of improved vertical resolution and model tuning on mixed layer models. In *NCOF Technical Report 2*, pp. 28.

Alexander, M. A., Scott, J. D. and Deser, C. (2000) Processes that influence sea surface temperature and ocean mixed layer depth variability in a coupled model. *J. Geophys. Res. - Oceans*, 105, 16823-16842.

Andersson, A. J. and Mackenzie, F. T. (2004) Shallow-water oceans: a source or sink of atmospheric $CO_2$? *Frontiers Ecol. Environ.*, 2(7), 348-353.

Andersson, A. J., Mackenzie, F. T. and Lerman, A. (2005) Coastal ocean and carbonate systems in the high $CO_2$ world of the Anthropocene. *Am. J. Sci.*, 305(9), 875-918.

Andersson, A. J., Mackenzie, F. T. and Lerman, A. (2006) Coastal ocean $CO_2$-carbonic acid-carbonate sediment system of the Anthropocene. *Global Biogeochem. Cycles*, 20, GB1S92, doi:10.1029/2005GB002506.

Andersson, A. J., Mackenzie, F. T. and Ver, L. M. (2003) Solution of shallow-water carbonates: An insignificant buffer against rising atmospheric $CO_2$. *Geology*, 31(6), 513-516.

Ando, K. and Kuroda, Y. (2002) Two modes of salinity and temperature in the surface layer of the Pacific warm pool. *J. Oceanogr.*, 58, 599-609.

Andrews, J. C. (1983) Water masses, nutrient levels and seasonal drift on the outer Central Queensland shelf (Great Barrier Reef). *Aust. J. Mar. Freshw. Res.*, 34, 821-834.

Andrews, J. C. and Clegg, S. (1989) Coral Sea circulation and transport deduced from modal information models. *Deep-Sea Res. A*, 36(6), 957-974.

Andrews, J. C. and Gentien, P. (1982) Upwelling as a Source of Nutrients for the Great Barrier Reef Ecosystems: A Solution to Darwin's Question? *Mar. Ecol. Prog. Ser.*, 8, 257-269.

Anthony, K. R. N., Kline, D. I., Diaz-Pulido, G., Dove, S. and Hoegh-Guldberg, O. (2008) Ocean acidification causes bleaching and productivity loss in coral reef builders. *PNAS*, 105, 17442-17446.

Archer, D. and Maier-Reimer, E. (1994) Effect of deep-sea sedimentary calcite preservation on atmospheric $CO_2$ concentration. *Nature*, 367(6460), 260-263.

Archer, D., Martin, P., Buffett, B., Brovkin, V., Rahmstorf, S. and Ganopolski, A. (2004) The importance of ocean temperature to global biogeochemistry. *Earth Planet. Sci. Lett.*, 222(2), 333-348.

Archer, D. E., Eshel, G., Winguth, A., Broecker, W., Pierrehumbert, R., Tobis, M. and Jacob, R. (2000) Atmospheric $pCO_2$ sensitivity to the biological pump in the ocean. *Global Biogeochem. Cycles*, 14(4), 1219-1230.

Archer, D. E., Takahashi, T., Sutherland, S., Goddard, J., Chipman, D., Rodgers, K. and Ogura, H. (1996) Daily, seasonal and interannual variability of sea-surface carbon and nutrient concentration in the equatorial Pacific Ocean. *Deep-Sea Res. II*, 43(4-6), 779-808.

Aumann, H. H., Gregorich, D. T., Broberg, S. E. and Elliott, D. A. (2007) Seasonal correlations of SST, water vapor, and convective activity in tropical oceans: A new hyperspectral data set for climate model testing. *Geophys. Res. Lett.*, 34, L15813, doi:15810.11029/12006GL029191.

Aumont, O. and Bopp, L. (2006) Globalizing results from ocean in situ iron fertilization studies. *Global Biogeochem. Cycles*, 20, GB2017, doi:2010.1029/2005GB002591.

Aumont, O., Maier-Reimer, E., Blain, S. and Monfray, P. (2003) An ecosystem model of the global ocean including Fe, Si, P colimitations. *Global Biogeochem. Cycles*, 17, 1060-1060.

Babu, K. N., Sharma, R., Agarwal, N., Agarwal, V. K. and Weller, R. A. (2004) Study of the mixed layer depth variations within the north Indian Ocean using a 1-D model. *J. Geophys. Res.*, 109, C08016, doi:08010.01029/02003JC002024.

Baker, A. C., Starger, C. J., McClanahan, T. R. and Glynn, P. W. (2004) Coral reefs Corals' adaptive response to climate change. *Nature*, 430(7001), 741.

Bamber, J. L., Riva, R. E. M., Vermeersen, B. L. A. and LeBrocq, A. M. (2009) Reassessment of the Potential Sea-Level Rise from a Collapse of the West Antarctic Ice Sheet. *Science*, 324(5929), 901-903.

Barber, R. T. and Chavez, F. P. (1983) Biological consequences of El Niño. *Science*, 222, 1203-1210.

Barker, S., Higgins, J. A. and Elderfield, H. (2003) The future of the carbon cycle: review, calcification response, ballast and feedback on atmospheric $CO_2$. *Phil. Trans. R. Soc. Lond. A*, 361(1810), 1977-1999.

Barnes, D. J. (1982) Light response curve for calcification in the staghorn coral, *Acropora acuminata*. *Comp. Biochem. Physiol.*, 73A(1), 41-45.

Barnola, J. M., Raynaud, D., Korotkevich, Y. S. and Lorius, C. (1987) Vostok ice core provides 160,000-year record of atmospheric $CO_2$. *Nature*, 329(6138), 408-414.

Barth, J. A., Menge, B. A., Lubchenco, J., Chan, F., Bane, J. M., Kirincich, A. R., McManus, M. A., Nielsen, K. J., Pierce, S. D. and Washburn, L. (2007) Delayed upwelling alters nearshore coastal ocean ecosystems in the northern California current. *PNAS*, 104(10), 3719-3724.

Bates, N. R. (2002a) Interannual variability in the global ocean uptake of $CO_2$. *Geophys. Res. Lett.*, 29(5), 10.1029/2001GL013571.

Bates, N. R. (2002b) Seasonal variability of the impact of coral reefs on ocean $CO_2$ and air-sea $CO_2$ exchange. *Limnol. Oceanogr.*, 47(1), 43-52.

Bates, N. R., Knap, A. H. and Michaels, A. F. (1998) Contribution of hurricanes to local and global estimates of air-sea exchange of $CO_2$ *Nature*, 395(6697), 58-61.

Bates, N. R. and Merlivat, L. (2001) The influence of short-term wind variability on air-sea $CO_2$ exchange. *Geophys. Res. Lett.*, 28(17), 3281-3284.

Bathen, K. H. (1972) On the seasonal changes in the depth of the mixed layer in the North Pacific Ocean. *J. Geophys. Res.*, 77, 7138- 7150.

Battle, M., Bender, M. L., Tans, P. P., White, J. W. C., Ellis, J. T., Conway, T. and Francey, R. J. (2000) Global Carbon Sinks and Their Variability Inferred from Atmospheric $O_2$ and $d^{13}C$. *Science*, 287(5462), 2467-2470.

Bauer, S., Hitchcock, G. L. and Olson, D. B. (1991) Influence of monsoonally-forced Ekman dynamics upon surface-layer depth and plankton biomass distribution in the Arabian Sea. *Deep-Sea Res. II*, 38, 531-553.

Behrenfeld, M. J. and Falkowski, P. G. (1997) Photosynthetic rates derived from satellite-based chlorophyll concentration. *Limnol. Oceanogr.*, 42(1), 1-20.

Behrenfeld, M. J. and Kolber, Z. S. (1999) Widespread Iron Limitation of Phytoplankton in the South Pacific Ocean. *Science*, 283(5403), 840-843.

Berner, R. A. (1977) Sedimentation and dissolution of pteropods in the ocean. In *The Fate of Fossil Fuel $CO_2$ in the Oceans* (Eds. N. R. Andersen and A. Malahoff), Plenum, NY, pp. 243-260.

Berthelot, M., Friedlingstein, P., Ciais, P., Monfray, P., Dufresne, J. L., Treut, H. L. and Fairhead, L. (2002) Global response of the terrestrial biosphere to $CO_2$ and climate change using a coupled climate-carbon cycle model. *Global Biogeochem. Cycles*, 16(4), 1084, doi:1010.1029/2001GB001827.

Bjerknes, J. (1966) A possible response of the atmospheric Hadley circulation to anomalies of ocean temperature. *Tellus*, 18, 820-829.

Bjerknes, J. (1969) Atmospheric teleconnections from the equatorial Pacific. *Mon. Wea. Rev.*, 97(3), 163-172.

Bjerknes, V. (1904) Das Problem der Wettervorhersage, betrachtet vom Standpunkte der Mechanik und der Physik. *Meteor. Z.*, 21, 1-7.

Blackford, J. C. and Gilbert, F. J. (2007) *p*H variability and $CO_2$ induced acidification in the North Sea. *J. Mar. Sys.*, 64(1-4), 229-241.

Boland, F. M. and Church, J. A. (1981) The East Australian current 1978. *Deep-Sea Res. A*, 28(9), 937-957.

Bopp, L., Aumont, O., P. Cadule, Alvain, S. and Gehlen, M. (2005) Response of diatoms distribution to global warming and potential implications: A global model study. *Geophys. Res. Lett.*, 32, L19606, doi:19610.11029/12005GL023653.

Bopp, L., Kohfeld, K. E., Le Quéré, C. and Aumont, O. (2003) Dust impact on marine biota and atmospheric $CO_2$ during glacial periods. *Paleoceanography*, 18(2), 1046, doi:1010.1029/2002PA000810.

Bopp, L., LeQuéré, C., M.Heimann, Manning, A. C. and P.Monfray (2002) Climate-induced oceanic oxygen fluxes: Implications for the contemporary carbon budget. *Global Biogeochem. Cycles*, 16, doi: 10.10292001GB10001445.

Bopp, L., Monfray, P., Aumont, O., Dufresne, J.-L., LeTreut, H., Madec, G., Terray, L. and Orr, J. C. (2001) Potential impact of climate change of marine export production. *Global Biogeochem. Cycles*, 15, 81-99.

Borges, A. V. (2005) Do we have enough pieces of the jigsaw to integrate $CO_2$ fluxes in the Coastal Ocean? *Estuaries*, 28(1), 3-27.

Borges, A. V., Delille, B. and Frankignoulle, M. (2005) Budgeting sinks and sources of $CO_2$ in the coastal ocean: Diversity of ecosystems counts. *Geophys. Res. Lett.*, 32, L14601, doi:14610.11029/12005GL023053.

Borges, A. V., Delille, B., Schiettecatte, L.-S., Gazeau, F., Abril, G. and Frankignoulle, M. (2004) Gas transfer velocities of $CO_2$ in three European estuaries (Randers Fjord, Scheldt, and Thames). *Limnol. Oceanogr.*, 49(5), 1630-1641.

Borges, A. V. and Frankignoulle, M. (2002a) Distribution and air-water exchange of carbon dioxide in the Scheldt plume off the Belgian coast. *Biogeochemistry*, 59(1), 41-67.

Borges, A. V. and Frankignoulle, M. (2002b) Distribution of surface carbon dioxide and air-sea exchange in the upwelling system off the Galician coast. *Global Biogeochem. Cycles*, 16(2), 1020, doi:1010.1029/2000GB001385.

Borges, A. V. and Frankignoulle, M. (2003) Distribution of surface carbon dioxide and air-sea exchange in the English Channel and adjacent areas. *J. Geophys. Res.*, 108(C5), 3140, doi:3110.1029/2000JC000571.

Borges, A. V., Schiettecatte, L.-S., Abril, G., Delille, B. and Gazeau, F. (2006) Carbon dioxide in European coastal waters. *Estuarine, Coastal and Shelf Science*, 70(3), 375-387.

Borowitzka, M. A. and Larkum, A. W. D. (1976) Calcification in the green alga *Halimeda* III. The sources of carbon for photosynthesis and calcification and a model of the mechanism of calcification. *J. Exp. Bot.*, 27(100), 879-893.

Bostock, H. C., Opdyke, B. N., Gagan, M. K., Kiss, A. E. and Fifield, L. K. (2006) Glacial/interglacial changes in the East Australian current. *Climate Dynamics*, 26(6), 645-659.

Boutin, J., Etcheto, J., Dandonneau, Y., Bakker, D. C. E., Feely, R. A., Inoue, H. Y., Ishii, M., Ling, R. D., Nightingale, P. D., Metzl, N. and Wanninkhof, R. (1999) Satellite sea surface temperature: a powerful tool for interpreting in situ $pCO_2$ measurements in the equatorial Pacific Ocean. *Tellus B*, 51(2), 490-508.

Boyer, T. P. and Levitus, S. (2002) Harmonic analysis of climatological sea surface salinity. *J. Geophys. Res.*, 107(C12), 8006, doi:8010.1029/2001JC000829.

Brainerd, K. E. and Gregg, M. C. (1995) Surface mixed and mixing layer depths. *Deep-Sea Res. I*, 42(9), 1521-1543.

Brasse, S., Nellen, M., Seifert, R. and Michaelis, W. (2002) The carbon dioxide system in the Elbe estuary. *Biogeochemistry*, 59(1), 25-40.

Brewer, P. G. (1978) Direct observation of the oceanic $CO_2$ increase. *Geophys. Res. Lett.*, 5, 997-1000.

Brewer, P. G. (1997) Ocean chemistry of the fossil fuel $CO_2$ signal: the haline signal of "business as usual". *Geophys. Res. Lett.*, 24(11), 1367-1369.

Brewer, P. G., Glover, D. M., Goyet, C. and Shafer, D. K. (1995) The pH of the North Pacific: Improvements to the global model for sound absorption in seawater. *J. Geophys. Res.*, 100(C5), 8761-8776.

Brierley, C. M., Fedorov, A. V., Liu, Z., Herbert, T. D., Lawrence, K. T. and LaRiviere, J. P. (2009) Greatly Expanded Tropical Warm Pool and Weakened Hadley Circulation in the Early Pliocene. *Science*, 323(5922), 1714-1718.

Brinkman, R., Wolanski, E., Deleersnijder, E., McAllister, F. and Skirving, W. (2002) Oceanic inflow from the Coral Sea into the Great Barrier Reef. *Estuarine Coastal Shelf Sci.*, 54(4), 655-668.

Broecker, W. A. and Takahashi, T. (1966) Calcium carbonate precipitation on the Bahama Banks. *J. Geophys. Res.*, 71, 1575-1602.

Broecker, W. S. and Henderson, G. M. (1998) The sequence of events surrounding Termination II and their implication for the cause of glacial-interglacial $CO_2$ changes. *Paleoceanography*, 13, 352-364.

Broecker, W. S., Li, Y.-H. and Peng, T.-H. (1971) Carbon dioxide: Man's unseen artifact. In *Impingement of Man on the Oceans* (Ed. D. W. Hood), Wiley Intersci., Hoboken, N. J., pp. 287-324.

Broecker, W. S. and Peng, T.-H. (1982) *Tracers in the Sea*, Lamont-Doherty Geol. Obs., Palisades, N.Y., 690 pp.

Broecker, W. S. and Peng, T.-H. (1989) The cause of the glacial and interglacial atmospheric $CO_2$ change: A polar alkalinity hypothesis. *Global Biogeochem. Cycles*, 3(3), 215-239.

Broecker, W. S., Takahashi, T., Simpson, H. J. and Peng, T. H. (1979) Fate of fossil fuel carbon dioxide and the global carbon budget. *Science*, 206, 409-418.

Brown, B. E., Downs, C. A., Dunne, R. P. and Gibb, S. W. (2002) Exploring the basis of thermotolerance in the reef coral *Goniastrea aspera*. *Mar. Ecol. Ser.*, 242, 119-129.

Brunskill, G. J., Zagorskis, I. and Pfitzner, J. (2002) Carbon Burial Rates in Sediments and a Carbon Mass Balance for the Herbert River Region of the Great Barrier Reef Continental Shelf, North Queensland, Australia. *Estuarine Coastal Shelf Sci.*, 54(4), 677-700.

Bryan, K. and Cox, M. D. (1967) A numerical investigation of the oceanic general circulation. *Tellus*, 19(1), 54-80.

Buddemeier, R. W., Kleypas, J. A. and Aronson, R. B. (2004) Coral Reefs & Global Climate Change: Potential Contributions of Climate Change to Stresses on Coral Reef Ecosystems, Pew Center on Global Climate Change, Arlington, Va, pp. vi+44 pp.

Burrage, B. M. (1993) Coral Sea Currents. *Corella*, 17, 135-145.

Burrage, D. M., Black, K. P. and Ness, K. F. (1994) Long-term current prediction in the central Great Barrier Reef. *Continental Shelf Research*, 14(7-8), 803-829.

Burrage, D. M., Black, K. P. and Steinberg, C. R. (1995) Long-term sea-level variations in the central Great Barrier Reef. *Continental Shelf Research*, 15, 981-1014.

Burrage, D. M., Steinberg, C. R., Mason, L. B. and Bode, L. (2003) Tidal corrections for TOPEX altimetry in the Coral Sea and Great Barrier Reef Lagoon: Comparisons

with long-term tide gauge records. *J. Geophys. Res.*, 108(C7), 3241, doi:3210.1029/2000JC000441.

Burton, E. A. and Walter, L. M. (1987) Relative precipitation rates of aragonite and Mg calcite from seawater; temperature or carbonate ion control? *Geology*, 15(2), 111-114.

Busalacchi, A. J., Takeuchi, K. and O'Brien, J. J. (1983) On the interannual wind-driven response of the tropical Pacific Ocean. In *Hydrodynamics of the Equatorial Ocean* (Ed. J. C. J. Nihoul), Elsevier, New York, pp. 155-195.

Cai, W.-J., Dai, M. and Wang, Y. (2006) Air-sea exchange of carbon dioxide in ocean margins: A province-based synthesis. *Geophys. Res. Lett.*, 33, L12603, doi:12610.11029/12006GL026219.

Cai, W., Shi, G., Cowan, T., Bi, D. and Ribbe, J. (2005) The response of the Southern Annular Mode, the East Australian Current, and the southern mid-latitude ocean circulation to global warming. *Geophys. Res. Lett.*, 32, L23706, doi:23710.21029/22005GL024701.

Caldeira, K. and Wickett, M. E. (2003) Anthropogenic carbon and ocean pH. *Nature*, 425(6956), 365.

Caldeira, K. and Wickett, M. E. (2005) Ocean model predictions of chemistry changes from carbon dioxide emissions to the atmosphere and ocean. *J. Geophys. Res.*, 110, C09S04, doi:10.1029/2004JC002671.

Callendar, G. S. (1938) The artificial production of carbon dioxide and its influence on temperature. *Q. J. R. Meteorol. Soc.*, 64, 223-240.

Calvo, E., Marshall, J. F., Pelejero, C., McCulloch, M. T., Gagan, M. K. and Lough, J. M. (2007) Interdecadal climate variability in the Coral Sea since 1708 A.D. *Palaeogeo. Palaeoclim. Palaeoecol.*, 248(1-2), 190-201.

Camargo, S. J. and Sobel, A. H. (2005) Western North Pacific tropical cyclone intensity and ENSO. *J. Clim.*, 18(15), 2996-3006.

Cameron, D. R., Lenton, T. M., Ridgwell, A. J., Shepherd, J. G., Marsh, R. and Yool, A. (2005) A factorial analysis of the marine carbon cycle and ocean circulation controls on atmospheric $CO_2$. *Global Biogeochem. Cycles*, 19, GB4027, doi:4010.1029/2005GB002489.

Cane, M. A. (1983) Oceanographic events during El Niño. *Science*, 222(4629), 1189-1195.

Cane, M. A., Clement, A. C., Kaplan, A., Kushnir, Y., Pozdnyakov, D., Seager, R., Zebiak, S. E. and Murtugudde, R. (1997) Twentieth-century sea surface temperature trends. *Science*, 275(5302), 957-960.

Canuto, V. M., Howard, A., Cheng, Y. and Dubovikov, M. S. (2001) Ocean turbulence I: one-point closure model. Momentum and heat vertical diffusivities. *J. Phys. Oceanogr.*, 31, 1413-1426.

Cao, M. and Woodward, F. I. (1998) Dynamic responses of terrestrial ecosystem carbon cycling to global climate change. *Nature*, 393, 249-252.

Catubig, N. R., Archer, D. E., Francois, R., deMenocal, P., Howard, W. and Yu, E.-F. (1998) Global deep-sea burial rate of calcium carbonate during the last glacial maximum. *Paleoceanography*, 13(3), 298-310.

Cayan, D. R. (1992) Latent and Sensible Heat Flux Anomalies over the Northern Oceans: Driving the Sea Surface Temperature. *J. Phys. Oceanogr.*, 22, 859-881.

Cermeño, P., Dutkiewicz, S., Harris, R. P., Follows, M., Schofield, O. and Falkowski, P. G. (2008) The role of nutricline depth in regulating the ocean carbon cycle. *PNAS*, 105(51), 20344-20349. doi: 20310.21073/pnas.0811302106.

Chalker, B. E. and Taylor, D. L. (1978) Rhythmic variations in calcification and photosynthesis associated with the coral *Acropora cervicornis* (Lamarck). *Proc. R. Soc. London, Ser. B*, 201, 179-189.

Charney, J. G., Fjörtoft, R. and von Neumann, J. (1950) Numerical integration of the barotropic vorticity equation. *Tellus*, 2, 237-254.

Chave, K. E., Deffeyes, K. S., Weyl, P. K., Garrels, R. M. and Thompson, M. E. (1962) Observations on the Solubility of Skeletal Carbonates in Aqueous Solutions. *Science*, 137(3523), 33-34.

Chavez, F. P. and Toggweiler, J. R. (1995) Physical estimates of global new production: the upwelling contribution. In *Upwelling in the Ocean: Modeling Processes and Ancient Records* (Eds. C. P. Summerhayes, K. C. Emeis, M. V. Angel, R. L. Smith and B. Zeitzschel), J. Wiley & Sons, Chichester, pp. 313-320.

Chen, C.-T. A. and Borges, A. V. (2009) Reconciling opposing views on carbon cycling in the coastal ocean: Continental shelves as sinks and near-shore ecosystems as sources of atmospheric $CO_2$. *Deep-Sea Res. II*, 56(8-10), 578-590.

Chen, D., Busalacchi, A. J. and Rothstein, L. M. (1994) The roles of vertical mixing, solar radiation, and wind stress in a model simulation of the sea surface temperature seasonal cycle in the tropical Pacific Ocean. *J. Geophys. Res.*, 99(C10), 20345-20360.

Chen, J., Carlson, B. E. and Del Genio, A. D. (2002) Evidence for Strengthening of the Tropical General Circulation in the 1990s. *Science*, 295(5556), 838-841.

Chisholm, J. R. M. and Barnes, D. J. (1998) Anomalies in coral reef community metabolism and their potential importance in the reef CO2 source-sink debate. *PNAS*, 95(11), 6566-6569.

Chou, M.-D., Chou, S.-H. and Chan, P.-K. (2005) Influence of transient atmospheric circulation on the surface heating of the western Pacific warm pool. *Geophys. Res. Lett.*, 32, L08705, doi:08710.01029/02005GL022359.

Chou, S. H., Nelkin, E., Ardizzone, J. and Atlas, R. M. (2004) A Comparison of Latent Heat Fluxes over Global Oceans for Four Flux Products. *J. Climate*, 17(20), 3973-3989.

Choukroun, S., Ridd, P. V., Brinkman, R. and McKinna, L. I. W. (2010) On the surface circulation in the western Coral Sea and residence times in the Great Barrier Reef. *J. Geophys. Res.*, 115(C6), C06013.

Christensen, J. H., Hewitson, B., Busuioc, A., Chen, A., Gao, X., Held, I., Jones, R., Kolli, R. K., Kwon, W.-T., Laprise, R., Rueda, V. M., Mearns, L., Menéndez, C. G., Räisänen, J., Rinke, A., Sarr, A. and Whetton, P. (2007) Regional Climate Projections. In *Climate Change 2007: The Physical Science Basis. Contribution of Working Group I to the Fourth Assessment Report of the Intergovernmental Panel on Climate Change*, Cambridge University Press, Cambridge, United Kingdom and New York, NY, USA.

Church, J. A. (1987) East Australian Current adjacent to the Great Barrier Reef. *Aust. J. Mar. Freshw. Res.*, 38(6), 671-683.

Church, J. A. and Boland, F. M. (1983) A permanent undercurrent adjacent to the Great Barrier Reef. *J. Phys. Oceanogr.*, 13, 1747-1749.

Clausen, C. D. and Roth, A. A. (1975) Effect of temperature and temperature adaptation on calcification rate in the hermatypic coral *Pocillopora damicornis*. *Mar. Biol.*, 33, 93-100.

Coale, K. H., Fitzwater, S. E., Gordon, R. M., Johnson, K. S. and Barber, R. T. (1996a) Control of community growth and export production by upwelled iron in the equatorial Pacific Ocean. *Nature*, 379(6566), 621-624.

Coale, K. H., Johnson, K. S., Fitzwater, S. E., Gordon, R. M., Tanner, S., Chavez, F. P., Ferioli, L., Sakamoto, C., Rogers, P., Millero, F., Steinberg, P., Nightingale, P., Cooper, D., Cochlan, W. P., Landry, M. R., Constantinou, J., Rollwagen, G., Trasvina, A. and Kudela, R. (1996b) A massive phytoplankton bloom induced by an ecosystem-scale iron fertilization experiment in the equatorial Pacific Ocean. *Nature*, 383(6600), 495-501.

Coles, S. L. and Jokiel, P. L. (1978) Synergistic effects of temperature, salinity and light on the hermatypic coral *Montipora verrucosa*. *Marine Biology*, 49(3), 187-195.

Condie, S. A. and Dunn, J. R. (2006) Seasonal characteristics of the surface mixed layer in the Australasian region: implications for primary production regimes and biogeography. *Mar. Freshw. Res.*, 57(6), 569-590.

Conway, T. J., Tans, P. P., Waterman, L. S., Thoning, K. W., Kitzis, D. R., Masarie, K. A. and Zhang, N. (1994) Evidence for interannual variability of the carbon cycle from the National Oceanic and Atmospheric Administration/Climate Monitoring and Diagnostics Laboratory Global Air Sampling Network. *J. Geophys. Res.*, 99(D11), 22831-22855.

Cox, P. M., Betts, R. A., Jones, C. D., Spall, S. A. and Totterdell, I. J. (2000) Acceleration of global warming due to carbon-cycle feedbacks in a coupled climate model. *Nature*, 408(6809), 184-187.

Cramer, W., Bondeau, A., Woodward, F. I., Prentice, I. C., Betts, R. A., Brovkin, V., Cox, P. M., Fisher, V., Foley, J. A., Friend, A. D., Kucharik, C., Lomas, M. R., Ramankutty, N., Sitch, S., Smith, B., White, A. and Young-Molling, C. (2001) Global response of terrestrial ecosystem structure and function to $CO_2$ and climate

change: results from six dynamic global vegetation models. *Global Change Biology*, 7(4), 357-373.

Cravatte, S., Delcroix, T., Zhang, D., McPhaden, M. and Leloup, J. (2009) Observed freshening and warming of the western Pacific Warm Pool. *Climate Dynamics*, 33(4), 565-589.

Cronin, M. F., Fairall, C. W. and McPhaden, M. J. (2006) An assessment of buoy-derived and numerical weather prediction surface heat fluxes in the tropical Pacific. *J. Geophys. Res.*, 111, C06038, doi:06010.01029/02005JC003324.

Crowley, T. J. (2000) Causes of Climate Change Over the Past 1000 Years. *Science*, 289(5477), 270-277.

Curtis, S. and Hastenrath, S. (1999) Long-term trends and forcing mechanisms of circulation and climate in the equatorial Pacific. *Journal of Climate*, 12(4), 1134-1144.

da Silva, A. M., Young, C. C. and Levitus, S. (1994) Atlas of Surface Marine Data 1994, Vol. 3: Anomalies of Heat and Momentum Fluxes, NOAA Atlas NESDIS 8. U.S. Department of Commerce, NOAA, NESDIS, pp. 413.

Davis, R. E., deSzoeke, R. and Niiler, P. (1981) Variability in the upper ocean during MILE. Part II: Modeling the mixed layer response. *Deep-Sea Res. A*, 28(12), 1453-1475.

Dawe, J. T. and Thompson, L. (2006) Effect of ocean surface currents on wind stress, heat flux, and wind power input to the ocean. *Geophys. Res. Lett.*, 33, L09604, doi:09610.01029/02006GL025784.

de Boyer Montégut, C., Madec, G., Fischer, A. S., Lazar, A. and Iudicone, D. (2004) Mixed layer depth over the global ocean: An examination of profile data and a profile-based climatology. *J. Geophys. Res.*, 109(C12003), doi:10.1029/2004JC002378.

de Boyer Montégut, C., Mignot, J., Lazar, A. and Cravatte, S. (2007) Control of salinity on the mixed layer depth in the world ocean: 1. General description. *J. Geophys. Res.*, 112, C06011, doi:06010.01029/02006JC003953.

de Garidel-Thoron, T., Rosenthal, Y., Bassinot, F. and Beaufort, L. (2005) Stable sea surface temperatures in the western Pacific warm pool over the past 1.75 million years. *Nature*, 433(7023), 294-298.

Delcroix, T., Eldin, G., Radenac, M.-H., Toole, J. and Firing, E. (1992) Variation of the western equatorial Pacific Ocean, 1986-1988. *J. Geophys. Res.*, 97, 5423-5445.

Delille, B., Harlay, J., Zondervan, I., Jacquet, S., Chou, L., Wollast, R., Bellerby, R. G. J., Frankignoulle, M., Borges, A. V., Riebesell, U. and Gattuso, J.-P. (2005) Response of primary production and calcification to changes of $pCO_2$ during experimental blooms of the coccolithophorid Emiliania huxleyi. *Global Biogeochem. Cycles*, 19, GB2023, doi:2010.1029/2004GB002318.

Denman, K., Hofmann, E. and Marchant, H. (1996) Marine biotic responses to environmental change and feedbacks to climate. In *Climate Change 1995* (Eds. J. T. Houghton, L. G. M. Filho, B. A. Callander, N. Harris, A. Kattenberg and K. Maskell), Cambridge Univ. Press, New York, pp. 483-516.

Doney, S. C. and Glover, D. M. (2005) Recent advances in the ocean carbon system. *Eos Trans. AGU*, 86(42), 399-400.

Doney, S. C., Lindsay, K., Fung, I. and John, J. (2006) Natural Variability in a Stable, 1000-Yr Global Coupled Climate-Carbon Cycle Simulation. *J. Climate*, 19, 3033-3054.

Donguy, J. R. and Henin, C. (1975) Surface waters in the north of the Coral Sea. *Aust. J. Mar. Freshw. Res.*, 26, 293-296.

Donlon, C. J., Minnett, P. J., Gentemann, C., Nightingale, T. J., Barton, I. J., Ward, B. and Murray, M. J. (2002) Toward Improved Validation of Satellite Sea Surface Skin Temperature Measurements for Climate Research. *J. Clim.*, 15(4), 353-369.

Dore, J. E., Lukas, R., Sadler, D. W. and Karl, D. M. (2003) Climate-driven changes to the atmospheric $CO_2$ sink in the subtropical North Pacific Ocean. *Nature*, 424(6950), 754-757.

Drange, H., Alendal, G. and Johannessen, O. M. (2001) Ocean release of fossil fuel $CO_2$: A case study. *Geophys. Res. Lett.*, 28(13), 2637-2640.

Drew, E. A. (2001) Ocean nutrients to sediment banks via tidal jets and Halimeda meadows. In *Oceanographic Processes of Coral Reefs* (Ed. E. Wolanski), CRC Press, Boca Raton, Fla., pp. 255-267.

Dufresne, J.-L., Friedlingstein, P., Berthelot, M., Bopp, L., Ciais, P., Fairhead, L., Le Treut, H. and Monfray, P. (2002) On the magnitude of positive feedback between future climate change and the carbon cycle. *Geophys. Res. Lett.*, 29(10), 10.1029/2001GL013777.

Emerson, S. and Bender, M. L. (1981) Carbon fluxes at the sediment-water interface of the deep sea: calcium carbonate preservation. *J. Mar. Res.*, 39, 139-162.

Etcheto, J. and Merlivat, L. (1988) Satellite determination of the carbon dioxide exchange coefficient at the ocean-atmosphere interface: a first step. *J. Geophys. Res.*, 93(C12), 15669-15678.

Etheridge, D. M., Steele, L. P., Langenfelds, R. L., Francey, R. J., Barnola, J.-M. and Morgan, V. I. (1996) Natural and anthropogenic changes in atmospheric $CO_2$ over the last 1000 years from air in Antarctic ice and firn. *J. Geophys. Res.*, 101, 4115-4128.

Ewing, J. I., Houtz, R. E. and Ludwig, W. J. (1970) Sediment distribution in the Coral Sea. *J. Geophys. Res.*, 75, 1963-1972.

Fairhall, A. W. (1973) Accumulation of Fossil CO2 in the Atmosphere and the Sea. *Nature*, 245(5419), 20-23.

Falkowski, P. G., Barber, R. T. and Smetacek, V. (1998) Biogeochemical Controls and Feedbacks on Ocean Primary Production. *Science*, 281(5374), 200-206.

Fan, S.-M., Blaine, T. L. and Sarmiento, J. L. (1999) Terrestrial carbon sink in the Northern Hemisphere estimated from the atmospheric CO2 difference between Mauna Loa and the South Pole since 1959. *Tellus B*, 51(5), 863-870.

Fan, S., Gloor, M., Mahlman, J., Pacala, S., Sarmiento, J., Takahashi, T. and Tans, P. (1998) A Large Terrestrial Carbon Sink in North America Implied by Atmospheric and Oceanic Carbon Dioxide Data and Models. *Science*, 282(5388), 442-446.

Fangohr, S., Woolf, D. K., Jeffery, C. D. and Robinson, I. S. (2008) Calculating long-term global air-sea flux of carbon dioxide using scatterometer, passive

microwave, and model reanalysis wind data. *J. Geophys. Res.*, 113, C09032, doi:09010.01029/02005JC003376.

Federov, A. V. and Philander, S. G. H. (2000) Is El Niño changing? *Science*, 288, 1997-2001.

Feely, R. A., Boutin, J., Cosca, C. E., Dandonneau, Y., Etcheto, J., Inoue, H. Y., Ishii, M., Quere, C. L., Mackey, D. J. and McPhaden, M. (2002) Seasonal and interannual variability of $CO_2$ in the equatorial Pacific. *Deep-Sea Res. II* 49(13-14), 2443-2469.

Feely, R. A., Gammon, R. H., Taft, B. A., Pullen, P. E., Waterman, L. S., Conway, T. J., Gendron, J. F. and Wisegarver, D. P. (1987) Distribution of chemical tracers in the eastern equatorial Pacific during and after the 1982-1983 El Niño/Southern Oscillation event. *J. Geophys. Res.*, 92, 6545-6558.

Feely, R. A., Sabine, C. L., Hernandez-Ayon, J. M., Ianson, D. and Hales, B. (2008) Evidence for Upwelling of Corrosive "Acidified" Water onto the Continental Shelf. *Science*, 1155676.

Feely, R. A., Sabine, C. L., Lee, K., Berelson, W., Kleypas, J., Fabry, V. J. and Millero, F. J. (2004) Impact of Anthropogenic $CO_2$ on the $CaCO_3$ System in the Oceans. *Science*, 305(5682), 362-366.

Feely, R. A., Wanninkhof, R., Cosca, C. E., Murphy, P. P., Lamb, M. F. and Steckley, M. D. (1995) $CO_2$ distributions in the equatorial Pacific during the 1991-92 ENSO event. *Deep-Sea Res. II* 42(2-3), 365-386.

Feely, R. A., Wanninkhof, R., Goyet, C., Archer, D. E. and Takahashi, T. (1997) Variability of $CO_2$ distributions and sea-air fluxes in the central and eastern equatorial Pacific during the 1991-1994 El Niño. *Deep-Sea Res. II*, 44(9-10), 1851-1867.

Feely, R. A., Wanninkhof, R., Takahashi, T. and Tans, P. (1999) Influence of El Niño on the equatorial Pacific contribution to atmospheric $CO_2$ accumulation. *Nature*, 398, 597-601.

Fenton, M., Kelly, G., Vella, K. and Innes, J. (2007) Climate change and Great Barrier Reef: industries and communities. In *Climate Change and the Great Barrier Reef*

(Eds. J. J.E. and M. P.A.), Great Barrier Reef Marine Park Authority and Australian Greenhouse Office, Australia, pp. 745-772.

Folland, C. K., Parker, D. E., Colman, A. and Washington, R. (1999) Large scale modes of ocean surface temperature since the late nineteenth century. In *Beyond El Niño: Decadal and Interdecadal Climate Variability* (Ed. A. Navarra), Springer-Verlag, pp. 73-102.

Folland, C. K., Rayner, N. A., Brown, S. J., Smith, T. M., Shen, S. S. P., Parker, D. E., Macadam, I., Jones, P. D., Jones, R. N., Nicholls, N. and Sexton, D. M. H. (2001) Global temperature change and its uncertainties since 1861. *Geophys. Res. Lett.*, 28(13), 2621-2624.

Forster, P., Ramaswamy, V., Artaxo, P., Berntsen, T., Betts, R., Fahey, D. W., Haywood, J., Lean, J., Lowe, D. C., Myhre, G., Nganga, J., Prinn, R., Raga, G., Schulz, M. and Dorland, R. V. (2007) Changes in Atmospheric Constituents and in Radiative Forcing. In *Climate Change 2007: The Physical Science Basis. Contribution of Working Group I to the Fourth Assessment Report of the Intergovernmental Panel on Climate Change* (Eds. S. Solomon, D. Qin, M. Manning, Z. Chen, M. Marquis, K. B. Averyt, M.Tignor and H. L. Miller), Cambridge University Press, Cambridge, United Kingdom and New York, NY, USA.

Foster, I. T., Toonen, B. and Worley, P. H. (1996) Performance of Massively Parallel Computers for Spectral Atmospheric Models. *J. Atmos. Oceanic Technol.*, 13, 1031-1045.

Foujols, M.-A., Lévy, M., Aumont, O. and Madec, G. (2000) OPA 8.1 Tracer Model reference Manual. Note technique du pôle de modélisation, Institut Pierre Simon Laplace, IPSL, France, pp. 39.

Francey, R. J., Tans, P. P., Allison, C. E., Enting, I. G., White, J. W. C. and Trolier, M. (1995) Changes in oceanic and terrestrial carbon uptake since 1982. *Nature*, 373(6512), 326-330.

Frankignoulle, M., Abril, G., Borges, A., Bourge, I., Canon, C., Delille, B., Libert, E. and Théate, J.-M. (1998) Carbon Dioxide Emission from European Estuaries. *Science*, 282(5388), 434-436.

Frankignoulle, M. and Borges, A. V. (2001) European continental shelf as a significant sink for atmospheric carbon dioxide. *Global Biogeochem. Cycles*, 15(3), 569-576.

Frankignoulle, M., Bourge, I., Canon, C. and Dauby, P. (1996a) Distribution of surface seawater partial $CO_2$ pressure in the English Channel and in the Southern Bight of the North Sea. *Continental Shelf Research*, 16, 381-395.

Frankignoulle, M., Canon, C. and Gattuso, J. P. (1994) Marine calcification as a source of carbon dioxide: Positive feedback of increasing atmospheric $CO_2$. *Limnol. Oceanogr.*, 39, 458-462.

Frankignoulle, M., Gattuso, J.-P., Biondo, R., Bourge, I., Copin-Montégut, G. and Pichon, M. (1996b) Carbon fluxes in coral reefs. 2. Eulerian study of inorganic carbon dynamics and measurement of air-sea $CO_2$ exchanges. *Mar. Ecol. Prog. Ser.*, 145, 123-132.

Fransson, A., Chierici, M. and Nojiri, Y. (2006) Increased net $CO_2$ outgassing in the upwelling region of the southern Bering Sea in a period of variable marine climate between 1995 and 2001. *J. Geophys. Res.*, 111, C08008, doi:08010.01029/02004JC002759.

Friedlingstein, P., Bopp, L., Clais, P., Dufresne, J.-L., Fairhead, L., LeTreut, H., Monfray, P. and Orr, J. C. (2001) Positive feedback between future climate change and the carbon cycle. *Geophys. Res. Lett.*, 28, 1543-1546.

Friedrich, T., Oschlies, A. and Eden, C. (2006) Role of wind stress and heat fluxes in interannual-to-decadal variability of air-sea $CO_2$ and $O_2$ fluxes in the North Atlantic. *Geophys. Res. Lett.*, 33, L21S04, doi:10.1029/2006GL026538.

Fung, I. Y., Meyn, S. K., Tegen, I., Doney, S. C., John, J. G. and Bishop, J. K. B. (2000) Iron supply and demand in the upper ocean. *Global Biogeochem. Cycles*, 14(1), 281-296.

Furnas, M., Mitchell, A. W. and Skuza, M. (1997), River inputs of nutrients and sediment to the Great Barrier Reef, paper presented at State of the Great Barrier Reef World Heritage Area Workshop: proceedings of a technical workshop, Great Barrier Reef Marine Park Authority, Townsville, Queensland, Australia, 27-29 November 1995.

Furnas, M. J. and Mitchell, A. W. (1986) Phytoplankton dynamics in the central Great Barrier Reef - I. Seasonal changes in biomass and community structure and their relation to intrusive activity. *Continental Shelf Research*, 6(3), 363-384.

Furnas, M. J. and Mitchell, A. W. (1996a) Nutrient inputs into the central Great Barrier Reef (Australia) from subsurface intrusions of Coral Sea waters: a two-dimensional displacement model. *Continental Shelf Research*, 16(9), 1127-1148.

Furnas, M. J. and Mitchell, A. W. (1996b) Pelagic primary production in the Coral and southern Solomon Seas. *Mar. Freshw. Res.*, 47, 695-706.

Fyfe, J. C., Boer, G. J. and Flato, G. M. (1999) The arctic and antarctic oscillations and their projected changes under global warming. *Geophys. Res. Lett.*, 26(11), 1601-1604.

Gagan, M. K., Ayliffe, L. K., Beck, J. W., Cole, J. E., Druffel, E. R. M., Dunbar, R. B. and Schrag, D. P. (2000) New views of tropical paleoclimates from corals. *Quat. Sci. Rev.*, 19, 45-64.

Galperin, B., Kantha, L. H., Hassid, S. and Rosati, A. (1988) A quasi-equilibrium turbulent energy model for geophysical flows. *J. Atmos. Sci.*, 45, 55-62.

Ganachaud, A. and Wunsch, C. (2000) Improved estimates of global ocean circulation, heat transport and mixing from hydrographic data. *Nature*, 408(6811), 453-457.

Gardner, W. D., Gundersen, J. S., Richardson, M. J. and Walsh, I. D. (1999) The role of seasonal and diel changes in mixed-layer depth on carbon and chlorophyll distributions in the Arabian Sea. *Deep-Sea Res. II*, 46(8-9), 1833-1858.

Gattuso, J.-F., Pichon, M., B. Delesalle and Frankignoulle, M. (1993) Community metabolism and air-sea $CO_2$ fluxes in a coral reef ecosystem (Moorea, French Polynesia). *Mar. Ecol. Prog. Ser.*, 96, 259-267.

Gattuso, J.-P., Allemand, D. and Frankignoulle, M. (1999) Photosynthesis and Calcification at Cellular, Organismal and Community Levels in Coral Reefs: A Review on Interactions and Control by Carbonate Chemistry. *Amer. Zool.*, 39(1), 160-183.

Gattuso, J.-P. and Buddemeier, R. W. (2000) Ocean biogeochemistry: Calcification and $CO_2$, 407(6802), 311-313.

Gattuso, J. P., Frankignoulle, M., Bourge, I., Romaine, S. and Buddemeier, R. W. (1998) Effect of calcium carbonate saturation of seawater on coral calcification. *Glob. Planet. Change*, 18, 37-46.

Gent, P. R. (1991) The heat budget of the TOGA-COARE domain in an ocean model. *J. Geophys. Res.*, 96, 3323-3330.

Gillett, N. P. and Thompson, D. W. J. (2003) Simulation of Recent Southern Hemisphere Climate Change. *Science*, 302(5643), 273-275.

Gleckler, P. J., Sperber, K. R. and AchutaRao, K. (2006) Annual cycle of global ocean heat content: Observed and simulated. *J. Geophys. Res.*, 111, C06008, doi:06010.01029/02005JC003223.

GLOBALVIEW-$CO_2$ (2006) Cooperative atmospheric data integration project - carbon dioxide. CD-ROM, NOAACMDL, Boulder, CO. [Also available on Internet via anonymous FTP to ftp.cmdl.noaa.gov, Path: ccg/co2/GLOBALVIEW].

Gloor, M., Gruber, N., Sarmiento, J. L., Sabine, C., Feely, D. and Rödenbeck, C. (2003) A first estimate of present and preindustrial air-sea $CO_2$ flux patterns based on ocean interior carbon measurements and models. *Geophys. Res. Lett.*, 30(1), 1010, doi:1010.1029/2002GL015594.

Glynn, P. W. (1996) Coral reef bleaching: facts, hypotheses and implications. *Glob. Change Biol.*, 2(6), 495-509.

Glynn, P. W., Maté, J. L., Baker, A. C. and Calderón, M. O. (2001) Coral bleaching and mortality in panama and ecuador during the 1997-1998 El Niño-Southern Oscillation Event: spatial/temporal patterns and comparisons with the 1982-1983 event. *Bull. Mar. Sci.*, 69, 79-109.

Gnanadesikan, A. (1999) A simple predictive model for the structure of the oceanic pycnocline. *Science*, 283(5410), 2077-2079.

Gnanadesikan, A., Dixon, K. W., Griffies, S. M., Delworth, T. L., Harrison, M. J., Held, I. M., Hurlin, W. J., Pacanowski, R. C., Rosati, A., Samuels, B. L., Spelman, M. J., Stouffer, R. J., Winton, M., Wittenberg, A. T., Dunne, J. P. and al., e. (2006) GFDL's CM2 Global Coupled Climate Models. Part II: The baseline ocean simulation. *J. Clim.*, 19(5), 675-697.

Gnanadesikan, A., Sarmiento, J. L. and Slater, R. D. (2003) Effects of patchy ocean fertilization on atmospheric carbon dioxide and biological production. *Global Biogeochem. Cycles*, 17(2), 1050, doi:1010.1029/2002GB001940.

Gnanadesikan, A., Slater, R. D., Gruber, N. and Sarmiento, J. L. (2002) Oceanic vertical exchange and new production: A comparison between models and observations. *Deep-Sea Res. II*, 49, 363-401.

Godfrey, J. S., Cresswell, G. R. and Boland, F. M. (1980) Observations of low Richardson numbers and undercurrents near a front in the East Australian Current. *J. Phys. Oceanogr.*, 10(2), 301-307.

González-Dávila, M., Santana-Casiano, J. M., Rueda, M.-J., Llinás, O. and González-Dávila, E.-F. (2003) Seasonal and interannual variability of sea-surface carbon dioxide species at the European Station for Time Series in the Ocean at the Canary Islands (ESTOC) between 1996 and 2000. *Global Biogeochem. Cycles*, 17(3), 1076, doi:1010.1029/2002GB001993.

Goreau, T. F. and Goreau, N. I. (1959) The physiology of skeleton formation in corals. II. Calcium deposition by hermatypic corals under various conditions in the reef. *Biol. Bull.*, 117, 239-250.

Gould, J., Roemmich, D., Wijffels, S., Freeland, H., Ignaszewsky, M., Jianping, X., Pouliquen, S., Desaubies, Y., Send, U., Radhakrishnan, K., Takeuchi, K., Kim, K., Danchenkov, M., Sutton, P., King, B., Owens, B. and Riser, S. (2004) Argo profiling floats bring a new era of in-situ ocean observations. *Eos Trans. AGU*, 85(19), doi:10.1029/2004EO190002.

Gourdeau, L., Kessler, W. S., Davis, R. E., Sherman, J., Maes, C. and Kestenare, E. (2008) Zonal jets entering the Coral Sea. *J. Phys. Oceanogr.*, 38, 715-725.

Gouretski, V. and Koltermann, K. P. (2007) How much is the ocean really warming? *Geophys. Res. Lett.*, 34, L01610, doi:01610.01029/02006GL027834.

Gregg, M. C., Peters, H., Wesson, J. C., Oakey, N. S. and Shay, T. J. (1985) Intensive measurements of turbulence and shear in the equatorial undercurrent. *Nature*, 318(6042), 140-144.

Griffies, S., Böning, C., Bryan, F. O., Chassignet, E. P., Gerdes, R., Hasumi, H., Hirst, A. C., Treguier, A. M. and Webb, D. (2000) Developments in ocean climate modelling. *Ocean Modelling*, 2, 123-192.

Gruber, N. and Keeling, C. D. (2001) An improved estimate of the isotopic air-sea disequilibrium of $CO_2$: Implications for the oceanic uptake of anthropogenic $CO_2$. *Geophys. Res. Lett.*, 28(3), 555-558.

Gruber, N., Keeling, C. D. and Bates, N. R. (2002) Interannual variability in the North Atlantic Ocean carbon sink. *Science*, 298, 2374-2378.

Gruber, N., Sarmiento, J. L. and Stocker, T. F. (1996) An improved method for detecting anthropogenic $CO_2$ in the oceans. *Global Biogeochem. Cycles*, 10, 809-837.

Gurney, K. R., Law, R. M., Denning, A. S., Rayner, P. J., Baker, D., Bousquet, P., Bruhwiler, L., Chen, Y.-H., Ciais, P., Fan, S., Fung, I. Y., Gloor, M., Heimann, M., Higuchi, K., John, J., Maki, T., Maksyutov, S., Masarie, K., Peylin, P., Prather, M., Pak, B. C., Randerson, J., Sarmiento, J., Taguchi, S., Takahashi, T. and Yuen, C.-W. (2002) Towards robust regional estimates of CO2 sources and sinks using atmospheric transport models. *Nature*, 415(6872), 626-630.

Haidvogel, D. B., Arango, H. G., Hedstrom, K., Beckmann, A., Malanotte-Rizzoli, P. and Shchepetkin, A. F. (2000) Model evaluation experiments in the North Atlantic Basin: simulations in nonlinear terrain-following coordinates. *Dyn. Atmos. Oceans*, 32, 239-281.

Haidvogel, D. B. and Beckmann, A. (1999) *Numerical Ocean Circulation Modeling. Series on Environmental Science and Management*, Imperial College Press, 319 pp.

Hancock, G. J., Webster, I. T. and Stieglitz, T. C. (2006) Horizontal mixing of Great Barrier Reef waters: Offshore diffusivity determined from radium isotope distribution. *J. Geophys. Res.*, 111, C12019, doi:12010.11029/12006JC003608.

Hansell, D. A., Carlson, C. A., Bates, N. R. and Poisson, A. P. (1997) Horizontal and vertical removal of organic carbon in the equatorial Pacific Ocean: a mass balance assessment. *Deep-Sea Res. II*, 45, 2115-2130.

Hansen, L. D., Dipple, G. M., Gordon, T. M. and Kellett, D. A. (2005) Carbonated serpentinite (listwanite) at Atlin, British Columbia: A geological analogue to carbon dioxide sequestration. *Can. Mineral.*, 43(1), 225-239.

Harris, P. T., Heap, A., Passlow, V., Hughes, M., Daniell, J., Hemer, M. and Anderson, O. (2005) Tidally incised valleys on tropical carbonate shelves: An example from the northern Great Barrier Reef, Australia. *Marine Geology*, 220(1-4), 181-204.

Harris, R. P. (1994) Zooplankton grazing on the coccolithophore Emiliania huxleyi and its role in inorganic carbon flux. *Marine Biology*, 119, 431-439.

Harrison, D. E. (1996) Vertical velocity in the central tropical Pacific: a circulation model perspective for JGOFS. *Deep-Sea Res. II*, 43(4-6), 687-705.

Haugan, P. M. and Drange, H. (1996) Effects of $CO_2$ on the ocean environment. *Energy Convers. Mgmt*, 37, 1019-1022.

Hazeleger, W. (2005) Can global warming affect tropical ocean heat transport? *Geophys. Res. Lett.*, 32, L22701, doi:22710.21029/22005GL023450.

Hazeleger, W., Seager, R., Cane, M. A. and Naik, N. H. (2004) How Can Tropical Pacific Ocean Heat Transport Vary? *J. Phys. Oceanogr.*, 34(1), 320-333.

Heinze, C. (2004) Simulating oceanic $CaCO_3$ export production in the greenhouse. *Geophys. Res. Lett.*, 31, L16308, doi:16310.11029/12004GL020613.

Hendon, H. H. and Liebmann, B. (1990) A composite study of onset of the Australian summer monsoon. *J. Atmos. Sci.*, 47, 2227-2240.

Hennessy, K., Fitzharris, B., Bates, B. C., Harvey, N., Howden, S. M., Hughes, L., Salinger, J. and Warrick, R. (2007) Australia and New Zealand. In *Climate Change 2007: Impacts, Adaptation and Vulnerability. Contribution of Working Group II to the Fourth Assessment Report of the Intergovernmental Panel on Climate Change* (Eds. M. L. Parry, O. F. Canziani, J. P. Palutikof, P. J. v. d. Linden and C. E. Hanson), Cambridge University Press, Cambridge, UK, pp. 507-540.

Heywood, K. J., Naveira Garabato, A. C. and Stevens, D. P. (2002) High mixing rates in the abyssal Southern Ocean. *Nature*, 415(6875), 1011-1014.

Hinga, K. R. (2002) Effects of pH on coastal marine phytoplankton. *Mar. Ecol. Prog. Ser.*, 238, 281-300.

Hoegh-Guldberg, O. (1999) Climate change, coral bleaching and the future of the world's coral reefs. *Mar. Freshw. Res.*, 50(8), 839-866.

Hoegh-Guldberg, O., Mumby, P. J., Hooten, A. J., Steneck, R. S., Greenfield, P., Gomez, E., Harvell, C. D., Sale, P. F., Edwards, A. J., Caldeira, K., Knowlton, N., Eakin, C. M., Iglesias-Prieto, R., Muthiga, N., Bradbury, R. H., Dubi, A. and Hatziolos, M. E. (2007) Coral Reefs Under Rapid Climate Change and Ocean Acidification. *Science*, 318(5857), 1737-1742.

Hoffert, M. I., Caldeira, K., Benford, G., Criswell, D. R., Green, C., Herzog, H., Jain, A. K., Kheshgi, H. S., Lackner, K. S., Lewis, J. S., Lightfoot, H. D., Manheimer, W., Mankins, J. C., Mauel, M. E., Perkins, L. J., Schlesinger, M. E., Volk, T. and Wigley, T. M. L. (2002) Advanced Technology Paths to Global Climate Stability: Energy for a Greenhouse Planet. *Science*, 298(5595), 981-987.

Holmen, K. (1992) The global carbon cycle. In *Global Biogeochemical Cycles* (Eds. S. S. Butcher, R. J. Charlson, G. H. Orians and G. V. Wolfe), Academic Press, NY, pp. 239-262.

Hopley, D., Parnell, K. E. and Isdale, P. J. (1989) The Great Barrier Reef Marine Park: Dimensions and regional patterns. *Aust. Geogr. Studies*, 27, 47-66.

Houghton, J. T., Ding, Y., Griggs, D. J., Noguer, M., P. J. van der Linden, Dai, X., Maskell, K. and Johnson, C. A. (2001) *Climate Change 2001: The Scientific Basis: Contribution of Working Group I to the Third Assessment Report of the Intergovernmental Panel in Climate Change*, Cambridge Univ. Press, New York, 881 pp.

House, J. I., Prentice, C. I. and Quéré, C. L. (2002) Maximum impacts of future reforestation or deforestation on atmospheric $CO_2$. *Global Change Biology*, 8(11), 1047-1052.

Huisman, J., Pham Thi, N. N., Karl, D. M. and Sommeijer, B. (2006) Reduced mixing generates oscillations and chaos in the oceanic deep chlorophyll maximum. *Nature*, 439(7074), 322-325.

Hurrell, J. W. (1995) Decadal trends in the North Atlantic Oscillation: regional temperatures and precipitation. *Science*, 269(5224), 676-679.

Iglesias-Rodriguez, M. D., Armstrong, R., Feely, R., Hood, R., Kleypas, J., Milliman, J. D., Sabine, C. and Sarmiento, J. (2002) Progress made in study of ocean's calcium carbonate budget. *Eos*, 83(34), 365, 374-375.

Inoue, H. and Sugimura, Y. (1992) Variations and distributions of $CO_2$ in and over the equatorial Pacific during the period from 1986/88 El Niño event to the 1988/89 La Niña event. *Tellus B*, 44, 1-22.

Ishii, M. (2001) Seasonal variation in total inorganic carbon and its controlling processes in surface waters of the western North Pacific subtropical gyre. *Mar. Chem.*, 75, 17-32.

Ivins, E. R. (2009) Ice Sheet Stability and Sea Level. *Science*, 324(5929), 888-889.

Jacobson, A. R., Fletcher, S. E. M., Gruber, N., Sarmiento, J. L. and Gloor, M. (2007a) A joint atmosphere-ocean inversion for surface fluxes of carbon dioxide: 1. Methods and global-scale fluxes. *Global Biogeochem. Cycles*, 21, GB1019, doi:1010.1029/2005GB002556.

Jacobson, A. R., Fletcher, S. E. M., Gruber, N., Sarmiento, J. L. and Gloor, M. (2007b) A joint atmosphere-ocean inversion for surface fluxes of carbon dioxide: 2. Regional results. *Global Biogeochem. Cycles*, 21, GB1020, doi:1010.1029/2006GB002703.

Jaffrés, J. and Everingham, Y. (2005) An exploratory investigation of the relationship between decadal rainfall and climate indices. *Proc. Aust. Soc. Sugar Cane Technol.*, 27, 96-108.

Jaffrés, J. B. D., Shields, G. A. and Wallmann, K. (2007) The oxygen isotope evolution of seawater: A critical review of a long-standing controversy and an improved geological water cycle model for the past 3.4 billion years. *Earth-Science Reviews*, 83(1-2), 83-122.

Jamieson, J. C. (1953) Phase equilibrium in the system calcite-aragonite. *J. Chem. Phys.*, 21, 1385-1390.

Jeffrey, S. W. and Hallegraeff, G. M. (1990) Phytoplankton ecology of Australian waters. In *Biology of Marine Plants* (Eds. M. N. Clayton and R. J. King), Longman Cheshire, Melbourne, pp. 310-348.

Jickells, T. D., An, Z. S., Andersen, K. K., Baker, A. R., Bergametti, G., Brooks, N., Cao, J. J., Boyd, P. W., Duce, R. A., Hunter, K. A., Kawahata, H., Kubilay, N.,

laRoche, J., Liss, P. S., Mahowald, N., Prospero, J. M., Ridgwell, A. J., Tegen, I. and Torres, R. (2005) Global Iron Connections Between Desert Dust, Ocean Biogeochemistry, and Climate. *Science*, 308(5718), 67-71.

Jin, F.-F. (1997) An equatorial ocean recharge paradigm for ENSO. Part I: Conceptual model, 54, 811-829.

Joachimski, M. M., Simon, L., Geldern, R. v. and Lécuyer, C. (2005) Boron isotope geochemistry of Paleozoic brachiopod calcite: Implications for a secular change in the boron isotope geochemistry of seawater over the Phanerozoic. *Geochim. Cosmochim. Acta*, 69(16), 4035-4044.

Johnson, G. C., McPhaden, M. J. and Firing, E. (2001) Equatorial Pacific Ocean horizontal velocity, divergence, and upwelling. *J. Phys. Oceanogr.*, 31, 839-849.

Jokiel, P. L. and Coles, S. L. (1977) Effects of temperature on the mortality and growth of Hawaiian reef corals. *Mar. Biol.*, 43, 201-208.

Joos, F., Plattner, G.-K., Stocker, T. F., Marchal, O. and Schmittner, A. (1999) Global warming and marine carbon cycle feedbacks on future atmospheric $CO_2$. *Science*, 284(5413), 464-467.

Joos, F., Prentice, I. C., Sitch, S., Meyer, R., Hooss, G., Plattner, G.-K., Gerber, S. and Hasselmann, K. (2001) Global warming feedbacks on terrestrial carbon uptake under the Intergovernmental Panel on Climate Change (IPCC) emission scenario. *Global Biogeochem. Cycles*, 15, 891-907.

Joos, F., Sarmiento, J. L. and Siegenthaler, U. (1991) Estimates of the effect of Southern Ocean iron fertilization on atmospheric $CO_2$ concentrations. *Nature*, 349(6312), 772.

Julian, P. R. and Chervin, R. M. (1978) A study of the Southern Oscillation and the Walker Circulation Phenomenon. *Mon. Wea. Rev.*, 106, 1433-1451.

Kako, S. and Kubota, M. (2007) Variability of mixed layer depth in Kuroshio/Oyashio Extension region: 2005-2006. *Geophys. Res. Lett.*, 34, L11612, doi:11610.11029/12007GL030362.

Kara, A. B., Hurlburt, H. E. and Wallcraft, A. J. (2005) Stability-dependent exchange coefficients for air-sea fluxes. *J. Atmos. Oce. Tech.*, 22, 1080-1094.

Kara, A. B., Rochford, P. A. and Hurlburt, H. E. (2000a) An optimal definition for ocean mixed layer depth. *J. Geophys. Res.*, 105, 16803-16821.

Kara, A. B., Rochford, P. A. and Hurlburt, H. E. (2000b) Mixed layer depth variability and barrier layer formation over the North Pacific Ocean. *J. Geophys. Res.*, 105(C7), 16783-16801.

Kara, A. B., Rochford, P. A. and Hurlburt, H. E. (2002) Air-sea flux estimates and the 1997-1998 ENSO event. *Bound.-Layer Meteor.*, 103(3), 439-458.

Kara, A. B., Rochford, P. A. and Hurlburt, H. E. (2003) Mixed layer depth variability over the global ocean. *J. Geophys. Res.*, 108, doi:10.1029/2000JC000736.

Katsaros, K. B. (1977) The sea surface temperature deviation at very low wind speeds; Is there a limit? *Tellus B*, 29, 229-239.

Katsaros, K. B. (1980) The aqueous thermal boundary layer. *Bound.-Layer Meteor.*, 18, 107-127.

Kawahata, H., Suzuki, A., Ayukai, T. and Goto, K. (2000) Distribution of the fugacity of carbon dioxide in the surface seawater of the Great Barrier Reef. *Mar. Chem.*, 72, 257-272.

Kawahata, H., Suzuki, A. and Goto, K. (1997) Coral reef ecosystems as a source of atmospheric $CO_2$: evidence from $pCO_2$ measurements of surface waters. *Coral Reefs*, 16(4), 261-266.

Keeling, C. D. and Revelle, R. (1985) Effects of El Niño/Southern Oscillation on the atmospheric content of carbon dioxide. *Meteoritics*, 20, 437-450.

Keeling, C. D., Whorf, T. P., Wahlen, M. and van der Plicht, J. (1995) Interannual extremes in the rate of rise of atmospheric carbon dioxide since 1980. *Nature*, 375, 666-670.

Keeling, R. F. and Garcia, H. E. (2002) The change in oceanic O2 inventory associated with recent global warming. *PNAS*, 99(12), 7848-7853.

Keeling, R. F., Najjar, R. P., Bender, M. L. and Tans, P. P. (1993) What atmospheric oxygen measurements can tell us about the global carbon cycle. *Global Biogeochem. Cycles*, 7, 37-67.

Keeling, R. F., Piper, S. C., Bollenbacher, A. F. and Walker, J. S. (2008) Atmospheric $CO_2$ records from sites in the SIO air sampling network. In *Trends: A*

*Compendium of Data on Global Change*, Carbon Dioxide Information Analysis Center, Oak Ridge National Laboratory, U.S. Department of Energy, Oak Ridge, Tenn., U.S.A.

Keeling, R. F., Piper, S. C. and Heimann, M. (1996) Global and hemispheric $CO_2$ sinks deduced from changes in atmospheric $O_2$ concentration. *Nature*, 381(6579), 218-221.

Kessler, W. S. (2006) The circulation of the eastern tropical Pacific: A review. *Prog. Oceanogr.*, 69, 181-217.

Kessler, W. S. and Gourdeau, L. (2007) The annual cycle of circulation of the southwest subtropical Pacific, analyzed in an ocean GCM. *J. Phys. Oceanogr.*, 37(6), 1610-1627.

Kettle, H. and Merchant, C. J. (2005) Systematic errors in global air-sea $CO_2$ flux caused by temporal averaging of sea-level pressure. *Atmos. Chem. Phys.*, 5, 1459-1466.

King, B. and Wolanski, E. (1996) Tidal current variability in the Central Great Barrier Reef. *J. Mar. Sys.*, 9(3-4), 187-202.

Kinsey, D. W. and Hopley, D. (1991) The significance of coral reefs as global carbon sinks - response to Greenhouse. *Palaeogeo. Palaeoclim. Palaeoecol.*, 89, 363-377.

Kinzie, R. A., III, Takayama, M., Santos, S. R. and Coffroth, M. A. (2001) The Adaptive Bleaching Hypothesis: Experimental Tests of Critical Assumptions. *Biol. Bull.*, 200(1), 51-58.

Klaas, C. and Archer, D. E. (2002) Association of sinking organic matter with various types of mineral ballast in the deep sea: Implications for the rain ratio. *Global Biogeochem. Cycles*, 16(4), 1116, doi:1110.1029/2001GB001765.

Kleypas, J. A., Buddemeier, R. W., Archer, D., Gattuso, J.-P., Langdon, C. and Opdyke, B. N. (1999a) Geochemical Consequences of Increased Atmospheric Carbon Dioxide on Coral Reefs. *Science*, 284(5411), 118-120.

Kleypas, J. A., Buddemeier, R. W., Eakin, C. M., Gattuso, J.-P., Guinotte, J., Hoegh-Guldberg, O., Iglesias-Prieto, R., Jokiel, P. L., Langdon, C., Skirving, W. and Strong, A. E. (2005) Comment on ‘‘Coral reef calcification and climate change:

The effect of ocean warming,’’. *Geophys. Res. Lett.*, 32, L08601, doi:08610.01029/02004GL022329.

Kleypas, J. A., Feely, R. A., Fabry, V. J., Langdon, C., Sabine, C. L. and Robbins, L. L. (2006) Impacts of Ocean Acidification on Coral Reefs and Other Marine Calcifiers. A Guide for Future Research, Report of a workshop sponsored by NSF, NOAA and the USGS, St. Petersburg, FL, pp. 88.

Kleypas, J. A., McManus, J. W. and Meñez, L. A. B. (1999b) Environmental Limits to Coral Reef Development: Where Do We Draw the Line? *Amer. Zool.*, 39(1), 146-159.

Koeve, W. (2002) Upper ocean carbon fluxes in the Atlantic Ocean: The importance of the POC:PIC ratio. *Global Biogeochem. Cycles*, 16(4), 1056, doi:1010.1029/2001GB001836.

Krakauer, N. Y., Randerson, J. T., Primeau, F. W., Gruber, N. and Menemenlis, D. (2006) Carbon isotope evidence for the latitudinal distribution and wind speed dependence of the air-sea gas transfer velocity. *Tellus B*, 58(5), 390-417.

Kraus, E. B. (1972) *Atmosphere-Ocean Interaction*, Oxford Univ. Press, London, 275 pp.

Kraus, E. B. and Businger, J. A. (1994) *Atmosphere-Ocean Interaction*, Oxford Univ. Press, New York, 362 pp.

Ku, T. and Li, H. (1998) Speleothems as high-resolution paleoenvironment archives: Records from northeastern China. *Journal of Earth System Science*, 107(4), 321-330.

Kushner, P. J., Held, I. M. and Delworth, T. L. (2001) Southern Hemisphere atmospheric circulation response to global warming. *Journal of Climate*, 14(10), 2238.

Langdon, C. and Atkinson, M. J. (2005) Effect of elevated $pCO_2$ on photosynthesis and calcification of corals and interactions with seasonal change in temperature/irradiance and nutrient enrichment. *J. Geophys. Res.*, 110, C09S07, doi:10.1029/2004JC002576.

Langdon, C., Broecker, W. S., Hammond, D. E., Glenn, E., Fitzsimmons, K., Nelson, S. G., Peng, T.-S., Hajdas, I. and Bonani, G. (2003) Effect of elevated $CO_2$ on the community metabolism of an experimental coral reef. *Global Biogeochem. Cycles*, 17, 10.1029/2002GB001941.

Langdon, C., Takahashi, T., Sweeney, C., Chipman, D., Goddard, J., Marubini, F., Aceves, H., Barnett, H. and Atkinson, M. (2000) Effect of calcium carbonate saturation state on the calcification rate of an experimental coral reef. *Global Biogeochem. Cycles*, 14, 639-654.

Large, W. G., McWilliams, J. C. and Doney, S. C. (1994) Oceanic vertical mixing: a review and a model with a nonlocal boundary layer parameterization. *Rev. Geophys.*, 32, 363-403.

Lau, K. M. and Weng, H. (1999) Interannual, decadal-interdecadal, and global warming signals in sea surface temperature during 1955-97. *Journal of Climate*, 12(5), 1257-1267.

Lawrence, K. T. and Herbert, T. D. (2005) Late Quaternary sea-surface temperatures in the western Coral Sea: Implications for the growth of the Australian Great Barrier Reef. *Geology*, 33(8), 677-680.

Le Borgne, R., Feely, R. A. and Mackey, D. J. (2002) Carbon fluxes in the equatorial Pacific: a synthesis of the JGOFS programme. *Deep-Sea Res. II*, 49(13-14), 2425-2442.

Le Quéré, C., Orr, J. C., Monfray, P. and Aumont, O. (2000) Interannual variability of the oceanic sink of $CO_2$ from 1979 through 1997. *Global Biogeochem. Cycles*, 10, 783-796.

Le Quéré, C., Rödenbeck, C., Buitenhuis, E. T., Conway, T. J., Langenfelds, R., Gomez, A., Labuschagne, C., Ramonet, M., Nakazawa, T., Metzl, N., Gillett, N. and Heimann, M. (2007) Saturation of the southern ocean $CO_2$ sink due to recent climate change. *Science*, 10.1126/science.1136188.

Lean, J., Beer, J. and Bradley, R. (1995) Reconstruction of solar irradiance since 1610: Implications for climate change. *Geophys. Res. Lett.*, 22(23), 3195-3198.

Leclercq, N., Gattuso, J.-P. and Jaubert, J. (2000) $CO_2$ partial pressure controls the calcification rate of a coral community. *Global Change Biology*, 6(3), 329-334.

Leclercq, N., Gattuso, J.-P. and Jaubert, J. (2002) Primary production, respiration, and calcification of a coral reef mesocosm under increased $CO_2$ partial pressure. *Limnol. Oceanogr.*, 47, 558-564.

Ledwell, J. R., Montgomery, E. T., Polzin, K. L., St. Laurent, L. C., Schmitt, R. W. and Toole, J. M. (2000) Evidence for enhanced mixing over rough topography in the abyssal ocean. *Nature*, 403(6766), 179-182.

Ledwell, J. R., Watson, A. J. and Law, C. S. (1993) Evidence for slow mixing across the pycnocline from an open-ocean tracer-release experiment. *Nature*, 364(6439), 701-703.

Ledwell, J. R., Watson, A. J. and Law, C. S. (1998) Mixing of a tracer in the pycnocline. *J. Geophys. Res.*, 103(C10), 21499-21529.

Lee, C. M., Jones, B. H., Brink, K. H. and Fischer, A. S. (2000) The upper-ocean response to monsoonal forcing in the Arabian Sea: seasonal and spatial variability. *Deep-Sea Res. II*, 47(7-8), 1177-1226.

Lee, K. (2001) Global net community production estimated from the annual cycle of surface water total dissolved inorganic carbon. *Limnol. Oceanogr.*, 46(6), 1287-1297.

Lee, K., Tong, L. T., Millero, F. J., Sabine, C. L., Dickson, A. G., Goyet, C., Park, G.-H., Wanninkhof, R., Feely, R. A. and Key, R. M. (2006) Global relationships of total alkalinity with salinity and temperature in surface waters of the world's oceans. *Geophys. Res. Lett.*, 33, L19605, doi:19610.11029/12006GL027207.

Lerman, A. and Mackenzie, F. (2005) $CO_2$ air-sea exchange due to calcium carbonate and organic matter storage, and its implications for the global carbon cycle. *Aquatic Geochemistry*, 11(4), 345-390.

Levitus, S. (1982), Climatological atlas of the world ocean, NOAA Prof. Paper No. 13.

Levitus, S., Antonov, J. I. and Boyer, T. P. (2005) Warming of the world ocean, 1955-2003. *Geophys. Res. Lett.*, 32, L02604, doi:02610.01029GL021592.

Levitus, S., Antonov, J. I., Boyer, T. P. and Stephens, C. (2000) Warming of the world ocean. *Science*, 287(5461), 2225-2229.

Lewis, E. and Wallace, D. W. R. (1998) Program Developed for $CO_2$ System Calculations, ORNL/CDIAC-105. Carbon Dioxide Information Analysis Center, Oak Ridge National Laboratory, U.S. Department of Energy, Oak Ridge, Tennessee.

Lewis, M. R., Carr, M.-E., Feldman, G. C., Esaias, W. and McClain, C. (1990) Influence of penetrating solar radiation on the heat budget of the equatorial Pacific Ocean. *Nature*, 347(6293), 543-545.

Liss, P. S. and Merlivat, L. (1986) Air-sea gas exchange rates: Introduction and synthesis. In *The Role of Sea-Air Exchange in Geochemical Cycling* (Ed. P. Buat-Ménard), Reidel, Dordrecht, pp. 113-127.

Little, A. F., van Oppen, M. J. H. and Willis, B. L. (2004) Flexibility in Algal Endosymbioses Shapes Growth in Reef Corals. *Science*, 304(5676), 1492-1494.

Liu, J. and Curry, J. A. (2006) Variability of the tropical and subtropical ocean surface latent heat flux during 1989-2000. *Geophys. Res. Lett.*, 33, L05706, doi:05710.01029/02005GL024809.

Liu, Z. and Huang, B. (2000) Cause of tropical Pacific warming trend. *Geophys. Res. Lett.*, 27, 1935-1938.

Longhurst, A. R. (1998) *Ecological Geography of the Sea,* Academic Press, San Diego, 398 pp.

Lorbacher, K., Dommenget, D., Niiler, P. P. and Köhl, A. (2006) Ocean mixed layer depth: A subsurface proxy of ocean-atmosphere variability. *J. Geophys. Res.*, 111, C07010, doi:07010.01029/02003JC002157.

Lough, J. M. (2008) Shifting climate zones for Australia's tropical marine ecosystems. *Geophys. Res. Lett.*, 35, L14708, doi:14710.11029/12008GL034634.

Lough, J. M. and Barnes, D. J. (2000) Environmental controls on growth of the massive coral Porites. *J. Exp. Mar. Biol. Ecol.*, 245, 225-243.

Loukos, H., Vivier, F., Murphy, P. P., Harrison, D. E. and Le Quéré, C. (2000) Interannual Variability of Equatorial Pacific $CO_2$ Fluxes Estimated from Temperature and Salinity Data. *Geophys. Res. Lett.*, 27, 1735-1738.

Luick, J. L., Mason, L., Hardy, T. and Furnas, M. J. (2007) Circulation in the Great Barrier Reef Lagoon using numerical tracers and in situ data. *Continental Shelf Research*, 27(6), 757-778.

Lukas, R. and Lindstrom, E. (1991) The mixed layer of the western equatorial Pacific Ocean. *J. Geophys. Res.*, 96, 3343-3357.

Lyman, J. M., Willis, J. K. and Johnson, G. C. (2006) Recent cooling of the upper ocean. *Geophys. Res. Lett.*, 33, L18604, doi:18610.11029/12006GL027033.

Mackenzie, F. T., Lerman, A. and Andersson, A. J. (2004) Past and present of sediment and carbon biogeochemical cycling models. *Biogeosciences*, 1, 11-32.

Mackenzie, F. T., Lerman, A. and Ver, L. M. (2001) Recent past and future of the global carbon cycle. In *Geological Perspectives of Global Climate Change* (Eds. L. C. Gerhard, W. E. Harrison and B. M. Hanson), Am. Assoc. Pet. Geologists Special Publication, Tulsa, Oklahoma, pp. 51-82.

Mackenzie, F. T., Ver, L. M. and Lerman, A. (2002) Coastal zone biogeochemical dynamics under global warming. In *Frontiers in Geochemistry: Organic, Solution, and Ore Deposit Geochemistry* (Ed. W. G. Ernst), Bellwether Publishing Ltd. , Columbia, pp. 27-40.

Mackie, D. S., Boyd, P. W., McTainsh, G. H., Tindale, N. W., Westberry, T. K. and Hunter, K. A. (2008) Biogeochemistry of iron in Australian dust: From eolian uplift to marine uptake. *Geochem. Geophys. Geosyst.*, 9, Q03Q08, doi:10.1029/2007GC001813.

Madec, G., Delecluse, P., Imbard, M. and Lévy, C. (1998) OPA 8.1 Ocean General Circulation Model reference manual. Note du Pôle de modélisation, p. 91, Institut Pierre-Simon Laplace (IPSL), France.

Maes, C., Gourdeau, L., Couvelard, X. and Ganachaud, A. (2007) What are the origins of the Antarctic Intermediate Waters transported by the North Caledonian Jet? *Geophys. Res. Lett.*, 34, L21608, doi:21610.21029/22007GL031546.

Manabe, S. (1969) Climate and the ocean circulation - II. The atmospheric circulation and the effect of heat transfer by ocean currents. *Mon. Wea. Rev.*, 97(11), 775-805.

Manabe, S. and Bryan, K. (1969) Climate calculations with a combined ocean-atmosphere model. *J. Atmos. Sci.*, 26(4), 786-789.

Manabe, S. and Stouffer, R. J. (1994) Multiple century response of a coupled ocean-atmosphere model to an increase of atmospheric carbon dioxide. *J. Clim.*, 7, 5-23.

Manning, A. C., Keeling, R. F., Katz, L. E., Paplawsky, W. J. and McEvoy, E. M. (2003) Interpreting the seasonal cycles of atmospheric oxygen and carbon dioxide

concentrations at American Samoa Observatory. *Geophys. Res. Lett.*, 30(6), 1333, doi:1310.1029/2001GL014312.

Mantua, N. J. and Hare, S. R. (2002) The Pacific Decadal Oscillation. *J. Oceanogr.*, 58, 35-44.

Marchesiello, P., McWilliams, J. C. and Shchepetkin, A. (2001) Open boundary conditions for long-term integration of regional oceanic models. *Ocean Modelling*, 3, 1-20.

Marchesiello, P., McWilliams, J. C. and Shchepetkin, A. (2003) Equilibrium structure and dynamics of the California current system. *J. Phys. Oceanogr.*, 33, 753-783.

Marland, G., Boden, T. A. and Andres, R. J. (2005) Global, Regional, and National $CO_2$ Emissions. In Trends: A Compendium of Data on Global Change. Carbon Dioxide Information Analysis Center, Oak Ridge National Laboratory, U.S. Department of Energy, Oak Ridge, Tenn., USA.

Marshall, A. T. and Clode, P. (2004) Calcification rate and the effect of temperature in a zooxanthellate and an azooxanthellate scleractinian reef coral. *Coral Reefs*, 23, 218-224.

Marsland, S. J., Church, J. A., Bindoff, N. L. and Williams, G. D. (2007) Antarctic coastal polynya response to climate change. *J. Geophys. Res.*, 112, C07009, doi:07010.01029/02005JC003291.

Martin, J. H., Coale, K. H., Johnson, K. S., Fitzwater, S. E., Gordon, R. M., Tanner, S. J., Hunter, C. N., Elrod, V. A., Nowicki, J. L., Coley, T. L., Barber, R. T., Lindley, S., Watson, A. J., Van Scoy, K., Law, C. S., Liddicoat, M. I., Ling, R., Stanton, T., Stockel, J., Collins, C., Anderson, A., Bidigare, R., Ondrusek, M., Latasa, M., Millero, F. J., Lee, K., Yao, W., Zhang, J. Z., Friederich, G., Sakamoto, C., Chavez, F., Buck, K., Kolber, Z., Greene, R., Falkowski, P., Chisholm, S. W., Hoge, F., Swift, R., Yungel, J., Turner, S., Nightingale, P., Hatton, A., Liss, P. and Tindale, N. W. (1994) Testing the iron hypothesis in ecosystems of the equatorial Pacific Ocean. *Nature*, 371(6493), 123-129.

Martin, J. H., Fitzwater, S. E. and Gordon, R. M. (1990) Iron deficiency limits phytoplankton growth in Antarctic waters. *Global Biogeochem. Cycles*, 4(1), 5-12.

Marubini, F. and Atkinson, M. J. (1999) Effects of lowered pH and elevated nitrate on coral calcification. *Mar. Ecol. Prog. Ser.*, 188, 117-121.

Marubini, F., Barnett, H., Langdon, C. and Atkinson, M. J. (2001) Dependence of calcification on light and carbonate ion concentration for the hermatypic coral Porites compressa. *Mar. Ecol. Prog. Ser.* , 220, 153-162.

Marubini, F., Ferrier-Pages, C. and Cuif, J.-P. (2003) Suppression of skeletal growth in scleractinian corals by decreasing ambient carbonate-ion concentration: a cross-family comparison. *Proc. R. Soc. Lond. B*, 270(1511), 179-184.

Marubini, F., Ferrier-Pagès, C., Furla, P. and Allemand, D. (2008) Coral calcification responds to seawater acidification: a working hypothesis towards a physiological mechanism. *Coral Reefs*, 27(3), 491-499.

Marubini, F. and Thake, B. (1999) Bicarbonate addition promotes coral growth. *Limnol. Oceanogr.*, 44, 716-720.

Masumoto, Y. and Meyers, G. (1998) Forced Rossby waves in the southern tropical Indian Ocean. *J. Geophys. Res.*, 103(C12), 27589-27602.

Mata, M. M., Tomczak, M., Wijffels, S. and Church, J. A. (2000) East Australian Current volume transports at 30°S: Estimates from the World Ocean Circulation Experiment hydrographic sections PR11/P6 and the PCM3 current meter array. *J. Geophys. Res.*, 105(C12), 28509-28526.

Mata, M. M., Wijffels, S., Church, J. A. and Tomczak, M. (2006) Statistical description of the East Australian Current low-frequency variability from the WOCE PCM3 array. *Mar. Freshw. Res.*, 57(3), 273-290, DOI: 210.1071/MF05058.

Matear, R. J. (2001) Effects of numerical advection schemes and eddy parameterizations on ocean ventilation and oceanic anthropogenic $CO_2$ uptake. *Ocean Modelling*, 3(3-4), 217-248.

Matear, R. J. and Hirst, A. C. (1999) Climate change feedback on the future oceanic $CO_2$ uptake. *Tellus B*, 51(3), 722-733.

Matsoukas, C., Banks, A. C., Pavlakis, K. G., Hatzianastassiou, N., Jr., P. W. S. and Vardavas, I. (2007) Seasonal heat budgets of the Red and Black seas. *J. Geophys. Res.*, 112, C10017, doi:10010.11029/12006JC003849.

Matsumoto, K. (2007) Radiocarbon-based circulation age of the world oceans. *J. Geophys. Res.*, 112, C09004, doi:09010.01029/02007JC004095.

Matsumoto, K., Matsumoto, K., Sarmiento, J. L., Key, R. M., Aumont, O., Bullister, J. L., Caldeira, K., Campin, J.-M., Doney, S. C., Drange, H., Dutay, J.-C., Follows, M., Gao, Y., Gnanadesikan, A., Gruber, N., Ishida, A., Joos, F., Lindsay, K., Maier-Reimer, E., Marshall, J. C., Matear, R. J., Monfray, P., Mouchet, A., Najjar, R., Plattner, G.-K., Schlitzer, R., Slater, R., Swathi, P. S., Totterdell, I. J., Weirig, M.-F., Yamanaka, Y., Yool, A. and Orr, J. C. (2004) Evaluation of ocean carbon cycle models with data-based metrics. *Geophys. Res. Lett.*, 31, L07303, doi:07310.01029/02003GL018970.

Maxwell, W. G. H. (1968) *Atlas of the Great Barrier Reef*, Elsevier, New York, 258 pp.

McCreary, J. P., Kohler, K. E., Hood, R. R., Smith, S., Kindle, J., Fischer, A. S. and Weller, R. A. (2001) Influences of diurnal and intraseasonal forcing on mixed-layer and biological variability in the central Arabian Sea. *J. Geophys. Res.*, 106(C4), 7139-7155.

McKinley, G. A., Follows, M. J. and Marshall, J. (2004) Mechanisms of air-sea $CO_2$ flux variability in the equatorial Pacific and the North Atlantic. *Global Biogeochem. Cycles*, 18, GB2011, doi:2010.1029/2003GB002179.

McKinley, G. A., Takahashi, T., Buitenhuis, E., Chai, F., Christian, J. R., Doney, S. C., Jiang, M.-S., Lindsay, K., Moore, J. K., Le Quéré, C., Lima, I., Murtugudde, R., Shi, L. and Wetzel, P. (2006) North Pacific carbon cycle response to climate variability on seasonal to decadal timescales. *J. Geophys. Res.*, 111, C07S06, doi:10.1029/2005JC003173.

McNeil, B. I. and Matear, R. J. (2006) Projected climate change impact on oceanic acidification. *Carbon Balance and Management*, 1(2).

McNeil, B. I. and Matear, R. J. (2007) Climate change feedbacks on future oceanic acidification. *Tellus B*, 59(2), 191-198.

McNeil, B. I. and Matear, R. J. (2008) Southern Ocean acidification: A tipping point at 450-ppm atmospheric $CO_2$. *PNAS*, 105(48), 18860-18864.

McNeil, B. I., Matear, R. J. and Barnes, D. J. (2004) Coral reef calcification and climate change: The effect of ocean warming. *Geophys. Res. Lett.*, 31, L22309, doi:22310.21029/22004GL021541.

McNeil, B. I., Matear, R. J. and Barnes, D. J. (2005) Reply to comment by Kleypas *et al*. on ‘‘Coral reef calcification and climate change: The effect of ocean warming’’. *Geophys. Res. Lett.*, 32, L08602, doi:08610.01029/02005GL022604.

McNeil, B. I., Matear, R. J., Key, R. M., Bullister, J. L. and Sarmiento, J. L. (2003) Anthropogenic $CO_2$ uptake by the ocean based on the global chlorofluorocarbon data set. *Science*, 299, 235-239.

McPhaden, M. J. and Zhang, D. (2002) Slowdown of the meridional overturning circulation in the upper Pacific Ocean. *Nature*, 415(6872), 603-608.

Meehl, G., Teng, H. and Branstator, G. (2006) Future changes of El Niño in two global coupled climate models. *Climate Dynamics*, 26(6), 549-566.

Meehl, G. A. (1990) Development of global coupled ocean-atmosphere general circulation models. *Climate Dynamics*, 5(1), 19-33.

Meehl, G. A., Stocker, T. F., Collins, W. D., Friedlingstein, P., Gaye, A. T., Gregory, J. M., Kitoh, A., Knutti, R., Murphy, J. M., Noda, A., Raper, S. C. B., Watterson, I. G., Weaver, A. J. and Zhao, Z.-C. (2007) Global Climate Projections. In *Climate Change 2007: The Physical Science Basis. Contribution of Working Group I to the Fourth Assessment Report of the Intergovernmental Panel on Climate Change* (Eds. S. Solomon, D. Qin, M. Manning, Z. Chen, M. Marquis, K. B. Averyt, M. Tignor and H. L. Miller), Cambridge University Press, Cambridge, United Kingdom and New York, NY, USA.

Meehl, G. A. and Washington, W. M. (1996) El Niño-like climate change in a model with increased atmospheric $CO_2$ concentrations. *Nature*, 382(6586), 56-60.

Meinke, H., deVoil, P., Hammer, G. L., Power, S., Allan, R., Stone, R. C., Folland, C. and Potgieter, A. (2005) Rainfall variability at decadal and longer time scales: signal or noise? *J. Climate*, 18, 89-96.

Melillo, J. M., Steudler, P. A., Aber, J. D., Newkirk, K., Lux, H., Bowles, F. P., Catricala, C., Magill, A., Ahrens, T. and Morrisseau, S. (2002) Soil Warming and Carbon-Cycle Feedbacks to the Climate System. *Science*, 298(5601), 2173-2176.

Mellor, G. L. and Yamada, T. (1982) Developement of a turbulence closure model for geophysical fluid problems. *Rev. Geophys. Space Phys.*, 20, 851-875.

Messié, M. and Radenac, M.-H. (2006) Seasonal variability of the surface chlorophyll in the western tropical Pacific from SeaWiFS data. *Deep-Sea Res. I*, 53(10), 1581-1600.

Mignone, B. K., Gnanadesikan, A., Sarmiento, J. L. and Slater, R. D. (2006) Central role of Southern Hemisphere winds and eddies in modulating the oceanic uptake of anthropogenic carbon. *Geophys. Res. Lett.*, 33, L01604, doi:01610.01029/02005GL024464.

Mignone, B. K., Sarmiento, J. L., Slater, R. D. and Gnanadesikan, A. (2004) Sensitivity of sequestration efficiency to mixing processes in the global ocean. *Energy Convers. Mgmt*, 29(9-10), 1467-1478.

Mikaloff Fletcher, S. E., Gruber, N., Jacobson, A. R., Doney, S. C., Dutkiewicz, S., Gerber, M., Follows, M., Joos, F., Lindsay, K., Menemenlis, D., Mouchet, A., Müller, S. A. and Sarmiento, J. L. (2006) Inverse estimates of anthropogenic $CO_2$ uptake, transport, and storage by the ocean. *Global Biogeochem. Cycles*, 20, GB2002, doi:2010.1029/2005GB002530.

Millero, F. J. (1995) Thermodynamics of the carbon dioxide system in the oceans. *Geochim. Cosmochim. Acta*, 59(4), 661-677.

Milliman, J. D. (1974) *Recent Sedimentary Carbonates: Part 1 - Marine Carbonates*, Springer, New York, 375 pp.

Milliman, J. D. (1993) Production and accumulation of calcium carbonate in the ocean: budget of a nonsteady state. *Global Biogeochem. Cycles*, 7(4), 927-957.

Milliman, J. D. and Droxler, A. W. (1996) Neritic and pelagic carbonate sedimentation in the marine environment: ignorance is not bliss. *Geol. Rundschau*, 85, 496-504.

Milliman, J. D., Troy, P. J., Balch, W. M., Adams, A. K., Li, Y. H. and Mackenzie, F. T. (1999) Biologically mediated dissolution of calcium carbonate above the chemical lysocline? *Deep-Sea Res. I*, 46(10), 1653-1669.

Mitchell, A. W. and Furnas, M. J. (1996), Terrestrial inputs of nutrients and suspended sediments to the Great Barrier Reef lagoon, paper presented at Proceedings of the

Great Barrier Reef Science, Use and Management; a national conference, Great Barrier Reef Marine Park Authority, Townsville.

Mobasheri, M. R. (1995) *Heat Transfer in the Upper Layer of the Ocean with Application to the Satellite Sea Surface Temperature (SST) Measurement*, James Cook University of North Queensland, Townsville, Australia, 182 pp.

Monbet, P., Brunskill, G. J., Zagorskis, I. and Pfitzner, J. (2007) Phosphorus speciation in the sediment and mass balance for the central region of the Great Barrier Reef continental shelf (Australia). *Geochim. Cosmochim. Acta*, 71(11), 2762-2779.

Morse, J. W. and Mackenzie, F. T. (1990) *Geochemistry of Sedimentary Carbonates*, Elsevier, New York, xvi + 707 pp.

Moss, A. J., Rayment, G. E., Reilly, N. and Best, E. K. (1992) A Preliminary Assessment of Sediment and Nutrient Exports from Queensland Coastal Catchments. In *Queensland Department of Environment and Heritage Technical Report No. 5*, Queensland Government, Brisbane, Australia, pp. 28.

Mucci, A. (1983) The solubility of calcite and aragonite in seawater at various salinities, temperatures, and one atmosphere total pressure. *Am. J. Sci.*, 283(6-10), 780-799.

Murnane, R., Sarmiento, J. L. and Le Quéré, C. (1999) Spatial distribution of air-sea $CO_2$ fluxes and the interhemispheric transport of carbon by the oceans. *Global Biogeochem. Cycles*, 13(2), 287-305.

Naegler, T., Ciais, P., Rodgers, K. B. and Levin, I. (2006) Excess radiocarbon constraints on air-sea gas exchange and the uptake of $CO_2$ by the oceans. *Geophys. Res. Lett.*, 33, L11802, doi:11810.11029/12005GL025408.

Nakayama, N., Peltzer, E. T., Walz, P. and Brewer, P. G. (2005) First results from a controlled deep sea $CO_2$ perturbation experiment: Evidence for rapid equilibration of the oceanic $CO_2$ system at depth. *J. Geophys. Res.*, 110, C09S11, doi:10.1029/2004JC002597.

Naveira Garabato, A. C., Polzin, K. L., King, B. A., Heywood, K. J. and Visbeck, M. (2004) Widespread intense turbulent mixing in the Southern Ocean. *Science*, 303, 210-213.

Navon, I. M. (2009) Data Assimilation for Numerical Weather Prediction: A Review. In *Data Assimilation for Atmospheric, Oceanic and Hydrologic Applications* (Eds. S. K. Park and L. Xu), Springer Berlin Heidelberg, Berlin, Heidelberg, pp. 21-65.

Neil, D. T., Orpin, A. R., Ridd, P. V. and Yu, B. (2002) Sediment yield and impacts from river catchments to the Great Barrier Reef lagoon: a review. *Mar. Freshw. Res.*, 53(4), 733-752.

Newton, A., Thunell, R. and Stott, L. (2006) Climate and hydrographic variability in the Indo-Pacific Warm Pool during the last millennium. *Geophys. Res. Lett.*, 33, L19710, doi:19710.11029/12006GL027234.

Nicholls, N. (1992) Historical El Niño/Southern Oscillation variability in the Australasian region. In *El Niño: Historical and Palaeoclimatic Aspects of the Southern Oscillation* (Eds. H. F. Diaz and V. Markgraf), Cambridge University Press, Cambridge, pp. 151-173.

Nicholls, N., Gruza, V., Jouzel, J., Karl, T. R., Ogallo, L. A. and Parker, D. E. (1996) Observed climate variability and change. In *Climate Change 1995: The Science of Climate Change* (Eds. J. H. Houghton, L. G. Meira Filho, B. A. Callander, N. Harris, A. Kattenberg and K. Maskell), Cambridge University Press, Cambridge, pp. 133-192.

Nightingale, P. J., Malin, G., Law, C. S., Watson, A. J., Liss, P. S., Liddicoat, M. I., Boutin, J. and Upstill-Goddard, R. C. (2000) In situ evaluation of air-sea gas exchange parametrizations using novel conservative and volatile tracers. *Global Biogeochem. Cycles*, 14(1), 373-387.

Niiler, P. (1975) Deepening of the wind-mixed layer. *J. Mar. Res.*, 33, 405-422.

Niiler, P., Lee, D.-K. and Moisan, J. (2004) Observed mechanisms of El Niño SST evolution in the Pacific. *J. Mar. Res.*, 62(6), 771.

Nilsen, J. E. Ø. and Falck, E. (2006) Variations of Mixed Layer Depth and Water Properties in the Norwegian Sea for the period 1949-1999. *Prog. Oceanogr.*, 70(1), 58-90, doi:10.1016/j.pocean.2006.1003.1014.

Nimer, N. A., Brownlee, C. and Merrett, M. J. (1994) Carbon dioxide availability, intracellular pH and growth-rate of the coccolithophore Emiliania huxleyi. *Mar. Ecol. Prog. Ser.*, 109, 257-262.

Nof, D. and Middleton, J. H. (1989) Geostrophic Pumping, Inflows and Upwelling in Barrier Reefs. *J. Phys. Oceanogr.*, 19, 874-889.

Obata, A., Ishizaka, J. and Endoh, M. (1996) Global verification of critical depth theory for phytoplankton bloom with climatological in situ temperature and satellite ocean color data. *J. Geophys. Res. Lett.*, 101, 20657-20667.

Oeschger, H., Siegenthaler, U., Schotterer, U. and Gugelmann, A. (1975) A box diffusion model to study the carbon dioxide exchange in nature. *Tellus B*, 27, 168-192.

Ohde, S. and van Woesik, R. (1999) Carbon dioxide flux and metabolic processes of a coral reef, Okinawa. *Bulletin of Marine Science*, 65, 559-576.

Ohno, Y., Iwasaka, N., Kobashi, F. and Sato, Y. (2009) Mixed layer depth climatology of the North Pacific based on Argo observations. *J. Oceanogr.*, 65(1), 1-16.

Oort, A. H. and Yienger, J. J. (1996) Observed interannual variability in the Hadley circulation and its connection to ENSO. *J. Clim.*, 9(11), 2751-2767.

Orpin, A. R., Brunskill, G. J., Zagorskis, I. and Woolfe, K. J. (2004) Patterns of mixed siliciclastic-carbonate sedimentation adjacent to a large dry-tropics river on the central Great Barrier Reef shelf, Australia. *Aust. J. Earth Sci.*, 51(5), 665 - 683.

Orpin, A. R., Ridd, P. V. and Stewart, L. K. (1999) Assessment of the relative importance of major sediment-transport mechanisms in the central Great Barrier Reef lagoon. *Aust. J. Earth Sci.*, 46, 883-896.

Orr, J. C., Aumont, O., Yool, A., Plattner, G.-K., Joos, F., Maier-Reimer, E., Weirig, M.-F., Schlitzer, R., Caldeira, K., Wickett, M., Matear, R., Mignone, B., Sarmiento, J. and Davison, J. (2003) The GOSAC project to predict the efficiency of ocean $CO_2$ sequestration using 3-D ocean models. *Greenhouse Gas Control Technologies, Vols. I and II, Proceedings*, 1691-1694.

Orr, J. C., Fabry, V. J., Aumont, O., Bopp, L., Doney, S. C., Feely, R. A., Gnanadesikan, A., Gruber, N., Ishida, A., Joos, F., Key, R. M., Lindsay, K., Maier-Reimer, E., Matear, R., Monfray, P., Mouchet, A., Najjar, R. G., Plattner, G.-K., Rodgers, K. B., Sabine, C. L., Sarmiento, J. L., Schlitzer, R., Slater, R. D., Totterdell, I. J., Weirig, M.-F., Yamanaka, Y. and Yool, A. (2005a) Anthropogenic ocean acidification over the twenty-first century and its impact on calcifying organisms. *Nature*, 437(7059), 681-686.

Orr, J. C., Maier-Reimer, E., Mikolajewicz, U., Monfray, P., Sarmiento, J. L., Toggweiler, J. R., Taylor, N. K., Palmer, J., Gruber, N., Sabine, C. L., Quéré, C. L., Key, R. M. and Boutin, J. (2001) Estimates of anthropogenic carbon uptake from four three-dimensional global ocean models. *Global Biogeochem. Cycles*, 15, 43-60.

Orr, J. C., Pantoja, S. and Pörtner, H.-O. (2005b) Introduction to special section: The Ocean in a High-$CO_2$ World. *J. Geophys. Res.*, 110, C09S01, doi:10.1029/2005JC003086.

Palmer, J. R. and Totterdell, I. J. (2001) Production and export in a global ocean ecosystem model. *Deep-Sea Res. I*, 48(5), 1169-1198.

Park, G.-H., Lee, K., Wanninkhof, R. and Feely, R. A. (2006) Empirical temperature-based estimates of variability in the oceanic uptake of $CO_2$ over the past 2 decades. *J. Geophys. Res.*, 111(C7), C07S07, doi:10.1029/2005JC003090.

Patra, P. K., Maksyutov, S., Ishizawa, M., Nakazawa, T., Takahashi, T. and Ukita, J. (2005) Interannual and decadal changes in the sea-air $CO_2$ flux from atmospheric $CO_2$ inverse modeling. *Global Biogeochem. Cycles*, 19, GB4013, doi:4010.1029/2004GB002257.

Pearman, G. I. and Beardsmore, D. J. (1984) Atmospheric carbon dioxide measurements in the Australian region: Ten years of aircraft data. *Tellus*, 36B, 1-24.

Pelejero, C., Calvo, E., McCulloch, M. T., Marshall, J. F., Gagan, M. K., Lough, J. M. and Opdyke, B. N. (2005) Preindustrial to Modern Interdecadal Variability in Coral Reef pH. *Science*, 309(5744), 2204-2207.

Penven, P., Debreu, L., Marchesiello, P. and McWilliams, J. C. (2006) Evaluation and application of the ROMS 1-way embedding procedure to the central california upwelling system. *Ocean Modelling*, 12(1-2), 157-187.

Persson, A. (2005) Early operational Numerical Weather Prediction outside the USA: an historical Introduction. Part 1: Internationalism and engineering NWP in Sweden, 1952-69. *Meteorol. Appl.*, 12(2), 135-159.

Petit, J. R., Jouzel, J., Raynaud, D., Barkov, N. I., Barnola, J.-M., Basile, I., Bender, M., Chappellaz, J., Davis, M., Delaygue, G., Delmotte, M., Kotlyakov, V. M., Legrand, M., Lipenkov, V. Y., Lorius, C., PEpin, L., Ritz, C., Saltzman, E. and

Stievenard, M. (1999) Climate and atmospheric history of the past 420,000 years from the Vostok ice core, Antarctica. *Nature*, 399(6735), 429-436.

Peylin, P., Bousquet, P., Le Quéré, C., Sitch, S., Friedlingstein, P., McKinley, G., Gruber, N., Rayner, P. and Ciais, P. (2005) Multiple constraints on regional $CO_2$ flux variations over land and oceans. *Global Biogeochem. Cycles*, 19, GB1011, doi:1010.1029/2003GB002214.

Philander, S. G. H. (1979) Variability of the tropical oceans. *Dyn. Atmos. Oceans*, 3, 191-208.

Philander, S. G. H. (1983) El Nino Southern Oscillation phenomena. *Nature*, 302(5906), 295-301.

Pickard, G. L., Donguy, J. R., Henin, C. and Rougerie, F. (1977) *A review of the physical oceanography of the Great Barrier Reef and western Coral Sea*, Australian Government Publishing Service, Canberra, 134 pp.

Pickard, G. L. and Emery, W. J. (1990) *Descriptive Physical Oceanography*, Pergamon, Tarrytown, N.Y., 320 pp.

Pigram, C. J., Davies, P. J., Feary, D. A. and Symonds, P. A. (1992) Absolute magnitude of the second-order middle to late, Miocene sea-level fall, Marion Plateau, northeast Australia. *Geology*, 20(9), 858-862.

Plattner, G.-K., Joos, F. and Stocker, T. F. (2002) Revision of the global carbon budget due to changing air-sea oxygen fluxes. *Global Biogeochem. Cycles*, 16(4), 1096, doi:1010.1029/2001GB001746.

Platzman, G. W. (1979) The ENIAC Computations of 1950-Gateway to Numerical Weather Prediction. *Bull. Amer. Meteor. Soc.*, 60, 302-312.

Polovina, J. J., Mitchum, G. T. and Evans, G. T. (1995) Decadal and basin-scale variation in mixed layer depth and the impact on biological production in the Central and North Pacific, 1960-88. *Deep-Sea Res. I*, 42(10), 1701-1716.

Polzin, K. L., Toole, J. M., Ledwell, J. R. and Schmitt, R. W. (1997) Spatial variability of turbulent mixing in the abyssal ocean. *Science*, 276, 93-96.

Poulton, S. W. and Raiswell, R. (2002) The low-temperature geochemical cycle of iron: From continental fluxes to marine sediment deposition. *Am. J. Sci.*, 302(9), 774-805.

Power, S., Casey, T., Folland, C., Colman, A. and Mehta, V. (1999) Inter-decadal modulation of the impact of ENSO on Australia. *Clim. Dyn.*, 15, 319-324.

Power, S. and Colman, R. (2006) Multi-year predictability in a coupled general circulation model. *Climate Dynamics*, 26(2-3), 247.

Prentice, C., Farquhar, G. D., Fasham, M. J. R., Goulden, M. L., Heimann, M., Jaramillo, V. J., Kheshgi, H. S., Le Quéré, C., R. J. Scholes and Wallace, D. W. R. (2001) The carbon cycle and atmospheric carbon dioxide. In *Climate Change 2001: The Scientific Basis. Contribution of Working Group I to the Third Assessment Report of the Intergovernmental Panel on Climate Change* (Eds. J. T. Houghton, Y. Ding, D. J. Griggs, M. Noguer, P. J. van der Linden, X. Dai, K. Maskell and C. A. Johnson), Cambridge Univ. Press, New York, pp. 183-237.

Price, J. F. (1981) Upper ocean response to a hurricane. *J. Phys. Oceanogr.*, 11, 153-175.

Price, J. F., Weller, R. A. and Pinkel, R. (1986) Diurnal cycling: Observations of the upper ocean response to diurnal heating, cooling, and wind mixing. *J. Geophys. Res.*, 91, 8411-8427.

Prospero, J. M., Ginoux, P., Torres, O., Nicholson, S. E. and Gill, T. E. (2002) Environmental characterization of global sources of atmospheric soil dust identified with the NIMBUS 7 Total Ozone Mapping Spectrometer (TOMS) absorbing aerosol product. *Rev. Geophys.*, 40(1), 1002, doi:1010.1029/2000RG000095.

Qu, T. (1996) Seasonal heat budget in the tropical Western Pacific Ocean in a global GCM II. In five subregions. *Chinese Journal of Oceanology and Limnology*, 14(1), 83-90.

Qu, T. (2003) Mixed layer heat balance in the western North Pacific. *J. Geophys. Res.*, 108(C7), 3242, doi:3210.1029/2002JC001536.

Qu, T., Du, Y., Gan, J. and Wang, D. (2007) Mean seasonal cycle of isothermal depth in the South China Sea. *J. Geophys. Res.*, 112, C02020, doi:02010.01029/02006JC003583.

Qu, T. and Meyers, G. (2005) Seasonal variation of barrier layer in the southeastern tropical Indian Ocean. *J. Geophys. Res.*, 110 (C11), C11003, doi:11010.11029/12004JC002816

Quay, P. (1997) Was a carbon balance measured in the equatorial Pacific during JGOFS? *Deep-Sea Res. II*, 44(9-10), 1765-1781.

Quay, P., Sonnerup, R., Westby, T., Stutsman, J. and McNichol, A. (2003) Changes in the $^{13}C/^{12}C$ of dissolved inorganic carbon in the ocean as a tracer of anthropogenic $CO_2$ uptake. *Global Biogeochem. Cycles*, 17(1), 1004, doi:1010.1029/2001GB001817.

Quinn, T. M., Crowley, T. J., Taylor, F. W., Henin, C., Joannot, P. and Join, Y. (1998) A multicentury stable isotope record from a New Caledonia coral: Interannual and decadal sea surface temperature variability in the southwest Pacific since 1657 A.D. *Paleoceanography*, 13(4), 412-426.

Rabouille, C., Mackenzie, F. T. and Ver, L. M. (2001) Influence of the human perturbation on carbon, nitrogen, and oxygen biogeochemical cycles in the global coastal ocean. *Geochim. Cosmochim. Acta*, 65(21), 3615-3641.

Ralph, E. A. and Niiler, P. P. (1999) Wind-driven currents in the tropical Pacific. *J. Phys. Oceanogr.*, 29, 2121-2129.

Rao, R. R., Molinari, R. L. and Festa, J. F. (1989) Evolution of the climatological near-surface thermal structure of the tropical Indian Ocean: 1. Description of mean monthly mixed layer depth, and sea surface temperature, surface current, and surface meteorological fields. *J. Geophys. Res.*, 94, 10801-10815.

Raven, J. A. (1993) Limits on growth rates. *Nature*, 361(6409), 209-210.

Raymond, P. A., Bauer, J. E. and Cole, J. J. (2000) Atmospheric $CO_2$ evasion, dissolved inorganic carbon production, and net heterotrophy in the York River estuary. *Limnol. Oceanogr.*, 45(8), 1707-1717.

Reynaud-Vaganay, S., Gattuso, J.-P., Cuif, J.-P., Jaubert, J. and Juillet-Leclerc, A. (1999) A novel culture technique for scleractinian corals: application to investigate changes in skeletal $\delta^{18}O$ as a function of temperature. *Mar. Ecol. Prog. Ser.*, 180, 121-130.

Reynaud, S., Leclercq, N., Romaine-Lioud, S., Ferrier-Pages, C., Jaubert, J. and Gattuso, J.-P. (2003) Interacting effects of $CO_2$ partial pressure and temperature on photosynthesis and calcification in a scleractinian coral. *Global Change Biology*, 9(11), 1660-1668.

Richardson, L. F. (1922) *Weather Prediction by Numerical Process*, Cambridge University Press, Cambridge, 236 pp.

Ridgway, K. R. and Dunn, J. R. (2003) Mesoscale structure of the mean East Australian Current System and its relationship with topography. *Prog. Oceanogr.*, 56(2), 189-222.

Ridgway, K. R., Dunn, J. R. and Wilkin, J. L. (2002) Ocean interpolation by four-dimensional weighted least squares - application to the waters around Australasia. *J. Atmos. Ocean. Tech.*, 19(9), 1357-1375.

Ridgway, K. R. and Godfrey, J. S. (1994) Mass and heat budgets in the East Australian Current: a direct approach. *J. Geophys. Res.*, 99(C2), 3231-3248.

Riebesell, U., Schulz, K. G., Bellerby, R. G. J., Botros, M., Fritsche, P., Meyerhofer, M., Neill, C., Nondal, G., Oschlies, A., Wohlers, J. and Zollner, E. (2007) Enhanced biological carbon consumption in a high CO2 ocean. *Nature*, 450(7169), 545-548.

Riebesell, U., Zondervan, I., Rost, B., Tortell, P. D., Zeebe, R. E. and Morel, F. M. M. (2000) Reduced calcification of marine plankton in response to increased atmospheric $CO_2$. *Nature*, 407(6802), 364-367.

Robertson, J. E. and Watson, A. J. (1992) Thermal skin effect of the surface ocean and its implications for $CO_2$ uptake. *Nature*, 358(6389), 738-740.

Roemmich, D. and Gilson, J. (2009) The 2004-2008 mean and annual cycle of temperature, salinity, and steric height in the global ocean from the Argo Program. *Prog. Oceanogr.*, 82(2), 81-100.

Roemmich, D., Morris, M., Young, W. R. and Donguy, J. R. (1994) Fresh Equatorial Jets. *J. Phys. Oceanogr.*, 24(3), 540-558.

Roemmich, D. and Owens, W. B. (2000) The Argo project: Global ocean observations for understanding and prediction of climate variability. *Oceanography*, 13(2), 45-50.

Rothstein, L. M., Cullen, J. J., Abbott, M., Chassignet, E. P., Denman, K., Doney, S. C., Ducklow, H., Fennel, K., Follows, M., Haidvogel, D., Hoffman, E., Karl, D. M., Kindle, J., Lima, I., Maltrud, M., McClain, C., McGillicuddy, D. J., Olascoaga, M. J., Spitz, Y., Wiggert, J. and Yoder, J. (2006) Modeling Ocean Ecosystems: The Paradigm Program. *Oceanography*, 19(1), 22-51.

Rotschi, H. and Lemasson, L. (1967) Oceanography of the Coral and Tasman Seas. *Oceanogr. Mar. Biol. Ann. Rev.*, 5, 49-97.

Rowan, R. (2004) Coral bleaching Thermal adaptation in reef coral symbionts, 430(7001), 742.

Sabine, C. L., Feely, R. A., Gruber, N., Key, R. M., Lee, K., Bullister, J. L., Wanninkhof, R., Wong, C. S., Wallace, D. W. R., Tilbrook, B., Millero, F. J., Peng, T.-H., Kozyr, A., Ono, T. and Rios, A. F. (2004) The Oceanic Sink for Anthropogenic $CO_2$. *Science*, 305(5682), 367-371.

Sabine, C. L., Feely, R. A., Key, R. M., Bullister, J. L., Millero, F. J., Lee, K., Peng, T.-H., Tilbrook, B., Ono, T. and Wong, C. S. (2002a) Distribution of anthropogenic $CO_2$ in the Pacific Ocean. *Global Biogeochem. Cycles*, 16(4), 1083, doi:1010.1029/2001GB001639.

Sabine, C. L., Key, R. M., Feely, R. A. and Greeley, D. (2002b) Inorganic carbon in the Indian Ocean: Distribution and dissolution processes. *Global Biogeochem. Cycles*, 16(4), 1067, 1010.1029/2002GB001869.

Sabine, C. L. and Mackenzie, F. T. (1991) Oceanic sinks for anthropogenic $CO_2$. *Int. J. Energy Envir. Econ.*, 1, 119-127.

Saenko, O. A., Fyfe, J. C. and England, M. H. (2005) On the response of the ocean wind-driven circulation to $CO_2$ increase. *Climate Dynamics*, 25, 415-426.

Saenko, O. A. and Merryfield, W. J. (2005) On the Effect of Topographically Enhanced Mixing on the Global Ocean Circulation. *J. Phys. Oceanogr.*, 35(5), 826-834.

Sahlée, E., Smedman, A.-S. and Högström, U. (2009) Influence of the boundary layer height on the global air–sea surface fluxes. *Climate Dynamics*, 33(1), 33-44.

Saint-Cast, F. and Condie, S. A. (2006) Circulation modelling in Torres Strait, Geoscience Australia, Canberra, Record 2006/18, pp. 82.

Salinger, M. J., Renwick, J. A. and Mullan, A. B. (2001) Interdecadal Pacific Oscillation and South Pacific climate. *Int. J. Climatol.*, 21(14), 1705-1721.

Sanyal, A., Hemming, N. G., Hanson, G. N. and Broecker, W. S. (1995) Evidence for a higher pH in the glacial ocean from boron isotopes in foraminifera. *Nature*, 373(6511), 234-236.

Sarmiento, J. L., Dunne, J., Gnanadesikan, A., Key, R. M., Matsumoto, K. and Slater, R. (2002) A new estimate of the $CaCO_3$ to organic carbon export ratio. *Global Biogeochem. Cycles*, 16(4), 1107, doi:1110.1029/2002GB001919.

Sarmiento, J. L. and Gruber, N. (2002) Sinks for anthropogenic carbon. *Physics Today*, 30-36.

Sarmiento, J. L. and Gruber, N. (2006) *Ocean Biogeochemical Dynamics*, Princeton University Press, Princeton, New Jersey, 503 pp.

Sarmiento, J. L., Hughes, T. M. C., Stouffer, R. J. and Manabe, S. (1998) Simulated response of the ocean carbon cycle to anthropogenic climate warming. *Nature*, 393, 245-249.

Sarmiento, J. L. and Le Quéré, C. (1996) Oceanic carbon dioxide uptake in a model of century-scale global warming. *Science*, 274, 1346-1350.

Sarmiento, J. L., Monfray, P., Maier-Reimer, E., Aumont, O., Murnane, R. and Orr, J. (2000) Sea-air $CO_2$ fluxes and carbon transport: A comparison of three ocean general circulation models. *Global Biogeochem. Cycles*, 14(4), 1267-1281.

Sarmiento, J. L., Slater, R., Barber, R., Bopp, L., Doney, S. C., Hirst, A. C., Kleypas, J., Matear, R., Mikolajewicz, U., Monfray, P., Soldatov, V., Spall, S. A. and Stouffer, R. (2004) Response of ocean ecosystems to climate warming. *Global Biogeochem. Cycles*, 18, GB3003, doi:1029/2003GB002134.

Sarmiento, J. L. and Sundquist, E. T. (1992) Revised budget for the oceanic uptake of anthropogenic carbon dioxide. *Nature*, 356(6370), 589-593.

Sarmiento, J. L., Toggweiler, J. R. and Najjar, R. (1988) Ocean carbon-cycle dynamics and atmospheric $pCO_2$. *Phil. Trans. R. Soc. Lond. A*, 325(1088), 3-21.

Saunders, P. M. (1967) The Temperature at the Ocean-Air Interface. *J. Atmos. Sci.*, 24(3), 269-273.

Schiller, A., Oke, P. R., Brassington, G., Entel, M., Fiedler, R., Griffin, D. A. and Mansbridge, J. V. (2008) Eddy-resolving ocean circulation in the Asian-Australian region inferred from an ocean reanalysis effort. *Prog. Oceanogr.*, 76(3), 334-365.

Schluessel, P., Emery, W. J., Grasl, H. and Mammen, T. (1990) On the bulk-skin temperature difference and its impact on satellite remote sensing of sea surface temperature. *J. Geophys. Res.*, 95, 13341-13356

Schmittner, A. (2005) Decline of the marine ecosystem caused by a reduction in the Atlantic overturning circulation. *Nature*, 434, 628-633.

Schmittner, A., Oschlies, A., Giraud, X., Eby, M. and Simmons, H. L. (2005) A global model of the marine ecosystem for long-term simulations: sensitivity to ocean mixing, buoyancy forcing, particle sinking and dissolved organic matter cycling. *Global Biogeochem. Cycles*, 19, doi:10.1029/2004GB002283.

Schneider, N. and Müller, P. (1990) The meridional and seasonal structures of the mixed-layer depth and its diurnal amplitude observed during the Hawaii-to-Tahiti Shuttle experiment. *J. Phys. Oceanogr.*, 20(9), 1395-1404.

Schuster, U. and Watson, A. J. (2007) A variable and decreasing sink for atmospheric $CO_2$ in the North Atlantic. *J. Geophys. Res.*, 112, C11006, doi:11010.11029/12006JC003941.

Sciandra, A., Harlay, J., Lefèvre, D., Lemée, R., Rimmelin, P., Denis, M. and Gattuso, J. P. (2003) Response of coccolithophorid Emiliania huxleyi to elevated partial pressure of $CO_2$ under nitrogen limitation. *Mar. Ecol. Prog. Ser.*, 261, 111-122.

Shchepetkin, A. F. and McWilliams, J. C. (1998) Quasi-monotone advection schemes based on explicit locally adaptive dissipation. *Monthly Weather Rev.*, 126, 1541-1580.

Shchepetkin, A. F. and McWilliams, J. C. (2003) A method for computing horizontal pressure-gradient force in an oceanic model with a nonaligned vertical coordinate. *J. Geophys. Res.*, 108(C3), 3090, doi:3010.1029/2001JC001047.

Shchepetkin, A. F. and McWilliams, J. C. (2005) The regional oceanic modeling system (ROMS): a split-explicit, free-surface, topography-following-coordinate oceanic model. *Ocean Modelling*, 9(4), 347-404.

Shi, J.-Q., Durucan, S. and Fujioka, M. (2008) A reservoir simulation study of $CO_2$ injection and $N_2$ flooding at the Ishikari coalfield $CO_2$ storage pilot project, Japan. *Int. J. Greenhouse Gas Control*, 2(1), 47-57.

Shindell, D. T. and Schmidt, G. A. (2004) Southern Hemisphere climate response to ozone changes and greenhouse gas increases. *Geophys. Res. Lett.*, 31, L18209, doi:18210.11029/12004GL020724.

Shirayama, Y. and Thornton, H. (2005) Effect of increased atmospheric $CO_2$ on shallow-water marine benthos. *J. Geophys. Res.*, 110, C09S09.

Shuman, F. G. (1989) History of Numerical Weather Prediction at the National Meteorological Center. *Wea. Forecasting*, 4, 286-296.

Siegenthaler, U. and Oeschger, H. (1978) Predicting Future Atmospheric Carbon Dioxide Levels. *Science*, 199(4327), 388-395.

Siegenthaler, U. and Oeschger, H. (1987) Biospheric $CO_2$ emissions during the past 200 years reconstructed by deconvolution of ice core data. *Tellus B*, 39B, 140-154.

Sigman, D. M. and Boyle, E. A. (2000) Glacial/interglacial variations in atmospheric carbon dioxide. *Nature*, 407, 859-869.

Simpson, J. J. and Paulson, C. A. (1980) Small-Scale Sea Surface Temperature Structure. *J. Phys. Oceanogr.*, 10(3), 399-410.

Smagorinsky, J., Manabe, S. and Holloway, J. L. (1965) Numerical Results from a Nine-Level General Circulation Model of the Atmosphere. *Mon. Wea. Rev.*, 93(12), 727-768.

Smith, H. J., Fischer, H., Wahlen, M., Mastroianni, D. and Deck, B. (1999) Dual modes of the carbon cycle since the Last Glacial Maximum. *Nature*, 400(6741), 248-250.

Smith, J., Walker O., Marra, J., Hiscock, M. R. and Barber, R. T. (2000) The seasonal cycle of phytoplankton biomass and primary productivity in the Ross Sea, Antarctica. *Deep-Sea Res. II*, 47(15-16), 3119-3140.

Smith, S. V. (1985) Physical, chemical and biological characteristics of $CO_2$ gas flux across the Air-water interface. *Plant, Cell Environ.*, 8, 387-398.

Smith, S. V. and Buddemeier, R. W. (1992) Global change and coral reef ecosystems. *Annu. Rev. Ecol. Syst.*, 23, 89-118.

Smith, S. V. and Hollibaugh, J. T. (1993) Coastal metabolism and the oceanic organic carbon balance. *Rev. Geophys.*, 31(1), 75-89.

Smith, S. V. and Kinsey, D. W. (1978) Calcification and organic carbon metabolism as indicated by carbon dioxide. In *Coral Reefs: Research Methods* (Eds. D. R. Stoddart and R. E. Johannes), UNESCO, pp. 469-484.

Smith, S. V. and Pesret, F. (1974) Processes of carbon dioxide flux in the Fanning Island lagoon. *Pac. Sci.*, 28, 225-245.

Sokolov, S. and Rintoul, S. (2000) Circulation and water masses of the southwest Pacific: WOCE Section P11, Papua New Guinea to Tasmania. *Journal of Marine Research*, 58, 223-268.

Song, Y. and Haidvogel, D. B. (1994) A semi-implicit ocean circulation model using a generalized topography-following coordinate system. *J. Comp. Phys.*, 115(1), 228-244.

Spero, H. J., Bijma, J., Lea, D. W. and Bemis, B. E. (1997) Effect of seawater carbonate concentration on foraminiferal carbon and oxygen isotopes. *Nature*, 390, 497-500.

Sprintall, J. and Roemmich, D. (1999) Characterizing the structure of the surface layer in the Pacific Ocean. *J. Geophys. Res.*, 104(C10), 23297-23311.

Sprintall, J., Roemmich, D., Stanton, B. and Bailey, R. (1995) Regional climate variability and ocean heat transport in the southwest Pacific Ocean. *J. Geophys. Res.*, 100(C8), 15865-15872.

Sprintall, J. and Tomczak, M. (1992) Evidence of the barrier layer in the surface layer of the tropics. *J. Geophys. Res.*, 97, 7305-7316.

St. Laurent, L. C., Simmons, H. L. and Jayne, S. R. (2002) Estimating tidally driven mixing in the deep ocean. *Geophys. Res. Lett.*, 29, 2106, 2110.1029/2002GL2015 2633.

Steele, L. P., Krumme, P. B. and Langenfelds, R. L. (2007) Atmospheric $CO_2$ concentrations from sites in the CSIRO Atmospheric Research GASLAB air sampling network (August 2007 version). In *Trends: A Compendium of Data on Global Change, Carbon Dioxide Information Analysis Center*, Oak Ridge National Laboratory, U.S. Department of Energy, Oak Ridge, TN, U.S.A.

Steffen, W. (2006) Stronger Evidence But New Challenges: Climate Change Science 2001-2005, Australian Greenhouse Office, pp. 28.

Stott, L., Cannariato, K., Thunell, R., Haug, G. H., Koutavas, A. and Lund, S. (2004) Decline of surface temperature and salinity in the western tropical Pacific Ocean in the Holocene epoch. *Nature*, 431(7004), 56-59.

Stramma, L., Cornillon, P. and Price, J. F. (1986) Satellite Observations of Sea Surface Cooling by Hurricane. *J. Geophys. Res.*, 91, 5031-5035.

Stuiver, M., Quay, P. D. and Ostlund, H. G. (1983) Abyssal water carbon-14 distribution and the age of the world oceans. *Science*, 219, 849-851.

Sun, D.-Z. and Trenberth, K. E. (1998) Coordinated heat removal from the equatorial Pacific during the 1986-87 El Niño. *Geophys. Res. Lett.*, 25, 2659-2662.

Suzuki, A. (1998) Combined effects of photosynthesis and calcification on the partial pressure of carbon dioxide in seawater. *J. Oceanogr.*, 54, 1-7.

Suzuki, A., Gagan, M. K., Fabricius, K., Isdale, P. J., Yukino, I. and Kawahata, H. (2003) Skeletal isotope microprofiles of growth perturbations in *Porites* corals during the 1997-1998 mass bleaching event. *Coral Reefs*, 22(4), 357-369.

Suzuki, A. and Kawahata, H. (1999) Partial Pressure of Carbon Dioxide in Coral Reef Lagoon Waters: Comparative Study of Atolls and Barrier Reefs in the Indo-Pacific Oceans. *J. Oceanogr.*, 55(6), 731-745.

Suzuki, A. and Kawahata, H. (2003) Carbon budget of coral reef systems: an overview of observations in fringing reefs, barrier reefs and atolls in the Indo-Pacific regions. *Tellus B*, 55(2), 428-444.

Suzuki, A. and Kawahata, H. (2004) Reef water $CO_2$ system and carbon production of coral reefs: Topographic control of system-level performance. In *Global Environmental Change in the Ocean and on Land* (Eds. M. Shiyomi, H. Kawahata, H. Koizumi, A. Tsuda and Y. Awaya), Terra, Tokyo, pp. 229-248.

Suzuki, A., Kawahata, H., Ayukai, T. and Goto, K. (2001) The oceanic $CO_2$ system and carbon budget in the Great Barrier Reef, Australia. *Geophys. Res. Lett.*, 28(7), 1243-1246.

Suzuki, A., Nakamori, T. and Kayanne, H. (1995) The mechanism of production enhancement in coral reef carbonate systems: model and empirical results. *Sediment. Geol.*, 99(3-4), 259-280.

Sweeney, C., E. Gloor, Jacobson, A. R., Key, R. M., McKinley, G., Sarmiento, J. L. and Wanninkhof, R. (2007) Constraining global air-sea gas exchange for $CO_2$ with recent bomb $^{14}C$ measurements. *Global Biogeochem. Cycles*, 21, GB2015, doi:2010.1029/2006GB002784.

Szmant, A. M. and Gassman, N. J. (1990) The effects of prolonged "bleaching" on the tissue biomass and reproduction of the reef coral Montastrea annularis. *Coral Reefs*, 8(4), 217-224.

Taft, B. A. and Kessler, W. S. (1991) Variations of zonal currents in the central tropical Pacific during 1970 to 1987: Sea level and dynamic height measurements. *J. Geophys. Res.*, 96(C7), 12,599-512,618.

Takahashi, T. (1975) Carbonate chemistry of sea water and the calcite compensation depth in the oceans. In *Dissolution of Deep-Sea Carbonates* (Eds. W. V. Sliter, A. W. H. Bé and W. H. Berger), Spec. Publ. Cushman Found. Foraminiferal Res., pp. 11-26.

Takahashi, T. (1989) The carbon dioxide puzzle. *Oceanus*, 32(2), 22-29.

Takahashi, T., Broecker, W. S. and Langer, S. (1985) Redfield ratio based on chemical data from isopycnal surfaces. *J. Geophys. Res.*, 90(C4), 6907-6924.

Takahashi, T., Feely, R. A., Weiss, R. F., Wanninkhof, R. H., Chipman, D. W., Sutherland, S. C. and Takahashi, T. T. (1997) Global air-sea flux of $CO_2$: An estimate based on measurements of sea-air $pCO_2$ difference. *PNAS*, 94(16), 8292-8299.

Takahashi, T., Olafsson, J., Goddard, J., Chipman, D. W. and Sutherland, S. C. (1993) Seasonal variation of $CO_2$ and nutrients in the high-latitude surface oceans: a comparative study. *Global Biogeochem. Cycles*, 7(4), 843-878.

Takahashi, T., Sutherland, S. C., Feely, R. A. and Cosca, C. E. (2003) Decadal Variation of the Surface Water $pCO_2$ in the Western and Central Equatorial Pacific. *Science*, 302(5646), 852-856.

Takahashi, T., Sutherland, S. C., Sweeney, C., Poisson, A., Metzl, N., Tilbrook, B., Bates, N., Wanninkhof, R., Feely, R. A. and Sabine, C. (2002) Global sea-air $CO_2$ flux based on climatological surface ocean $pCO_2$, and seasonal biological and temperature effects. *Deep-Sea Res. II*, 49(9-10), 1601-1622.

Takahashi, T., Sutherland, S. C., Wanninkhof, R., Sweeney, C., Feely, R. A., Chipman, D. W., Hales, B., Friederich, G., Chavez, F., Sabine, C., Watson, A., Bakker, D. C. E., Schuster, U., Metzl, N., Yoshikawa-Inoue, H., Ishii, M., Midorikawa, T., Nojiri, Y., Körtzinger, A., Steinhoff, T., Hoppema, M., Olafsson, J., Arnarson, T. S., Tilbrook, B., Johannessen, T., Olsen, A., Bellerby, R., Wong, C. S., Delille, B., Bates, N. R. and de Baar, H. J. W. (2009) Climatological mean and decadal change in surface ocean $pCO_2$, and net sea-air $CO_2$ flux over the global oceans. *Deep-Sea Res. II*, 56(8-10), 554-577.

Tanaka, H. L., Ishizaki, N. and Kitoh, A. (2004) Trend and interannual variability of Walker, monsoon and Hadley circulations defined by velocity potential in the upper troposphere. *Tellus A*, 56(3), 250-269.

Tans, P. P., Fung, I. Y. and Takahashi, T. (1990) Observational constraints on the global atmospheric $CO_2$ budget. *Science*, 247, 1431-1438.

Teng, H., Masutani, S. M. and Kinoshita, C. M. (1997) Dispersion of $CO_2$ droplets in the deep ocean. *Energy Convers. Mgmt*, 38, S319-S324.

Thomas, H., England, M. H. and Ittekkot, V. (2001) An off-line 3D model of anthropogenic $CO_2$ uptake by the oceans. *Geophys. Res. Lett.*, 28(3), 547-550.

Thompson, D. W. J. and Solomon, S. (2002) Interpretation of Recent Southern Hemisphere Climate Change. *Science*, 296(5569), 895-899.

Thompson, R. O. R. Y. and Golding, T. J. (1981) Tidally induced “upwelling” by the Great Barrier Reef. *J. Geophys. Res.*, 86(C7), 6517-6521.

Thompson, R. O. R. Y. and Veronis, G. (1980) Transport calculations in the Tasman and Coral seas. *Deep-Sea Res. A*, 27(5), 303-323.

Thomson, R. E. and Fine, I. V. (2003) Estimating Mixed Layer Depth from Oceanic Profile Data. *J. Atmos. Oceanic Technol.*, 20(2), 319-329.

Thomson, R. E. and Wolanski, E. J. (1984) Tidal period upwelling within Raine Island Entrance, Great Barrier Reef. *J. Mar. Res.*, 42, 787-808.

Thoning, K. W., Tans, P. P. and Komhyr, W. D. (1989) Atmospheric carbon dioxide at Mauna Loa Observatory, 2. Analysis of the NOAA/GMCC data, 1974 1985. *J. Geophys. Res.*, 94, 8549-8565.

Tian, H., Melillo, J. M., Kicklighter, D. W., McGuire, A. D., Helfrich, J. V. K., III, Moore, B., III and Vörösmarty, C. J. (1998) Effect of interannual climate variability on carbon storage in Amazonian ecosystems. *Nature*, 396(6712), 664-667.

Toggweiler, J. R. and Carson, S. (1995) What are upwelling systems contributing to the ocean's carbon and nutrient budgets? In *Upwelling the Ocean: Modern Processes and Ancient Records* (Eds. C. P. Summerhayes, K. C. Emeis, M. V. Angel, R. L. Smith and B. Zeitzschel), J. Wiley & Sons, Chichester, pp. 337-360.

Toggweiler, J. R. and Russell, J. (2008) Ocean circulation in a warming climate. *Nature*, 451(7176), 286-288.

Toggweiler, J. R. and Samuels, B. (1998) On the ocean's large-scale circulation near the limit of no vertical mixing. *J. Phys. Oceanogr.*, 28(9), 1832-1852.

Tomczak, M. and Godfrey, J. S. (1994) *Regional Oceanography: an Introduction*, Pergamon Press, London.

Trenberth, K. E. and Caron, J. M. (2001) Estimates of meridional atmosphere and ocean heat transports. *J. Clim.*, 14(16), 3433-3443.

Trenberth, K. E., Stepaniak, D. E. and Caron, J. M. (2000) The global monsoon as seen through the divergent atmospheric circulation. *J. Clim.*, 13(22), 3969-3993.

Tribble, J. S. and Mackenzie, F. T. (1998) Recrystallization of magnesian calcite overgrowths on calcite seeds suspended in seawater. *Aquat. Geochem.*, 4(3 - 4), 337-360.

Tsunogai, S., Watanabe, S. and Sato, T. (1999) Is there a "continental shelf pump" for the absorption of atmospheric CO2? *Tellus B*, 51(3), 701-712.

Udaya Bhaskar, T. V. S., Swain, D. and Ravichandran, M. (2006) Inferring mixed-layer depth variability from Argo observations in the western Indian Ocean. *J. Mar. Res.*, 64, 393-406.

Umlauf, L. and Burchard, H. (2003) A generic length-scale equation for geophysical turbulence models. *J. Marine Res.*, 61, 235-265.

UNESCO (1983) Algorithms for computation of fundamental properties of seawater. In *UNESCO Technical Paper in Marine Science*, pp. 53.

Usdowski, E. and Hoefs, J. (1993) Oxygen isotope exchange between carbonic acid, bicarbonate, carbonate, and water: A re-examination of the data of (1950) and an expression for the overall partitioning of oxygen isotopes between the carbonate species and water. *Geochim. Cosmochim. Acta*, 57(15), 3815-3818.

van Oppen, M. J. H., Mahiny, A. J. and Done, T. J. (2005) Geographic distribution of zooxanthella types in three coral species on the Great Barrier Reef sampled after the 2002 bleaching event. *Coral Reefs*, 24(3), 482-487.

Van Scoy, K. A., Morris, K. P., Robertson, J. E. and Watson, A. J. (1995) Thermal skin effect and the air-sea flux of carbon dioxide: A sesonal high-resolution estimate. *Global Biogeochem. Cycles*, 9(2), 253-262.

Vaughan, T. W. (1919) Corals and the formation of coral reefs. *Annu. Rep. Smithson. Inst.*, 17, 189-238.

Vecchi, G. A., Soden, B. J., Wittenberg, A. T., Held, I. M., Leetmaa, A. and Harrison, M. J. (2006) Weakening of tropical Pacific atmospheric circulation due to anthropogenic forcing. *Nature*, 441(7089), 73-76.

Vialard, J. and Delecluse, P. (1998) An OGCM study for the TOGA decade. Part II : Barrier-layer formation and variability. *J. Phys. Oceanogr.*, 28(6), 1089-1106.

Volk, T. and Hoffert, M. I. (1985) Ocean carbon pumps: Analysis of relative strengths and effciencies in ocean-driven $pCO_2$. In *Carbon Dioxide and the Carbon Cycle, Archean to Present* (Eds. E. T. Sundquist and W. S. Broecker), Geophys. Monogr. Ser., AGU, Washington, D.C., pp. 99-110.

Wang, X. and Chao, Y. (2004) Simulated Sea Surface Salinity variability in the tropical Pacific. *Geophys. Res. Lett.*, 31, L02302, doi:02310.01029/02003GL018146.

Wang, X., Christian, J. R., Murtugudde, R. and Busalacchi, A. J. (2006) Spatial and temporal variability of the surface water $pCO_2$ and air-sea $CO_2$ flux in the equatorial Pacific during 1980-2003: A basin-scale carbon cycle model. *J. Geophys. Res.*, 111, C07S04, doi:10.1029/2005JC002972.

Wanninkhof, R. (1992) Relationship between wind speed and gas exchange over the ocean. *J. Geophys. Res.*, 97, 7373-7382.

Wanninkhof, R., Doney, S., Takahashi, T. and McGillis, W. (2001) The effect of using averaged winds on global air-sea $CO_2$ fluxes. In *Gas Transfer at Water Surfaces*

(Eds. M. A. Donelan, W. M. Drennan, E. S. Saltzman and R. Wanninkhof), AGU Press, pp. 351-356.

Wanninkhof, R., Feely, R. A., Chen, H., Cosca, C. and Murphy, P. P. (1996) Surface water $fCO_2$ values in the eastern equatorial Pacific during the 1992-1993 El Niño. *J. Geophys. Res.*, 101, 16333-16343.

Wanninkhof, R. and McGillis, W. R. (1999) A cubic relationship between air-sea $CO_2$ exchange and wind speed. *Geophys. Res. Lett.*, 26(13), 1889-1892.

Ware, J. R., Smith, S. V. and Reaka-Kudla, M. L. (1992) coral reefs: sources or sinks of atmospheric $CO_2$? *Coral Reefs*, 11, 127-130.

Watson, A. J., Bakker, D. C. E., Ridgwell, A. J., Boyd, P. W. and Law, C. S. (2000) Effect of iron supply on Southern Ocean $CO_2$ uptake and implications for glacial atmospheric $CO_2$. *Nature*, 407(6805), 730-733.

Watson, A. J. and Lefèvre, N. (1999) The sensitivity of atmospheric $CO_2$ concentrations to input of iron to the oceans. *Tellus B*, 51(2), 453-460.

Webb, D. J. (2000) Evidence for shallow zonal jets in the South Equatorial Current region of the southwest Pacific. *J. Phys. Oceanogr.*, 30, 706-720.

Webster, P. J., Magana, V. O., Palmer, T. N., Shukla, J., Tomas, R. A., Yanai, M. and Yasunari, T. (1998) Monsoons: Processes, predictability, and the prospects for prediction. *J. Geophys. Res.*, 103(C7), 14451-14510.

Weiss, R. F. (1974) Carbon dioxide in water and seawater: the solubility of a non-ideal gas. *Mar. Chem.*, 2(3), 203-215.

Weiss, R. F., Jahnke, R. A. and Keeling, C. D. (1982) Seasonal effects of temperature and salinity on the partial pressure of $CO_2$ in seawater. *Nature*, 300, 511-513.

Weller, R. A. (1987) Oceanography: Mixing the upper ocean. *Nature*, 328, 13-14.

Willis, J. K., Lyman, J. M., Johnson, G. C. and Gilson, J. (2007) Correction to "Recent cooling of the upper ocean". *Geophys. Res. Lett.*, 34, L16601, doi:16610.11029/12007GL030323.

Wilson, R., Tudhope, A., Brohan, P., Briffa, K., Osborn, T. and Tett, S. (2006) Two-hundred-fifty years of reconstructed and modelled tropical temperatures. *J. Geophys. Res.*, 111, C10007, doi: 10010.11029/12005JC003188.

Winckler, G., Anderson, R. F., Fleisher, M. Q., McGee, D. and Mahowald, N. (2008) Covariant Glacial-Interglacial Dust Fluxes in the Equatorial Pacific and Antarctica. *Science*, 320(5872), 93-96.

Winguth, A., Mikolajewicz, U., Gröger, M., Maier-Reimer, E., Schurgers, G. and Vizcaíno, M. (2005) Centennial-scale interactions between the carbon cycle and anthropogenic climate change using a dynamic Earth system model. *Geophys. Res. Lett.*, 32, L23714, doi:23710.21029/22005GL023681.

Wolanski, E. (1994) *Physical Oceanographic Processes of the Great Barrier Reef*, CRC Press, Boca Raton, Fla., 194 pp.

Wolanski, E., Drew, E., Abel, K. M. and O'Brien, J. (1988) Tidal jets, nutrient upwelling and their influence on the productivity of the alga Halimeda in the Ribbon Reefs, Great Barrier Reef. *Estuarine Coastal Shelf Sci.*, 26(2), 169-201.

Wolanski, E., Norro, A. and King, B. (1995) Water circulation in the Gulf of Papua. *Continental Shelf Research*, 15(2-3), 185-212.

Wolanski, E. and Spagnol, S. (2000) Sticky Waters in the Great Barrier Reef. *Estuarine Coastal Shelf Sci.*, 50(1), 27-32.

Wolf-Gladrow, D. A., Riebesell, U., Burkhardt, S. and Bijma, J. (1999) Direct effects of $CO_2$ concentration on growth and isotopic composition of marine plankton. *Tellus B*, 51(2), 461-476.

Wollast, R. (1994) The relative importance of biomineralization and dissolution of $CaCO_3$ in the global carbon cycle. In *Past and present biomineralization processes: Considerations about the carbonate cycle* (Ed. F. Doumenge), Bulletin de l'Institut Océanographique, Monaco, pp. 13-34.

Wollast, R., Garrels, R. M. and Mackenzie, F. T. (1980) Calcite-seawater reactions in ocean surface waters. *Am. J. Sci.*, 280, 831-848.

Wong, A. P. S., Johnson, G. C. and Owens, W. B. (2003) Delayed-Mode Calibration of Autonomous CTD Profiling Float Salinity Data by θ-S Climatology. *J. Atmos. Oceanic Technol.*, 20, 308-318.

Wong, C. S., Chan, Y. H., Page, J. S., Smith, G. E. and Bellegay, R. D. (1993) Changes in equatorial $CO_2$ flux and new production estimated from $CO_2$ and nutrient levels in Pacific surface waters during the 1986/87 El Niño. *Tellus B*, 45(1), 64-79.

Wong, C. S. and Matear, R. J. (1996) Effects of circulation and mixing on the disposal of $CO_2$ in the North Pacific. *Energy Convers. Mgmt*, 37(6-8), 1007-1012.

Wong, C. S. and Matear, R. J. (1998) Ocean disposal of $CO_2$ in the North Pacific Ocean: Assessment of $CO_2$ chemistry and circulation on storage and return to the atmosphere. *Waste Management*, 17(5-6), 329-335.

Woodruff, S. D., Slutz, R. J., Jenne, R. L. and Steurer, P. M. (1987) A comprehensive ocean-atmosphere data set. *Bull. Amer. Meteor. Soc.*, 68, 1239-1250.

Woolfe, K. J., Larcombe, P., Orpin, A. R., Purdon, R. G., Michaelsen, P., McIntyre, C. M. and Amjad, N. (1998) Controls upon inner-shelf sedimentation, Cape York Peninsula, in the region of 12°S. *Aust. J. Earth Sci.*, 45(4), 611-621.

Woolfe, K. J., Larcombe, P. and Stewart, L. K. (2000) Shelf sediments adjacent to the Herbert River delta, Great Barrier Reef, Australia. *Aust. J. Earth Sci.*, 47(2), 301-308.

Wu, R., Kirtman, B. P. and Pegion, K. (2007) Surface latent heat flux and its relationship with sea surface temperature in the National Centers for Environmental Prediction Climate Forecast System simulations and retrospective forecasts. *Geophys. Res. Lett.*, 34, L17712, doi:17710.11029/12007GL030751.

Wyrtki, K. (1977) Sea Level During the 1972 El Niño. *J. Phys. Oceanogr.*, 7, 779-787.

Yeh, S.-W., Yim, B. Y., Noh, Y. and Dewitte, B. (2009) Changes in mixed layer depth under climate change projections in two CGCMs. *Climate Dynamics*, 33(2), 199-213.

You, Y. (1995) Salinity variability and its role in the barrier-layer formation during TOGA-COARE. *J. Phys. Oceanogr.*, 25(11), 2778-2807.

Zawada, D. G., Zaneveld, J. R. V., Boss, E., Gardner, W. D., Richardson, M. J. and Mishonov, A. V. (2005) A comparison of hydrographically and optically derived mixed layer depths. *J. Geophys. Res.*, 110, C1100, doi:1110.1029/2004JC002417.

Zeebe, R. E. (1999) An explanation of the effect of seawater carbonate concentration on foraminiferal oxygen isotopes. *Geochim. Cosmochim. Acta*, 63(13/14), 2001-2007.

Zeebe, R. E. and Wolf-Gladrow, D. (2001) *$CO_2$ in seawater: equilibrium, kinetics, isotopes*, Elsevier, Amsterdam, 346 pp.

Zhang, X. and Cai, W.-J. (2007) On some biases of estimating the global distribution of air-sea $CO_2$ flux by bulk parameterizations. *Geophys. Res. Lett.*, 34, L01608, doi:01610.01029/02006GL027337.

Zhang, Y., Wallace, J. M. and Battisti, D. S. (1997) ENSO-like interdecadal variability: 1900-93. *J. Clim.*, 10, 1004-1020.

Zhong, S. and Mucci, A. (1989) Calcite and aragonite precipitation from seawater solutions of various salinities: Precipitation rates and overgrowth compositions. *Chemical Geology*, 78(3-4), 283-299.

Zhu, Q., Aller, R. C. and Fan, Y. (2006) Two-dimensional pH distributions and dynamics in bioturbated marine sediments. *Geochim. Cosmochim. Acta*, 70(19), 4933-4949.

Zondervan, I., Rost, B. and Riebesell, U. (2002) Effect of $CO_2$ concentration on the PIC/POC ratio in the coccolithophore *Emiliania huxleyi* grown under light-limiting conditions and different daylengths. *J. Exp. Mar. Biol. Ecol.*, 272, 55-70.

Zondervan, I., Zeebe, R., Rost, B. and Riebesell, U. (2001) Decreasing marine biogenic calcification: A negative feedback on rising atmospheric $pCO_2$. *Global Biogeochem. Cycles*, 15(2), 507-516.

Zuddas, P. and Mucci, A. (1998) Kinetics of calcite precipitation from seawater: II. The influence of the ionic strength. *Geochim. Cosmochim. Acta*, 62(5), 757-766.

# A1 Glossary

## A1.1 Definitions

Argo: Argo is an array of free-drifting floats, which globally measures around 3,000 vertical temperature and salinity profiles of the upper 2000 m of the ocean. The name was chosen from Greek mythology wherein Jason sailed in a ship called "Argo" to retrieve the Golden Fleece.

Autotrophy: Autotrophic organisms employ inorganic molecules (e.g. inorganic $CO_2$) and an external energy source (e.g. solar energy) to create complex organic compounds (cf. primary production), e.g. via photosynthesis.

Baroclinity: A measure of stratification in a fluid. In a baroclinic circulation, density is dependent on both pressure and temperature (cf. barotropy).

Barotropy: In a barotropic circulation, density is only dependant on pressure such that isobars and isopycnals coincide with each other. The tropical latitudes are generally barotropic zones (cf. baroclinity).

Barrier Layer: A barrier layer is formed when the MLD is shallower than the ILD and MLD and is defined as being the region between the MLD and ILD. It is generally a result of freshening, e.g. due to heavy precipitation.

Carbon Dioxide Information Analysis Center (CDIAC): Organisation within the US Department of Energy, responsible for compilation, quality assessment, storage and distribution of climate change related data, including $CO_2$ and other greenhouse gases.

Central processing unit (CPU): A microprocessor chip (a part of a computer), which performs most of the data processing.

CO2SYS: A freely available computer program employed to obtain missing carbonate system parameters (total inorganic $CO_2$, total alkalinity, ph, $fCO_2/pCO_2$) if at least two of these were measured. Program also requires values for temperature and salinity.

Data assimilation: Incorporation of observations (e.g. temperature, salinity, $CO_2$) into numerical models; commonly used in weather and climate forecasts.

Distal coastal region: Continental shelf, excluding near-coastal areas (cf. proximal coastal region)

Eastern Australian Current (EAC): Warm western boundary current of the south Pacific gyre.

El Niño-Southern Oscillation (ENSO): ENSO is strongly linked to interannual variability in weather and climate, including rainfall, SST and SLP anomalies, throughout all major ocean basins and most continents. ENSO has a frequency domain of 2.5 to 8 years.

Fossil layers: Also called secondary pycnoclines. They mainly appear during spring and are linked to regions of Subtropical Mode Water formation in the southwest Pacific and northeast Pacific Ocean (Sprintall and Roemmich, 1999).

Hadley circulation: A roughly zonally symmetric meridional circulation, rising over the Intertropical Convergence Zone (ITCZ) and descending over the subtropical high-pressure belt. It is driven by meridional differential heating, with the equatorial warm pool supplying most of the thermal energy to drive the Hadley Cell.

Heterotrophy: Process in which living organisms (heterotrophs) obtain energy by breaking down organic molecules from food.

Hovmöller plot: Two-dimensional diagram of how a parameter fluctuates in space-time, with one axis referring to time and the other to a spatial variable.

Indonesian Throughflow (ITF): Ocean current that transports water from the Pacific Ocean through the Indonesian Archipelago into the Indian Ocean.

Inter-decadal Pacific Oscillation (IPO): IPO is a low-frequency (15-30 years) climate index based on Pacific Ocean SST (cf. Pacific Decadal Oscillation). A positive IPO index is linked to warmer than usual temperatures within the tropical Pacific whereas the water in other regions is cooler than average. Conversely, tropical Pacific SST is reduced when the IPO index is negative. Notably, Australian rainfall predictability is dramatically increased during negative IPO phases due to stronger teleconnections of rainfall with ENSO events.

Intertropical Convergence Zone (ITCZ): Tropical zone of convergence of trade winds from both hemispheres. Rising air is resulting in heavy rainfall in

the ITCZ region. The position of the ITCZ is varying seasonally with the movement of the sun.

Isopybar: Surface of constant pressure.

Isopycnal: Surface of constant density.

Japanese Oceanographic Data Center (JODC): Japanese organisation in charge of compilation and distribution of marine data obtained from various Japanese research institutes and organisations.

Kelvin waves: An internal gravity wave that is travelling eastward along the equatorial Pacific Ocean. Low-frequency Kelvin waves are triggered by fluctuations in equatorial wind speed at the ocean surface. Kelvin waves have no meridional (north-south) velocity component

Latent heat flux (LHF, $Q_{lat}$): Heat flux from the water surface to the atmosphere due to evaporation. Units are Watt per square metre [$W/m^2$].

Little Ice Age (LIA): Period of global cooling between around 1400 and 1850 AD. The cooling in the northern hemisphere is well established whereas there is some controversy about to what extent the LIA has affected the southern hemisphere. The LIA coincided with periods of anomalously low solar activity (e.g. Maunder Minimum: 1645-1715 AD) and increased volcanic activity.

Mixed layer: Surface region of quasi-homogenous salinity, temperature and density created by the history of mixing (cf. mixing layer). The seasonal mixed layer is defined as being the maximum depth reached by the mixing layer over a diurnal or longer timescale.

Mixed layer depth (MLD): Zone of very abrupt change in either temperature and/or salinity, which defines the lower limit of the turbulent mixed layer.

Mixing layer: The mixing layer is the zone within the water column, which is currently and actively being mixed by turbulent processes, generally driven by surface forcing (cf. mixed layer). It is characterised by greater vertical homogeneity than the mixed layer.

Pacific Decadal Oscillation (PDO): PDO is a low-frequency (15-30 years) index based on North Pacific Ocean SST (cf. Interdecadal Pacific Oscillation). A

positive PDO index tends to coincide with warmer SST in the Eastern Pacific and colder SST in the North Pacific.

Photosynthesis: Process in which living organisms convert solar energy, $CO_2$ and water into glucose and oxygen ($O_2$).

Practical Salinity Scale (PSS): Scale used to measure the salinity of seawater. PSS is defined as the conductivity ratio of seawater to a standard potassium chloride (KCl) solution. PSS has no units.

Primary Production: Production of organic material from inorganic matter (e.g. $CO_2$) and solar energy, mainly via photosynthesis; equivalent to autotrophy.

Primitive Equations: Set of nonlinear differential equations - used to approximate global atmospheric flow.

Proximal Coastal Region: Area nearby the shore; includes ecosystems adjacent to the coastline, i.e. estuaries, mangroves and salt marshes (cf. distal coastal region)

Redfield Ratio: The ratio of carbon, nitrogen and phosphorus ($C_{org}$:N:P).

Schmidt Number: Ratio of kinematic viscosity to mass diffusivity

Sensible Heat Fluxes: Heat flux as a result of temperature differences between water and air, and between water and rain.

Southern Oscillation Index (SOI): Based on the sea level pressure (SLP) difference between Tahiti and Darwin.

Speleothems: From Greek “cave deposit”; the majority of speleothems are made of calcareous rock ($CaCO_3$); the term is encompassing numerous depositional cave features (e.g. stalactites).

Sverdrup (Sv): Unit of measure of volume transport ($10^6$ $m^3/s$ or 0.001 $km^3/s$). The entire global input of fresh water from rivers to the ocean is equal to about 1 Sv.

Turbulent Fluxes: Both latent heat flux and sensible heat flux are characterised as turbulent fluxes.

Walker Circulation: Atmospheric circulatory cell driven by the east-west temperature contrast in the underlying SST along the equatorial Pacific. It is characterised by a large-scale east-west overturning of air across the

equatorial Pacific Ocean, with convection to the west and subsidence to the east.

## A1.2 Glossary of Acronyms

| | |
|---|---|
| Agrif | Adaptive Grid Refinement In Fortran |
| BLT | barrier layer thickness |
| CARS | CSIRO Atlas of Regional Seas |
| CDIAC | Carbon Dioxide Information Analysis Center |
| Chl-a | chlorophyll a |
| CM2.1 | climate model version 2.1 |
| CMAP | CPC Merged Analysis of Precipitation |
| CO2* | $CO_{2aq} + H_2CO_3$ |
| $[CO_2]$ | $CO_2$ concentration |
| COADS | Comprehensive Ocean-Atmosphere Data Set |
| CPU | central processing unit |
| csv | comma-separated values |
| CTD | Conductivity-Temperature-Depth |
| DBDB | Digital Bathymetric Data Base |
| DIC | dissolved inorganic carbon |
| DOC | dissolved organic carbon |
| DOM | dissolved organic matter |
| EAC | Eastern Australian Current |
| ECMWF | European Centre for Medium-Range Weather Forecasts |
| ENIAC | Electronic numerical integrator and calculator |
| ENSO | El Niño-Southern Oscillation |
| EUC | Equatorial Undercurrent |
| $fCO_2$ | fugacity of $CO_2$ |
| GBR | Great Barrier Reef |
| HAMOCC5 | Hamburg Model of Carbon Cycle version 5 |
| hmc | high-magnesian calcite |
| HYCOM | HYbrid Coordinate Ocean Model |

| | |
|---|---|
| ILD | isothermal layer depth |
| IPO | Interdecadal Pacific Oscillation |
| ITCZ | Intertropical Convergence Zone |
| ITF | Indonesian Throughflow |
| JGOFS | Joint Global Ocean Flux Study |
| JODC | Japanese Oceanographic Data Center |
| K | gas exchange/transfer coefficient; K = k*s |
| k | gas transfer velocity; k = K/s |
| LHF | latent heat flux |
| ML | mixed layer |
| MLD | mixed layer depth |
| MODIS | Moderate Resolution Imaging Spectroradiometer |
| MPP | massive(ly) parallel processing |
| NAO | North Atlantic Oscillation |
| NASA | National Aeronautics and Space Administration |
| netcdf | network Common Data Form |
| NODC | National Oceanographic Data Center |
| NWP | numerical weather prediction |
| OGCM | Ocean General Circulation Model |
| OHT | ocean heat transport |
| $pCO_2$ | partial pressure of $CO_2$ |
| PDO | Pacific Decadal Oscillation |
| PISCES | Pelagic Interaction Scheme for Carbon and Ecosystem Studies |
| POC | particulate organic carbon |
| POM | particulate organic matter |
| ppmv | parts per million per volume |
| PSS | Practical Salinity Scale |
| $Q_{lat}$ | latent heat flux ($W/m^2$) |
| $Q_{sen}$ | sensible heat fluxes ($W/m^2$) |
| QLD | Queensland |
| ROMS | Regional Ocean Model System |

| | |
|---|---|
| s | solubility of $pCO_2$ in seawater (concentration/pressure) |
| SAM | southern annular mode |
| Sc | Schmidt number |
| SeaWiFS | Sea-Viewing Wide Field-of-View Sensor |
| SEC | Southern Equatorial Current |
| SHF | sensible heat fluxes |
| SLP | sea level pressure |
| SO | Southern Ocean |
| SSS | sea surface salinity |
| SST | sea surface temperature |
| STC | Subtropical Cells |
| Sv | Sverdrup |
| TA | total alkalinity |
| $tCO_2$ | total dissolved inorganic carbon (also $\sum CO_2$) |
| WOD | World Ocean Database |
| $xCO_2$ | mole fraction of $CO_2$ |

# A2 Giovanni – Satellite Data

## A2.1 Giovanni_multi_plots_Jan.m

```
%% Giovanni_multi_plots_Jan.m
% How to concatenate Giovanni netcdf files (example for January)
% Global: i=1:4320 ; j=1:2160        Coral Sea: i= 3865:4200 ; j= 721:1020
% grids with no data have the value 65535 (i.e. missing values and landmasses)
% Giovanni gridsize is 1/12 degrees
%
clear
 % add these two paths to be able to write netcdfs:
path(path,'C:/mexcdf/snctools')
path(path,'C:/mexcdf/mexnc')
% open the Giovanni files:
ncid1 =
netcdf.open('./day/T20010012001031.L3m_MO_SST_9.G3.nc','NC_NOWRITE');
T1=netcdf.getVar(ncid1,3); % extract SST
ncid2 =
netcdf.open('./day/T20020012002031.L3m_MO_SST_9.G3.nc','NC_NOWRITE');
T2=netcdf.getVar(ncid2,3);
ncid3 =
netcdf.open('./day/T20030012003031.L3m_MO_SST_9.G3.nc','NC_NOWRITE');
T3=netcdf.getVar(ncid3,3);
ncid4 =
netcdf.open('./day/T20040012004031.L3m_MO_SST_9.G3.nc','NC_NOWRITE');
T4=netcdf.getVar(ncid4,3);
ncid5 =
netcdf.open('./day/T20050012005031.L3m_MO_SST_9.G3.nc','NC_NOWRITE');
T5=netcdf.getVar(ncid5,3);
ncid6 =
netcdf.open('./day/T20060012006031.L3m_MO_SST_9.G3.nc','NC_NOWRITE');
T6=netcdf.getVar(ncid6,3);
ncid7 =
netcdf.open('./day/T20070012007031.L3m_MO_SST_9.G3.nc','NC_NOWRITE');
T7=netcdf.getVar(ncid7,3);
ncid8 =
netcdf.open('./day/T20080012008031.L3m_MO_SST_9.G3.nc','NC_NOWRITE');
T8=netcdf.getVar(ncid8,3);
ncid9 =
netcdf.open('./day/T20090012009031.L3m_MO_SST_9.G3.nc','NC_NOWRITE');
T9=netcdf.getVar(ncid9,3);
ncid10 =
netcdf.open('./day/T20100012010031.L3m_MO_SST_9.G3.nc','NC_NOWRITE');
T10=netcdf.getVar(ncid10,3);
%
SST_Jan=zeros(336,300,10);
```

```
SST_Jan(:,:,1)=T1(3865:4200,721:1020);
SST_Jan(:,:,2)=T2(3865:4200,721:1020);
SST_Jan(:,:,3)=T3(3865:4200,721:1020);
SST_Jan(:,:,4)=T4(3865:4200,721:1020);
SST_Jan(:,:,5)=T5(3865:4200,721:1020);
SST_Jan(:,:,6)=T6(3865:4200,721:1020);
SST_Jan(:,:,7)=T7(3865:4200,721:1020);
SST_Jan(:,:,8)=T8(3865:4200,721:1020);
SST_Jan(:,:,9)=T9(3865:4200,721:1020);
SST_Jan(:,:,10)=T10(3865:4200,721:1020);
%
for i=1:336;
   for j=1:300;
      for l=1:10;
         if SST_Jan(i,j,l)>40;            % assign NaN values to all grids without data
            SST_Jan(i,j,l)=NaN;
         end
      end
   end
end
%
SST_Jan_mean=zeros(336,300);
dividor=zeros(336,300);
for i=1:336;
   for j=1:300;
      for l=1:10;
         if isnan(SST_Jan(i,j,l))==0;    % for all non-zero values...
            dividor(i,j)=dividor(i,j)+1;  % count the number (n) of data available per grid
            SST_Jan_mean(i,j)=SST_Jan_mean(i,j)+SST_Jan(i,j,l); % SST sum
         end
      end
   end
end
%
for i=1:336;
   for j=1:300;
      if dividor(i,j)>0
         SST_Jan_mean(i,j)=SST_Jan_mean(i,j)./dividor(i,j); % (SST sum)/n
      end
   end
end
%
Lat=(-30):1/12:(-5-1/12);       %  Giovanni resolution is 1/12 degrees
Lon=(142):1/12:(170-1/12);
lat_rho=repmat(Lat,336,1);
lon_rho=repmat(Lon,300,1);
```

```
lon_rho=lon_rho';
% save the concatenated multi-monthly Giovanni SST average as a netcdf
 [dx, dy] = size(SST_Jan_mean);
ncid = netcdf.create('Jan_SST_mean_geo.nc','NC_NOCLOBBER');
dim1 = netcdf.defDim(ncid,'lon',dx);    % Define the dimensions of the variables
dim2 = netcdf.defDim(ncid,'lat',dy);
lon_rhoID = netcdf.defVar(ncid,'lon_rho','double',[dim1 dim2]); % Define lon_rho in the
file
lat_rhoID = netcdf.defVar(ncid,'lat_rho','double',[dim1 dim2]);
aervarID = netcdf.defVar(ncid,'SST','double',[dim1 dim2]);
netcdf.putAtt(ncid,aervarID,'units','°C');     % Assign unit attributes
netcdf.endDef(ncid);    % Leave define mode and enter data mode to write data.
netcdf.putVar(ncid,lon_rhoID,lon_rho);    % Write data to variable
netcdf.putVar(ncid,lat_rhoID,lat_rho);
netcdf.putVar(ncid,aervarID,SST_Jan_mean);    % Write data to variable
netcdf.close(ncid);
```

## A2.2 ROMS_Giovanni_intercomparison.m

```
%% ROMS_Giovanni_intercomparison.m
% The following is a matlab script written to facilitate the comparison of the ROMS SST
% with the satellite-derived SST, and it includes a upscaling of the satellite data.
clear
 % add these two paths to be able to write netcdfs:
path(path,'C:/mexcdf/snctools') %
path(path,'C:/mexcdf/mexnc')
%% ROMS
ncidR = netcdf.open('roms_avg_Y10_380_cat2.nc','NC_NOWRITE'); % open the ROMS
file
T=netcdf.getVar(ncidR,18);
lon_rho=netcdf.getVar(ncidR,7);lat_rho=netcdf.getVar(ncidR,8);
lat_rho=lat_rho(1:85,:);lon_rho=lon_rho(1:85,:);
Lon=lon_rho(:,1);
Lat=lat_rho(1,:);
%
SST_Roms=zeros(85,73,1,12);
for i=1:85
   for j=1:73
      for l=1:6
         SST_Roms(i,j,1,1)=SST_Roms(i,j,1)+T(i,j,32,l+0);
         SST_Roms(i,j,1,2)=SST_Roms(i,j,2)+T(i,j,32,l+6);
         SST_Roms(i,j,1,3)=SST_Roms(i,j,3)+T(i,j,32,l+12);
         SST_Roms(i,j,1,4)=SST_Roms(i,j,4)+T(i,j,32,l+18);
         SST_Roms(i,j,1,5)=SST_Roms(i,j,5)+T(i,j,32,l+24);
         SST_Roms(i,j,1,6)=SST_Roms(i,j,6)+T(i,j,32,l+30);
         SST_Roms(i,j,1,7)=SST_Roms(i,j,7)+T(i,j,32,l+36);
```

```
            SST_Roms(i,j,1,8)=SST_Roms(i,j,8)+T(i,j,32,l+42);
            SST_Roms(i,j,1,9)=SST_Roms(i,j,9)+T(i,j,32,l+48);
            SST_Roms(i,j,1,10)=SST_Roms(i,j,10)+T(i,j,32,l+54);
            SST_Roms(i,j,1,11)=SST_Roms(i,j,11)+T(i,j,32,l+60);
            SST_Roms(i,j,1,12)=SST_Roms(i,j,12)+T(i,j,32,l+66);
        end
    end
end
SST_Roms=squeeze(SST_Roms/6);
%
%% Giovanni
ncid1 = netcdf.open('./Jan_SST_mean_geo.nc','NC_NOWRITE');
T1=netcdf.getVar(ncid1,2); % extract SST
ncid2 = netcdf.open('./Feb_SST_mean_geo.nc','NC_NOWRITE');
T2=netcdf.getVar(ncid2,2);
ncid3 = netcdf.open('./Mar_SST_mean_geo.nc','NC_NOWRITE');
T3=netcdf.getVar(ncid3,2);
ncid4 = netcdf.open('./Apr_SST_mean_geo.nc','NC_NOWRITE');
T4=netcdf.getVar(ncid4,2);
ncid5 = netcdf.open('./May_SST_mean_geo.nc','NC_NOWRITE');
T5=netcdf.getVar(ncid5,2);
ncid6 = netcdf.open('./Jun_SST_mean_geo.nc','NC_NOWRITE');
T6=netcdf.getVar(ncid6,2);
ncid7 = netcdf.open('./Jul_SST_mean_geo.nc','NC_NOWRITE');
T7=netcdf.getVar(ncid7,2);
ncid8 = netcdf.open('./Aug_SST_mean_geo.nc','NC_NOWRITE');
T8=netcdf.getVar(ncid8,2);
ncid9 = netcdf.open('./Sep_SST_mean_geo.nc','NC_NOWRITE');
T9=netcdf.getVar(ncid9,2);
ncid10 = netcdf.open('./Oct_SST_mean_geo.nc','NC_NOWRITE');
T10=netcdf.getVar(ncid10,2);
ncid11 = netcdf.open('./Nov_SST_mean_geo.nc','NC_NOWRITE');
T11=netcdf.getVar(ncid11,2);
ncid12 = netcdf.open('./Dec_SST_mean_geo.nc','NC_NOWRITE');
T12=netcdf.getVar(ncid12,2);
%
SST=zeros(336,300,12);
SST(:,:,1)=T1(:,:);
SST(:,:,2)=T2(:,:);
SST(:,:,3)=T3(:,:);
SST(:,:,4)=T4(:,:);
SST(:,:,5)=T5(:,:);
SST(:,:,6)=T6(:,:);
SST(:,:,7)=T7(:,:);
SST(:,:,8)=T8(:,:);
SST(:,:,9)=T9(:,:);
```

```
SST(:,:,10)=T10(:,:);
SST(:,:,11)=T11(:,:);
SST(:,:,12)=T12(:,:);
%
Lat_orig=(-30):1/12:(-5-1/12);
Lon_orig=(142):1/12:(170-1/12);
% get same lat/long as ROMS
lons1=Lon';   % 1x85 vector (ROMS is already reduced)
lats1=Lat;      % 1x73 vector (reduce Giovanni)
[lats_m1,lons_m1]=meshgrid(lats1,lons1); % creates a lat/long 76x85 matrix
%
SST_Giov=zeros(85,73,12); %K=[];
for i=1:length(lons1)
   for j=1:length(lats1)
      for t=1:12 % t=month
   SST_Giov(i,j,t)=interp2(Lat_orig,Lon_orig,SST(:,:,t),lats_m1(i,j),lons_m1(i,j),'linear');
   if SST_Roms(i,j,t)==0
      SST_Giov(i,j,t)=0;
   end
   if SST_Giov(i,j,1)<22.9 || i==75 && j==26 || i==55 && j==59
      SST_Giov(i,j,t)=0;
      SST_Roms(i,j,t)=0;
   end
      end
   end
end
%
%% create joined netcdf
 [dx, dy, dt] = size(SST_Roms);
ncid = netcdf.create('linear_Giovanni_Roms_land4.nc','NC_NOCLOBBER');
dim1 = netcdf.defDim(ncid,'lon',dx);    % Define the dimensions of the variables
dim2 = netcdf.defDim(ncid,'lat',dy);
dim3 = netcdf.defDim(ncid,'time',dt);
lon_rhoID = netcdf.defVar(ncid,'lon_rho','double',[dim1 dim2]); % Define a new variable
lat_rhoID = netcdf.defVar(ncid,'lat_rho','double',[dim1 dim2]);
SST1ID = netcdf.defVar(ncid,'SST_Roms','double',[dim1 dim2 dim3]);
SST2ID = netcdf.defVar(ncid,'SST_Giov','double',[dim1 dim2 dim3]);
netcdf.putAtt(ncid,SST1ID,'units','°C');     % Assign unit attributes
netcdf.putAtt(ncid,SST2ID,'units','°C');
netcdf.endDef(ncid);    % Leave define mode and enter data mode to write data.
netcdf.putVar(ncid,lon_rhoID,lon_rho);    % Write data to variable
netcdf.putVar(ncid,lat_rhoID,lat_rho);
netcdf.putVar(ncid,SST1ID,SST_Roms);
netcdf.putVar(ncid,SST2ID,SST_Giov);
netcdf.close(ncid);
nc_dump('linear_Giovanni_Roms_land4.nc');
```

# A3 CO2SYS Sensitivity Study

The following section is a sensitivity analysis to seek the most sensitive parameter(s) from which to derive $fCO_2$ from the available temperature, salinity and carbon data.

## A3.1 Carbonate Species Distribution

To investigate the sensitivity of various biochemical parameters to changes in 1) salinity, 2) phosphate, 3) silicate, 4) temperature, 5) total alkalinity, 6) $tCO_2$ and 7) *p*H, all but one of the 6 input variables (only two geochemical parameters can be used as input variables, cf. section 7.2.2) were kept constant (Table A3.1.1). Three groups were created, with total alkalinity and $tCO_2$ utilised as predictors in group 1, total alkalinity and *p*H in group 2, and $tCO_2$ and *p*H in group 3 (Table A3.1.2).

For all three groups, temperature significantly influences the proportion of carbon present as $CO_2^*$ ($CO_{2aq} + H_2CO_3$) when all other predictor variables are kept constant ($R^2$ = 0.993-0.998, Figure A3.1.1). It is noteworthy that the trend for group 1 differs considerably from the others, with the temperature-$CO_2^*$ correlation being strongly positive and $CO_2^*$ [%] (proportion of carbon species present as $CO_2^*$) being significantly higher. The former is a result of *p*H not being a predictor variable and was thus not kept constant by CO2SYS. That is, as temperature is increased, *p*H as a consequence declines, which in turn increases the proportion of carbon present as $CO_2^*$, even though the direct impact of temperature is a $CO_2^*$ [%] reduction. The extent of the upward shift for group 1, in turn, depends on the values chosen for the constant predictors.

**Table A3.1.1. List of predictor variables, and the chosen constant and range for each parameter. Both constants and ranges were chosen to most closely match or encompass the values likely found within the Coral Sea.**

| predictor | constant | range |
|---|---|---|
| salinity [PSS] | 35 | 32.6-36.0 |
| phosphate [µmol/kg] | 0 | 0.0-5.5 |
| silicate [µmol/kg] | 0 | 0.0-1.0 |
| temperature [°C] | 26.2 | 18.6-31.0 |
| total alkalinity [µmol/kg] | 2400 | 2000-3000 |
| $tCO_2$ [µmol/kg] | 2100 | 1900-2400 |
| *p*H | 8.2 | 8.0-8.4 |

**Table A3.1.2. List of parameters that were allowed to vary in each subgroup. Each of the three groups utilises salinity, phosphate, silicate and temperature as predictor parameters. In addition, two out of three geochemical parameters (total alkalinity, $tCO_2$ and pH) are employed as predictors as well, allowing the third variable to always vary freely within that group.**

| Group / Subgroup | 1 | 2 | 3 |
|---|---|---|---|
| **1** | salinity, *p*H | salinity, $tCO_2$ | salinity, total alkalinity |
| **2** | phosphate, *p*H | phosphate, $tCO_2$ | phosphate, total alkalinity |
| **3** | silicate, *p*H | silicate, $tCO_2$ | silicate, total alkalinity |
| **4** | temperature, *p*H | temperature, $tCO_2$ | temperature, total alkalinity |
| **5** | total alkalinity, *p*H | total alkalinity, $tCO_2$ | |
| **6** | $tCO_2$, *p*H | | total alkalinity, $tCO_2$ |
| **7** | | $tCO_2$, *p*H | total alkalinity, *p*H |

Out of all predictor parameters, variability in *p*H most significantly impacts on ocean carbon geochemistry (carbonate species distribution, $fCO_2$ and $CaCO_3$ saturation state ($\Omega$) of aragonite and calcite. For fixed values of the other predictor parameters, a *p*H decline results in a larger proportion of $CO_2^*$ being present in the ocean waters (Figure A3.1.2), with their relationship generally being quadratic. The only exception to this is when both *p*H and temperature are allowed to vary (i.e. as in sub-sample 4 of group 1), as described in the previous paragraph. The net impact is a reduced rate of change in $CO_2^*$ [%] as a result of competing effects by *p*H and temperature as (cf. Figure A3.1.3).

Total alkalinity in general also displays a negative, quadratic relationship with $CO_2^*$ [%] (Figure A3.1.4), as long as *p*H is allowed to vary concomitantly. If *p*H is set to a fixed value (group 2, as well as subgroup 3.6; cf. Figure A3.1.5), there is no shift in carbonate species distribution with increasing total alkalinity as the latter only impacts on $tCO_2$. That is, all carbonate species will change in abundance proportionately. Similarly, $CO_2^*$ [%] remains invariable if $tCO_2$ is only allowed to influence total alkalinity, with *p*H being a constant (Figure A3.1.6). If *p*H is permitted to co-fluctuate with $tCO_2$, there is a positive, quadratic relationship between $tCO_2$ and $CO_2^*$ [%].

The direct impact of salinity on carbonate species distribution is negligible (±0.01%). However, similar to temperature, an increase in salinity results in lower *p*H, although this

negative association is only minor, thus not significantly impacting on the carbon distribution (±0.02%) within the range of salinities usually found in the upper ocean.

Nutrients (phosphate and silicate) do not display strong correlations with any of the other variables (result not shown).

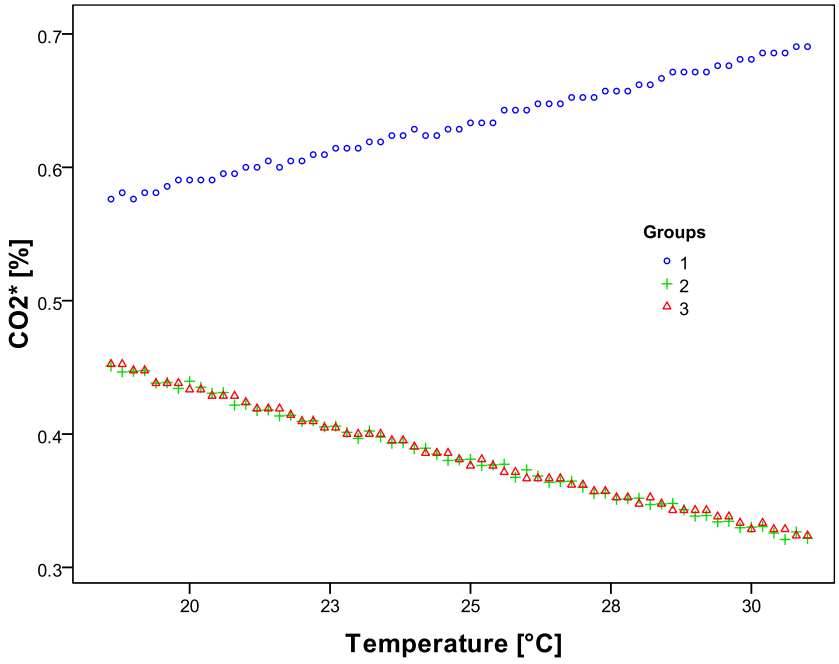


**Figure A3.1.1. Co-variation of temperature (predictor variable) and percentage of $CO_2^*$. Total alkalinity and $tCO_2$ were utilised as predictors in group 1, total alkalinity and pH in group 2, and $tCO_2$ and pH in group 3.**

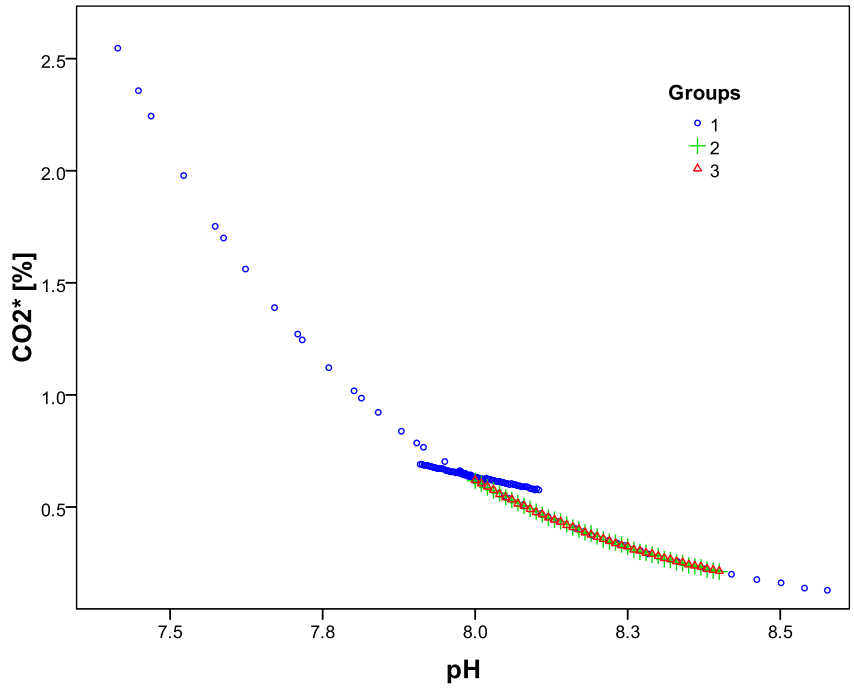


**Figure A3.1.2. Co-variation of *p*H and percentage of $CO_2^*$ (groups as in Figure A3.1.1). See also Figure A3.1.3 for a subdivision of group 1.**

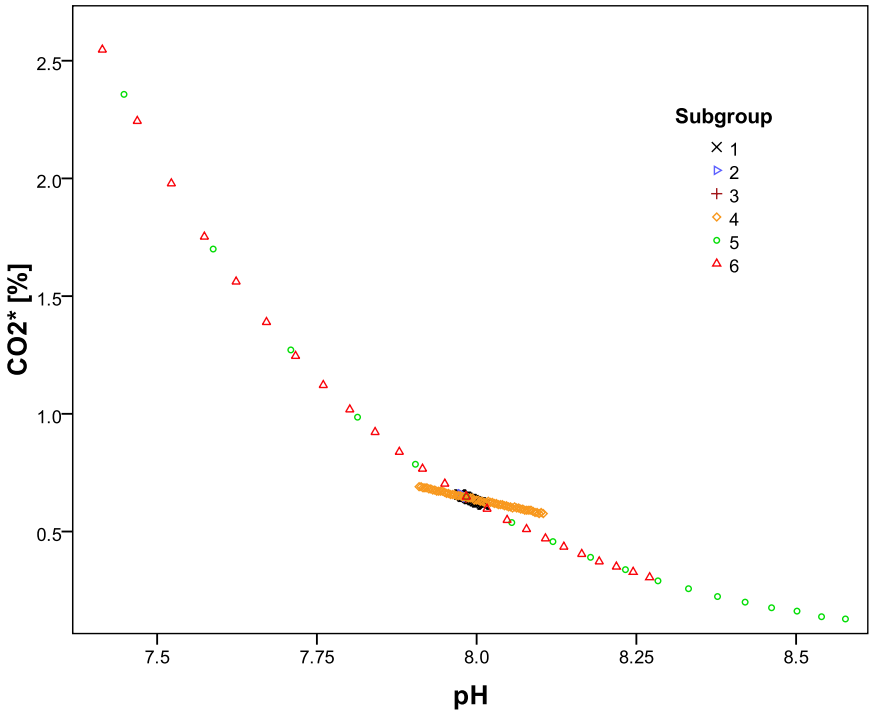


**Figure A3.1.3. Co-variation of *p*H and percentage of $CO_2^*$ for group 1. Subgroup 4 (all predictors but temperature were forced to remain constant, shown in orange) is the only subcategory displaying a distinctive relationship with $CO_2^*$ [%].**

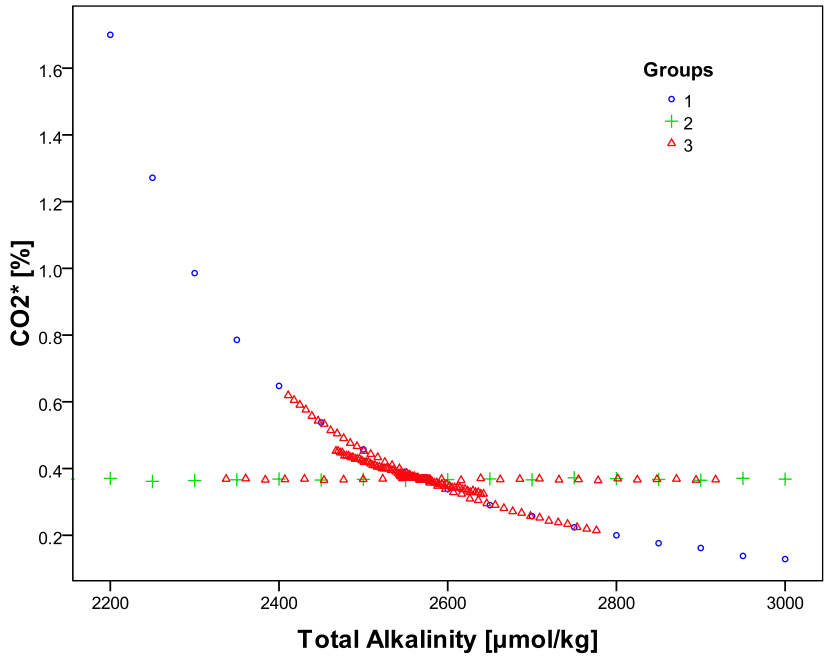


**Figure A3.1.4. Co-variation of total alkalinity and percentage of $CO_2^*$ (groups as in Figure A3.1.1). See also Figure A3.1.4 for a subdivision of group 3.**

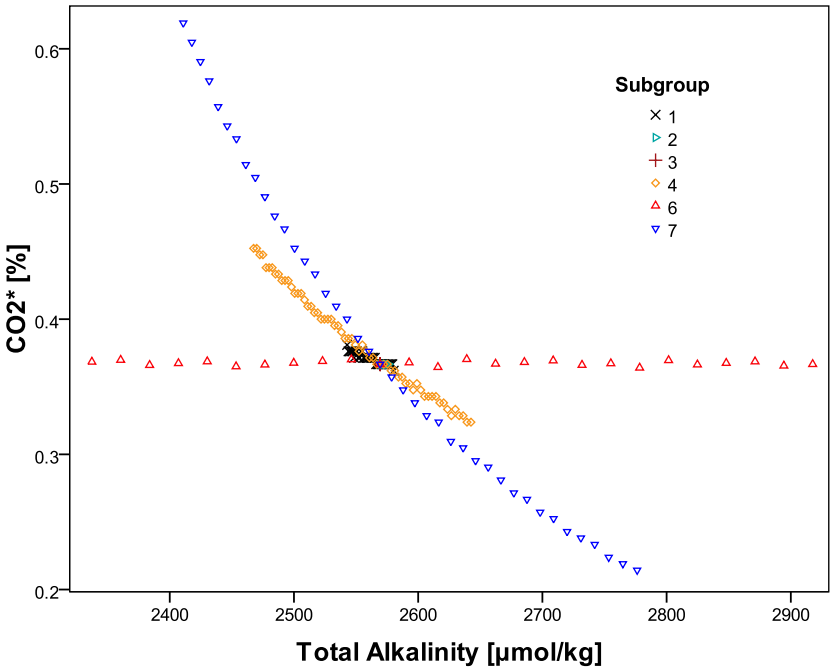


**Figure A3.1.5. Connection of total alkalinity and percentage of $CO_2^*$ for group 3. Subgroup 6, in which *p*H was kept constant, is the only subcategory not inducing a change in $CO_2^*$ [%].**

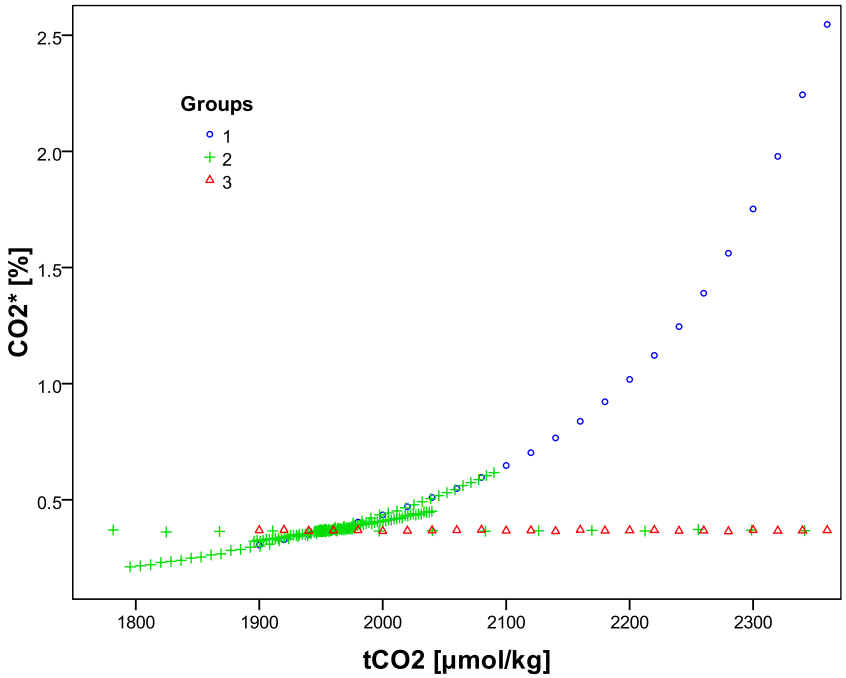


**Figure A3.1.6. Relationship between $tCO_2$ and percentage of $CO_2^*$ (groups as in Figure A3.1.1). See also Figure A3.1.7 for a subdivision of group 2.**

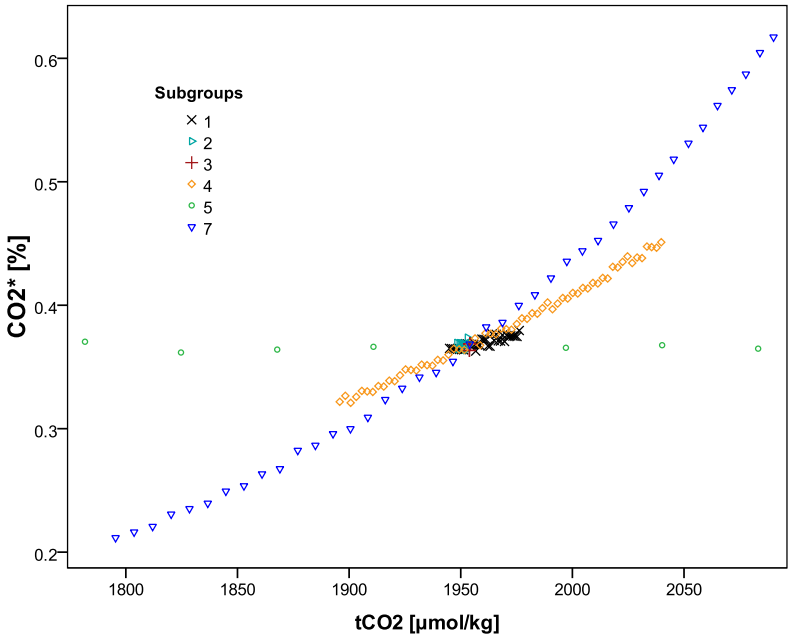


**Figure A3.1.7. Link between $tCO_2$ and percentage of $CO_2^*$ for group 2. Subgroup 5, in which *p*H was kept constant and total alkalinity allowed to vary, is the only subcategory not displaying a change in $CO_2^*$ [%].**

# A4 ROMS Documentation

The following are mostly extracts taken from online sources simply for summary purposes. For further details, refer to https://www.myroms.org/wiki/index.php/Documentation_Portal (ROMS-Rutgers) and http://roms.mpl.ird.fr/documentation.html (ROMS-Agrif).

## A4.1 Equations of Motion

The Regional Ocean Model System (ROMS) is a free-surface, terrain-following, 'primitive equations' ocean model widely used by the scientific community for a diverse range of applications. The algorithms that comprise ROMS are described in detail in Shchepetkin and McWilliams (2003, 2005).

The 'primitive equations' are based on the Boussinesq approximation (i.e. where density variations are neglected everywhere except in the gravitational force) and hydrostatic vertical momentum balance (i.e. parallel to gravity) and are expressed in an Earth-centered, Cartesian system of coordinates rotating at an angular velocity. The 'primitive equations' in Cartesian coordinates are shown below (cf. The momentum balance in the x- and y-directions are:

$$\frac{\partial u}{\partial t} + \vec{v} \cdot \nabla u - fv = -\frac{\partial \Phi}{\partial x} - \frac{\partial}{\partial z}\left(\overline{u' w'} - \nu \frac{\partial u}{\partial z}\right) + F_u + D_u$$

$$\frac{\partial v}{\partial t} + \vec{v} \cdot \nabla v - fu = -\frac{\partial \Phi}{\partial y} - \frac{\partial}{\partial z}\left(\overline{v' w'} - \nu \frac{\partial v}{\partial z}\right) + F_v + D_v$$

The list and explanation of variables is given in Table A4.1.1. An overbar represents a time average, whereas a prime represents a fluctuation about the mean.

The time evolution of a scalar concentration field, C(x,y,z,t) (e.g. salinity, temperature, or nutrients), is governed by the advective-diffusive equation:

$$\frac{\partial C}{\partial t} + \vec{v} \cdot \nabla C = -\frac{\partial}{\partial z}\left(\overline{C' w'} - \nu_\theta \frac{\partial C}{\partial z}\right) + F_C + D_C$$

The equation of state is given by $\rho = \rho(T,S,P)$.

As mentioned earlier, in the Boussinesq approximation, density variations are neglected in the momentum equations except in their contribution to the buoyancy force in the vertical momentum equation. Under the hydrostatic approximation, it is further assumed that the vertical pressure gradient balances the buoyancy force:

$$\frac{\partial \Phi}{\partial z} = -\frac{\rho g}{\rho_o}$$

The final equation expresses the continuity equation for an incompressible fluid:

$$\frac{\partial u}{\partial x} + \frac{\partial v}{\partial y} + \frac{\partial w}{\partial z} = 0$$

**Table A4.1.1. List of variables.**

| Variable | Description |
|---|---|
| $D_u$, $D_v$, $D_C$ | diffusive terms |
| $F_u$, $F_v$, $F_C$ | forcing terms |
| f(x,y) | Coriolis parameter |
| g | acceleration of gravity |
| h(x,y) | bottom depth |
| $\upsilon$, $\upsilon_\theta$ | molecular viscosity and diffusivity |
| $K_M$, $K_C$ | vertical eddy viscosity and diffusivity |
| P | total pressure $P \approx -\rho_o gz$ |
| ø(x,y,z,t) | dynamic pressure $ø = (P/\rho_o)$ |
| $\rho_o + \rho(x,y,z,t)$ | total *in situ* density |
| S(x,y,z,t) | salinity |
| t | time |
| T(x,y,z,t) | potential temperature |
| u, v, w | the (x,y,z) components of vector velocity $\vec{v}$ |
| x, y | horizontal coordinates |
| z | vertical coordinate |
| $\varsigma$(x,y,t) | the surface elevation |
| $Q_C$ | surface concentration flux |
| $\tau_s^x$, $\tau_s^y$ | surface wind stress |
| $\tau_b^x$, $\tau_b^y$ | bottom stress |

These equations are closed by parameterising the Reynolds stresses and turbulent tracer fluxes as:

$$\overline{u'w'} = -K_M \frac{\partial u}{\partial z}; \qquad \overline{v'w'} = -K_M \frac{\partial v}{\partial z}; \qquad \overline{C'w'} = -K_C \frac{\partial C}{\partial z}$$

The vertical boundary conditions can be prescribed as follows:

top ($z = \varsigma(x,y,t)$):

$$K_M \frac{\partial u}{\partial z} = \tau_s^x (x, y, t)$$

$$K_M \frac{\partial v}{\partial z} = \tau_s^y (x, y, t)$$

$$K_C \frac{\partial C}{\partial z} = \frac{Q_C}{\rho_o c \rho}$$

$$w = \frac{\partial \varsigma}{\partial t}$$

and bottom ($z = - h(x,y)$):

$$K_M \frac{\partial u}{\partial z} = \tau_b^x (x, y, t)$$

$$K_M \frac{\partial v}{\partial z} = \tau_b^y (x, y, t)$$

$$K_C \frac{\partial C}{\partial z} = 0$$

$$- w + \vec{v} \cdot \nabla h = 0$$

## A4.2 Split-Explicit Time-Stepping

For computational economy, the hydrostatic 'primitive equations' for momentum are solved using a split-explicit time-stepping scheme which requires special treatment and coupling between barotropic (fast) and baroclinic (slow) modes. A finite number of barotropic time steps, within each baroclinic step, are carried out to evolve the free-surface and vertically integrated momentum equations. In order to avoid the errors associated with the aliasing of frequencies resolved by the barotropic steps but unresolved by the baroclinic step, the barotropic fields are time averaged before they replace those values obtained with a longer baroclinic step. A cosine-shape time filter, centered at the new time level, is used for the averaging of the barotropic fields (Shchepetkin and McWilliams, 2005). In addition, the separated time-stepping is constrained to maintain exactly both volume conservation and consistancy preservation properties which are needed for the tracer equations (Shchepetkin and McWilliams,

2005). The time-stepping algorithm in ROMS allows a substantial increase in the permissible time-step size due to enhanced stability (Shchepetkin and McWilliams, 2005). This is achieved by a specially designed predictor-corrector time step, where once the velocity is computed for the new sub-step (predictor or corrector), it is immediately used for the computation of tracers, and vice versa, with similar properties for the sea level free-surface and barotropic momentum. This scheme closely couples the fields, suppresses computational modes, and has a dissipation-dominant truncation error for the physical mode (as opposed to a dispersion-dominant error of the commonly used leap-frog or forward-backward time steps). As a consequence ROMS yields physically meaningful (i.e.: smooth on the grid scale) vertical velocity fields, which is known to be difficult with a hydrostatic, primitive-equation ocean model. The expanded regime of stability allows a larger time steps, by a factor of about four, which more than offsets the increased cost of the predictor-corrector algorithm. Yet a further gain in computational efficiency comes from putting the relatively expensive transport parameterisation outside the predictor-corrector cycle, thus halving their computational cost. Numerical time stepping uses a discrete approximation to $\frac{\partial \Phi(t)}{\partial t} = F(t)$, where ø represents one of u, v, C, or ς and F(t) corresponds to all forcing terms on the right-hand-side. Not all versions of ROMS use the same time-stepping algorithm.

In the vertical, the ‘primitive equations’ are discretised over variable topography using stretched terrain-following coordinates (Figure A4.2.1) (Song and Haidvogel, 1994). The stretched coordinates allow increased resolution in areas of interest, such as thermocline and bottom boundary layers. The default stencil uses centred, second-order finite differences on a staggered vertical grid. Options for higher order stencil are available via a conservative, parabolic spline reconstruction of vertical derivatives (Shchepetkin and McWilliams, 2005). This class of model exhibits stronger sensitivity to topography which results in pressure gradient errors. These errors arise due to splitting of the pressure gradient term into an along-sigma component and a hydrostatic correction (for details, see Haidvogel and Beckmann, 1999). The numerical algorithm in ROMS is designed to reduce such errors (Shchepetkin and McWilliams, 2003).

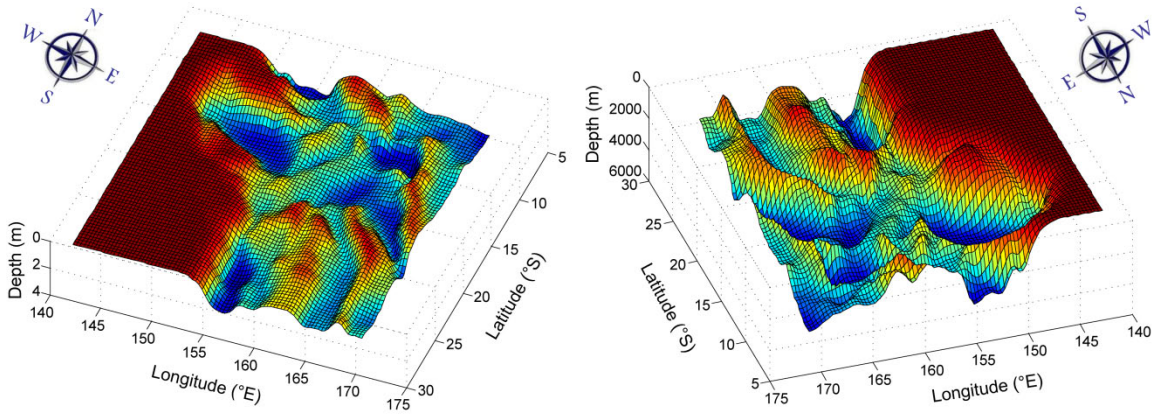


**Figure A4.2.1. Surface plots of the vertical coordinate (z) for the shallowest (z=32, left) and deepest (z=1, right) depth levels within the Coral Sea. ROMS utilises the sigma coordinate system, i.e. stretched, terrain-following vertical coordinates. In the horizontal, orthogonal curvilinear coordinates are employed for the free-surface model. For the Coral Sea study, ROMS was run with 32 vertical levels and a horizontal grid resolution of 1/3°.**

In the horizontal, the primitive equations are evaluated using boundary-fitted, orthogonal curvilinear coordinates on a staggered Arakawa C-grid. The general formulation of curvilinear coordinates includes both Cartesian (constant metrics) and spherical (variable metrics) coordinates. Coastal boundaries can also be specified as a finite-discretised grid via land/sea masking. As in the vertical, the horizontal stencil utilizes a centred, second-order finite differences. However, the code is designed to make the implementation of higher order stencils easily.

ROMS has various options for advection schemes: second- and forth-order centred differences; and third-order, upstream biased. The later scheme is the model default and it has a velocity-dependent hyper-diffusion dissipation as the dominant truncation error (Shchepetkin and McWilliams, 1998). These schemes are stable for the predictor-corrector methodology of the model. In addition, there is an option for conservative parabolic spline representation of vertical advection which has dispersion properties similar to an eight-order accurate conventional scheme.

There are several subgrid-scale parameterizations in ROMS. The horizontal mixing of momentum and tracers can be along vertical levels, geopotential (constant depth) surfaces (chosen here), or isopycnic (constant density) surfaces.

The vertical mixing parameterization in ROMS can be either by local or nonlocal closure schemes. The local closure schemes are based on the level 2.5 turbulent kinetic energy equations by (Mellor and Yamada, 1982) and the Generic Length Scale (GLS) parameterization (Umlauf and Burchard, 2003). The non-local closure scheme, used in this study, is based on the K-profile planetary (KPP) boundary layer formulation by Large *et al*. (1994). The K-profile scheme has been expanded to include both surface and bottom oceanic boundary layers. The GLS is a two-equation turbulence model that allows a wide range of vertical mixing closures. Several stability functions (Galperin *et al.*, 1988; Canuto *et al.*, 2001) have been also added to provide further flexibility.

ROMS is a very modern code and modular code written in F90/F95. It uses C-preprocessing to activate the various physical and numerical options. The code can be run in either serial or parallel computers. The code uses a coarse-grained parallelization paradigm which partitions the computational 3D grid into tiles. Each tile is then operated on by different parallel threads. Originally, the code was designed for shared-memory computer architectures and the parallel compiler-dependent directives (OpenMP Standard) are placed only in the main computational routine of the code. An MPI version of the code has been developed so both shared and distributed-memory paradigms coexist together in a single code. Currently, the data exchange between nodes is done with MPI.

ROMS has extensive pre- and post-processing software for data preparation, analysis, plotting, and visualization. The entire input and output data structure of the model is via NetCDF which facilitates the interchange of data between computers, user community, and other independent analysis software.

## A4.3 Preprocessing

In order to be able to compile ROMS, the model has to be preprocessed by running several MATLAB files in a specific order in the run directory (RUN_dir):

1. make_grid.m
2. make_forcing.m
3. make_QSCAT_clim.m OR make_clim.m
4. make_clim_orca05.m

5. make_clim_pisces.m
6. make_dust.m

Most of these files will call another script, *romstools_param.m*, in which most of the necessary changes can be made when running ROMS at various locations or grids. *make_grid* creates the grid file for the area of interest (NOTE: the MATLAB output will provide the user with values for the model dimensions, LLm0 and MMm0, which will have to be substituted into *param.h* before model compilation); *make_forcing* first provides the matrices with zeroes and definitions of variables. It then fills the matrices with data derived from the Comprehensive Ocean-Atmosphere Data Set (COADS) (e.g. Woodruff *et al.*, 1987; da Silva *et al.*, 1994), which contains the most complete observational sea surface dataset since 1854. COADS is frequently used to provide boundary conditions in long-term integrations of ocean and atmosphere general circulation models (GCMs) (da Silva *et al.*, 1994). Data parameters incorporated in COADS include zonal and meridional wind components, air temperature, SST, sea level pressure (SLP), dew point depression, cloudiness and 'present weather' (da Silva *et al.*, 1994). The file *make_QSCAT_clim* is then invoked to override the COADS-derived wind data within the netcdf forcing file. Quikscat contains satellite-derived wind data, which has a higher resolution (1/4°) compared to COADS (1°). Furthermore, Quikscat data is newer (1999 onwards) than COADS (1984-2000). Both *make_forcing* and *make_QSCAT_clim* provide ocean surface forcing, which includes solar shortwave radiation, surface net heat flux sensitivity, SST, SSS, surface freshwater flux (E-P), surface net heat flux and surface momentum stress in u- and v-components.

The lateral boundary conditions and the initial conditions are added with either the *make_clim_orca05* or the *make_clim* file (see appendix A4.3.1). Parameters included into the climate netcdf file are salinity, potential temperature, momentum in u and v components and free surface. To add biological forcing to the climate file, *make_clim_pisces* is invoked. The latter file will include nitrate, phosphate, silicon, oxygen, DIC, total alkalinity, DOC and iron into the climate file. *make_dust*, finally, will create an additional netcdf file, *roms_frcbio.nc*, which contains dust forcing. The addition of this forcing file is important since dust contains a substantial amount of iron, which

can significantly enhance phytoplankton growth and, thus, alter the carbon cycle (cf. Winckler *et al.*, 2008).

### A4.3.1 ORCA vs WOA/Levitus

There are two file options for the climate forcing; one is *make_clim*, which invokes the World Ocean Atlas 2005 (WOA05) dataset, and the other is *make_clim_orca05*, which will call model output data derived from ORCA. ORCA, in turn, derived its output from the ocean general circulation model (OGCM) OPA (Océan PAralléllisé), which is a coarse resolution, primitive equation model (Madec *et al.*, 1998; Foujols *et al.*, 2000). For most model runs, *make_clim_orca05* was chosen over *make_clim* since the latter has a very low resolution and therefore large errors compared to the model derived output. Specifically, *make_clim* does not provide a very good structure for currents, thus being a disadvantage compared to *make_clim_orca05*.

### A4.3.2 Output of Preprocessing

Altogether, the preprocessing results in the output of six netcdf files, five of which will be required during compiling of ROMS:

1. roms_grid.nc ← make_grid.m
2. roms_forcing.nc ← make_forcing.m AND make_QSCAT_clim.m
3. make_ini.nc ← make_clim_orca05.m AND make_clim_pisces.m
4. roms_oa.nc ← make_clim_orca05.m AND make_clim_pisces.m
5. roms_clim.nc ← make_clim_orca05.m AND make_clim_pisces.m
6. roms_frcbio.nc ← make_dust.m

The file *roms_oa.nc* (oa = objective analysis), generated by *make_clim_orca05.m* and/or *make_clim.m*, is an intermediate file, wherein hydrographic data is stored on a vertical grid instead of a horizontal grid. It is not used in ROMS and can thus be removed.

## A4.4 Model Run

### A4.4.1 Compiling and Running

Before compiling ROMS, the file *cppdefs.h* may have to be checked to see whether ROMS has been configured correctly. For model runs on regional scales, “REGIONAL” needs to be defined. If open boundaries are required on any of the four borders (east, west, south, north), then the appropriate border(s) will have to be defined (cf. “Open Boundary Conditions” within *cppdefs.h*). If biological output is desired, then “BIOLOGY” should be defined as well.

Care has to be taken that the physical grid and array dimensions (LLm0 and MMm0) are defined correctly in the file *param.h*. Both values are provided when running the MATLAB file *make_grid.m* during preprocessing. In order for the correct dimensions to be read into the compiler, the configuration name (e.g. Coral Sea) in *param.h* and *cppdefs.h* will have to match. Otherwise, an error message will be received when attempting to run ROMS.

If parallelisation is desired to speed up the model run, either MPI or OpenMP will have to be defined in *cppdefs.h*, with appropriate changes in *param.h* to specify the amount of nodes and processors to be used.

Once *param.h* and *cppdefs.h* have been checked and updated, the file *jobcomp.h* is invoked in linux in RUN_dir to compile the model using all netcdf files obtained during preprocessing:

./jobcomp

After the model has been successfully compiled, there are several options to run the model, the most basic one being:

./roms roms.in >roms.out

If the run is successful, two main netcdf files will be created:

file_name_his.nc

file_name_avg.nc

Their filename and output frequency is given in *roms.in*. Make sure to either remove all output files from the output folder or change the names of the output files (in *roms.in*) if ROMS is run more than once since the previous files will be overridden.

Note that >roms.out is not strictly necessary to add but is useful to keep track of the output during and after the run since the progress of the model run will be saved under roms.out. Similar to the netcdf files, either move or change the name of the output-file (e.g. roms1.out) since it will be overridden as well by the next run.

In addition to the above output files, two biological output files will be created if BIOLOGY has been defined in cppdefs.h:

file_name_diabio_avg.nc

file_name_diabio_his.nc

### A4.4.2 Multiple Output Files during a Model Run

Before running a model, the output rate has to be specified (e.g. output for every $5^{th}$ day is to be saved into netcdf files). For model runs in excess of a year, or for model runs over a large area, it is recommended to create monthly output files (e.g. 1-month worth of data with output given for every $5^{th}$ day), which has several benefits. Firstly, it avoids the creation of excessively large output files (>1 GB). In addition, unscheduled termination of running jobs frequently occurs, resulting in loss of data or incomplete output files. Monthly output files are not only smaller in size but they also assure the user that, in the event of an unscheduled job termination, the model can be restarted and completed more efficiently and quickly: ROMS can simply be resumed after the last successfully completed month, which saves a lot of computing time. If, after the completion of a simulation, yearly output files are preferable, the monthly files can be concatenated (joined) with freely available software (e.g. ncrcat, nco.sourceforge.net/nco.html) to form a yearly file.

To create multiple monthly (or yearly) output files, a pbs file, roms_run.pbs, can be utilised when submitting a job, i.e. instead of “./roms roms.in”, “./roms_run.pbs” is invoked at job submission. This pbs script enables the user to easily adjust the desired output type (monthly vs yearly), amount of months and/or years (length of model run), and the timing (date of first/last model output).

## A4.5 Spin-up

In general, complex 3-dimensional models such as ROMS have to be run for several model-years before an equilibrium state is achieved under the applied forcing. For a seasonal run with no interannual or climate forcing, seasonal variation is expected but there should be no change in the forcing beyond the seasonal signal. In the case of ROMS_Agrif, constant forcing for the Coral Sea is achieved after the fourth model year. This spin-up is short compared to global models, which frequently require 100-3000 modelling years due to the much larger area. For the Coral Sea, the spin-up time is also reduced when the area is forced at all borders (i.e. east, west, south and north are specified as open boundaries).

In the Coral Sea, statistical equilibrium is achieved after about one model year run. The volume averaged kinetic energy ($E_{kin}$) and the surface averaged $E_{kin}$ stabilise first, whereas temperature and salinity will take longer, around 2-3 years for the surface ocean in Coral Sea. Conversely, a spin-up of 100-1000 years would be required to reach equilibrium in the deep ocean due to slow currents and small gradients. The ROMS-Pisces output presented in this thesis is derived from the $11^{th}$ model year, after a spin-up period of 10 years.

## A4.6 MLD_obtainer_geotrue.m

```
%% MLD_obtainer_geotrue.m
% how to obtain MLD from salinity and temperature profiles using the threshold method
%                                                    - Jasmine Jaffres, September 2010
%% how to obtain density
% Density (?, kg/m3) is calculated using the One Atmosphere International Equation of State of Seawater, 1980
% T = temperature [°C]; S = practical salinity
% area: 142<lon<(170+1/3); -29.5<lat<-6.9022;
clear
% add these two paths to be able to write netcdfs:
path(path,'C:/mexcdf/snctools')
path(path,'C:/mexcdf/mexnc')
%
ncid = netcdf.open('roms_avg_Y10_380_cat2.nc','NC_NOWRITE'); % open the ROMS file
T=netcdf.getVar(ncid,18);
S=netcdf.getVar(ncid,19);
```

```
lon_rho=netcdf.getVar(ncid,7);lat_rho=netcdf.getVar(ncid,8);
Lon=lon_rho(:,1); % Lon=142:1/3:(170+1/3);
Lat=lat_rho(1,:); % ~Lat=-30:1/3:-6;
%
% ?w = density of the Standard Mean Ocean Water (SMOW)
pw=zeros(86,73,32,72); density=zeros(86,73,32,72);
for i=1:86
   for j=1:73
      for k=1:32
         for l=1:72
pw(i,j,k,l) = 999.842594 + 6.793952*10^(-2)* T(i,j,k,l) - 9.09529*10^(-3)* T(i,j,k,l)^2 +
1.001685*10^(-4)* T(i,j,k,l)^3 - 1.120083* 10^(-6)* T(i,j,k,l)^4 + 6.536332* 10^(-9)*
T(i,j,k,l)^5;
density(i,j,k,l) = pw(i,j,k,l) + (8.24493*10^(-1) - 4.0899*10^(-3)* T(i,j,k,l) +
7.6438*10^(-5)* T(i,j,k,l)^2 - 8.2467* 10^(-7)* T(i,j,k,l)^3 + 5.3875* 10^(-9)*
T(i,j,k,l)^4)* S(i,j,k,l) + (-5.72466* 10^(-3) + 1.0227* 10^(-4)* T(i,j,k,l) - 1.6546* 10^(-
6)* T(i,j,k,l)^2)* S(i,j,k,l)^(3/2) + 4.8314* 10^(-4)* S(i,j,k,l)^2;
         end
      end
   end
end
%
%% how to obtain depth (rather than grid numbers)
% % use script zlevs.m from the ROMS toolbox to obtain depth
h=netcdf.getVar(ncid,3); % h = bathymetry
zeta=netcdf.getVar(ncid,13,[0 0 0],[86 73 72]);
theta_s=6;theta_b=0;hc=10;N=32; % constants set in roms.in
type=1; % type 1 = rho point; type 2 = w point
[M,L,time]=size(zeta); %[M,L]=size(h); % length/size of h [x,y]=[86 73]
%
% Set S-Curves in domain [-1 < sc < 0] at vertical W- and RHO-points.
cff1=1./sinh(theta_s);
cff2=0.5/tanh(0.5*theta_s);
if type==2
   sc=((0:N)-N)/N;
   N=N+1;
else
   sc=((1:N)-N-0.5)/N;
end
Cs=(1.-theta_b)*cff1*sinh(theta_s*sc)+theta_b*(cff2*tanh(theta_s*(sc+0.5))-0.5);
%
% Create S-coordinate system: based on model topography h(i,j), fast-time-averaged
% free-surface field (zeta) and vertical coordinate transformation metrics compute
evolving
% depths of the three-dimensional model grid.
hinv=1./h;
```

```
hinv3D=zeros(M,L,time);
for l=1:time
     hinv3D(:,:,l)=hinv;
end
h3D=zeros(M,L,time);
for l=1:time
     h3D(:,:,l)=h;
end
cff=hc*(sc-Cs);
cff1=Cs;
cff2=sc+1;
z=zeros(M,L,N,time); % z=zeros(N,M,L);
for k=1:N
    z0=cff(k)+cff1(k)*h3D;
    z(:,:,k,:)=z0+zeta.*(1.+z0.*hinv3D); % depth (z) in meters
end
%
```

**%% how to obtain the MLD**

```
% For the threshold method, deltaT = 0.03 kg/m3 was used to obtain the MLD
d10=zeros(86,73,72);
density10=zeros(86,73,72);
densityMLD=zeros(86,73,72); % density at the depth of the mixed layer
for l=1:72
   for j=1:73
      for i=1:86
           d10(i,j,l)=find(z(i,j,:,l)>-10,1); % gives vertical grid number where depth<10m
           density10(i,j,l)=density(i,j,d10(i,j,l),l); % density at 10 m depth
           densityMLD(i,j,l)=density10(i,j,l)+0.03; % density at depth of MLD
      end
   end
end
%
% find depth (m) where densityMLD=density
grid_d_MLD=zeros(86,73,72);
MLD=zeros(86,73,72);
for l=1:72
   for j=1:73
      for i=1:86
         if density(i,j,:,l)>1001 % to avoid overlap with 100_0 ppm level
            grid_d_MLD(i,j,l)=find(density(i,j,:,l)<densityMLD(i,j,l),1);
            MLD(i,j,l)=z(i,j,grid_d_MLD(i,j,l),l);
         else
            grid_d_MLD(i,j,l)=0;
            MLD(i,j,l)=0;
         end
      end
```

```
   end
end
%
%% how to save MLD in a netcdf file
[dx, dy, dt] = size(MLD);    % Get the dimensions of data to be written to file
ncidM = netcdf.create('MLD_380_geo.nc','NC_WRITE');    % Create netcdf files
dim1 = netcdf.defDim(ncidM,'lon',dx);    % Define the dimensions of the variables
dim2 = netcdf.defDim(ncidM,'lat',dy);
dim3 = netcdf.defDim(ncidM,'time',dt);
lon_rhoID = netcdf.defVar(ncidM,'lon_rho','double',[dim1 dim2]); % Define a new
variable lat_rhoID = netcdf.defVar(ncidM,'lat_rho','double',[dim1 dim2]);
MLD_ID = netcdf.defVar(ncidM,'MLD','double',[dim1 dim2 dim3]);
netcdf.putAtt(ncidM,MLD_ID,'units','m');     % Assign unit attributes
netcdf.endDef(ncidM);    % Leave define mode and enter data mode to write data.
netcdf.putVar(ncidM,lon_rhoID,lon_rho);    % Write data to variable
netcdf.putVar(ncidM,lat_rhoID,lat_rho);
netcdf.putVar(ncidM,MLD_ID,MLD);
netcdf.close(ncidM);
```

# A5 Digital Excel Data Files

Digital data on which much of this thesis is based can be provided upon contacting the author.

# A6 Relevant Publications

The following peer-refereed papers are pertinent to the thesis. If interested, copies can be obtained from the author:

Jaffrés, J. and Everingham, Y. (2005) An exploratory investigation of the relationship between decadal rainfall and climate indices. *Proc. Aust. Soc. Sugar Cane Technol.*, *27*, 96-108.

Jaffrés, J. B. D., Shields, G. A. and Wallmann, K. (2007) The oxygen isotope evolution of seawater: A critical review of a long-standing controversy and an improved geological water cycle model for the past 3.4 billion years. *Earth-Science Reviews*, *83*, 83-122.